

Influence of grain morphology on strengthening of aluminium and magnesium alloys

A thesis submitted for the degree of Doctor of Philosophy (PhD)

By

Shishir Keerti

Brunel Centre of Advanced Solidification Technology

Brunel University London

United Kingdom

August 2024

*This thesis is dedicated to
my family for their
love, support and encouragement*

Abstract

The Hall-Petch equation is commonly employed to establish a connection between the yield strength/hardness of metallic materials and the grain diameter (d). However, for alloys having grains with dendritic morphology, a more accurate representation of the Hall-Petch equation involves substituting d with the secondary dendritic arm spacing (SDAS), denoted as λ_2 . This thesis underscores the significance of considering a perimeter-associated parameter, rather than relying solely on d or λ_2 , to account for strength contribution from morphological changes in various alloys. To express the complexity of dendritic / grain morphology in 2 dimension, a perimeter associated parameter (p') has been proposed. And, a comprehensive generic Hall-Petch relation expressed as $\sigma = \sigma_0 + k''/\sqrt{p'}$, where p' signifies the area per unit perimeter which can be accurately measured using digital imaging tools and k'' is the slope representing Hall-Petch constant, is being proposed. To substantiate the validity of this proposed relation, controlled solidification experiments were conducted on Al-Si and Al-Ce binary alloys, encompassing a range of cooling rates from 0.000167 °C/s to 0.34 °C/s. The degree of dendritic structure in primary α -Al was deliberately manipulated through solute content, such as the addition of Si or Ce. Notably, the relationship between λ_2 and the corresponding p' is observed to be non-linear, both experimentally and theoretically. This underscores the critical importance of incorporating the perimeter-associated parameter p' as a fundamental strength metric in the Hall-Petch relation. The resulting changes in hardness, in conjunction with evolving grain morphologies, were meticulously analysed. The experimental data from a spectrum of observed morphologies (faceted, rosette, and dendritic) fit more effectively with our proposed generic Hall-Petch relationship compared to conventional representations.

To assess the applicability of the new Hall-Petch relationship across different alloy systems, magnesium (Mg) alloys were also investigated. Wedge mould castings of commercially

available AZ91D alloy and Mg-5 and 9 wt.% binary alloys were examined. The diverse cooling rates induced by the wedge mould, along with varying solute content, led to a range of morphologies in the magnesium grains. Tensile tests were conducted on both as-cast and solution-treated AZ91D alloy to examine the relationship between d , λ_2 , p' , and yield strength (YS). The proposed generic Hall-Petch relationship yields better coefficient of regression when p' is considered instead of d or λ_2 . This underscores the significance of incorporating perimeter-associated parameters to accurately quantify the variation in the morphology of grain structures across different alloys.

During the examination of dendritic structure morphology in Al-Ce binary alloys, high thermal stability of $\text{Al}_{11}\text{Ce}_3$ was recognised. Spheroidization experiments were conducted to evaluate the coarsening resistance of the $\text{Al}_{11}\text{Ce}_3$ phase in Al-5Ce alloy, with comparisons made to Al-5Si alloy through circularity measurements. The circularity of $\text{Al}_{11}\text{Ce}_3$ changed from 0.64 to 0.66, while the circularity of eutectic Si changed from 0.55 to 0.8 during isothermal annealing at 400°C. To exploit the superior thermal stability of Al-Ce alloys, new alloys incorporating various compositions of Sc, Zr, Si and Mg for their mechanical properties at elevated temperatures. Specimens were fabricated using gravity and high-pressure die casting techniques. The addition of 0.2 wt.% Sc and 0.2 wt.% Zr resulted in the formation of nanoscale $\text{Al}_3\text{Sc,Zr}$ precipitates with an average particle size of approximately 3 nm at the peak aged condition of 300°C. Moreover, the addition of 0.4 wt.% Sc and 0.2 wt.% Zr refined the grain structure, leading to the formation of grains with an average size of approximately 20 μm . Specimens cast through HPDC were tested at room and elevated temperatures ranging from 150 to 300°C. The yield strength (YS) of Al-10Ce-0.2Sc-0.2Zr was measured to be 115 MPa with a retention factor of 0.9 at 300°C.

Acknowledgement

Foremost, I wish to extend my deepest gratitude to my supervisor, Prof. Hari Babu Nadendla, whose expertise, guidance, and unwavering support have been pivotal in the completion of this thesis. His constructive feedback and thoughtful mentorship have not only directed the course of this research but also significantly contributed to my development as a researcher.

I am also deeply grateful to Prof. Dmitry, Prof. Hamid, and Dr. Yan Huang for their supportive guidance throughout the research process, offering inspiring discussions and constructive suggestions. My sincere appreciation extends to my colleagues Dr. Xinliang, Dr. Onuh, Dr. Erdem, and Ms. Spandana for their invaluable support during the experimental work and technical assistance.

A heartfelt thank you is owed to Dr. Loredana, Mr. Peter Lloyd, and Mr. Jon Gadd for their crucial assistance during the experimental phases. I am particularly indebted to Dr. Qing Cai for his essential support in TEM analysis.

Finally, I am profoundly thankful to my family, especially my wife, Mrs. Rachell Peters. I consider myself extremely fortunate to have their unwavering support and love throughout this journey. Her selfless and caring commitment towards me has made this experience fruitful and enjoyable.

Table of content

1	Introduction.....	25
1.1	Background	25
1.2	Research objectives	29
1.3	Outline of thesis	30
2	Literature review	32
2.1	Solidification in Al alloys	32
2.1.1	Constitutional undercooling.....	32
2.2	Classical nucleation theory.....	33
2.3	Homogenous nucleation.....	33
2.3.1	Heterogeneous Nucleation.....	35
2.4	Growth after nucleation.....	38
2.4.1	Planar growth.....	38
2.4.2	Dendritic growth in alloys	39
2.5	Scaling of dendrites.....	42
2.6	Dendritic arm coarsening	46
2.7	Hall-Petch relationship.....	48
2.7.1	Dislocation pile-up model.....	48
2.7.2	Grain boundary source model.....	50
2.7.3	Slip distance model	52
2.7.4	Composite model	53
2.8	limitations of Hall-Petch relationship	56
2.9	Hall-Petch relationship and texture dependence of k in Mg alloys.....	58
2.10	Dendritic orientation selection.....	62
2.10.1	Solute induced grain orientation transition	62
2.11	Binary Al-Si alloy system.....	67

2.12	High temperature application of Al alloys	69
2.12.1	Solubility of Ce in Aluminium.....	70
2.12.2	Role of Sc and Zr in Al-Ce alloys	72
2.12.3	Al–Si–Mg–Ce system	74
2.13	Summary.....	75
3	Methodology	77
3.1	Material	77
3.2	Casting methods	78
3.2.1	Controlled solidification	78
3.2.2	Gravity die casting processes.....	79
3.2.3	HPDC operations	81
3.2.4	Directional solidification	82
3.3	Metallography	83
3.3.1	Mounting and polishing	83
3.3.2	Etching	85
3.4	Anodizing.....	85
3.5	Microstructural analysis	86
3.5.1	Optical microscopy	86
3.5.2	Quantitative microstructural measurements using image processing.....	87
3.5.3	Scanning electron microscopy	94
3.5.4	EBSD	95
3.5.5	TEM	95
3.6	Mechanical behaviour assessment	98
3.6.1	Vickers hardness	98
3.6.2	Brinell hardness	99
3.6.3	Tensile testing	100

3.7	Statistical analysis	101
4	Influence of grain morphology on the strengthening behaviour of Al-Si alloys	103
4.1	Introduction	103
4.2	Theoretical aspect - Correlation between dendrite perimeter and λ_2	104
4.3	Microstructure observation	107
4.4	Dendrite perimeter.....	115
4.5	Correlation between hardness and p'	116
4.6	Strength contribution from α -Al dendrites	117
4.7	Influence of dendrite growth direction on Hall-Petch constant	123
4.8	Statistical significance of p'	128
4.9	Conclusion.....	129
5	Effect of dendritic morphology on the strength of Al-Ce alloys	130
5.1	Introduction	130
5.2	Microstructural observations.....	130
5.3	Hardness of Al-Ce alloys at various cooling rates	135
5.4	Hardness contribution from eutectic fraction.....	139
5.5	Conclusion.....	145
6	Influence of grain morphology on the strength of Mg alloys	146
6.1	Introduction	146
6.2	Microstructure analysis of Mg alloys.....	147
6.2.1	Effect of cooling rate on the grain size in AZ91D alloy	152
6.2.2	SDAS and p' correlation in AZ91D alloy	155
6.3	Mechanical properties evaluation.....	156
6.3.1	Microstructural features and yield strength correlation	160
6.3.2	Yield strength- grain size and morphology correlation in as cast condition....	166

6.3.3	Yield strength- grain size and morphology correlation in as solution treated material	169
6.4	Conclusion.....	170
7	Development of high thermally stable Al-Ce alloys.....	171
7.1	Introduction	171
7.2	Spheroidization of eutectic Si	173
7.3	Thermal stability of eutectic Si and Al ₁₁ Ce ₃ phases	175
7.4	Thermal stability of Al-Ce binary alloys.....	182
7.5	As cast microstructure of die cast alloys	183
7.6	Thermal stability of developed alloys	186
7.7	Microstructure after heat treatment	189
7.8	Fabrication through HPDC route	195
7.9	Mechanical behaviour at room and elevated temperature.....	198
6.7	Conclusions	199
8	Conclusion	201
9	Suggestions for future work.....	203
9.1	Effect of particles on the modification of dendritic morphology.....	204

Table of figures

Figure 1.1 Illustration of dislocations piling up against the grain boundary in (a) faceted equiaxed grains and (b) dendritic grains in which the length between dislocation source and the grain boundary varies spatially.	27
Figure 1.2 Illustration of dendrites for a given alloy having same λ_2 but with (a) coarse (b) fine dendritic grains.....	28
Figure 2.1 Formation of constitutionally undercooled region due to higher solute content....	33
Figure 2.2 Schematic illustration of the free-energy barrier to nucleation [39]	34
Figure 2.3 Illustration of heterogeneous nucleation of a solid from a liquid on a flat surface	36
Figure 2.4 Graphical representation depicting the relationship between the free energy barrier and nucleus radius for homogeneous and heterogeneous nucleation processes	37
Figure 2.5 (a) illustration of planar growth resulting in columnar grains in practical casting conditions (b) optical micrograph of wedge mould casting of Mg highlighting the columnar grains nucleating from the mould walls.....	39
Figure 2.6 Illustration showing the dendrites growing from the surface of mould wall, illustration reprinted from [45]	41
Figure 2.7 Relation between the normal velocity and growth velocity of.....	41
Figure 2.8 Dendrites formation with indicative length scales in (a) a succinonitrile-4% acetone solution, adopted from [36] (b) a succinonitrile-0.3% acetone solution, figure adopted from [50].....	43
Figure 2.9 Comparison between the Kurz-Fisher, Hunt and Trivedi model by fitting models in the experimental data from Ref [56]. Plot is reprinted from [58]	46

Figure 2.10 Relationship between cooling rate and SDAS in Al and Mg binary alloys dotted lines are the fitted curves of Flemming’s model with $n = 1/3$, data has been collected and replotted from ref [60,61]47

Figure 2.11. Illustration of dislocations originating from a source within a grain, piling up along a slip plane at the grain boundary49

Figure 2.12 Formation of ledges at the grain boundaries as proposed by Li reprinted from reference [66].....51

Figure 2.13 Schematic illustration of slip distance model: dislocation slip length is less in a smaller grain, the dislocation density is higher.....53

Figure 2.14 Cross-section of cubic grains with a grain size of d , featuring work-hardened grain boundary (GB) layers with a thickness of $2t$54

Figure 2.15 Illustration of spherical grain structure composed to grain interior and grain boundary with flow stresses σ_i and σ_b respectively.....55

Figure 2.16 Illustration of dislocations piling up against the grain boundary in (a) faceted equiaxed grains and (b) dendritic grains in which the length between dislocation source and the grain boundary varies spatially.58

Figure 2.17 Illustration of slips and twins system (TT: tension twin, CT: compression twin) in Mg crystal . Figure is reprinted from [76]59

Figure 2.18 Illustration of tensile specimen taken from rolled AZ31 plate at different orientations , ND, TD and RD signifies normal, transverse and rolling directions. Corresponding active twin and slip systems and k values are presented for each specimen. Figure is adopted from Ref [83].....60

Figure 2.19 Longitudinal section of the feathery grain structure obtained in an Al-Cu-Mg alloy, G is the thermal gradient for directional solidification, reprinted from Ref [97]	64
Figure 2.20 Plots showing the dendritic orientation transition (DOT) in Al-Zn alloys. (a) Change in the angle between $\langle 100 \rangle$ and dendritic growth direction of Al-Zn dendrites in directionally solidified Al-Zn alloys as a function nominal composition of Zn. Optical micrographs are presented for Al-50 and 90 wt.% alloys. A continuous increase of misorientation from 0 to 45° over the Zn concentration ranging from 25 to 55wt.% is noticeable. (b) Equiaxed dendrites and growth directions from phase-field simulations are presented as a function of ε_1 . A change in dendritic growth orientation is evident for the values of ε_1 ranging between the two dashed lines. The image in right upper corner illustrates the 2 D cross section of solid liquid boundary at equal intervals of time in a (001) plane for parameters corresponding to point b. Both plots are reprinted from Ref [31]	67
Figure 2.21 equilibrium phase diagram for the Al-Si system along with typical microstructures observed in hypoeutectic and hypereutectic Al-Si alloys	68
Figure 2.22 Schematic showing the effect of Ce content on morphology of the eutectic phase $Al_{11}Ce_3$ [113].	71
Figure 2.23 The lattice structure of Al_3Sc [115].....	72
Figure 2.24 (a) Solidification path of the Al-7Si- 0.6Mg-0.4Ce alloy obtained by the simulation under the Scheil-Gulliver conditions. (b) Experimentally measured data by DSC[125]	75
Figure 3.1 (a) Elite laboratory Chamber Furnaces fitted with eurotherm 2416 controller (b) Illustration of chamber showing the position of crucible and thermocouple.....	79
Figure 3.2 solidification path for Al-Si and Al-Ce binary alloys for controlled solidification experiments	79

Figure 3.3 Illustration of (a) cylindrical and (b) wedge mould.....	80
Figure 3.4. Casting operation for producing Al-Ce high temperature alloys using book mould casting, illustration is adopted from [126]	81
Figure 3.5 (a) High pressure die casting machine (b) casting chamber with tensile bar dies (c) the dimension of tensile bar specimen with overflow and biscuit (reprinted from[127])	82
Figure 3.6 illustration of (a) casting setup for directional solidification experiments (b) macro etched directionally solidified Al-8Si alloy.	83
Figure 3.7 Illustration of castings produced through (a) controlled cooling (b) wedge mould casting (c) book mould casting. Grey area shows the location from where the samples were extracted for metallographic observations.	84
Figure 3.8 Typical microstructures of (a) macro etched sample of slow cooled Al-2Si alloy (b) AZ91D alloy etched with picric acid and (c) anodized Al-5Si sample.	86
Figure 3.9 Carl Zeiss AxioScope A1 optical microscope.....	87
Figure 3.10 Schematic representation of (a) linear intercept method for the measurement of grain size in AZ91 alloy (b) SDAS measurement in Al-5Si alloy.....	88
Figure 3.11 Example of measurement of p' using freehand selection tool in ImageJ software. Microstructure of Al-8Si alloy solidified at 0.34°C/s is taken to illustrate the accuracy of measurement of p'	89
Figure 3.12 Microstructure of (a) macro etched Al-8Si alloy solidified at $0.00167^{\circ}\text{C/s}$ (b) traced perimeter of α -Al dendrites in a selected region highlighted by red.	90
Figure 3.13 An example of measured maximum and minimum lamellar spacing in the microstructure of Al-12.7Si alloy solidified at $0.00167^{\circ}\text{C/s}$	90

Figure 3.14 An example of measuring the aspect ratio of Si particle showing the accuracy of measurement using ImageJ. The accuracy of ImageJ software in area selection and fitting an equivalent ellipse with major axis equal to the maximum length and minor axis equal to the maximum width of in an irregular shape has been highlighted. This approach was used in quantifying the change in morphology of eutectic Si in Al-Si alloy and $Al_{11}Ce_3$ intermetallic in terms of changing aspect ratios and roundness, in Al-Ce binary alloys during spheroidization experiments.92

Figure 3.15 Workflow of image processing in ImageJ software to measure the morphological features like aspect ratio and area fraction of second phase particles (a) optical micrograph of heat treated Al-5Si alloy demonstrating spheroidization of Si particles. (b) Optical micrograph changed into a binary image for second phase identification, followed by (c) threshold operation, showing the selected area for measurements, in red colour. (d) Equivalent ellipses were fitted to measure the aspect ratios of selected particles.93

Figure 3.16 LEO scanning electron microscope.....94

Figure 3.17 The sample position inside vacuum chamber of Supra SEM, image is reprinted from [134].....95

Figure 3.18 Gatan PIPS 691 used for the milling of 3mm discs.....96

Figure 3.19 The Jeol 2100F Field Emission Gun Transmission Electron Microscope.97

Figure 3.20 Picture of (a) Wilson vo100 Vickers microhardness indenter (b) illustration of indenter impression (c) indentation impression with measured diagonals99

Figure 3.21 Brinell hardness tests used in the this study (a) Wilson BH3000 (*Buehler, UK*) Brinell hardness tester (b) illustration of Brinell hardness test (c) an example of indentation with measured diameter of impression, in Al-8Si alloy solidified at $0.34^{\circ}C/s$ 100

Figure 3.22 Picture of Instron 5500 universal electromechanical tester with ambient and high temperature tensile testing set up.....	101
Figure 4.1 Illustration of a dendrite.	105
Figure 4.2 The relationship between calculated p' using Eq. 4.6 and λ_2 , showing non-linearity in wide range of cooling conditions. Inset shows the consistency of non-linearity in the practical casting conditions. Shaded regions show the range of λ_2 in Al alloys cast through die casting and sand casting conditions[143–147].....	106
Figure 4.3 Macroetched microstructures of Al solidified at (a) 0.000167 °C/s (b) 0.00167 °C/s (c) 0.0133 °C/s (d) 0.0167 °C/s (d) 0.34 °C/s. Grain size decreases significantly varying from several mm to μm from lowest to highest cooling rate. Average grain size is shown in the respective microstructures.	108
Figure 4.4 Macroetched microstructures of (a) Al (b) Al-2Si (c) Al-5Si (d) Al-8Si (e) Al-12.6Si cooled at 0.000167°C/s, highlighting the influence of Si content on the grain size. Grain size decreases significantly with increasing Si content. Average grain size is shown in the respective microstructures.....	108
Figure 4.5 Microstructures of Al-2Si solidified at (a) 0.000167 °C/s (b) 0.00167 °C/s (c) 0.34 °C/s. For a constant Si concentration, grain structure gets finer as the cooling rate increases. Average grain size is shown in the respective microstructures.	109
Figure 4.6 As cast microstructures of Al-Si binary alloys at several cooling conditions and compositions.	110
Figure 4.7 As polished microstructures of (a) Al-2Si (b) Al-5Si (c) Al-8Si and (d) Al-12.6 Si solidified at 0.34 °C/s. Si morphology changes with the increasing Si content as eutectic Si becomes coarser. Change in eutectic point can be inferred in fast cooled Al-12.6 alloy with formation of primary Si.	111

Figure 4.8 Variation of (a) λ_2 as a function of cooling rate and (b) p' as a function of cooling rate. Solid lines are the best-fit to $\lambda_2 \propto \dot{T}^{-n}$ and $p' \propto \dot{T}^{-m}$ with the inset of relation between $n-m$ and Si content..... 113

Figure 4.9 Plot showing the poor value of coefficient of regression when (a) $p' \propto \dot{T}^m$ (dashed line) is fitted in the experimentally measured data with a value of m taken 1/3 (b) $p' \propto \dot{T}^{-m}$ (solid lone) type relationship is fitted in experimental data with best fitted values of m 114

Figure 4.10 Relation between experimental p' and λ_2 showing the nonlinearity in Al-8 wt.% Si alloy. For comparison purpose, $1/p'$ vs λ_2 is also plotted. Solid lines are guide to the eye. Shaded region is the data obtained from analysing wedge mould casting. 115

Figure 4.11 Brinell hardness of all alloys at several cooling rates. 116

Figure 4.12 Relationship between (a) BHN and λ_2 and (b) BHN and p' . Solid lines are linear fit to the HP type relationships. 117

Figure 4.13 Relationship between (a) BHN_m and λ_2 and (b) BHN_m and p' . The solid line is a fit to the HP relationship..... 119

Figure 4.14 HP type relationship between (a) BHN_m and p' , (b) BHN_m and λ_2 and (c) BHN_m and d for Al-8Si alloy solidified at various cooling rates. The legends are experimental data and the solid lines are linear fit..... 120

Figure 4.15 HP type relationship between BHN_m and p' for all Al-Si alloy systems highlighting the contribution of solution strengthening on the hardness and effect of Si content on the k''_m value..... 120

Figure 4.16 polarised micrographs of directionally solidified (a-d) Al, (e-h) Al-5Si, (i-l) Al-8Si 124

Figure 4.17 Optical micrographs of DS Al-2Si and Al-8Si alloys, showing the angle between the primary and secondary arms	125
Figure 4.18 EBSD mapping of (a) Al and (b) Al-8Si, indicating the transformation of preferred growth direction of dendrites in DS samples	126
Figure 4.19 Plot showing the variation of angle between the α -Al growth direction and the principal crystal axis as a function of Si content. The optical micrographs showing columnar grain morphology as a consequence of directional solidification. Pole figures of columnar grains, shown as inset, showing the dendrite orientation transition from $\langle 100 \rangle$ for Al and to $\langle 110 \rangle$ for Al-8Si alloys. For Al-8Si alloy, 45° side branching within the columnar dendrite can be observed in the microstructure. Examples of equiaxed grains with $\langle 100 \rangle$ and $\langle 110 \rangle$ growth orientations generated from phase field is reprinted from Ref. [175].	127
Figure 5.1 As cast microstructures of Al-Ce binary alloys at several cooling conditions and compositions.	132
Figure 5.2 . Variation of λ_2 as a function of cooling rate with solid lines being the Kattamis and Flemming coarsening model.....	133
Figure 5.3 Variation of p' as a function of cooling rate. Solid lines are the best-fit	134
Figure 5.4 Relationship between p' and cooling rate when data is fitted with $p' \propto T^{-m}$ type of equation with $m = 0.33$	134
Figure 5.5 Relation between experimental p' and λ_2 showing the nonlinearity in Al-8Ce alloy. Solid line is guide to the eye.	135
Figure 5.6. Brinell hardness of all alloys at several cooling rates.	137
Figure 5.7. HP type relationship between BHN and λ_2 for all the Al-Ce binary alloys	138

Figure 5.8 Relationship between BHN and p' . Solid lines are fit to the experimental data with the new HP relationship.....	139
Figure 5.9. Optical microstructures of Al-14Ce alloys solidified at (a) 0.000167 °C/s (b) 0.0133°C/s.....	140
Figure 5.10 Microstructures of Al-2Ce solidified at(a) 0.000167° C and (b) 0.034° C, showing the very fine and coarse morphology of $Al_{11}Ce_3$ phase.....	141
Figure 5.11 Relationship between (a) BHN_m and λ_2 , the solid lines are fits to the HP relationships given in Eqs. (5.3)	143
Figure 5.12 Relationship between (a) BHN_m and p' The solid lines are fits to the new HP relationships given in Eqs. (5.4)	143
Figure 5.13 HP type relationships [BHN_m vs p' and BHN vs p'] for all Al-Ce alloy systems. A significant increase in intercept due to solid solution strengthening contribution to the hardness can be clearly seen. Increase in k''_m value with the increased Ce content can also be seen...	144
Figure 6.1. Microstructural variations across the cross-section of AZ91 alloy cast in a wedge mould casting, highlighting the change in grain size with changing cooling rates.	148
Figure 6.2 Microstructures of as cast AZ91D alloy, solidified at (a) 0.11°C/s (b) 0.011°C/s	149
Figure 6.3 SEM microstructure of as cast AZ91 D alloy highlighting the β - $Mg_{17}Al_{12}$ phase and illustrating the SDAS measurement.....	149
Figure 6.4 (a) SEM micrograph of as cast AZ91D alloy highlighting the continuous and discontinuous precipitates pointed by red arrows (b) EDX peaks for major secondary phases in the matrix. Spot 1: Matrix, spot 2: Al-Mn based secondary particle, spot 3: divorced β - $Mg_{17}Al_{12}$ phase, spot 4: lamellar β - $Mg_{17}Al_{12}$ phase.....	151

Figure 6.5 Optical micrographs of as cast (a) Mg-5Al and Mg-9Al binary alloys cast in wedge mould. The morphology of grains has been altered by varying the solute concentration and the grain size variation has been induced by variable cooling rates along the length of wedge mould casting (b) grain size as a function of distance from the tip of the wedge mould casting, solid line is the guide to eye. 152

Figure 6.6 Effect of variable cooling rates on the microstructural features of AZ91D alloy was evaluated by measuring grain size, SDAS and p' at different distance from the tip of wedge. (a) Variation of measured average grain diameter (d) at different locations in wedge (b) λ_2 of dendrites and (c) p' measured at different distances from the tip of wedge. 153

Figure 6.7 λ_2 as a function of the cooling rate for alloy AZ91D from data present in the literature [185–187]. Solid line is the fitted equation (6.1) 154

Figure 6.8. SEM micrographs of as cast AZ91D wedge mould casting at top and bottom ends 155

Figure 6.9. Relation between experimental p' and λ_2 showing the nonlinearity in AZ91D alloy. Solid line is guide to the eye. 156

Figure 6.10 Graph showing the variation of hardness at different locations represented by the distance from the tip of the wedge mould casting and corresponding microstructures of the cross section at which the hardness measurements were taken 157

Figure 6.11 Relationship between the HVN and average grain diameter (d). The solid line is the fit to HP type relationship. The hardness values were measured at different locations in the wedge mould casting and corresponding grain size at the same location was measured. 158

Figure 6.12 Relationship between the HVN and (a) λ_2 (b) p' . The solid lines are the fit to HP type relationship, given by $HVN = HVN_{o,\lambda_2} + k' / \lambda_2^{0.5}$, and $HVN = HVN_{o,p'} + k'' / p'^{0.5}$ 159

Figure 6.13 Relationship between the *HVN* and (a) *d* (b) *p'*. The solid lines are the fit to HP type relationship, given by $HVN = HVN_{o,d} + k' / \lambda_2^{0.5}$, and $HVN = HVN_{o,p'} + k'' / p'^{0.5}$ 160

Figure 6.14 Illustration of wedge mould casting, showing (a) the area of extraction of tensile specimen (b) dimensions of the ASTM E8 subsize samples. 162

Figure 6.15 Illustration of the wedge mould casting showing the sections of tensile bar extraction. The polarised micrographs shows the corresponding microstructures of the tensile specimen in as cast and solution treated conditions..... 163

Figure 6.16 SEM microstructure of AZ91D alloy in (a) solution treated condition (b) EDS peaks and corresponding elemental point analysis of undissolved secondary phase and matrix, highlighted by red arrows. 164

Figure 6.17 The grain sizes as a function of the position in the wedge cast sample of..... 165

Figure 6.18 Measured hardness values of tensile specimen in as cast and solution treated conditions..... 166

Figure 6.19 Relation between YS and average grain diameter of AZ91D alloy in as cast condition. The experimental data has been fitted with the conventional HP relation of the form $\sigma = \sigma_0 + k d^{-0.5}$ 167

Figure 6.20 Relationship between YS and SDAS in AZ91D alloy in as cast condition. Solid line the HP relationship fitted to the experimental data..... 168

Figure 6.21 Relationship between YS and *p'* in AZ91D alloy in as cast condition. Solid line the HP relationship fitted to the experimental data..... 169

Figure 6.22 Relationship between the YS and (a) *d* (b) *p'*. The solid lines are the fit to HP type relationship, given by $\sigma = \sigma_0 + k d^{-0.5}$, and $\sigma = \sigma_0 + k p p'^{-0.5}$ 170

Figure 7.1 SEM micrographs of Al-Ce binary alloys (a) Al-2Ce (b) Al-5Ce (c) Al-20Ce (d) Al-30Ce.	172
Figure 7.2 Plot showing the change in morphology of eutectic Si and $Al_{11}Ce_3$ particles during isothermal ageing experiments conducted at 400°C, aiming to initiate the spheroidization of eutectic particles over varying time durations. The circularity shape descriptor is employed to quantify the morphology of these particles, which indicates how close a shape is to a perfect circle.	176
Figure 7.3 Relationship between experimentally measured radius of Si coral branches (ρ) and disintegration time at 400°C. Solid line is the fitted model given in Equations 8.1 and 8.2.	179
Figure 7.4 Optical micrographs of Al-5Si alloy after 1h heat treatment at (a) 380°C (b) 430°C (c) 480°C (d) 530°C (e) 580°C.	180
Figure 7.5 SEM micrographs of Al-5Ce alloy heat treated for 1h at (a) 370°C (b) 420 °C (c) 470°C (d) 520°C (e) 570°C (f) 640°C.	181
Figure 7.6 Plot showing the change in morphology, quantified by circularity of eutectic Si and $Al_{11}Ce_3$ particles during spheroidization experiments conducted at different temperatures with 1h holding time.	181
Figure 7.7 plot illustrates the hardness variation of an Al-10Ce alloy subjected to heat treatment for different durations at 400°C, showcasing minimal property degradation of Al-Ce alloys at elevated temperatures.	182
Figure 7.8 Microstructures of alloys in as cast condition (a) alloy 1 (b) alloy 2 (c) alloy 3 (d) alloy 4 (e) alloy 5 (f) alloy 6.	184
Figure 7.9 Structure of $Al_{11}Ce_3$ shown in SEM images of (a) Alloy 2 (b) Alloy 3; $Al_3(Sc, Zr)$ precipitates in (c) Alloy 4.	185

Figure 7.10 SEM micrograph of as cast (a) Alloy 5 with EDS point analysis of Al_2CeSi_2 phase; (b) BSE image of Alloy 6, (c) high magnification BSE image of Alloy 6; EDS element maps of (d) Al, (e) Ce, (f) Zr, (g) Si and (h) Sc.	185
Figure 7.11 Hardness of alloys in as cast condition.....	186
Figure 7.12 Ageing response of Alloy 1,2,3 and 4 at (a) 250°C (b) 300°C (c) 350°C (d) 400°C.	187
Figure 7.13 Hardness of alloy 5 and 6 in as cast and solution treated condition.....	188
Figure 7.14 Ageing response of alloys 5 and 6 after solution treatment.	189
Figure 7.15 Microstructures of alloy 1 (Al-10Ce) after 1 and 25 hours of ageing at 250°C, 300°C, 350°C and 400°C; (a) 250°C for 1 h (b) 300°C for 1 (c) 350°C for 1 h (d) 400°C for 1 h (e) 250°C for 25 h (f) 300°C for 25 h (g) 350°C for 25 h (h) 400°C for 25 h.	189
Figure 7.16 Microstructures of alloy 2 after 1 and 25 hours of ageing at 250°C, 300°C, 350°C and 400°C; (a) 250°C for 1 (b) 300°C for 1 h (c) 350°C for 1 h (d) 400°C for 1 h (e) 250°C for 25 h (f) 300°C for 25 h (g) 350°C for 25 h (h) 400°C for 25 h.	190
Figure 7.17 STEM images of Alloy 2 peak aged at 300°C.	191
Figure 7.18 Microstructures of alloy 3 after 1 and 25 hours of ageing at 250°C, 300°C, 350°C and 400°C; (a) 250°C at 1 h (b) 300°C at 1 h (c) 350°C at 1 h (d) 400°C at 1 h (e) 250°C at 25 h (f) 300°C at 25 h (g) 350°C at 25 h (h) 400°C at 25 h.	191
Figure 7.19 (a) TEM bright field image of Alloy 3 peak aged at 300°C (b) HRTEM of Alloy 3 peak aged at 300°C.	192
Figure 7.20 Microstructures of alloy 4 after 1 and 25 hours of ageing at 250°C, 300°C, 350°C and 400°C; (a) 250°C for 1 h (b) 300°C for 1 h (c) 350°C for 1 h (d) 400°C for 1 h (e) 250°C for 25 h (f) 300°C for 25 h (g) 350°C for 25 h (h) 400°C for 25 h.	193

Figure 7.21 (a) HRTEM of Alloy 4 peak aged at 300°C with corresponding FTT patten (b) Bright field image of peak aged Alloy 4.....	193
Figure 7.22 Microstructures of (a) as cast alloy 5 (b) as cast alloy 6 (c) solution treated alloy 5 (d) solution treated alloy 6.	194
Figure 7.23 Microstructures of solution treated alloy 5 and 6 after ageing at 250°C; (a) alloy 5 aged for 1 h (b) alloy 5 aged for 25 h (c) alloy 6 aged for 1 h (d) alloy 6 aged for 25 h.	195
Figure 7.24 Microstructures of alloys cast by HPDC (a) alloy1 (b) alloy 2 (c) alloy 3 (d) alloy 4 (e) alloy 5 and (f) alloy 6.	196
Figure 7.25 Hardness of alloy 1, 2,3,4, 5 and 6 cast by HPDC in as cast condition.	197
Figure 7.26 Fabrication of box component using industrial casting route.	197
Figure 7.27 Tensile behaviour of newly developed alloys at ambient and elevated temperatures (a) yield strength (b) UTS (c) elongation (d) retention factor.	199
Figure 9.1 Microstructure of 3TiB grain refiner showing (a) formation of particles and Al ₃ Ti phase (b) SEM micrograph showing TiB ₂ clusters at the grain boundary.....	205
Figure 9.2 Optical micrographs of Al-2Si alloy with <i>q</i> wt.% TiB ₂ grain refiner ,where <i>q</i> = (a) 0.25 (c) 0.5 (e) 1 (g) 2 (i) 2.5 and their reference counterparts.	206

List of tables

Table 1-1 Illustration of types of microstructures and the corresponding conventional HP type relations in literature.	27
Table 2-1 preferred crystallographic growth direction of dendrites in various materials.....	43
Table 2-2. k and x values for various HP models	56
Table 2-3: Mechanical properties of binary Al-Ce alloys	71
Table 3-1 Chemical composition of LM0.....	77
Table 3-2 Chemical composition of pure Mg	77
Table 3-3 Chemical composition of Al-20Si master alloy	77
Table 3-4 Chemical composition of Al-30Ce master alloy	78
Table 3-5 Steps for polishing Al alloys	84
Table 3-6 The procedural steps for the PIPS milling operation involved in thinning discs for TEM analysis	97
Table 4-1: R^2 values of generic HP relationship and conventional HP relationship.....	128
Table 7-1 numeral values used for the calculation of disintegration time of Si particles.....	178
Table 7-2 Nomenclature and composition of alloys	183

1 Introduction

1.1 Background

Investigating the mechanisms that contribute to the strengthening of metals plays a crucial role in comprehending their deformation characteristics and predicting their properties. Several strengthening models have been developed in last few decades in order to facilitate the design and development of new metallic materials with higher structural integrity. The grain structure dictates the strengthening behaviour of a metallic material and therefore, manipulation of microstructure can govern the mechanical properties. In a polycrystalline material, grain boundaries act as the obstacle in the movement of dislocations, resulting in higher strength for materials with finer grain structure and vice versa. The relationship between the yield strength and grain size was first presented by Hall and Petch[1,2], namely the famous Hall-Petch relationship, given by

$$\sigma = \sigma_0 + k d^{-x} \quad (1.1)$$

where, σ_0 is the stress required to generate dislocation also known as the friction stress, k is the constant known as HP constant and d is the average diameter of grains in a material. Generally, the Hall-Petch relationship is applicable in materials with average grain diameter greater than 10nm[3].

This relationship has been found to be consistent in predicting the strength of a material with faceted grains when $x = 1/2$, although several other values are also reported and are discussed in the literature section. Nevertheless, the conventional HP relationship (equation(1.1)) is widely applicable in a wide spectrum of materials.

However, for high solute containing alloys, the grain structure is not faceted, but a variety of grain morphologies can be observed ranging from rosettes to full grown dendrites. For a dendritic structure, a HP type relationship is reported by replacing d with secondary dendritic arm spacing (SDAS, λ_2) whereas for a complete eutectic alloy, same equation is reported by replacing d with lamellar spacing (λ). Although, empirically, these equations holds well, but no theory is present in the literature directly relating λ_2 and λ with YS.

The morphology of a grain is known to influence the yield strength of a material [4,5], in a recent study by M. Jiang [6], dislocation dynamics simulations were used to develop a model which integrates the effect of grain shape and orientation on the flow stress of a polycrystalline material. The HP constant in this study was found to be highly sensitive to the grain shape with higher aspect ratio. A generalized form of HP relationship was presented incorporating the effect of grain shape through a shape factor associated with the area swept by the dislocation and average dislocation loop length, pointing out the importance of grain morphology consideration in grain boundary strengthening. Since, new developments are being made in solidification process of metals, more intricate grain morphologies can be produced by controlling the composition and applying sophisticated melt processing techniques. Techniques, such as ultrasonic cavitation, high shearing, electromagnetic stirring are known to produce complex microstructures, which cannot be considered as spherical or faceted grains [7–10]. Apart from melt treatment and processing methods, recent developments [11][12] show that the dendritic growth can also be influenced by the presence of ex-situ particles.

The complexity in the morphology of a grain can be seen in Table 1, wherein different types of grains with varying morphology and the HP relationship for all cases is presented [8]. For a fully dendritic structure, conventionally, the HP relation directly translates into a relation

between the YS and λ_2 , without any theoretical background relating λ_2 directly with the dislocations. Primarily, the distance between the dislocation source and the grain boundary in a dendrite cannot be constant spatially due to the complex morphology (Figure 1.1), and the stress induced by the piling up of dislocations at the grain boundaries in such complex structures should be dependent on the surface area of the grain. Nonetheless, HP relation widely observed in most of the cases, the manipulation of grain structure by controlling the processing conditions and chemistry of an alloy [13–16] raises concerns on the accuracy of λ_2 as the substitute of grain diameter (d) in an alloy with dendritic structure.

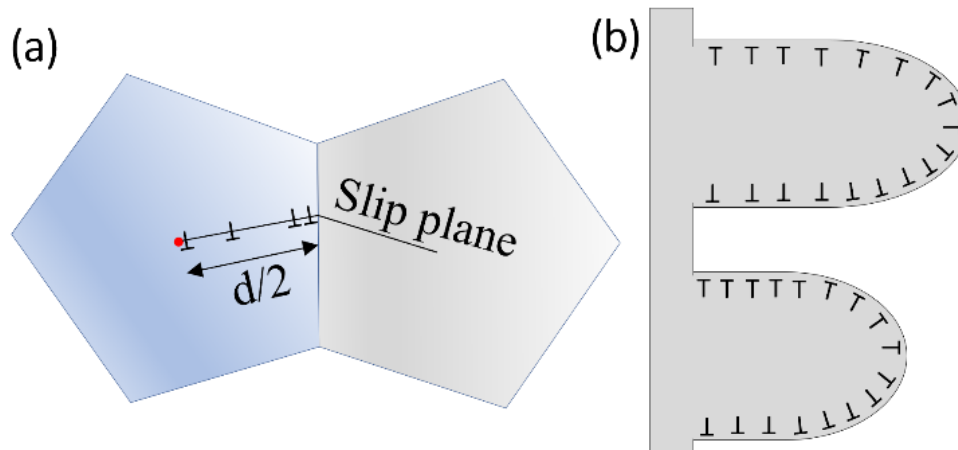
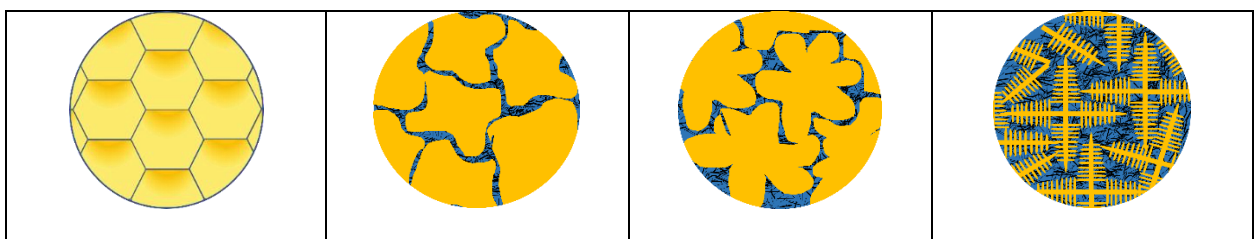
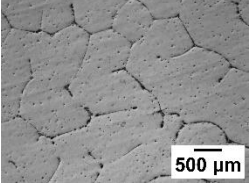
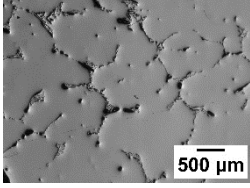
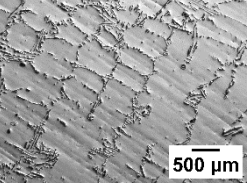
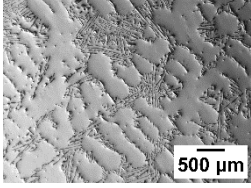


Figure 1.1 Illustration of dislocations piling up against the grain boundary in (a) faceted equiaxed grains and (b) dendritic grains in which the length between dislocation source and the grain boundary varies spatially.

Table 1-1 Illustration of types of microstructures and the corresponding conventional HP type relations in literature.



			
Facetted grains (e.g. pure aluminium)	Rosette type grains (e.g. Al-2Si alloy)	Rosette-Dendritic (e.g. Al-5Si alloy)	Dendritic structure (e.g. Al-8Si alloy)
$\sigma = \sigma_o + \frac{k}{\sqrt{d}}$ [17–20]	$\sigma = \sigma_o + \frac{k}{\sqrt{d}}$ [21–23]	$\sigma = \sigma_o + \frac{k}{\sqrt{d}}$ [24–26]	$\sigma = \sigma_o + \frac{k'}{\sqrt{\lambda_2}}$ [27–29]

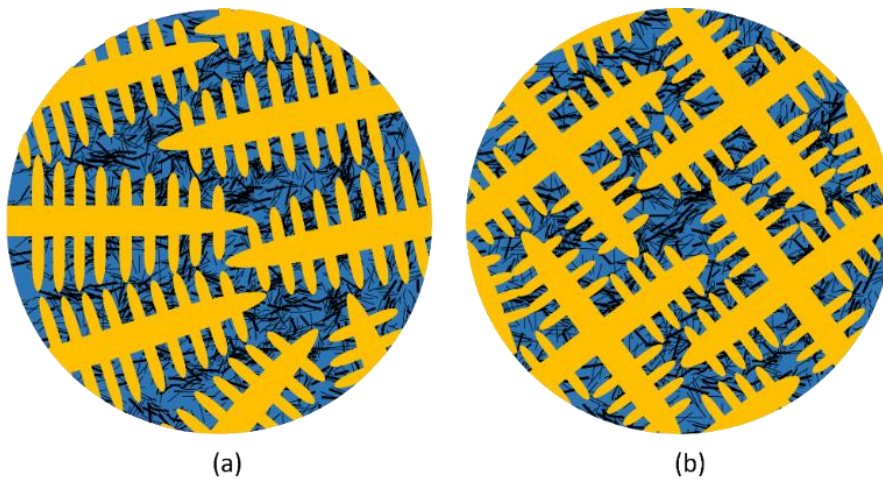


Figure 1.2 Illustration of dendrites for a given alloy having same λ_2 but with (a) coarse (b) fine dendritic grains.

Figure 1.2 shows a scenario in which an alloy having same λ_2 but with different size of dendrites which resulting in significantly varied interfacial area. This scenario occurs when grain refiner is added [30] and λ_2 based HP type relation do not consider this aspect. Similarly, dendrites with same λ_2 can have different morphology depending on the solute content [31] and also presence of nano-particles in the melt can lead to growth of dendrites with varied morphology [11,12,32,33]

As the finer grain structures can accommodate higher dislocation density, there arises a need to introduce a parameter which captures the variation of grain morphology and can be adopted to predict the strength as a function of grain boundary complexity. A notable gap exists in the literature, as there are no available experimental studies systematically addressing the influence of grain structure, particularly in alloys with intricate grain morphologies. This highlights the importance of investigating the influence of grain morphology on strength, with a specific focus on grain boundary structure. The review by Cordero et al. (Six decades of the Hall–Petch effect – a survey of grain-size strengthening studies on pure metals [3]) addressed the importance of considering grain boundary structure on the grain size strengthening and highlighted it as a fertile territory for future work. With time, several researchers have made modifications to the fundamental HP to account for the aspects which are rather ignored or were not present at the time of development of this equation.

Dendrites exhibit intricate morphologies, and numerous researchers have demonstrated that quantifying dendritic complexity is achievable through parameters such as projection area and contour length. In 2D, the interfacial area concentration of a dendrite has been shown to be represented by the perimeter per unit area [34,35]. While these measurements were primarily made by investigating non-metallic materials, we have extended this approach to metallic materials to comprehensively characterize grain morphology. This thesis introduces a novel perimeter-associated parameter (p') designed to capture variations in grain morphology and propose a comprehensive generic Hall-Petch relation expressed as $\sigma = \sigma_0 + k''/\sqrt{p'}$, where p' signifies the area per unit perimeter of a grain structure in 2D, which can be accurately measured using digital imaging tools and k'' is the slope representing Hall-Petch constant.

1.2 Research objectives

The objectives of this research are given below:

- a. To investigate the influence of grain morphology variation on the strength of Al-Si, Al-Ce and Mg-Al binary alloys.
- b. To investigate the applicability and accuracy of the new parameter (p') in predicting the yield strength of an alloy through conventional HP type relationship.
- c. To utilize the observed thermal stability of $Al_{11}Ce_3$ phase which was identified during the hardness testing of Al-Ce alloys, in designing Al-Ce high pressure die castable alloys demonstrating improvement in high temperature tensile properties.

1.3 Outline of thesis

This thesis is divided into 9 chapters, chapter 2 discusses the literature on the solidification behaviour of metals. The growth morphology of grains and concepts explaining the instability of growth front are discussed. The conventional models relating the grain boundary and yield strength are also discussed. In addition to models, the application of HP relationship in Al and Mg alloys has been presented. Chapter 3 describes the experimental procedures and characterization techniques conducted in the study. Image processing techniques to quantify the microstructural features are discussed in detail. In chapter 4, results of grain morphology and hardness correlation in binary Al-Si binary alloys are presented. Discussion on the morphological change of α -Al dendrites by controlling the solute content and solidification rate is also presented. The new perimeter based parameter namely p' has been introduced to quantify the grain boundary concentration in a given area of microstructure. To highlight the need of considering the new parameter p' , we have confirmed a nonlinear relation between p' and SDAS, which has been derived theoretically and was verified experimentally. A modified HP type correlation between strength and p' is presented in detail. Brinell hardness number is used as an strength indicator. During the development of new HP relationship, a change in the HP slope with increasing Si content was observed, which is generally attributed to the texture of

the material. To discuss the potential change in the HP constant due to solute induced orientation transition of grains, we have devised directional solidification experiments and have assessed the change in preferred dendritic growth direction using electron backscatter diffraction technique. In chapter 6, Al-Ce binary alloys are studied and new generic HP relationship for each alloy is presented. Due to negligible solubility of Ce in Al, the contribution from solid solution strength in Al-Ce is absent. Additionally, owing to the lack of coherency between the $Al_{11}Ce_3$ phase and the Al matrix, the strength contribution from the second phase is also marginal. As a consequence of low strengthening from second phase, influence of dendritic morphology on the strength of Al-Ce alloys is prominent and is presented by the generic HP relationship.

In chapter 7, this new approach to relate the morphology of dendrites and yield strength has been extended to Mg alloys. AZ91 D and Mg-Al binary alloys with varying Al concentrations has been studied at several cooling rates and yield strength has been measured as a function of grain morphology. During the grain morphological study of Al-Ce binary alloys, the high temperature stability of Al-Ce intermetallic caught our attention and this aspect of Al-Ce system was studied further and results are presented in chapter 8. A comparison of thermal stability of eutectic Si and $Al_{11}Ce_3$ was studied by conducting isothermal and isochronal heat treatments. New alloys were designed by the addition of Sc, Mg, Si and Zr and their influence on the temperature stability of Al-Ce alloys, cast using high pressure die casting method is resented. The precipitation behaviour and high temperature tensile strength of these alloys are discussed. Chapter 8 summarizes the finding of this study and chapter 9 discusses the future work required to strengthen and extend the proposed generic HP relationship to various other scenarios.

2 Literature review

2.1 Solidification in Al alloys

In this chapter, the classical nucleation theories and solidification processes leading to unstable growth front in alloys are reviewed. Dendritic growth theories and models to predict the morphology parameters of a dendritic structure are presented.

The grain size strengthening and models predicting the correlation between the strength of a material and grain size are reviewed.

2.1.1 Constitutional undercooling

Constitutional undercooling, a pivotal phenomenon in metallurgical processes, arises during the solidification of alloys. It is characterized by the rejection of solute elements from the solid phase into the liquid melt, leading to the creation of a solute-rich melt preceding the solid/liquid interface. Within this region, the liquidus temperature is lower than the actual temperature of the liquid melt, resulting in a thermal disequilibrium (Figure 2.1). Constitutional undercooling during solidification is dependent on the thermal gradient (G_T) being lower than the liquidus gradient (G_L) and the temperature within the boundary layer being beneath the equilibrium liquidus temperature [36]. This undercooling phenomenon significantly influences the microstructural evolution of alloys, impacting grain refinement, segregation, and nucleation processes. The constitutional undercooling is given as

$$\Delta T_c = T_L - T^* = -m_L (C_L^* - C_o) \quad (2.1)$$

where T_L denotes the liquidus temperature, m_L is the slope of the liquidus line, C_L^* is the composition at the interface of the liquid and C_o is the bulk composition of the liquid. During the heat transfer from the solid phase to the undercooled melt in the drop tube process, a negative thermal gradient prevails within the drop tube apparatus.

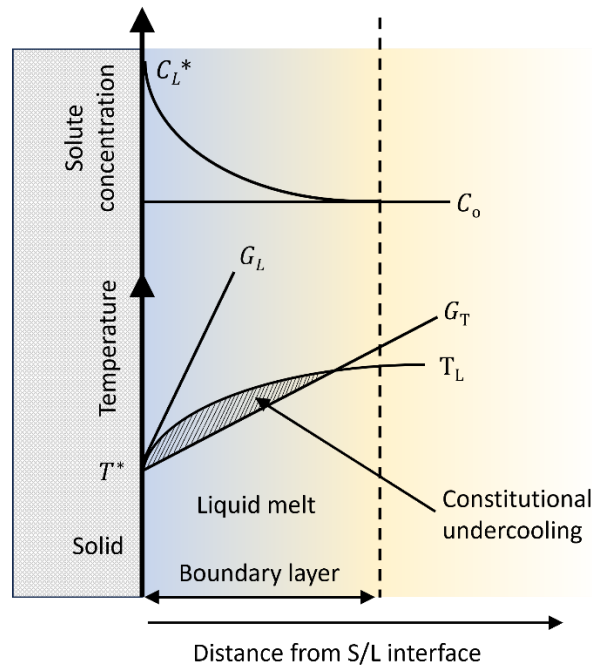


Figure 2.1 Formation of constitutionally undercooled region due to higher solute content.

2.2 Classical nucleation theory

2.3 Homogenous nucleation

The first attempts to understand nucleation as the fundamental phase transition governing crystal formation were documented in 1876 by J.W. Gibbs [37]. The classical nucleation theory (CNT) was proposed by Volmer and Weber in 1925 [38], postulates that nucleation proceeds through the formation of a critical nucleus within a supersaturated or supercooled phase. This critical nucleus is characterized by a specific size and energy barrier that must be overcome for it to nucleate and grow, ultimately leading to the formation of a new phase. This theory is based

on the free energy changes from liquid to solid. When a liquid is cooled down till it reaches a temperature lower than its melting point, T_m , small clusters of atoms start to form and the volume free energy of the melt decreases and can be given by

$$\Delta G_V = \frac{\Delta H_f(T_m - T)}{T_m} \quad (2.2)$$

where ΔH_f is the latent heat of fusion and T is the melt temperature. The total free energy change of the system can be expressed as the summation of change of free energy caused by interfacial energy and volume free energy, and can be expressed as

$$\Delta G = 4\pi r^2 \gamma_{SL} - \frac{4}{3} \pi r^3 \Delta G_V \quad (2.3)$$

where, ΔG is the Gibbs free energy, r is radius of cluster of atom, γ_{SL} is the surface tension of the solid/liquid interface (Figure 2.2).

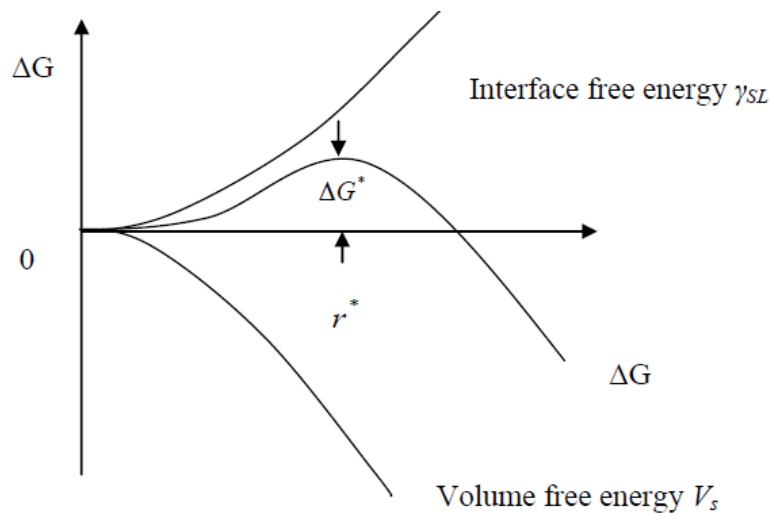


Figure 2.2 Schematic illustration of the free-energy barrier to nucleation [39]

The formation of clusters is restricted above the melting temperature (T_m) as they will undergo remelting. When the solid starts to form in the liquid, its free energy increases and reaches a

maximum, ΔG^* when $dG = 0$, and subsequently it starts decreasing. The radius corresponding to this critical nucleus size is denoted as r^* [39]. The system reduces its free energy by melting the solid phase, when the radius of cluster is lesser than the critical radius ($r < r^*$). Conversely, growth is favorable for the reduction of free energy of the system, when the cluster size exceeds the critical nucleus size ($r > r^*$)[40]. At the point where $\Delta G = 0$, indicating equilibrium, when r equals r^* , the critical nucleus is effectively in an unstable equilibrium with the surrounding liquid phase. By differentiating eqn. 2.3, the expression for r^* can be derived

$$r^* = \frac{2\gamma_{SL}}{\Delta G_V} \quad 2.4$$

putting value of r^* in equation 2.3, giving

$$\Delta G^* = \frac{16\pi\gamma_{SL}^3}{3(\Delta G_V)^2} \quad 2.5$$

2.3.1 Heterogeneous Nucleation

The nucleation is considered to be heterogeneous when it takes places on the surface of mould or any impurity present in the system. This type of nucleation is more common in practical solidification processes where undercooling is lower than that of homogeneous nucleation. This theory of nucleation was developed by Turnbull et al. [41] in which a spherical cap forms on a planar substrate shown in Figure 2.3. γ_{SL} , γ_{SM} and γ_{ML} are surface tension between nucleus (κ) and liquid (L), nucleus (S) and substrate (M) as well as substrate (M) and liquid (L). Because of the presence of substrate, the free energy for nucleation decreases and the driving force of nucleation is lower than homogeneous nucleation.

The excess free energy associated with the formation of embryo can be given by [42,43]

$$\Delta G_{het} = -V_S\Delta G_V + A_{SL}\gamma_{SL} + A_{SM}\gamma_{SM} - A_{ML}\gamma_{ML} \quad (2.6)$$

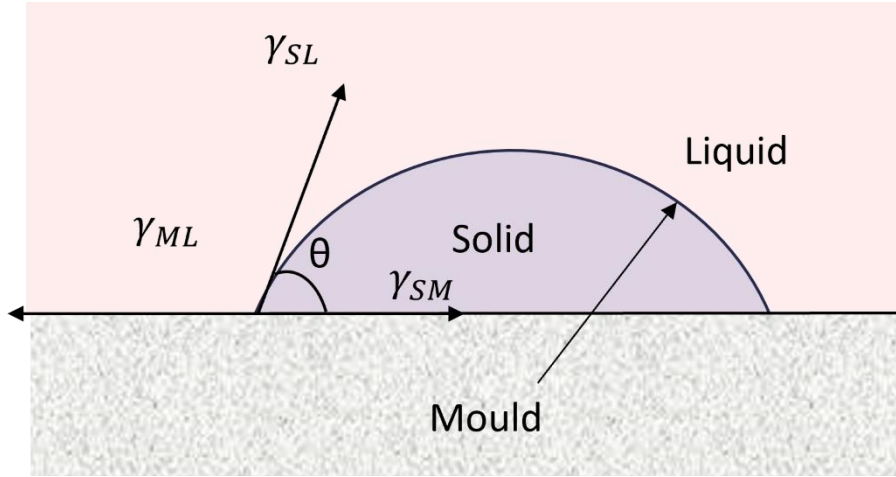


Figure 2.3 Illustration of heterogeneous nucleation of a solid from a liquid on a flat surface

where V_s is the volume of embryo, A_{SL} , A_{SM} and A_{ML} are the areas of the solid/liquid, solid/mould and mould/liquid interfaces, and γ_{SL} , γ_{SM} and γ_{ML} are the free energies of the solid/liquid, solid/mould and mould/liquid interfaces. Assuming γ_{SL} is isotropic, the total interfacial energy of the system is minimized if the embryo is a spherical cap. Surface tension force balance in the plane of the flat surface can be written as

$$\gamma_{ML} = \gamma_{SM} + \gamma_{SL} \cos\theta \quad (2.7)$$

Giving

$$\cos\theta = \frac{\gamma_{ML} - \gamma_{SM}}{\gamma_{SL}} \quad (2.8)$$

where θ is the contact angle. The free energy of heterogeneous nucleation can be written as

$$\Delta G_{net} = \left[-\frac{4}{3}\pi r^3 \Delta G_V + 4\pi r^2 \gamma_{SL} \right] s(\theta) \quad (2.9)$$

where

$$s(\theta) = \frac{(2+\cos\theta)(1-\cos\theta)^2}{4} \quad (2.10)$$

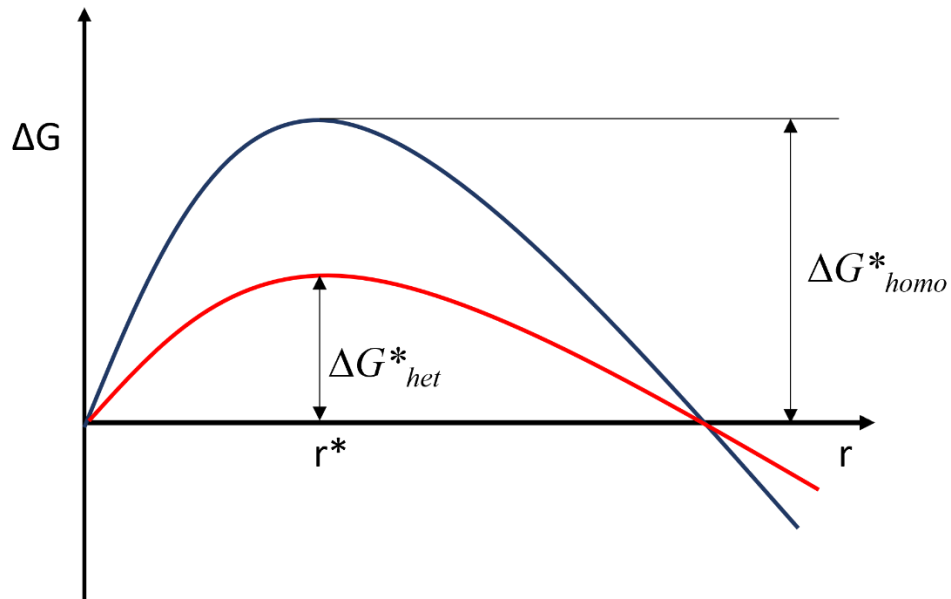


Figure 2.4 Graphical representation depicting the relationship between the free energy barrier and nucleus radius for homogeneous and heterogeneous nucleation processes

It can be noticed that the equation 2.9 is of the same form as equation 2.3 with additional term $S(\theta)$. Total free energy change (ΔG_{het}^*) to form a stable nuclei with critical radius (r_{het}^*) during heterogeneous nucleation can be given by differentiation expression given in equation 2.9.

$$r^* = \frac{2\gamma_{SL}}{\Delta G_V} \quad 2.11$$

And

$$\Delta G_{het}^* = \frac{16\pi\gamma_{SL}^3}{3(\Delta G_V)^2} S(\theta) \quad 2.12$$

The difference in the energy barrier for the formation of stable nuclei during homogenous and heterogeneous nucleation can be seen in Figure 2.4.

Since, the numerical value of $S(\theta) \leq 1$, it can be inferred that the energy barrier against heterogeneous nucleation is smaller than that of homogeneous nucleation by a $S(\theta)$ factor, which can be seen in Figure 2.4.

2.4 Growth after nucleation

After nucleation, the solidification occurs as several nucleus grows in the preferable directions to form grains. There are two major patterns in which the growth front moves into the liquid and forms grains. The pattern and form of the interface influence both the grain morphology of the resultant microstructure. The two growth modes can be differentiated as planar and dendritic.

2.4.1 Planar growth

Planar growth in metal solidification refers to the directional expansion of solidification fronts, wherein the interface between the liquid and solid phases maintains a flat, planar shape as the solid phase grows. During the process of solidification, there exist a difference between the temperature of cold mould surface and hot liquid melt, leading to a thermal gradient between the melt and surface. In practical casting operations, the process of nucleation begins at the surface of the mould, and the subsequent growth of the solid phase progresses towards the centre of the casting. During planar growth, atoms from the liquid phase attach to the solid phase, extending its boundaries in a well-defined direction. This growth mode is particularly prevalent in systems with low undercooling and high thermal gradients, facilitating the orderly arrangement of atoms into crystal structures. This growth occurs along preferred crystallographic directions determined by the inherent characteristics of the solidifying crystal.

As the solidification process proceeds, the multiple crystal growths are initiated at the several active nuclei at the mould walls. The growth rate of crystals is dictated by the thermal gradient

between liquid melt and surface of mould. The lateral growth of these crystals is restricted by the impingement of neighbouring grains. This scenario leads to planar or plane-front growth, where a seemingly flat interface advances into the molten material resulting the formation of columnar grains, which are often observed in the cast ingots (Figure 2.5a). The growth direction of these grains is the opposite direction of heat extraction from the melt.

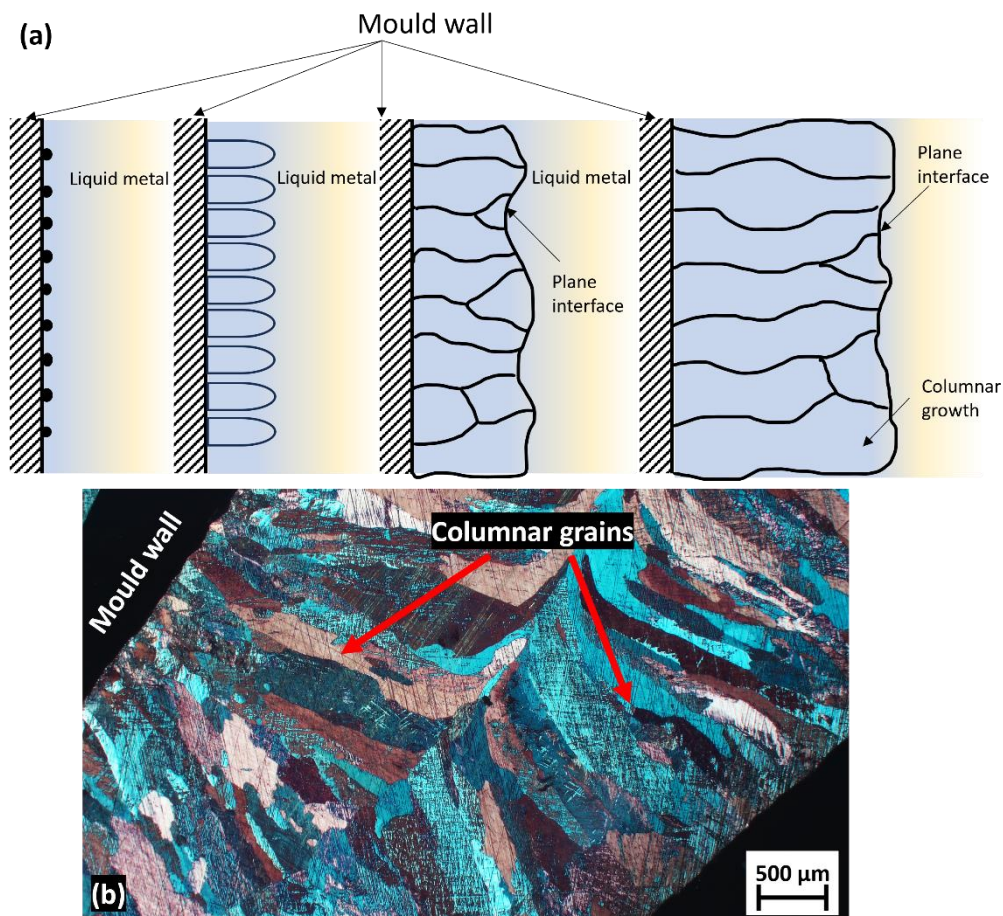


Figure 2.5 (a) illustration of planar growth resulting in columnar grains in practical casting conditions (b) optical micrograph of wedge mould casting of Mg highlighting the columnar grains nucleating from the mould walls.

2.4.2 Dendritic growth in alloys

In the process of solidifying a metal or alloy melt, dendritic crystalline growth arises as the interface between solid and liquid phases progresses into a region of supercooled liquid, where

the temperature is lower than at the interface. As solidification advances, even slight disturbances in this interface, caused by temperature fluctuations or variations in solute concentration, can trigger the formation of dendritic patterns (Figure 2.6). This instability is affected by the anisotropic nature of crystal growth and is controlled by the crystallographic orientations that dictate the preferred directions of growth.

The grains nucleate from the nucleation sites present either at the mould surface or in the melt in the form of impurities and these structures grow in globular shape up to a critical radius. Beyond this radius, the solidification front experiences an instability and form dendritic structures. Mullins and Sekerka [44] first investigated the behaviour of an infinitesimal perturbation of a spherical solid by a single spherical harmonic. According to them, for a stable growth of planar solid interface, the critical wavelength of the perturbation is given by

$$\lambda_{MS} = 2\pi \sqrt{\frac{2\omega d_o}{V}} \quad (2.13)$$

where, λ_{MS} is the critical perturbation wavelength, ω is the thermal diffusivity, V is growth velocity and d_o is the capillary length, which can be given by

$$d_o = \frac{T_m \gamma_{SL} C_p}{L^2} \quad (2.14)$$

where, T_m is the melting point of metal; γ_{SL} is the surface tension of the solid–liquid interface; C_p is the heat capacity of the liquid phase; L is the heat of fusion. They found that the small perturbation usually keeps the growing interface planar. However, beyond a critical value, these perturbations can grow over time, resulting in the growth instability and formation of complex dendritic morphologies.

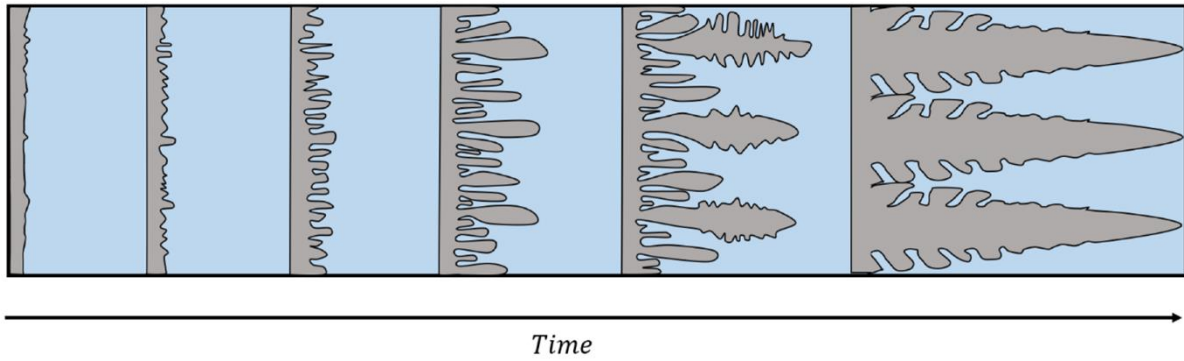


Figure 2.6 Illustration showing the dendrites growing from the surface of mould wall, illustration reprinted from [45]

The dendritic tip was suggested to be parabolic by Papapetrou[46] in 1953. He was the first to demonstrate that the shape of a solid-liquid interface should be such that the normal velocity V_n of an interface element located at an angle φ with respect to the growth axis must satisfy the relation (Figure 2.7)

$$V_n = V \cos \varphi \tag{2.15}$$

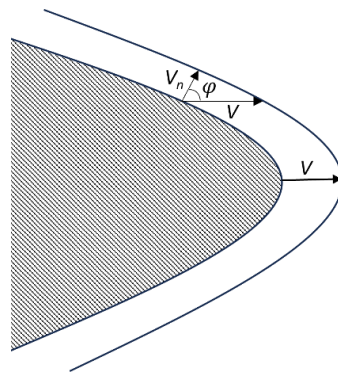


Figure 2.7 Relation between the normal velocity and growth velocity of dendrite growth

Papapetrou further argued that, in steady state growth, to preserve the fixed concentration and thermal profile of a growing parabolic shaped dendrite, it is essential that the growing dendrite

rejects a part of latent heat and solute ahead of the growing tip and residual heat is dissipated along the sides. In 1947, Ivantsov [47] provided differential equation for the steady state diffusion in the case of an parabolic plate-like dendrite (2D) and a paraboloid of revolution (3D needle crystal) with constant temperature and concentration at the interface of the growth front, giving

For 2 dimensions,

$$\Omega_c = \sqrt{\pi P_c} \exp^{P_c} (1 - \operatorname{erf} \sqrt{P_c}) \quad (2.16)$$

For 3 dimensions,

$$\Omega_c = P_c \exp^{P_c} E_1(P_c) \quad (2.17)$$

where, P_c is the solute Peclet number ($VR/2D$); V is the growth velocity; \hat{R} is the dendritic tip radius; D is the solute diffusivity; $E_1(P_c)$ is the exponential integral and Ω_c is the solute undercooling. Horvay and Cahn[48], then extended this study to elliptical paraboloid shape.

Moreover, the cooling rate and extent of undercooling exert considerable influence on dendritic morphology. The radius of dendritic tips is contingent upon solidification velocity: lower velocities yield dendrites with notably larger tip radii, whereas higher velocities result in a reduction of tip radius. During rapid solidification, dendritic morphology undergoes a transition from fully branched structures to globular/cellular dendrites [49].

2.5 Scaling of dendrites

During dendritic solidification, the crystals tend to grow along energetically favoured directions due to the anisotropy of surface energy. The preferred crystallographic growth direction in metals with different crystal structures is given in table 2.1

Table 2-1 preferred crystallographic growth direction of dendrites in various materials

Crystal structure	Preferred growth direction	Examples
FCC	$\langle 100 \rangle$	Al, Cu, Ni
BCC	$\langle 100 \rangle$	δ -Fe, NH ₄ Cl, Succino nitrile (SCN)
Tetragonal	$\langle 110 \rangle$	Sn
HCP	$\langle 10\bar{1}0 \rangle$	Zn

Generally, a dendritic structure can be characterized by three length scales, namely primary dendritic arm spacing (PDAS, λ_1), secondary dendritic arm spacing (SDAS, λ_2) and dendrite tip radius (\bar{R}). The illustration in Figure 2.8 shows the length scales in a typical dendrite of succino nitrile.

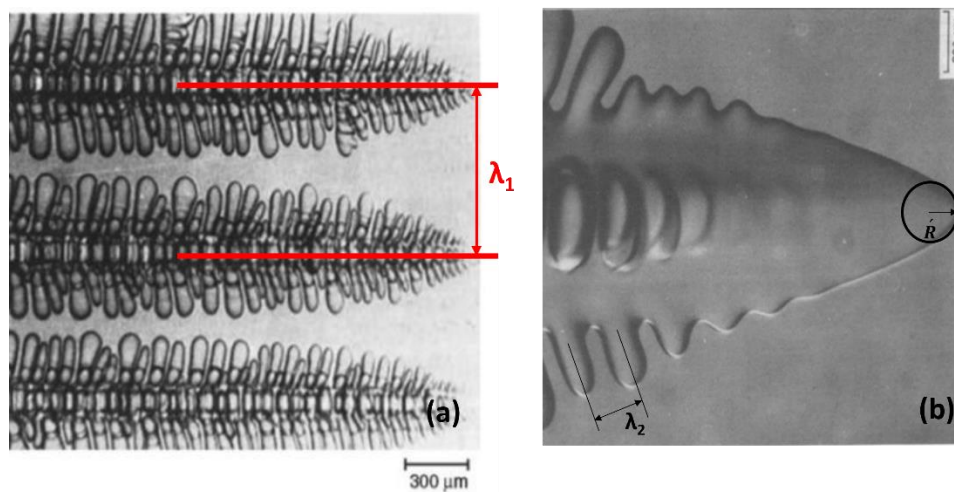


Figure 2.8 Dendrites formation with indicative length scales in (a) a succinonitrile-4% acetone solution, adopted from [36] (b) a succinonitrile-0.3% acetone solution, figure adopted from [50]

In directional solidification conditions, the arrangement of primary trunks of dendrites, when viewed perpendicular to the growth direction, solidified microstructures exhibit intricate spatial

and temporal patterns defined by the parameter λ_1 (Figure 2.8a). The structure of primary arms are important for the determination of mechanical properties as they influence the homogeneity of second phases in the alloy [51,52]. The value of λ_1 is dependent on the alloy composition (C_o) and solidification variables, namely, thermal gradient (G), growth velocity (V) and melt flow. To relate λ_1 with the directional solidification process variables, Hunt made the first attempt and proposed a model in 1975 [53], for low and high growth velocity (V) regimes,

For low V regime

$$\lambda_1 = 2.83 \left(\Delta T_o D \Gamma k^* - \frac{k^* G D}{V} \right)^{0.25} V^{-0.25} G^{-0.5} \quad (2.18)$$

For high V regime

$$\lambda_1 = 2.83 (\Delta T_o D \Gamma k^*)^{0.25} V^{-0.25} G^{-0.5} \quad (2.19)$$

where, k^* is the partitioning coefficient, Γ is the Gibb's Thompson coefficient and ΔT_o is the equilibrium solidification rage, given by

$$\Delta T_o = \left[-m_L (1 - k^*) \frac{C_o}{k^*} \right] \quad 2.19(a)$$

Following Hunt's model, Kurz [54] presented the relationship between the \hat{R} and solidification parameters.

$$\lambda_1 = \left[\frac{6 \Delta T'}{G(1 - k^*)} \left(\frac{D}{V} - \frac{\Delta T_o k^*}{G} \right) \right]^{0.5} \quad (2.20)$$

$$\lambda_1 = 4.3 \Delta T'^{0.5} \left(\frac{D \Gamma}{\Delta T_o k^*} \right)^{0.25} V^{-0.25} G^{-0.5} \quad (2.21)$$

where, $\Delta T'$ is the difference between the non-equilibrium solidus and the tip temperature which is given by

$$\Delta T' = T_L - T_e - \Delta T \quad 2.21(a)$$

where T_L is the liquidus temperature; T_e is the eutectic temperature.

In 1984, Trivedi [55] evaluated the Kurz model against the Hunt model by analysing experimental data of growth experiments on succinonitrile, obtained by K. Somboonsuk et al.[56] . This comparative study was aimed to assess the applicability and accuracy of both models in explaining the observed phenomena. At high V , these models held a good agreement with the experimental data, however, both models posed a discrepancy in the gradient of fit line, shown in Figure 2.9. To better explain the experimental results of K. Somboonsuk et al.[56], Trivedi modified the Hunt's model and gave a relationship, as followed

$$\lambda_1 = 2.83(\Delta T_o D \Gamma k^* X)^{0.25} V^{-0.25} G^{-0.5} \quad (2.22)$$

where $X = \frac{j}{2}(j+1)(j+2)$ for an approximately spherical growth front. j is the harmonic of the perturbation which decides the instability of the interface. Huang and Glicksman [57] have reported $j = 6$ for the marginal stability condition in a spherical growth front with radius R . Figure 2.9 highlights the excellent fit of Trivedi model in experimentally measured λ_1 .

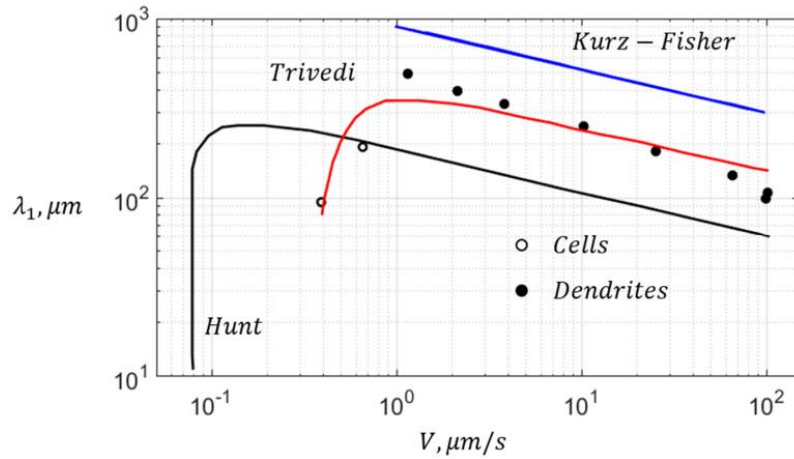


Figure 2.9 Comparison between the Kurz-Fisher, Hunt and Trivedi model by fitting models in the experimental data from Ref [56]. Plot is reprinted from [58]

2.6 Dendritic arm coarsening

The prediction of secondary arm spacing is essential to understand the solidification behaviour of metals. As the perturbations in unstable solid liquid interface grows, they become cell like and become secondary dendritic arms. The spacing between these arms of completely solidified microstructures can be predicted by modelling the coarsening mechanisms during solidification. Kattamis and Flemming [59] proposed a isothermal coarsening model for the growth of secondary arms, wherein the thinner dendritic arms dissolves in the melt and deposits on the bigger arms, resulting in coarser microstructure. This model is analogous to Ostwald ripening model for precipitates.

The difference in the radii of arms, induces a difference in chemical potential resulting in the diffusion of solute from thinner arms to the thicker arms, until the thinner arms are completely dissolved. The mathematical expression for this model can be given by

$$\lambda_2 = 5.5(Mt_f)^n \quad (2.23)$$

where

$$M = \frac{-\Gamma D \ln \left[\frac{C_b}{C_o} \right]}{m_L (1 - k^*) (C_b - C_o)} \quad (2.24)$$

where Γ is the Gibbs–Thomson coefficient, D is diffusion coefficient in liquid, m_L is the slope of liquidus, k^* is partitioning coefficient, C_o is the solute composition and C_b is the composition of the liquid at the base of dendrite which is reached at the solidification time t_f . In a eutectic solidification process, C_b is equal to the eutectic composition. And, n is the coarsening exponent.

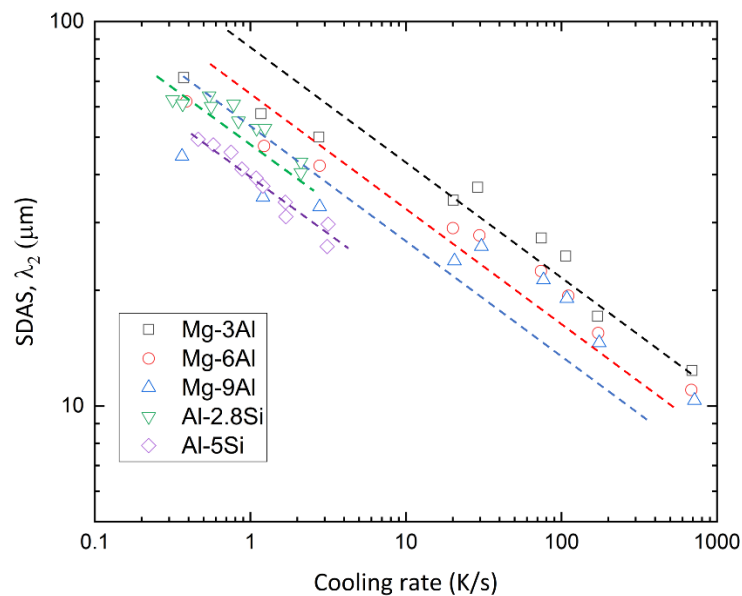


Figure 2.10 Relationship between cooling rate and SDAS in Al and Mg binary alloys
dotted lines are the fitted curves of Flemming’s model with $n = 1/3$, data has been
collected and replotted from ref [60,61]

The most acceptable value of n is $1/3$. However, several other values are also reported in the literature.

Figure 2.10 shows the experimentally measures λ_2 data for several Al and Mg binary alloys obtained from the literature, plotted against the cooling rate and fitted with the Flemming model

with $n = 1/3$. The model shows a good fitting with the experimental data highlighting the influence of solute content and cooling rate on the predicted λ_2 .

2.7 Hall-Petch relationship

The Conventional Hall-Petch (HP) relationship which is widely used to describe the correlation of strength and the grain size was proposed by Hall and Petch over six decades ago. The first observation of this relation was independently made by Hall [1] and Petch [2] in low carbon steel. According to this relationship, the strength, σ of the polycrystalline material is given by

$$\sigma = \sigma_0 + k d^{-x} \quad (2.25)$$

where, σ_0 is the stress required to generate dislocation also known as the friction stress, k is the constant known as HP constant and d is the average diameter of grains in a material.

Nevertheless, the physical mechanism underpinning this relationship remains unclear. Over the past few decades, numerous models have been formulated in an attempt to elucidate the HP equation. A comprehensive review by Schuh[3] present the models developed over six decades, to describe the relationship between σ and d . The four widely accepted models for grain size strengthening are:

1. Dislocation pile-up model;
2. Grain boundary source model;
3. The slip distance model;
4. Composite model

2.7.1 Dislocation pile-up model

Eshelby's [62] pile up model is widely accepted explanation for HP relationship in polycrystalline materials which is based on dislocation motion hindrance by the grain

boundaries. The Pile-Up Theory is an extension of the HP relationship and focuses on the behaviour of dislocations within the crystal lattice of a material. Dislocations are line defects in the crystal structure that greatly influence a material's mechanical properties. Pile-Up Theory suggests that as dislocations move through a material, they tend to accumulate at grain boundaries, creating localized stress concentrations. In this theory, it is assumed that a dislocation source, in the grain also known as Frank-Read source, emits multiple dislocations when acted upon by load, τ . These dislocations then pile up on a slip plane against an obstacle like a grain boundary or a precipitate (Figure 2.11).

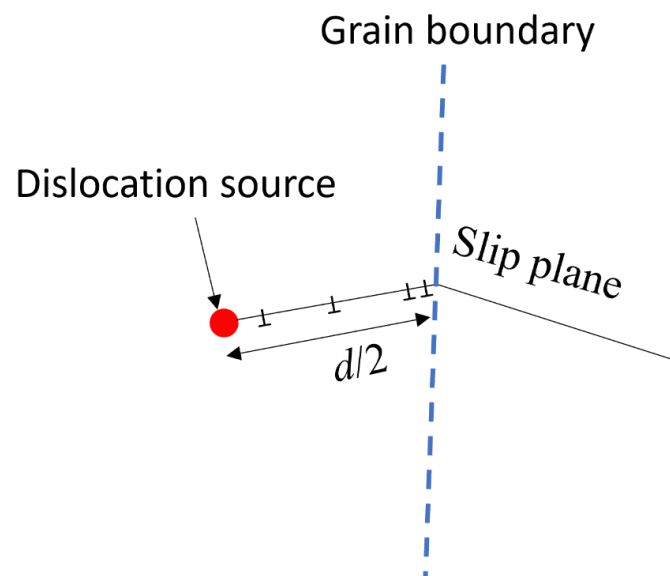


Figure 2.11. Illustration of dislocations originating from a source within a grain, piling up along a slip plane at the grain boundary

The number of like sign dislocations, n^* , that can be arranged in length L_s between the dislocation source and grain boundary on a slip plane is given by Nabarro [63].

$$n^* = \frac{k\pi\tau_s L_s}{G b} \quad (2.26)$$

where τ_s is average shear stress, $k = 1$ for edge and $1-\nu$ for screw dislocation, \mathbf{b} is Burgers vector and G is shear modulus. The length L is considered to be in the middle of the grain i.e. $L_s = d/2$.

The stress exerted by an array of n^* dislocations on the slip plane is given by $n^*\tau_s$. When this stress exerted by the leading dislocation reaches a threshold value (τ_c), dislocations in the neighbouring grain are produced and henceforth the material yields under external load, giving the expression for HP relation.

$$\tau = \tau_o + \sqrt{\frac{4Gb\tau_c}{\pi d}} \quad (2.27)$$

where τ_o is the friction stress. The distance between the obstacle and dislocation source in the slip plane is assumed to be $d/2$, where d is the grain size, which makes the yield strength dependent on the grain size.

2.7.2 Grain boundary source model

The concept of dislocation generation from Frank-Read source and their piling up against the grain boundaries, was developed to describe the grain size strengthening in steel. However, the direct observations, such as through scanning electron microscope (SEM) images depicting dislocation pile-up at boundaries, has been lacking. The absence of evidence regarding pile-up at grain boundaries has led to the proposition of alternative explanations for grain size strengthening.

To address this issue, Li [64] first proposed the grain boundary source model in 1967. In this model, grain boundaries are considered the dislocation source. The grain boundary structures known as ledges are assumed to eject dislocations, which forms a forest of dislocations at the

grain boundaries. These dislocation then migrate into the grain interior through the dislocation forest. The example of grain boundary ledge generating dislocation is shown in Figure 2.12. Unlike the accumulation of dislocations at grain boundaries, direct experimental verification of grain boundary ledges was initially documented by Murr [65] through transmission electron microscopy (TEM). Various materials including Ni, Al, Cu, Mo, Ta, Ir, 304 Stainless Steel, and Inconel 600 were examined before and after plastic deformation, revealing the emission of dislocations from grain boundary ledges, thus substantiating the validity of Li's model.

To quantify the work hardening effect due to dislocation accumulation, Taylor's equation can be used to relate the stress induced by dislocation forest and dislocation density. The number of ledge in the grain boundary is taken as \dot{q} per unit length which gives the dislocation density in the forest to be $8 \dot{q}/\pi s$. Where s is the grain boundary length, by using Taylor's equation, the stress can be given by

$$\tau = \tau_o + MGb \sqrt{\frac{8\dot{q}}{\pi d}} \quad (2.28)$$

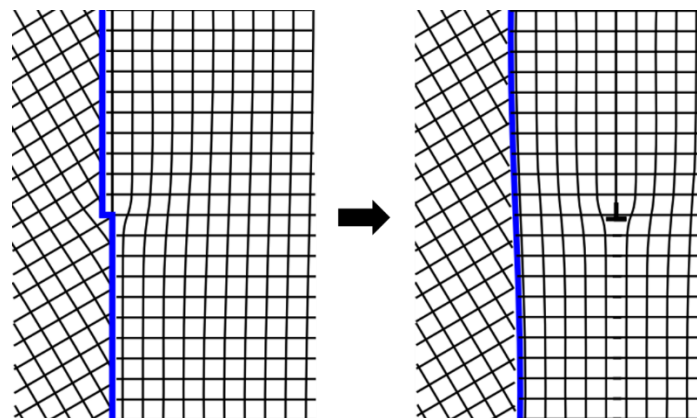


Figure 2.12 Formation of ledges at the grain boundaries as proposed by Li reprinted from reference [66]

where M is Taylor constant, generally reported to be 0.4. Li also observed the dependence of grain boundary ledges on the grain boundary misorientation (θ) and proposed that grain boundary ledge length should increase with increasing misorientation, which was then experimentally confirmed by Bernstein and Rath [67] in Fe-0.15 Ti steel, wherein grain boundary ledge density increases with increasing grain misorientation. Nevertheless, the grain boundary ledge theory underscores the significance of structure of grain boundary and not just the grain size on the strength of a material.

2.7.3 Slip distance model

Connard et al.[68,69] proposed a model relating the dislocation density with the slip distance. According to this model, at a constant strain, the higher dislocation density in a grain is dependent on the slip distance, implying smaller the average grain size, higher is the dislocation density (Illustration shown in Figure 2.13). To derive an expression of dislocation density, they used the relationship previously given by Cottrell [70]

$$\varepsilon = \alpha_1 \rho b \chi \quad (2.29)$$

where α_1 is a constant of the value of 1.4, b is the burgers' vector and χ is the average free path each dislocation moves. They assumed the proportional relationship between the grain diameter and χ , giving $\chi = \acute{z}d$, where, \acute{z} is a proportionality constant. By substituting the value of χ and rearranging, equation 2.29 can be rewritten as

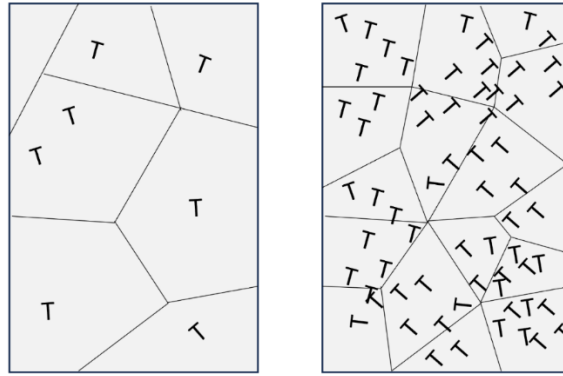


Figure 2.13 Schematic illustration of slip distance model: dislocation slip length is less in a smaller grain, the dislocation density is higher

$$\rho = \frac{\varepsilon}{\alpha_1 b \bar{z} d} \quad (2.30)$$

By using Taylor's work hardening equation, the expression for stress can be given by

$$\tau = \tau_o + M G b \sqrt{\frac{b \varepsilon}{\alpha_1 \bar{z} d}} \quad (2.31)$$

where, M is a Taylor constant, G is the shear modulus.

2.7.4 Composite model

In this model, it is assumed that the polycrystalline materials are made up of grains with two regions, first being the grain interior, which has a lower flow stress and the grain boundary which has a higher flow stress [71]. Figure 2.14 illustrates a cubic grain structure with different zones. For a cubic grain structure, the YS of the composite structure can be given by

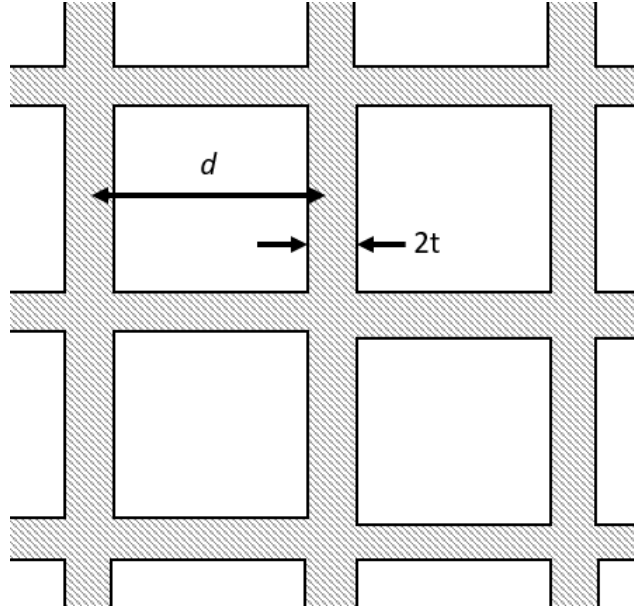


Figure 2.14 Cross-section of cubic grains with a grain size of d , featuring work-hardened grain boundary (GB) layers with a thickness of $2t$.

$$\sigma = \left\{ \frac{(d - 2t)^2}{d^2} \right\} \sigma_i + \left\{ \frac{d^2 - (d - 2t)^2}{d^2} \right\} \sigma_b \quad (2.32)$$

where, σ_i is the flow stress of grain interior and σ_b is the flow stress of grain boundary. Using the same approach, Meyersm and Ashworth [72] provided the expression for a composite spherical grain structure, given by

$$\sigma = \sigma_i + \frac{8(\sigma_b - \sigma_i) t}{d} - 16(\sigma_b - \sigma_i) \left(\frac{t}{d} \right)^2 \quad (2.33)$$

It can be inferred from Equation 2.33 that, for a constant t , the value of second term approaches zero as the grain size increases which results in a dependence of σ on $1/d$. However, when the grain size decreases the second term becomes more prominent. Therefore to obtain the classic relation between σ and d . Meyersm and Ashworth [72], have proposed an assumption for model, i.e.

$$t = \psi d^{0.5} \quad (2.34)$$

where, ψ is an adjustable parameter. This assumption implies that the grain size increases rapidly with small change in the grain boundary width. By substituting the value of t from equation 2.34 in equation 2.33, the expression for yield strength (YS) can be given by

$$\sigma = \sigma_i + \frac{8\psi(\sigma_b - \sigma_i)}{d^{0.5}} - 16\psi(\sigma_b - \sigma_i) \frac{\psi^2}{d} \quad (2.35)$$

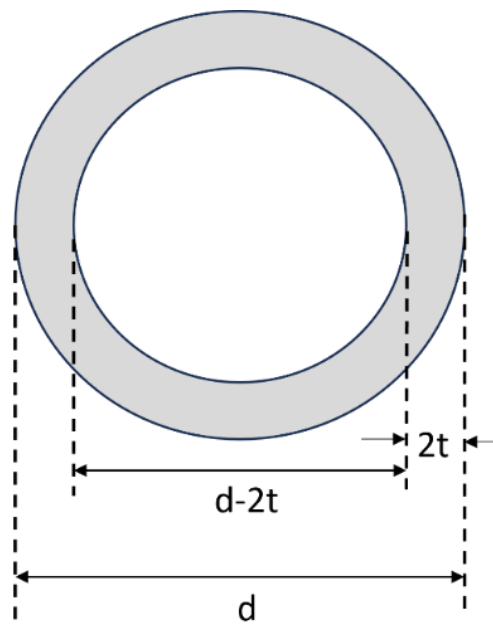


Figure 2.15 Illustration of spherical grain structure composed to grain interior and grain boundary with flow stresses σ_i and σ_b respectively

According to equation 2.35, it can be inferred that relationship between YS and d follows a HP type relationship for large grains, as the first term in equation 2.35 becomes more dominant. Whereas, for smaller grains, second term is more dominant and first term is negligible.

In essence, the HP relationship comprises two primary elements: the first component of friction stress of a single crystal and second component of the contribution of grain size strengthening,

which itself consists of two components. The first component involves the constant ‘ k ’, while the second component pertains to the power term ‘ x ’. Both of these components are dependent on the specific dislocation model employed to articulate the strengthening mechanism. Table 2.2 lists the k and x values in aforementioned grain size strengthening models.

Table 2-2. k and x values for various HP models

	Pile up model	Grain boundary source model	Slip distance model	Composite model
x	0.5	0.5	0.5	0.5
k	$\sqrt{\frac{4Gb\tau_c}{\pi}}$	$MGb \sqrt{\frac{8\dot{\gamma}}{\pi}}$	$MGb \sqrt{\frac{b\varepsilon}{\alpha_1 \dot{\gamma}}}$	$8\psi(\sigma_b - \sigma_i)$

2.8 limitations of Hall-Petch relationship

Two major parameters that have been in scrutiny for decades in HP relationship are the exponent x and HP constant k . Significant efforts have been invested in determining appropriate scaling exponent values (x) for specific datasets, materials, and material types (e.g., FCC or BCC metals). Numerous researchers have explored exponents other than $x = 1/2$, introducing values like $x = 1/4$ and $x = 0.66$. Baldwin [73] demonstrated that the quality of fit of Eq. (1) to many datasets was as good with exponents x from $x = 1/4$ to $x = 1$ as it was with the $x = 1/2$. Similar observations were reported by Aghaei [74] for AISI 301 Stainless Steel wherein the equation showed equally good fits for $x = 1$ and $1/3$.

The second weakness of this equation is the inverse proportionality of second component itself. There is no conclusive experimental evidence for the inverse square root dependence of strength upon grain size, the HP law, despite the data for most metallic materials fitting this

Eqn. particularly well. Li et al. [75] analysed several cases by fitting of data with several other mathematical relations like $1/d$, $\ln(d)/d$ with satisfactory quality of fitting.

The third limitation of this equation lies in the assumption that the distance between the leading dislocation and the dislocation source is equivalent to the average grain diameter (d). While this assumption holds true for faceted grains with a constant distance ($d/2$) between the dislocation source and the grain boundary, it becomes problematic for non-equiaxed grains. In such cases, where the spatial variation of this distance occurs, it is essential to account for this morphological complexity in the HP relationship. One such attempt to incorporate the effect of grain morphology on yield strength was made in a recent study by Jiang et al. [6] by using dislocation dynamics simulation to investigate the effect of three different morphologies of copper grains on the YS. A generalized form of HP relationship (Eq.2.36) was presented incorporating the effect of grain shape through effective grain size d_{eff} accounting for grain shape. This model is based on the calculated area swept by the dislocation S and average dislocation loop length C , pointing out the importance of grain morphology consideration in grain boundary strengthening.

$$\sigma_y = \sigma_o + \frac{k}{\sqrt{d_{eff}}} \quad (2.36)$$

where,

$$d_{eff} = \left(\frac{4S}{C}\right)^2 \times \frac{1}{\sqrt[3]{V_d}} \quad (2.37)$$

where, V_d is the volume of a grain.

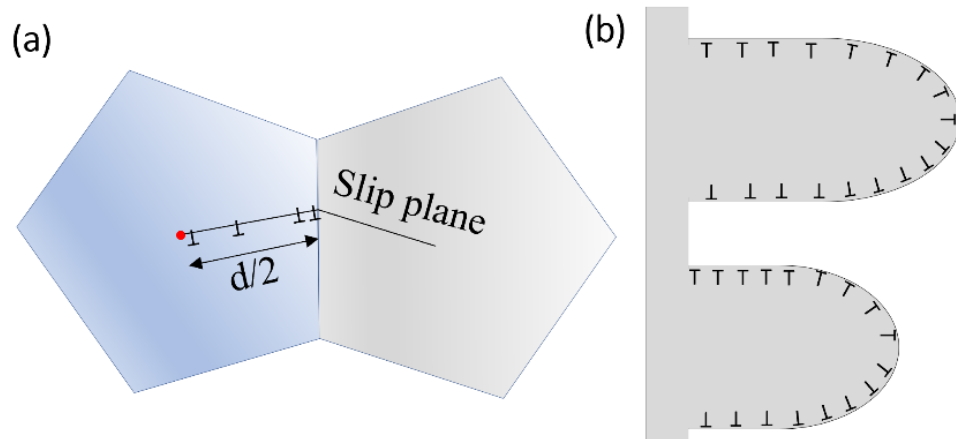


Figure 2.16 Illustration of dislocations piling up against the grain boundary in (a) faceted equiaxed grains and (b) dendritic grains in which the length between dislocation source and the grain boundary varies spatially.

2.9 Hall-Petch relationship and texture dependence of k in Mg alloys

HP relation in Mg alloys is of special importance as it highlights the influence of texture on the strengthening behaviour of the material. Texture and loading conditions show a higher influence on the HP constant in HCP materials than FCC or BCC materials due to lower number of slip systems. Deformation modes in Mg alloys are complicated and includes basal slip ($\{0001\}$ ($\{0001\} \langle 1120 \rangle$), prismatic slip ($\{1010\} \langle 1120 \rangle$), pyramidal $\langle a \rangle$ slip ($\{1011\} \langle 1120 \rangle$), pyramidal $\langle c + a \rangle$ slip ($\{1122\} \langle 1123 \rangle$) with varying critical resolved shear stress (CRSS) values for each mode.

Typically, basal slip systems are predominant at room temperature deformation due to their low activation energy [76–79]. Nevertheless, the activation of prismatic and pyramidal slips can be achieved through solute addition, tailored processing conditions, and specific loading directions in textured materials. Several studies on pure magnesium single crystal have reported that the critical resolved shear stress (CRSS) to activate non-basal slip is significantly higher than that of basal slip, being roughly two orders of magnitude higher than basal slip at ambient-

temperature. These factors significantly influence the deformation behaviour and the HP relationship in highly textured materials.

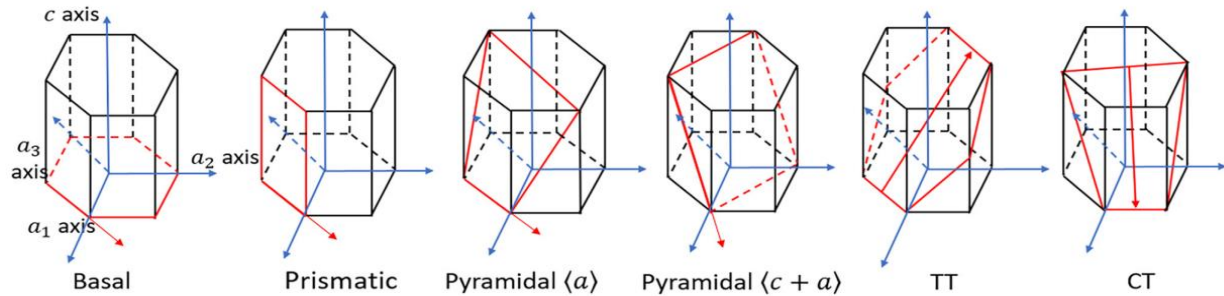


Figure 2.17 Illustration of slips and twins system (TT: tension twin, CT: compression twin) in Mg crystal . Figure is reprinted from [76]

The influence of active deformation modes in Mg alloys, is evident in HP constant. In Mg alloys, numerous studies reveal a significant disparity in k values for the same alloy undergone different thermo-mechanical processes as processing is known to influence the texture of Mg alloys. For example, Wang et al. [80] reported that the measured k value of friction stir processed (FSPed) Mg alloy AZ31 was $160 \text{ MPa } \mu\text{m}^{1/2}$, whereas for hot extruded samples, k value was reported to be $303 \text{ MPa } \mu\text{m}^{1/2}$. This observation was attributed to the evolution of texture during mechanical processing. Similarly, the k value for as rolled AZ31 ($230 \text{ MPa } \mu\text{m}^{1/2}$) was found to be almost double than the ECAPed counterparts ($170 \text{ MPa } \mu\text{m}^{1/2}$) [81]. Wang et al. also reported the difference in k value for electron beam welding (EBW) and hot rolled AZ31 alloy. The measured k value during tension for EBW specimen was $202 \text{ MPa} \cdot \text{m}^{1/2}$. The variation in the HP constant is commonly attributed to the predominant deformation modes that are active under stress and typically, the deformation mode with a higher critical resolved shear stress (CRSS) value results in a higher k value [82].

The activation of slip system is also subjected to the loading directions. For instance, Wang and Choo [83] demonstrated the variation of k from 158 to 411 MPa m^{1/2} in specimen taken from rolled AZ31 plate.

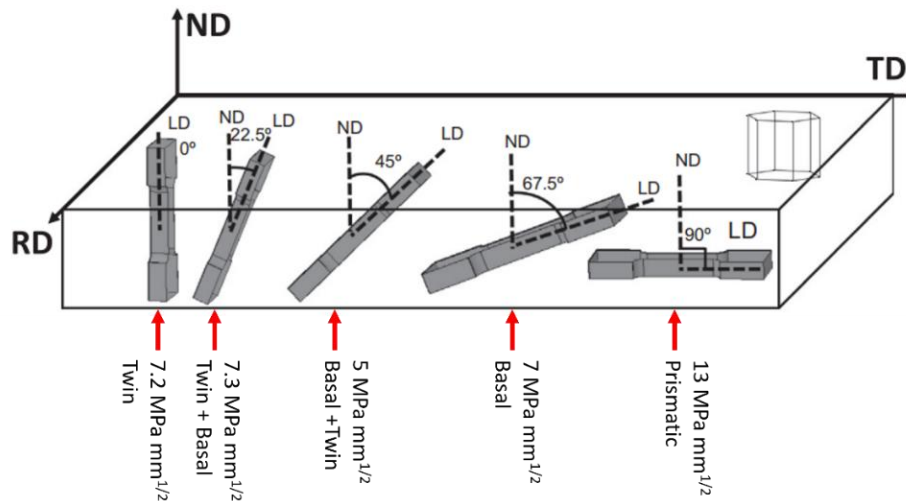


Figure 2.18 Illustration of tensile specimen taken from rolled AZ31 plate at different orientations , ND, TD and RD signifies normal, transverse and rolling directions. Corresponding active twin and slip systems and k values are presented for each specimen.

Figure is adopted from Ref [83]

The loading direction was varied from 0 to 90° with respect to the normal direction (ND). Schematic in Figure 2.18 shows the direction of specimen extracted from the rolled AZ31 plate with corresponding k value and active slip and twin systems. The variation in texture of the specimen due to changing angle between the loading direction and normal direction has an evident influence on the activation of slip systems and this is evident in the variation of k values. Yuan et al. [84] tested FSPed AZ31 alloy along the processing direction (PD) and the transverse direction (TD) and found that measured k value in the PD was 119 MPa m^{1/2}, whereas k value in TD was measured to be 236 MPa m^{1/2}. This variation was attributed to the tilting of basal poles towards PD, promoting basal slip activation during loading in PD and k value for basal slip is lower [85].

Several studies have also shown the influence of testing condition (tension/ compression) on the k value. For instance, Kim et al. [86] reported the k value of rolled plate AZ31 alloy tested under rolling direction compression to be 472 MPa m^{1/2}. Whereas, for tension, k value was reported to be 207 MPa m^{1/2}. This behaviour is similar to the tension/compression along RD or TD of an AZ31 rolled plate. The disparity in k values of Mg alloys is considerable. However, the dependence of k value on texture in BCC and FCC metals is not dominant[87,88] since, in cubic metals the effects of crystal orientation are limited by the large number of slip systems available.

According to dislocation pile-up model, Armstrong suggested the plastic deformation as a process of dislocation source operation by the stress concentration at the grain boundary. Following the relationship between the stress concentration and the critical shear stress for source operation, the HP coefficient k can be expressed as[87]

$$k = M(\alpha\pi M^* \tau_c G \mathbf{b})^{1/2} \quad (2.38)$$

$$k = M^2 \tau_c h^{1/2} \quad (2.39)$$

where M is the Taylor factor relating tensile strength to the resolved shear stress of a polycrystal, M^* is the Sachs orientation factor, G is the shear modulus, \mathbf{b} is the Burgers vector, an average dislocation character is expressed in the factor $\alpha = 2(1-\nu)/(2-\nu)$, with ν being Poisson's ratio, τ_c is the resolved shear stress required to operate the dislocation source near the grain boundary dislocation. And h is the distance between the dislocation pile up and dislocation source in adjacent grain. Recently, a similar equation was presented by Wang et al.[83]

$$k = M(\alpha \tau_c G \mathbf{b})^{1/2} \quad (2.40)$$

These equations are suitable for calculating k value for materials with low texture dependence, like BCC and FCC [89,90]. For HCP materials, [91–93] where k value has a higher anisotropy, these relations often fail. To account for the complexity of texture on the k value, Guan et al. [94] proposed a new relationship, considering the effect from both internal and external stress in a grain in contrast to previous equations, where only external stress is considered. The relationship is given by

$$k = 2 \sigma_d m'^{-1} h^{0.5} \quad (2.41)$$

where term σ_d signifies magnitude of the texture effects on k from the external stress and is measured as the difference between the activation energy of active deformation modes in two adjacent grains. Similarly, m' reflects the effect of internal stress on k and can be given by

$$m' = \cos \alpha \cos \hat{\beta} \quad (2.42)$$

where α and $\hat{\beta}$ are the angles of the slip planes and slip directions between two adjacent grains. This equation was reported to accurately predict the k values in extruded Mg AZ31 rod, a hot-rolled AZ31 plate, and an AZ31 plate subjected to friction stir processing (FSP).

2.10 Dendritic orientation selection

2.10.1 Solute induced grain orientation transition

Materials undergoing solidification manifest two primary growth modes: faceted and non-faceted. Faceted growth entails the formation of distinct, well-defined crystallographic planes, typically observed in materials with significant structural disparities between their liquid and solid states. Here, growth is chiefly dictated by atomic attachment kinetics. In contrast, non-faceted crystals exhibit a rough interface at the microscopic level and are frequently encountered in metallic systems. Under certain conditions, planar fronts of various

crystallographic indices can grow at nearly identical velocities, yielding smoothly shaped crystals.

In the case of alloys, the instabilities of the solid–liquid front, associated with the rejection of solute species and leading to the development of dendrites, are influenced by the slight anisotropy of the solid/liquid surface tension and atom attachment kinetics. At the unstable perturbation at the solid/liquid interface, since atoms do not belong to either solid or liquid phase, atoms have to accommodate the structural difference between the liquid and solid phase. The excessive free Gibbs energy per unit area of the interface is known as the interfacial energy γ_{SL} .

In metals the attachment kinetics is reported to be rapid and the solid liquid interface is assumed to be in local thermodynamic equilibrium and the dendritic growth directions is primarily determined by the anisotropy of interfacial energy [95]. The interfacial energy of a cubic crystal suspended in a liquid is given by $\gamma_{SL}(\hat{n})$, where \hat{n} is the normal direction of the interface. In three dimensions, the value of γ_{SL} can be expressed as cubic harmonics [31], given by

$$\gamma_{SL}(\acute{\alpha}, \acute{\epsilon}) = \gamma_o [1 + \epsilon_1 K_1(\acute{\alpha}, \acute{\epsilon}) + \epsilon_2 K_2(\acute{\alpha}, \acute{\epsilon}) + \dots] \quad (2.43)$$

where γ_o is the mean value of γ ; $\acute{\alpha}$ and $\acute{\epsilon}$ are the spherical coordinates of the interface normal; ϵ_1 and ϵ_2 are the anisotropy parameters and K_1 and K_2 are the cubic harmonics.

The expansion of this term has laid grounds to the MD simulation of the growth selection of dendrite and consideration of the first and second harmonics of anisotropy parameters ϵ_1 and ϵ_2 are important to explain the anisotropy of a solid liquid interface and modelling the dendritic growth directions [95].

In practical observations, the solid liquid interface anisotropy has been reported to influence the dendritic growth morphologies and produce grains with unusual morphologies. For instance, Henry et al [96] reported the formation of “feathery crystals” in directionally solidified (1Dimensional) Al-Cu alloy and direct-chill (DC) cast Al-Mg-Si alloy. Electron Backscattered Diffraction (EBSD) analysis, combined with electronic and optical microscopy observations confirmed the splitting of dendrites to form a feathery morphology. They reported that the feathery morphology of these grain constitutes of lamellae of $\langle 110 \rangle$ dendrites, which are split in their centre by a (111) twin plane and extending on both sides with $\langle 110 \rangle$ arms. However, no clear explanation was provided for the mechanism behind the formation of such grains. Later, Henry et al. [97] reported the formation of similar feathery grains in directionally solidified Al-Cu-Mg alloy. The dendrites constituted of feathery grains which were composed of twinned $\langle 110 \rangle$ trunks and either twinned or untwinned $\langle 110 \rangle$ arms. To illustrate the morphology of feathery grains, an example is shown in Figure 2.19. The formation of these grains was attributed to a combination of change in anisotropic properties such as interfacial energy or atom attachment kinetics coupled with the twinning initiation due to stacking fault.

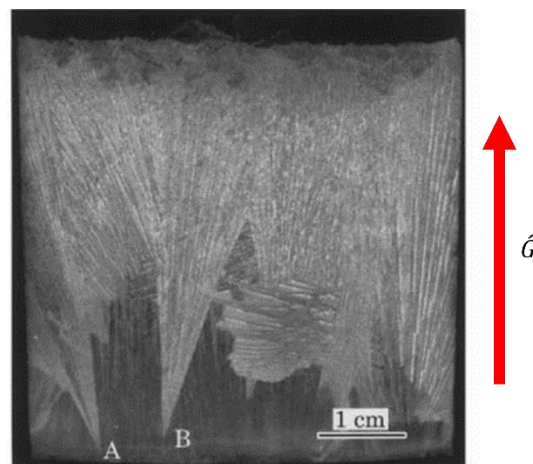


Figure 2.19 Longitudinal section of the feathery grain structure obtained in an Al-Cu-Mg alloy, \hat{G} is the thermal gradient for directional solidification, reprinted from Ref [97]

Several researchers have reported the significant impact of solute atom's lattice structure on the anisotropy of solid/liquid interfacial energy of aluminium and magnesium, consequently influencing the growth direction of dendrites. In the case of Al, characterized by relatively weak anisotropy, elements such as Zn with a hexagonal structure has an approximate 30% anisotropy between the c-axis and the basal plane, are known for its effectiveness in inducing perturbations and generating intricate grain morphologies. As mentioned earlier, the innate tendency of Al grains is to grow in $\langle 100 \rangle$ direction, however addition of elements such as Zn has shown to change the preferred dendritic growth direction.

The deviation of growth direction of primary dendrites in Al-Zn alloy was observed by Moroz et al. [98] in Al-Zn-Si thin coatings deposited on steel sheets by hot dipping. EBSD analysis of 20 μ m thin coatings were conducted and result confirmed the change in growth direction of Al dendrites. An equiaxed dendrite with $\{001\}$ plane aligned with the coating surface showed an eight fold symmetry pattern growing in $\langle 320 \rangle$ instead of a usual fourfold symmetry along $\langle 100 \rangle$ direction. Influence of Zn on the dendritic orientation transition (DOT) has been extensively studied by Rappaz and group. Gonzales and Rappaz [99] systematically studied the influence of Zn on the DOT of Al in Al-Zn binary alloys. Alloys ranging from 5-90 wt.% Zn were solidified in a Bridgeman furnace and microstructures were analysed using EBSD. A continuous change in preferential growth direction of Al dendrites was observed with increasing Zn concentration. The Al dendrites changed their growth direction from $\langle 100 \rangle$ to $\langle 110 \rangle$ in a $\{100\}$ plane between 25 and 60 wt.% Zn. Below 25 wt.%, the growth direction remained $\langle 100 \rangle$ and above 60 wt.% the growth direction remained $\langle 110 \rangle$ up to 90 wt.% (Figure 2.20a). This transition in the grain growth orientation was attributed to the weak interfacial solid-liquid anisotropy of Al. Following these observations Haxhimali and Rappaz [31] conducted phase field modelling of growth morphology of equiaxed grains of Al-Zn binary alloys. Hyperbranched dendrites with 4 tips emerging from each $\langle 100 \rangle$ direction

deviated to $\langle 110 \rangle$ direction in the $\{100\}$ plane as the anisotropy parameter of first order ε_1 increases as the Zn content increases from 25 to 60 wt.% Zn (Figure 2.20b). These results corroborated the experimental results presented earlier. Following these observations, Friedli et al. [100] conducted the x-ray tomography experiments to understand the 3D evolution of Al-Zn dendrites during DOT. Bridgman solidification experiments were conducted on Al-Zn alloys and characterization of as cast alloys was conducted using x-ray tomography. The observation confirmed the DOT reported in the previous studies and at intermediate compositions, i.e., between 25 and 55 wt. %, a sea weed morphology of the dendrites growing in $\langle 320 \rangle$ was reported. The seaweed microstructures did not exhibit clear trunks and arms but were nevertheless textured.

Similar to DOT in Al alloys, influence of solute on the growth orientation in Mg alloys is also present in literature [101,102]. In Mg alloys, Yang et al. [16] used X Ray tomography and EBSD techniques to reveal the changes in morphology of α -Mg with increasing Zn content. At lower solute content (Zn = 0 - 20 wt.%) the morphology of α -Mg dendrite changed from 18 branches with growth direction of primary branches $\langle 11\bar{2}0 \rangle$ and $\langle 11\bar{2}3 \rangle$ to 12 branches with growth direction along $\langle 11\bar{2}3 \rangle$ when Zn is more than 40 wt.%.

This continuous DOT has a direct influence on the texture of directionally solidified alloys and thus has important implications for controlling the mechanical properties of cast alloys.

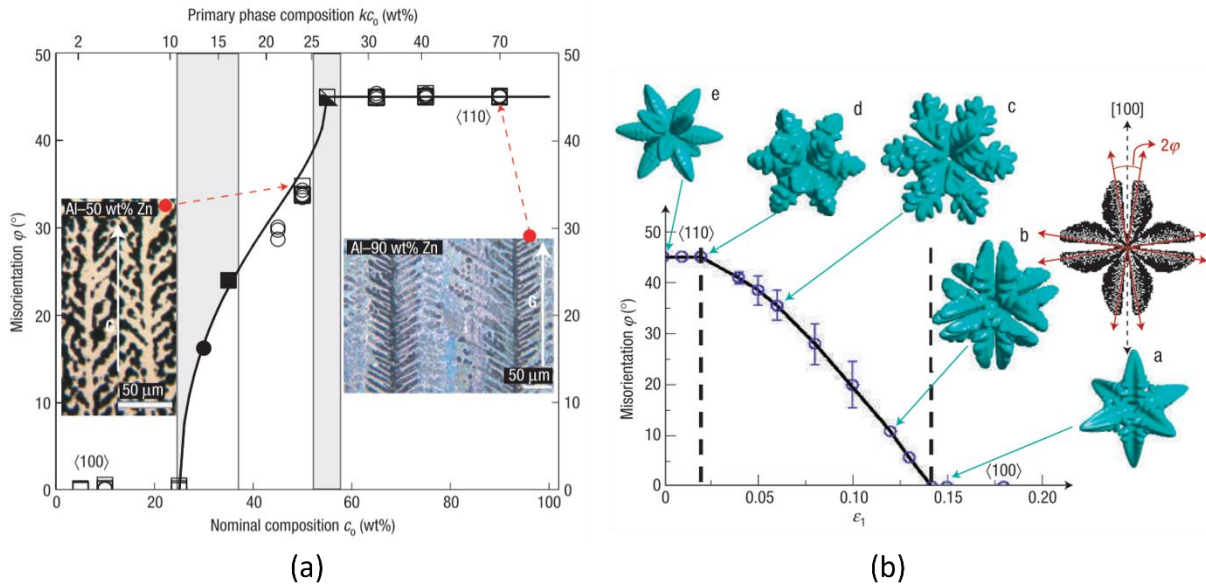


Figure 2.20 Plots showing the dendritic orientation transition (DOT) in Al-Zn alloys. (a) Change in the angle between $\langle 100 \rangle$ and dendritic growth direction of Al-Zn dendrites in directionally solidified Al-Zn alloys as a function nominal composition of Zn. Optical micrographs are presented for Al-50 and 90 wt.% alloys. A continuous increase of misorientation from 0 to 45° over the Zn concentration ranging from 25 to 55wt.% is noticeable. (b) Equiaxed dendrites and growth directions from phase-field simulations are presented as a function of ϵ_1 . A change in dendritic growth orientation is evident for the values of ϵ_1 ranging between the two dashed lines. The image in right upper corner illustrates the 2 D cross section of solid liquid boundary at equal intervals of time in a (001) plane for parameters corresponding to point b. Both plots are reprinted from Ref [31]

2.11 Binary Al-Si alloy system

Al-Si alloys hold significant technological importance due to their exceptional casting properties, high wear resistance, high corrosion resistance, and good mechanical strength. Al-Si system is a eutectic system with limited solubility of Si in Al. Figure 2.21 shows the binary phase diagram of Al-Si system using Thermo-Calc. The maximum solubility of Si of Si in Al

is 1.6 wt.% at 577°C (eutectic temperature). The eutectic composition of this system is at 12.6 wt.%.

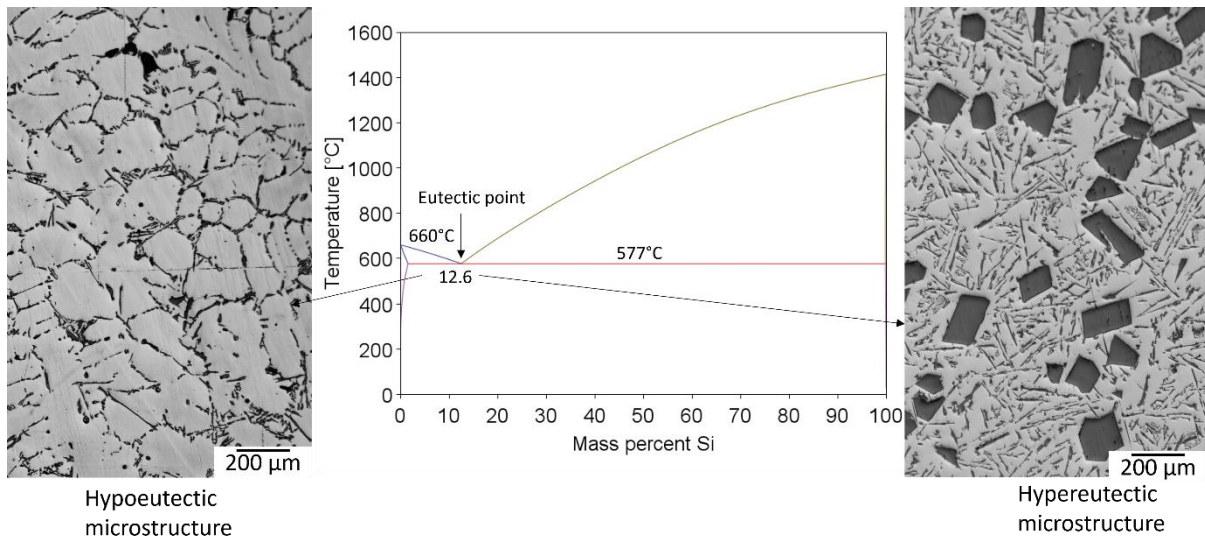


Figure 2.21 equilibrium phase diagram for the Al-Si system along with typical microstructures observed in hypoeutectic and hypereutectic Al-Si alloys

The eutectic reaction during phase transformation is given by an equation of the form



where, L is the liquid, α is solid solution of Si in Al and β is Si. Although the maximum solubility of Si in Al is at eutectic temperature, at room temperature the solubility is merely 0.002 at.%. However, the influence of nonequilibrium solidification conditions on the increased solubility of Si has been reported by various researchers [103–105]

For instance, Uzon et al.[104] studied the influence of cooling rate on the mechanical behaviour of rapidly solidified Al-8, 10 and 12 wt. % Si alloys, using melt-spinning technique. XRD analysis revealed an increase in the solubility of Si in α -Al, which was also reflected in

threefold increase in Vickers hardness observed in melt-spun alloys compared to their conventionally cast counterparts.

Figure 2.21 shows the microstructures of typical Al-Si alloys at hypoeutectic and hypereutectic compositions. The hypoeutectic alloys consist of ductile α -Al phase and a very hard, brittle Si phase. Whereas in hypereutectic compositions, due to zero solubility of Al in Si, there is no β -phase, and the microstructure is generally composed of α -Al, eutectic Si and primary Si particles embedded in the matrix.

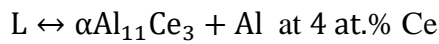
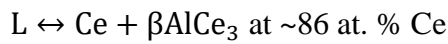
2.12 High temperature application of Al alloys

The earliest attempts to study high strength thermally stable alloys can be traced back to 1950 [106,107]. Traditionally, Sc and Zr are the most suitable alloying elements for making high temperature heat treatable alloys than conventional Al alloys. Recent years show a slight drift to a more economical rare earth metal, Ce. Several studies on the chemistry of Ce containing alloys and its strengthening behaviour have provided adequate knowledge for the development of high-performance Ce containing Al alloys. For example, a prior investigation by David Weiss[108] demonstrated a comparison between Al-8Ce-10Mg ternary alloy and conventional piston alloys wherein the Al-8Ce-10Mg alloy showed significantly higher mechanical strength at elevated temperature. In another study by Wang et al. at[109], effect of Yttrium on the HPDC Al-8Ce alloy was investigated. Al-8Ce-3Y alloy was cast using HPDC and was further tested at high temperature and compared with the properties of conventional piston alloys. Al-8Ce-3Y significantly outperformed the common piston alloys at a temperature of 300°C after holding at 200 hours.

It's evident that the Ce addition has a positive effect on Al alloys and the fundamentals of Ce in Al are discussed below.

2.12.1 Solubility of Ce in Aluminium

Ce forms five compounds in Al-Ce binary alloy. These compounds are AlCe_3 , Al_2Ce , AlCe , $\text{Al}_{11}\text{Ce}_3$ and Al_3Ce . The reaction of eutectic reactions of these phases can be found in ref [110].



Although Ref [110] shows the major compounds forming in the eutectic reactions in Al-Ce binary system, later reassessments by Gao [111] using SEM and DTA, as well as initio calculations showed the presence of AlCe_2 and Al_4Ce at a limited range of temperatures. Amongst all these compounds, $\text{Al}_{11}\text{Ce}_3$ is the most reported phase. The intermetallic formed in binary Al-Ce alloys upon the solidification of αAl is $\text{Al}_{11}\text{Ce}_3$ with lattice parameters: $a = 4.395\text{\AA}$, $b = 10.09\text{\AA}$ and $c = 13.025\text{\AA}$. Ce has a very low diffusivity in Al [112] which offers resistance to coarsening at higher temperature and keeping the phase thermally stable. This compound forms highly interconnected eutectics exhibiting lath type structure which can grow up to several hundred nanometres in length[113]. At a closer look, these intermetallic are fine rods packed together in a colony giving it a lamellar structure. These colonies have an orientation with other colonies and are of same size of several micrometres for a hypoeutectic alloy.

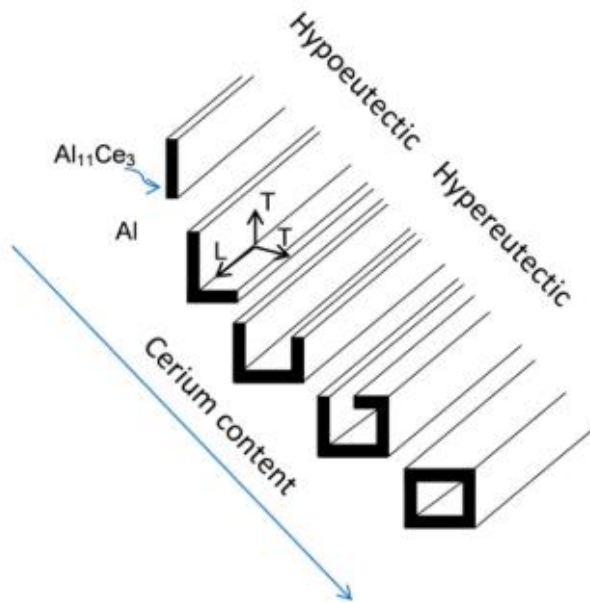


Figure 2.22 Schematic showing the effect of Ce content on morphology of the eutectic phase $Al_{11}Ce_3$ [113].

The morphology of these eutectic shows a dependence on the Ce content. A study by Frank et al.[114] illustrated the morphological modification in a series of Al-Ce binary alloys with Ce ranging from 5 to 20wt.%. SEM and TEM images of Al-5,10,15 and 10wt.%Ce were analysed to assess the effect of Ce content on the eutectic morphology. Illustration in Figure 2.23 shows the transition of shape of the eutectic rods in a lamella. Although, the stability of this phase is very high up to a temperature of $\sim 400^{\circ}C$ [108], at room temperature, $Al_{11}Ce_3$ is not an effective strengthening phase. Table 2-3 shows the YS of binary Al-Ce alloys.

Table 2-3: Mechanical properties of binary Al-Ce alloys

S.No	Alloy	Ultimate Tensile Strength (MPa) As cast	Yield Strength (MPa) As cast	% Elongation, As cast
1	Al-16Ce	144	68	2.5
2	Al-12Ce	163	58	13.5
3	Al-10Ce	152	50	8

4	Al-8Ce	148	40	19
5	Al-6Ce	103	30	25

The hardness of $Al_{11}Ce_3$ phase in Al-20Ce binary alloy was recorded to be 350HV which is 10 times higher than the Al matrix (34HV). Unfortunately, this strength doesn't translate into the eutectic Al-Ce alloy which shows a hardness ranging from 45 to 50HV.

2.12.2 Role of Sc and Zr in Al-Ce alloys

Like Ce, Sc is a rare earth element and exhibits similar properties by the virtue of low solubility in Al matrix. Much interest has been attained by Sc due to its precipitation strengthening behaviour in Al matrix at high temperature. But, due to high cost associated with the availability of the raw material, Sc is not an economically viable element for manufacturing purpose. Sc has a relatively higher diffusivity in Al and forms nano scaled coherent Al_3Sc precipitate with $L1_2$ crystallography. The crystalline structure can be described as an ordered face centred cubic with Sc atoms in the corners and Al atoms in the centre of the face. Figure 2.24 shows the structure of Al_3Sc phase.

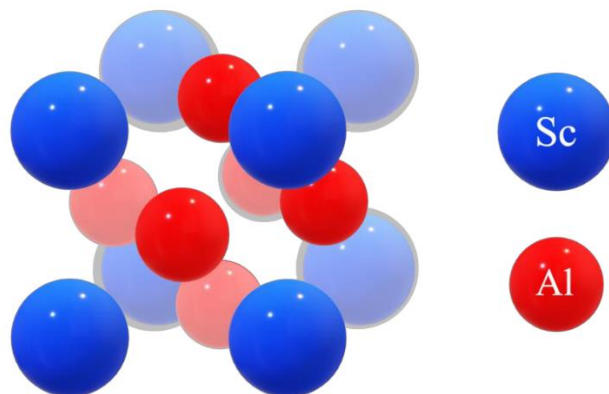


Figure 2.23 The lattice structure of Al_3Sc [115]

The Al_3Sc has a low density of 3.03 g. cm^{-3} and melts peritectically at a very high temperature of 1320°C [116] which makes it thermally stable and high in number density when precipitating from super saturated Al matrix. Due to low density and solubility, even a small concentration of Sc has proven to elevate the strength of Al alloy by optimum ageing. For example, the hardness of Al-0.18Sc alloy was increased from 200MPa to 780MPa by ageing at 300°C [117]. In another study by Seidman et al. [118], it was demonstrated that the micro alloying with Sc(<3wt.%) improved the creep resistance up to 300°C . Although Sc provides a good strengthening by low addition, at temperature higher than $\sim 300^\circ\text{C}$ for long operating hours due to coarsening of Al_3Sc , the degradation of mechanical properties is observed.

Sc is commonly mixed with Zr while designing an alloy. Zr has a low diffusivity in Al[119] and it forms similar L1_2 ordered precipitates. However, the precipitation of Zr in Al is very slow as compared to Sc. Since the diffusivity of Zr in Al is low, the precipitates it forms are resistant to coarsening than Al_3Sc phase. In Al-Sc-Zr, the Al_3Sc precipitates form early during the ageing and acts as the nucleation sites for Zr atoms, forming $\text{Al}_3(\text{Sc}, \text{Zr})$ precipitate with a core rich in Sc and an outer shell rich in Zr which provides resistance to coarsening[120]. Therefore, addition of Zr along with Sc serves two purposes, one being the resistance provided against coarsening and secondly the amount of Sc needed for effective strengthening is reduced. Although the effect of Sc and Zr on Al alloys is well discussed in the literature, no significant study is available to evaluate the precipitation behaviour of Sc and Zr in Al-Ce alloys. Recently Wang et al.[121] studied the effect of micro alloying of Al-5Ce with Sc(0.2 wt.%) and Zr(0.2 wt.%). The grain refinement behaviour of Zr and Sc was significant with the refinement of $\text{Al}_{11}\text{Ce}_3$ phase in the eutectic. The morphology of eutectic was modified from lamellae to thin rods which was attributed to Zr addition. This modification impacted the elongation, increasing from 17.5% to 23%. Same trend was followed by yield strength which was 155MPa for Al-5Ce -0.2Sc-0.2Zr as compared to 49 of Al-5Ce base alloy, after heat

treatment. This improvement was attributed to much known precipitation of Sc and Zr within the Al-5Ce matrix. Traces of solubility of Zr in the $Al_{11}Ce_3$ phase were recorded with EDS, but no reaction of Sc with Ce was noticed. Nonetheless, these results make Sc and Zr a good candidate for designing complex alloy systems with Al-Ce base alloy.

2.12.3 Al–Si–Mg–Ce system

Al-Si alloys are the widely used alloys in the automotive industries due to good castability, high strength to weight ratio and good wear resistance[122]. Addition of Mg to this alloy system improves the heat treatment response by the virtue of solution strengthening and formation of Mg_2Si precipitates. The base alloy with eutectic Si provides a good matrix strength by load bearing effect from plate like Si particles, but low ductility in hypereutectic Al-Si alloys usually requires modification of eutectic by alloying. Addition of Ce helps in the modification of microstructure and elevating the overall properties. Several studies show the positive effect of Ce addition in the Al-Si-Mg ternary alloys in terms of YS and wear resistance. Animesh et al.[123] reported the thermal stability of Al-12Ce-4Si-0.4Mg alloy at a temperature of 300°C. Similar improvement was reported by Daud et al.[124] in the wear resistance of Al-12Si hypereutectic alloy with the addition of 0.02wt.% Ce. A significant improvement in the wear resistance was noticed in dry sliding condition using a pin on disk set-up.

The thermodynamic analysis of the Al-Si-Mg-Ce quaternary system requires the description of the 6 binary systems namely, Al-Si, Al-Mg, Al-Ce, Mg-Si, Mg-Ce and Si-Ce. The attempt of the unification of thermodynamics description of these binary systems in Al-Ce-Mg-Si quaternary diagram with Al rich corner along with the experimental validation was made by Zhang et al.[125]. Al–7Si– 0.6Mg–0.4Ce quaternary alloy was studied to validate the phase transition obtained from the Gulliver–Scheil simulation with the experimentally measured phases from the solidified as cast microstructures. Four transformations during the

solidification of quaternary alloy were reported: formation of primary Al at 613°C, followed by the formation of binary eutectic Al+Si at 571°C, followed by the ternary formation of Al+Si+AlCeSi₂ at 568°C, followed by the final quaternary formation of Al+Si+AlCeSi₂+Mg₂Si at 558°C. The model predicted solidification path of the Al–7Si–0.6Mg–0.4Ce alloy compared with the heating and cooling curve measured by DSC is shown in figure 2.25.

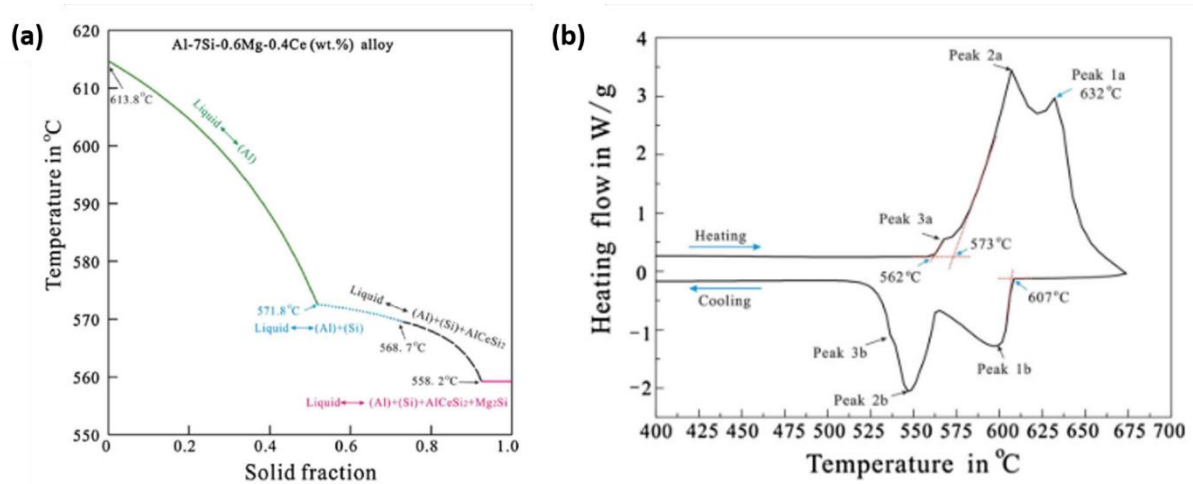


Figure 2.24 (a) Solidification path of the Al–7Si– 0.6Mg–0.4Ce alloy obtained by the simulation under the Scheil–Gulliver conditions. (b) Experimentally measured data by DSC[125]

2.13 Summary

In present chapter, dendritic solidification theories has been presented. Influence of solute atoms on the formation of complex grain morphologies in Al and Mg alloys are also presented. The conventional theories interpreting the physical significance of grain boundary strengthening effect in metals shows the link between the dislocation movement and grain boundaries. However, the role of structure of grain boundaries on the strengthening of a metallic material remains a less explored territory. As discussed, the structure of a grain’s boundary is dictated by the morphology of grain and computational simulation approaches have shown that the morphology of a grain has a profound effect on its yield strength. This

aspect needs more exploration and an approach to link the morphological changes found in practically observed grain structures, with the experimentally measured strength in metallic materials. To tackle these aspects of a grain structure, this thesis aims to answer the following research questions

- How to capture/ quantify the morphological changes in grains using effective measurement techniques?
- Study the influence of morphology of primary dendritic structure on the strength of Al and Mg alloys.
- How to incorporate the grain morphological complexity in Hall-Petch relationship?

Conventionally, the morphology of a dendrite in two dimensions is reported to be quantified by measuring the grain boundary concentration or perimeter per unit area[34], and this work adopts the approach and aim to integrate the quantifiable parameter (p') into the conventional Hall-Petch type relationship to signify the influence of morphological changes on the yield strength of these alloys.

3 Methodology

3.1 Material

For the morphological study of Al and Mg binary alloys, commercially pure Al and Mg supplied by *Norton Aluminium Ltd, Staffordshire, UK* and *Shanghai Xinglu Chemical, China* were used respectively in this study. The as received composition of these metal ingots is shown in table 3-1 and 3-2.

Table 3-1 Chemical composition of LM0

Cu	Zn	Si	Fe	Cr	Ni	Ti	Al
0.001	0.003	0.013	0.08	0.001	0.005	0.06	Balance

Table 3-2 Chemical composition of pure Mg

Cu	Zn	Si	Fe	Ni	Al	Ti	Mg
0.001	0.002	0.013	0.002	0.001	0.019	0.06	Balance

The alloying elements were introduced into the matrix by Al-20Si and Al-30Ce master alloys supplied by *Shanghai Xinglu Chemical, China*. The chemical composition is given in table 3-3 and 3-4

Table 3-3 Chemical composition of Al-20Si master alloy

Fe	Si	Mn	Cu	Ni	Cr	Ti	Al
----	----	----	----	----	----	----	----

0.07	19-21	0.04	0.002	0.002	0.001	0.01	Balance
------	-------	------	-------	-------	-------	------	---------

Table 3-4 Chemical composition of Al-30Ce master alloy

Ce	Si	Fe	Cu	Ni	Zn	Ti	Al
28-31	0.1	0.1	0.002	0.05	0.05	0.01	Balance

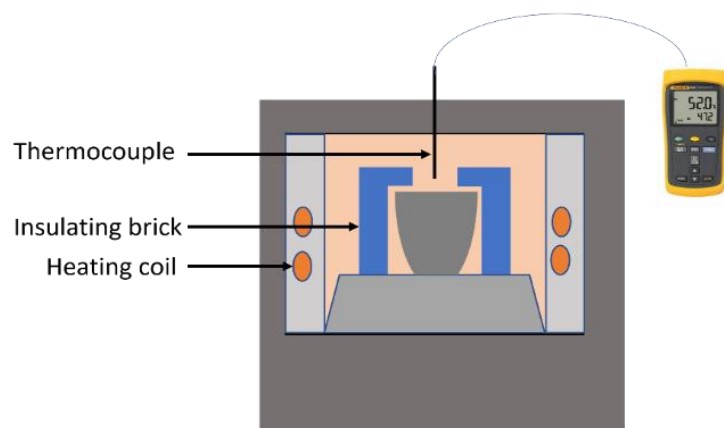
3.2 Casting methods

3.2.1 Controlled solidification

To produce a wide range of microstructural features, the melt was solidified in *Elite* Laboratory Chamber Furnaces (Figure 3.1). To control the heating and cooling profiles, a Eurotherm 2416 proportional-integral-derivative (PID) controller was used. Large batches of Al-Si and Al-Ce alloys with 2, 5, 8, 13wt.% Si and 2, 5, 8, 14wt.% Ce composition were produced in a Carbolite electrical resistance furnace, by melting mixtures of appropriate quantities of 99.99% pure aluminium, Al-20%Si and Al-30wt%Ce master alloys. The chemical composition of produced alloys is verified with optical emission spectroscopy. For controlled solidification of Al-Si alloys, the melt volume is fixed and the adapted heating-cooling profile is shown in Figure 3.2



(a)



(b)

Figure 3.1 (a) Elite laboratory Chamber Furnaces fitted with eurotherm 2416 controller

(b) Illustration of chamber showing the position of crucible and thermocouple

Melt was then transferred to small crucibles and placed in Elite laboratory chamber furnace to solidify under controlled cooling conditions. Before the commencement of cooling process, melt was held for 30 min inside the preheated furnace for the temperature to stabilise. The mass of alloys was fixed to 200g and depending on alloy composition the appropriate values for $T_1(T_{\text{liquidus}} + 5^\circ\text{C})$ and $T_2(T_{\text{eutectic}} - 5^\circ\text{C})$ were chosen. To produce 0.34°C/s and 0.0133°C/s , the melt was solidified at ambient temperature and inside a switched off Carbolite furnace at 750°C in a preheated crucible and the cooling rate is monitored using thermo-couple placed in the vicinity of melt.

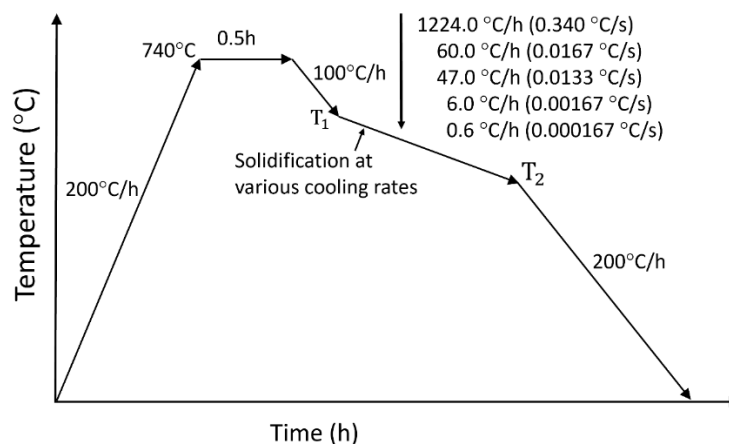


Figure 3.2 solidification path for Al-Si and Al-Ce binary alloys for controlled solidification experiments

3.2.2 Gravity die casting processes

To further vary the cooling rates in Al and Mg alloys, wedge mould castings were produced for all the previously mentioned compositions (Figure 3.3b). For Al alloys, the melt was prepared in electric furnace followed by degassing and was poured at a temperature of 750°C

whereas for Mg alloys the pouring temperature was maintained at 680°C. To keep the cooling rates constant, the inner surface temperature of wedge mould was monitored using an infrared thermometer gun and was maintained at 180°C at the time of transferring the melt.

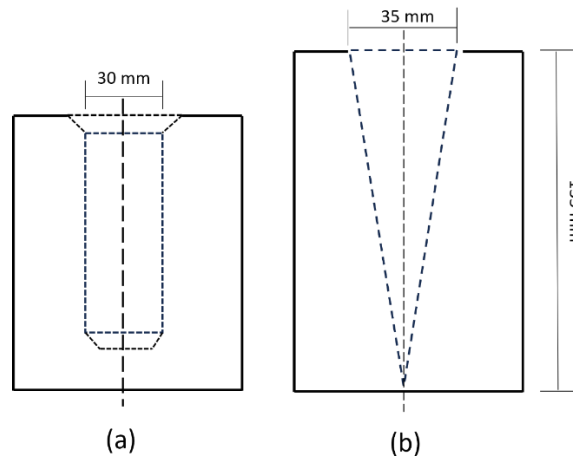


Figure 3.3 Illustration of (a) cylindrical and (b) wedge mould

To decide the optimum level of Ce in binary alloys, a preliminary examination of eutectic phase in Al-Ce binary alloys was conducted by casting Al-2,5,8,12,20 and 30 wt.% Ce alloys by melting the right composition of pure Al and master alloy in Carbolite electric furnace in a graphite crucible and pouring the melt at 750°C into a 30 mm cylindrical steel mould preheated at 200°C (Figure 3.3a).

To further study the thermal stability aspect of Al-Ce alloy systems, a range of several compositions were produced using the book mould casing . 99.99% pure aluminium was melted in a crucible in the electric furnace at a temperature of 780°C and appropriated amount of Al-30wt%Ce, Al-2wt.%Sc and Al-10wt.%Zr master alloys were added to the melt, followed by degassing and pouring into the mould at 750°C. Two castings per alloy were produced and samples were extracted for aging experiments. Figure 3.4 shows the illustration of book mould casting process.

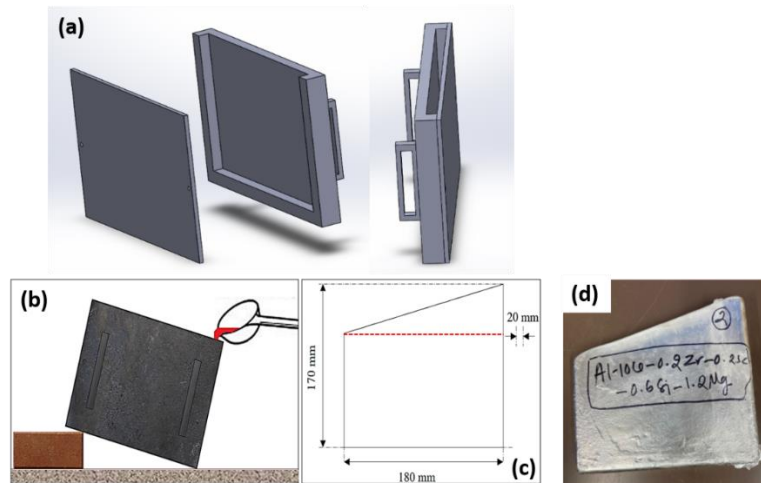


Figure 3.4. Casting operation for producing Al-Ce high temperature alloys using book mould casting, illustration is adopted from [126]

3.2.3 HPDC operations

A Frech 4500kN cold chamber HPDC machine was used to cast eight ASTM B557 standard round tensile test bars with a gauge dimension of $\phi 6.35 \text{ mm} \times 50 \text{ mm}$ in each shot. Figure 3.5 shows the setup of HPDC chamber with die-set in cold chamber. Figure 3.5(c) shows the illustration of die-set showing the round tensile bars casted by the die. The dies were preheated by the means of hot oil at a temperature of 250°C and shot sleeve was preheated at 180°C . During each shot, the mass of melt was fixed to 800 g and the pouring temperature of the melt on ladle was measured to be 750°C before feeding into the shot sleeve. The injection speed of casting was fixed to $\sim 2.3 \text{ m/s}$ and gate speed of $\sim 62 \text{ m/s}$.

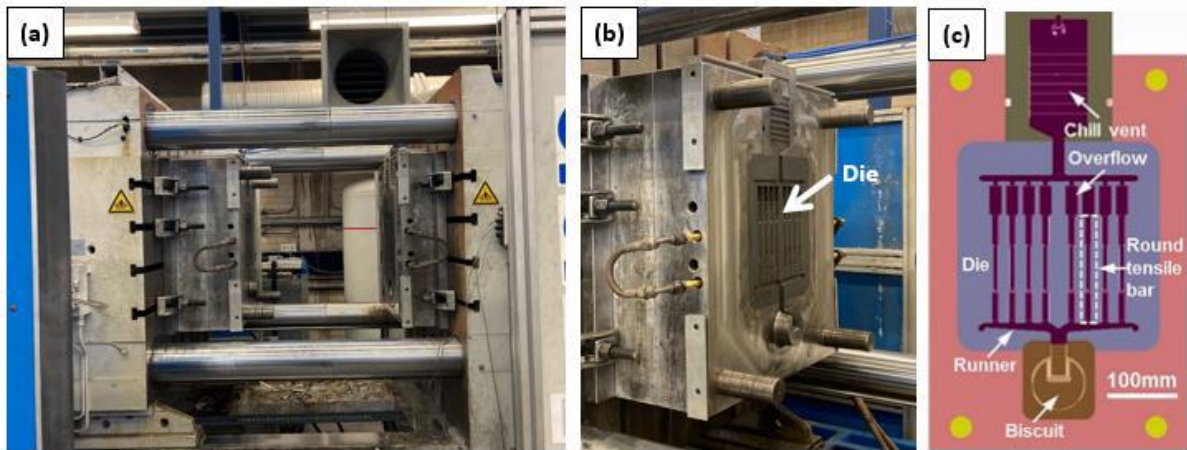


Figure 3.5 (a) High pressure die casting machine (b) casting chamber with tensile bar dies (c) the dimension of tensile bar specimen with overflow and biscuit (reprinted from[127])

3.2.4 Directional solidification

To investigate the change in preferred growth orientation of Al dendrites with increasing Si content, directional solidification experiments were conducted on Al-Si binary alloys. A refractory material based cylindrical mould, with 15 mm diameter and 40 mm height, was constructed for directional solidification experiments. To eliminate radial heat-dissipation, the mould was wrapped in 5 cm thick insulation material and this assembly was preheated to 10°C higher than the pouring temperature of the liquid metal to establish isothermal condition across the radius. To extract heat directionally from the melt, a cold copper block was inserted at the bottom of cylindrical mould. Once the mould is filled with liquid metal, the top is covered with pre-heated insulating material to minimize heat radiation loss, illustration of casting set up is shown in Figure 3.6a. The macro-etched cross-section, shown in Figure 3.6b, confirms the columnar growth along vertical thermal gradient driven by directional solidification condition. Pure Al and Al-Si binary alloys were poured at a temperature of 750°C. For each composition, two castings were produced.

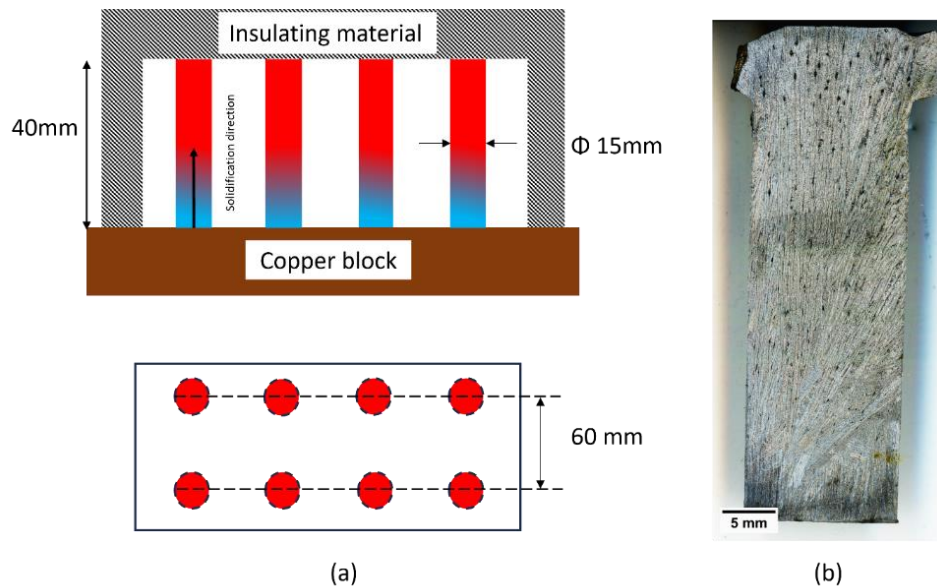


Figure 3.6 illustration of (a) casting setup for directional solidification experiments (b) macro etched directionally solidified Al-8Si alloy.

3.3 Metallography

3.3.1 Mounting and polishing

Al-Si and Al-Ce binary alloys cast via controlled cooling samples were cut from sections of the castings. To keep the observations consistent, all the samples were taken from same positions in the castings (shown in Figure 3.7). For cylindrical mould castings the samples were taken 20mm from the bottom. For book mould castings, the samples were extracted 10 mm from the bottom of the ingot and in the middle of short direction with a section of 20 mm × 20 mm. For wedge mould castings, the samples were extracted from a slice of strip taken 20mm from the side. Each sample was hot mounted on Bakelite resin and SimpliMet 3000 mounting machine (*Buehler, UK*) and was ground and polished using ATM saphir polishing machine.

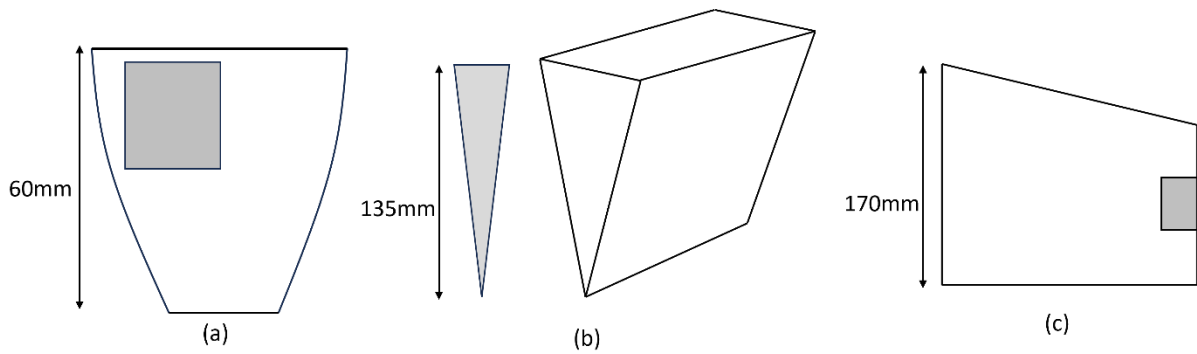


Figure 3.7 Illustration of castings produced through (a) controlled cooling (b) wedge mould casting (c) book mould casting. Grey area shows the location from where the samples were extracted for metallographic observations.

To obtain a consistent finish of surface, the specimen were ground using grit SiC papers starting from 120 grit and final polishing was carried out on a cloth with 1 μ m colloidal silica suspension. The steps of sample preparation is shown in table 3-5.

Table 3-5 Steps for polishing Al alloys

Surface	Abrasive/Size	Load (N)	Base speed (rpm)	Time
CarbiMet	320 grit SiC water cooled	5	300	Until plane
TextMet C	9 μ m MetaDi Diamond	5	150	5:00
TextMet C	3 μ m MetaDi Diamond	5	150	4:00
TextMet C	1 μ m MetaDi Diamond	5	150	2:00

ChemoMet	0.05 μm SiO ₂	5	150	1:30
	OPS			

3.3.2 Etching

3.3.2.1 Macro etching for Al alloys

To assess the variation of grain size in Al-Si and Al-Ce binary alloys solidified at different cooling rates, samples were macro etched using a solution of ferric chloride and water. The samples were first ground using grit 120, 800 and 1200 grit SiC papers. Following grinding, samples were immersed in the ferric chloride solution for at least 2 minutes until grain structure was revealed ((Figure 3.8a).

3.3.2.2 Chemical etching process for Mg alloys

For the characterization of α -Mg dendrites in AZ91 and Mg-Al alloys, chemical etching of polished alloys were performed by immersing the specimens in a solution of 4.2 g picric acid, 15 ml acetic acid, 70 ml ethanol and 15 ml distilled water initiating a controlled chemical reaction. The microstructures were observed under polarised light (Figure 3.8b).

3.4 Anodizing

Al-Si and Al-Ce samples were anodized by immersing the fine polished samples in the electrolyte with 20% perchloric acid solution in acetic acid. The electrolyte solution and sample were connected to electrodes and 30V was applied to the system. The time of anodization was optimized for each alloy ranging from 2 to 3 minutes. The microstructures were observed under polarised field (Figure 3.8c).

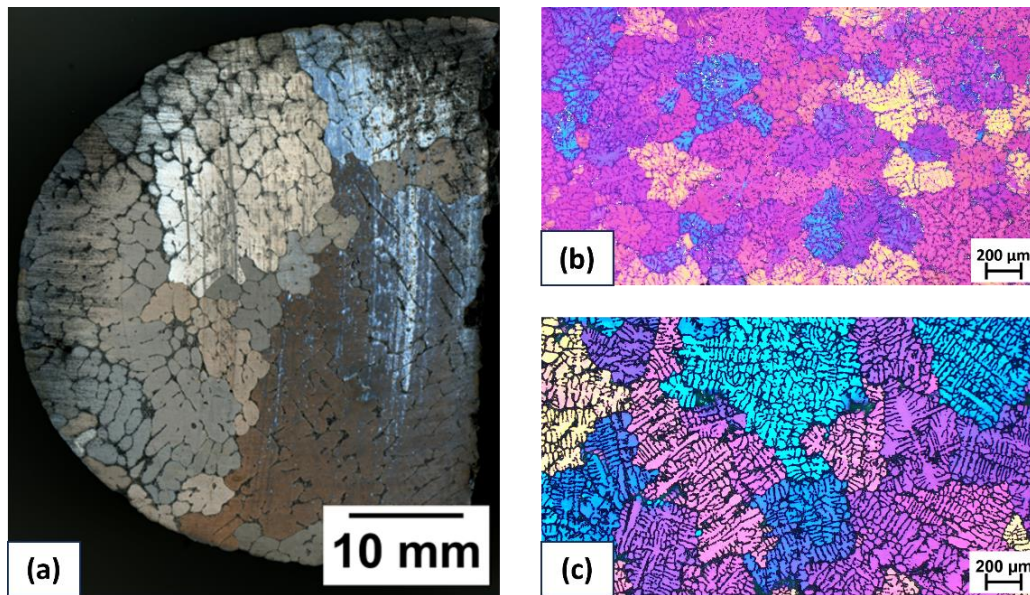


Figure 3.8 Typical microstructures of (a) macro etched sample of slow cooled Al-2Si alloy (b) AZ91D alloy etched with picric acid and (c) anodized Al-5Si sample.

3.5 Microstructural analysis

3.5.1 Optical microscopy

Carl Zeiss AxioScope A1 optical microscope (Figure 3.9) was used for the microstructural characterization of polished samples. Images were captured at 20X to 1000X magnifications under bright and polarized field for etched and anodized samples. The images were captured by AxioCam MRm digital camera on the top of microscope and saved with the image processing software AxioVision 4.9.

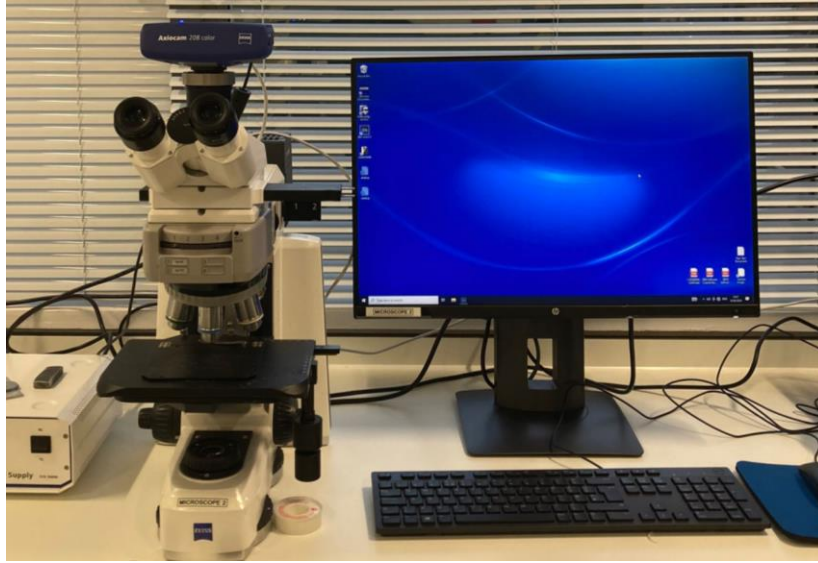


Figure 3.9 Carl Zeiss AxioScope A1 optical microscope

3.5.2 Quantitative microstructural measurements using image processing

3.5.2.1 Grain size and SDAS

Average grain size and Secondary Dendrite Arm Spacing (SDAS) were assessed through the utilization of ImageJ software. Polarized micrographs of anodized samples were analysed at various magnifications, and the resultant average values were recorded. The equiaxed dendrites and faceted grains were measured employing the linear intercept method. The expression for the average grain size can be given as follows

$$D_z = \frac{\overline{L_z}}{N_z} \quad 3.1(a)$$

$$\lambda_2 = \frac{\overline{L_z}}{N_z - 1} \quad 3.1(b)$$

where, D_z is the mean intercept length, $\overline{L_z}$ is the line length, N_z is the number of intersections of grain boundaries and z is the line number. To obtain an average grain size, several test lines are superimposed on the microstructure, one example is shown in the Figure 3.10a.

Similarly, to characterize the dendritic morphology in Al and magnesium Mg alloys, Secondary Dendrite Arm Spacing (SDAS, λ_2) was determined from optical micrographs using ImageJ software. as shown in Figure 3.10b.

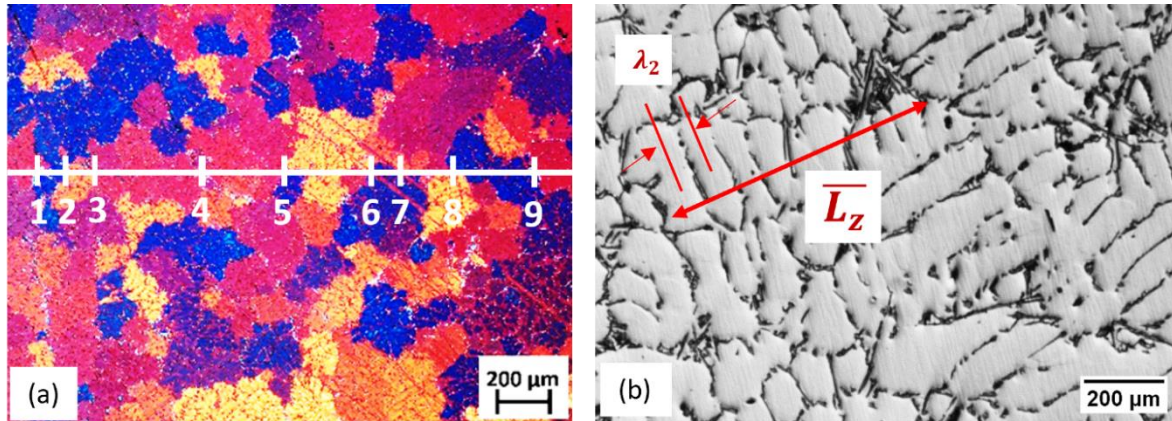


Figure 3.10 Schematic representation of (a) linear intercept method for the measurement of grain size in AZ91 alloy (b) SDAS measurement in Al-5Si alloy

3.5.2.2 Perimeter measurement

ImageJ Software[128] was used to measure the microstructural features like perimeter, lamellar spacing and aspect ratio of eutectic particles. To measure the perimeter of α -Al dendrites, freehand selection tool was used for tracing the outline of dendrites. An example of measurement of perimeter is shown for Al-8Si alloy solidified at 0.34°C/s is shown in Figure 3.11. To minimize the error in measurements, at least 5 images at different magnifications from each sample were processed, which covered an area of $\sim 600 \text{ mm}^2$ in total.

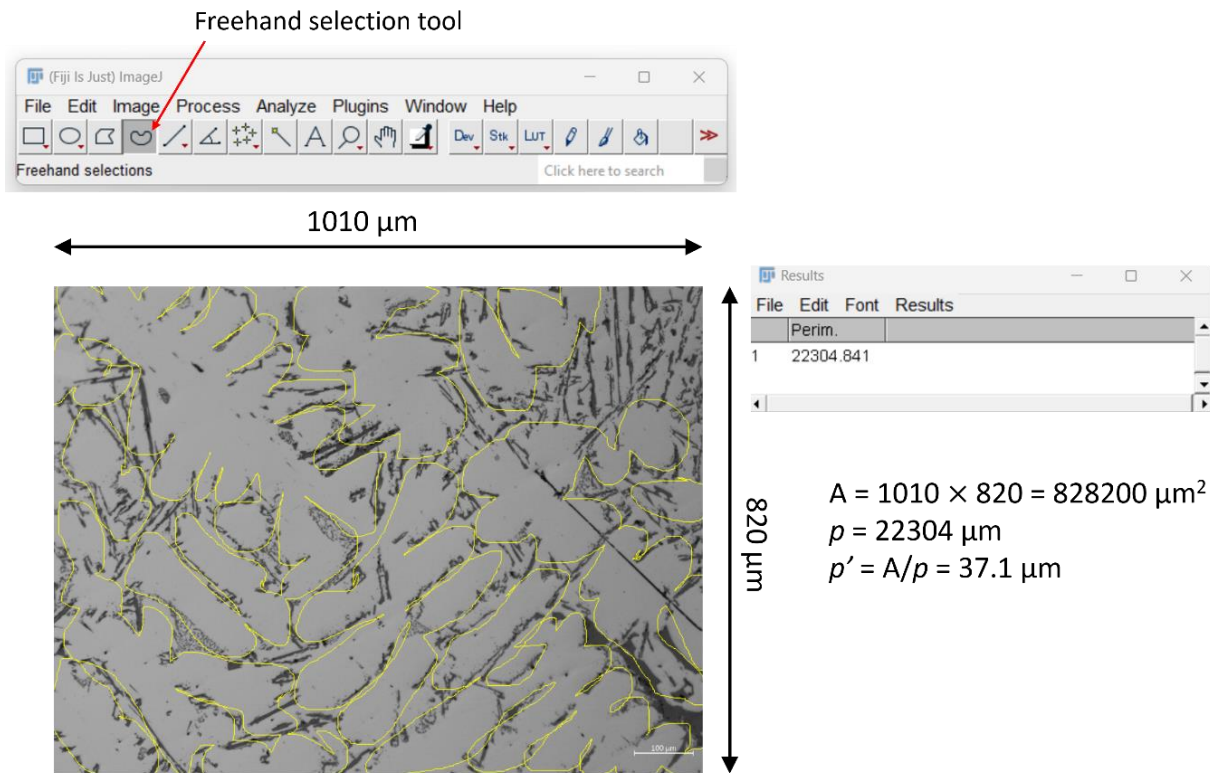


Figure 3.11 Example of measurement of p' using freehand selection tool in ImageJ software. Microstructure of Al-8Si alloy solidified at 0.34°C/s is taken to illustrate the accuracy of measurement of p' .

Due to larger dendritic structure in slowly cooled samples the optical micrographs cannot accommodate the microstructural features, hence scanned images of macro etched samples were used to make the measurements. One example of traced perimeter of dendrites using the microstructure of macro etched Al-8Si sample solidified at 0.00167°C/s is shown in Figure 3.12.

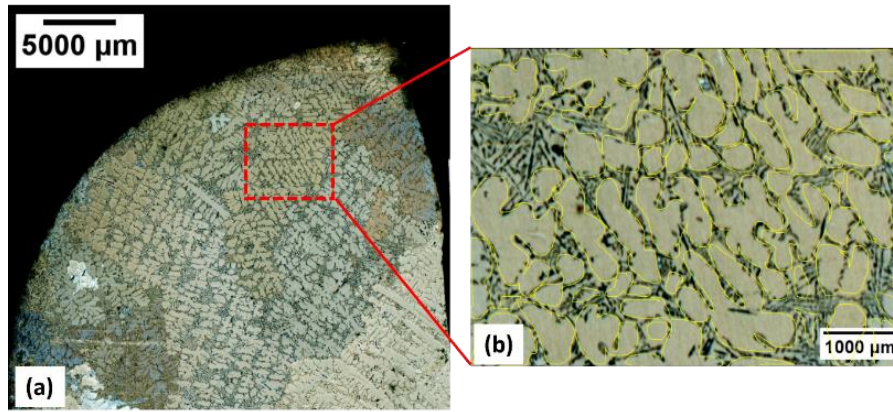


Figure 3.12 Microstructure of (a) macro etched Al-8Si alloy solidified at 0.00167°C/s (b) traced perimeter of α -Al dendrites in a selected region highlighted by red.

3.5.2.3 Lamellar spacing

For the measurement of lamellar spacing, line selection tool was used to estimate the spacing of eutectic Si. Since eutectic Si lamellar are not parallel, average lamellar spacing was measured by using maximum and minimum lamellar spacing, given by

$$\lambda = \frac{\lambda_M + \lambda_m}{2} \quad 3.2$$

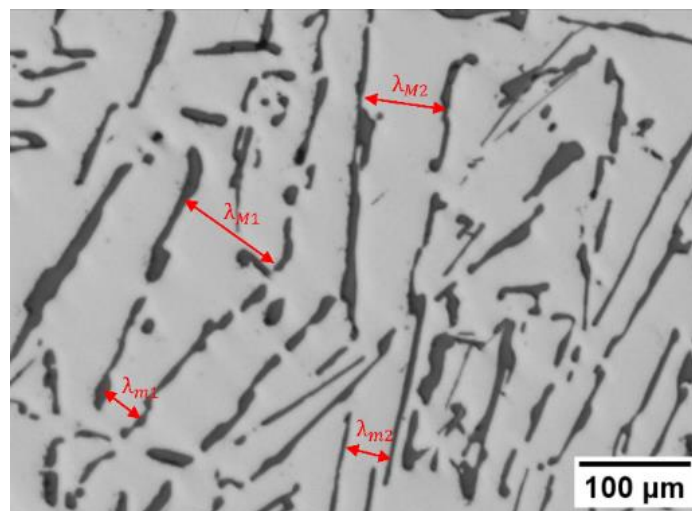


Figure 3.13 An example of measured maximum and minimum lamellar spacing in the microstructure of Al-12.7Si alloy solidified at 0.00167°C/s.

where, λ_M is maximum lamellar spacing and λ_m is the minimum lamellar spacing between two adjacent Si particles. In total ~ 250 measurements were made at different magnifications for each composition. An example of measurement is shown in Figure 3.13.

3.5.2.4 Circularity and aspect ratio measurement

To measure the aspect ratio of eutectic particles, an approach of fitting equivalent ellipses in the complex shapes was employed. Aspect ratio of the eutectic Si and Al₁₁Ce₃ intermetallic particles were measured by dividing the major and minor axis of fitted equivalent ellipse. This technique has been proven to accurately characterize the shape of nonuniform particles in multiple fields of science like geology, civil engineering and material science [129–131]. This technique involves enclosing individual particles within ellipses that best match their shape, allowing for accurate determination of their aspect ratios – the ratio of the major axis to the minor axis. Figure 3.14d shows the accuracy of the fitted ellipse method in measuring the aspect ratio of particles in a selected region. An isolated eutectic Si particle is shown in Figure 3.13a, in which an equivalent ellipse is fitted. The value of major and minor axes of the fitted ellipse shows a difference of <3% when compared with the longest axes of the particle in longitudinal and transverse directions. This measurement shows the reliability and flexibility of using tool for the aspect ratio measurements of a large number of particles in a bigger region.

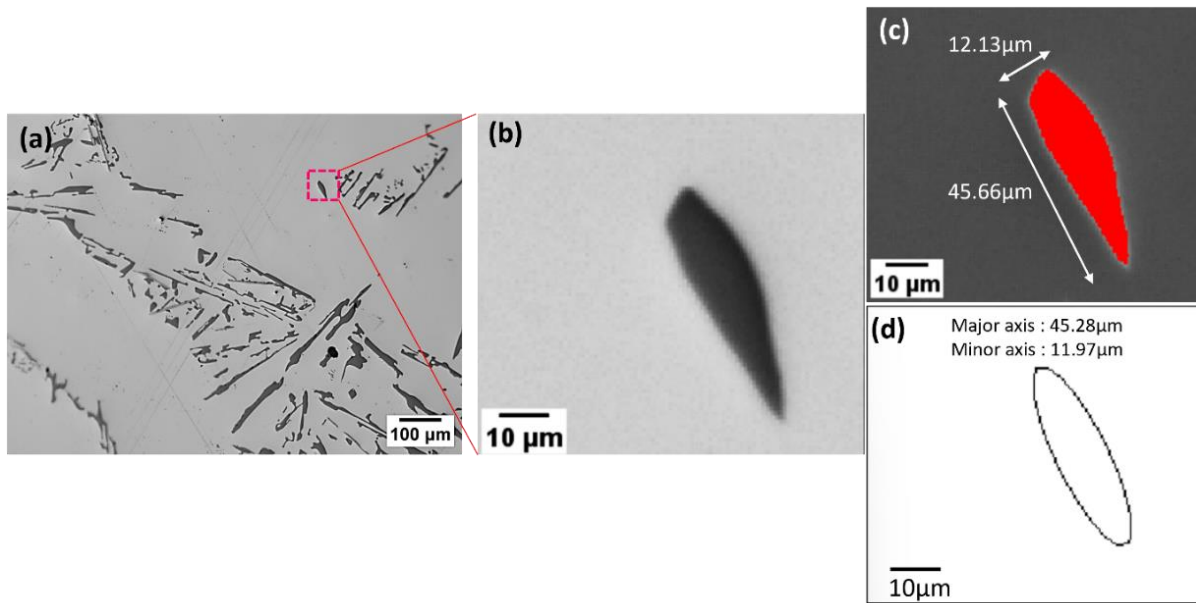


Figure 3.14 An example of measuring the aspect ratio of Si particle showing the accuracy of measurement using ImageJ. The accuracy of ImageJ software in area selection and fitting an equivalent ellipse with major axis equal to the maximum length and minor axis equal to the maximum width of in an irregular shape has been highlighted. This approach was used in quantifying the change in morphology of eutectic Si in Al-Si alloy and $Al_{11}Ce_3$ intermetallic in terms of changing aspect ratios and roundness, in Al-Ce binary alloys during spheroidization experiments.

Figure 3.15 shows the flow of operations employed for the measurement of average aspect ratio and roundness of second phase particles. First, the raw image is converted into 8 bit format followed by changing into a binary image (Figure 3.15b), to enhance the contrast between the matrix and eutectic particles. Subsequently, a thresholding process was applied to facilitate the identification and selection of particles (Figure 3.15c). Once the threshold parameters were optimized to correctly identify the particle boundaries, analyse particles command was commenced for the measurements (Figure 3.15d). To keep the measurements accurate, high magnification images were used for analysis. In total 1000 particles in each samples were measured to get the average aspect ratio in every composition.

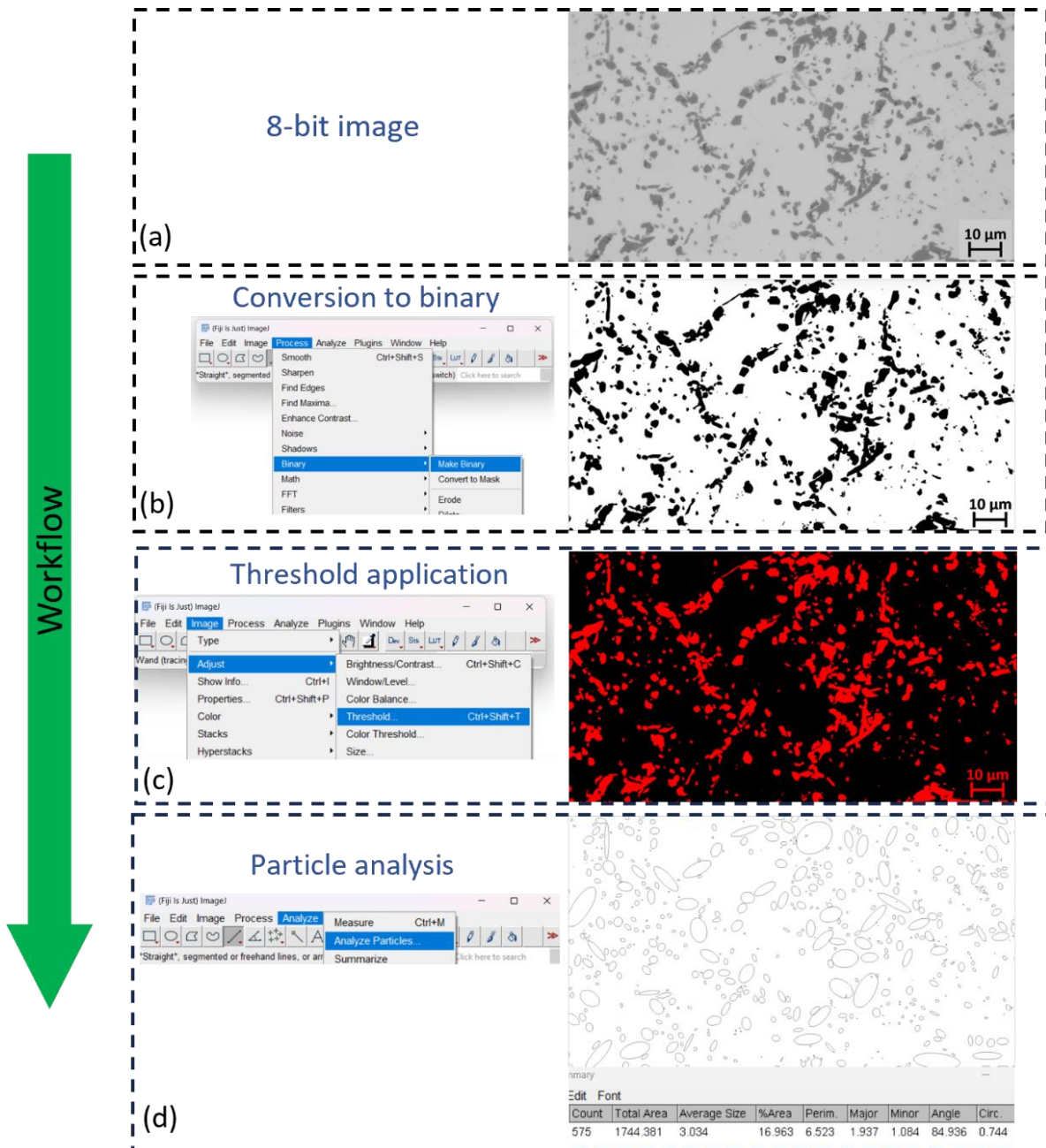


Figure 3.15 Workflow of image processing in ImageJ software to measure the morphological features like aspect ratio and area fraction of second phase particles (a) optical micrograph of heat treated Al-5Si alloy demonstrating spheroidization of Si particles. (b) Optical micrograph changed into a binary image for second phase identification, followed by (c) threshold operation, showing the selected area for measurements, in red colour. (d) Equivalent ellipses were fitted to measure the aspect ratios of selected particles.

To quantify the degree of spheroidization of eutectic Si and Al₁₁Ce₃ intermetallic particles, particle shape identifier i.e. circularity was measured in heat treated Al-Si and Al-Ce binary alloys. It quantifies the degree to which a particle resembles a perfect circle and is defined as the ratio of the particle's area to the area of a circle with the same perimeter and is given by

$$circularity = \frac{p_{eu}^2}{4\pi A_{eu}} \quad 3.3$$

P_{eu} and A_{eu} are perimeter and area of a particle. To total 1000 particles were analysed and average is reported.

3.5.3 Scanning electron microscopy

LEO 1455VP scanning electron microscope (SEM) equipped with Energy Dispersive X-Ray Spectroscopy (EDX) was used to examine the microstructural features of alloys. EDX elemental mapping was conducted with a voltage of 20V and 20mm working distance. The results were capture by Oxfordshire elemental mapping software. Secondary and electron backscatter mode were used to capture the high magnification images of eutectic and precipitates. The working voltage for imaging was 5kv with a working distance of 8mm from the samples which were mounted on conductive raisin.

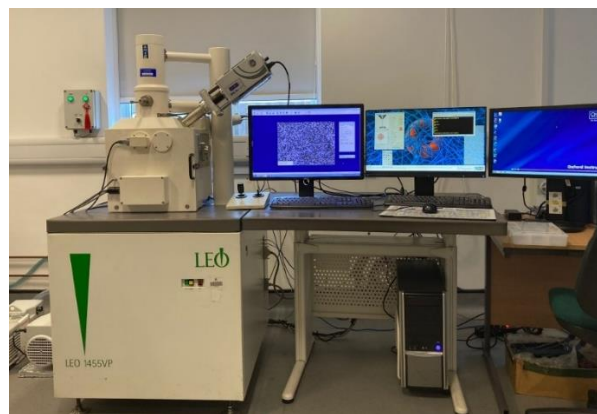


Figure 3.16 LEO scanning electron microscope

3.5.4 EBSD

The samples for EBSD measurements were carefully prepared by standard metallographic process followed by vibration polishing at 100 Hz using Qpol Vibro equipment at 80% power for 8 hours. EBSD analysis of the longitudinal cross section for Al, Al-5Si and Al-8Si were performed on Zeiss Supra 35 SEM with high sensitivity Hikari EBSD camera (20 kV voltage, 10-15 mm working distance). The data recording and indexing were performed using EDAX Teams software. ATEX software [132] was used for the acquired EBSD data analysis. Examined area for assessing the dendrite growth orientation are 2.8 mm × 2.6 mm with step size of 4 μm. For hypereutectic alloys, up to 7 locations have been analysed. The misorientation [133] between the $\langle 100 \rangle$ direction and the primary dendrite growth direction is extracted from an average of ~30 directionally solidified grains in the longitudinal cross section.

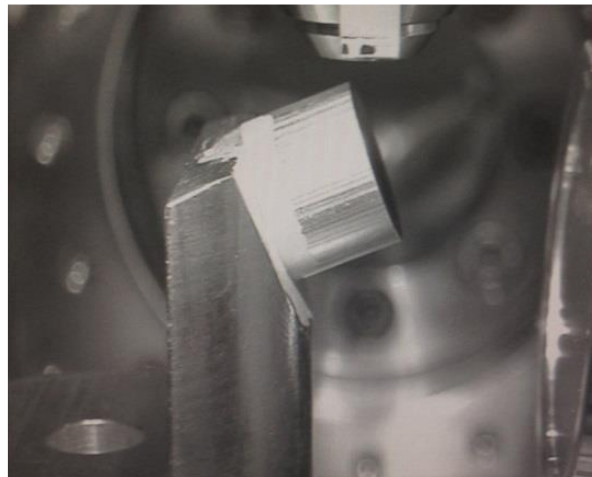


Figure 3.17 The sample position inside vacuum chamber of Supra SEM, image is reprinted from [134]

3.5.5 TEM

A JEOL 2100F transmission electron microscope was used to characterise the nanoscale precipitates in the Al-Ce-Sc-Zr alloys (Figure 3.19). A double-tilt specimen holder manufactured by JEOL Ltd., Tokyo, Japan, was employed for TEM imaging (HRTEM) and

select area diffraction (SAD) acquisition with the accelerating voltage of 200 kV. The samples for TEM analysis were prepared by Gatan 691 Precision Ion Polishing System (PIPS) milling. 1mm thick sheet of heat treated specimen were cut using a diamond cutting machine (ACCUTOM-10, Struers Ltd) at 3000 rpm and 0.00812 mm/s approaching speed. The thickness of samples was further reduced to 150 μ m by grinding with 1200 grid SiC paper. Once the desired thickness was obtained, 3mm diameter discs were punched out of the foil using a disc punching machine (Gatan). Further thinning of discs was carried out by using 25000 grid SiC paper. The final thickness of discs obtained by mechanical grinding before ion milling was ~ 40 μ m.

Gatan, PIPS 691 (Figure 3.18) precision argon ion polishing system was used to final ion polish the discs. The samples were fixed in the sample holder and were placed in the air locked chamber for the ion milling operation. The final thickness of the samples after ion milling was 20 μ m. The steps followed for the milling of Al-Ce-Sc-Zr alloys is listed in table 3-6.

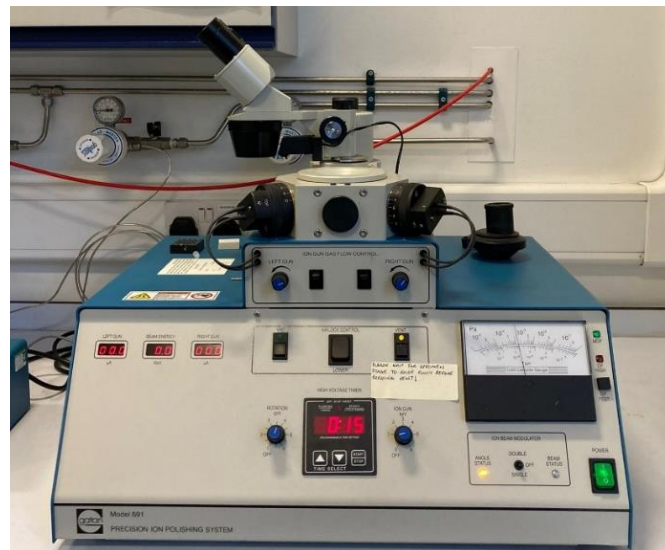


Figure 3.18 Gatan PIPS 691 used for the milling of 3mm discs.

Table 3-6 The procedural steps for the PIPS milling operation involved in thinning discs for TEM analysis





Step	Angle (°)	Voltage (kV)	Rotation (rpm)	Time (Min)	Mode	Illustration
1	5	5	3	240	Dual	
2	4	3.8	3	40	Dual	
3	3.5	3	3	20	Dual	
4	3	1.5	3	5	Dual	



Figure 3.19 The Jeol 2100F Field Emission Gun Transmission Electron Microscope.

3.6 Mechanical behaviour assessment

3.6.1 Vickers hardness

Vickers hardness tests were performed on the hot mounted samples post polishing at room temperature using an automatic Wilson vo100 Vickers microhardness indenter. Micro hardness tests consist of a Vickers's indenter which operates under the applied load and penetrates into the surface (Figure 3.20) and based on the surface area of indent, hardness value is calculated. The *HVN* number is then determined by the ratio F/A_v , where F is the force applied to the diamond in kilograms-force and A_v is the surface area of the resulting indentation in square millimetres. A_v can be determined by the formula.

$$A_v = \frac{D_{av}^2}{2\sin 68^\circ} \quad (3.4)$$

The *HVN* is calculated by using the equation

$$HVN = \frac{1.854 F}{D_{av}^2} \quad (3.5)$$

where, D_{av} is the average of diagonals of the impression made by the indenter. In present study, a diamond shaped indenter was used and a load of 100g was applied with a dwell time of 10 s at random positions and diagonals of post indentation impression were measured to precisely calculate the hardness values (*HVN*). For each sample, 12 measurements were taken and average with standard deviation is reported.

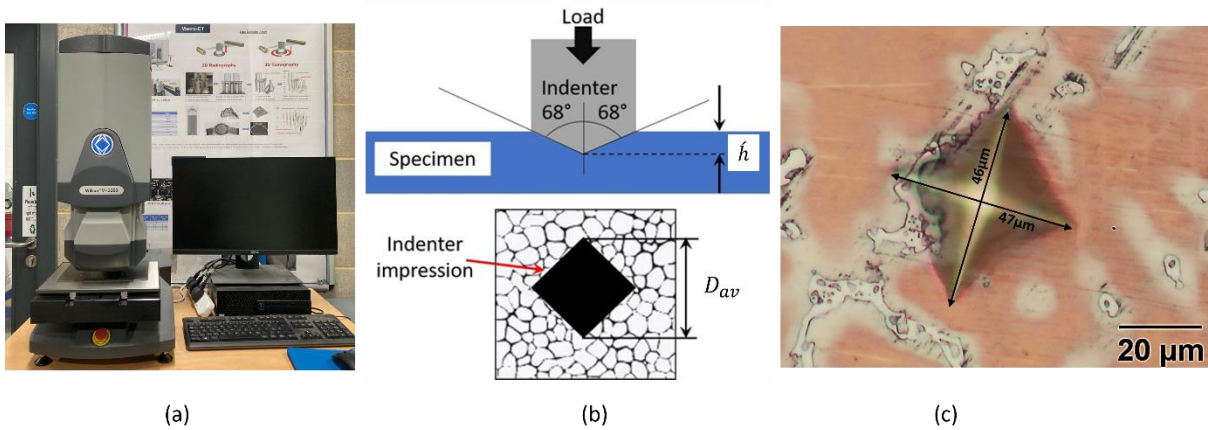


Figure 3.20 Picture of (a) Wilson vo100 Vickers microhardness indenter (b) illustration of indenter impression (c) indentation impression with measured diagonals

3.6.2 Brinell hardness

To accommodate a higher surface area under the indenter, Brinell hardness tests were conducted on the cold mounted samples using a Wilson BH3000 (*Buehler, UK*) Brinell hardness tester. A spherical steel indenter with a diameter 5mm, at a load of 250kgf and dwell time of 10 s was used to take at least 6 reading at random locations. The expression used to calculate the *BHN* is

$$BHN = \frac{2F}{\pi U(U - \sqrt{U^2 - u^2})} \quad (3.6)$$

where, F is applied load measured in kilogram force (kgf), U is the diameter of indenter ball (5mm in present study) and u is the mean diameter of indenter impression in mm. Figure 3.21c, shows an example of measurement of mean diameter of indentation in Al-8Si alloy solidified at 0.34°C/s.

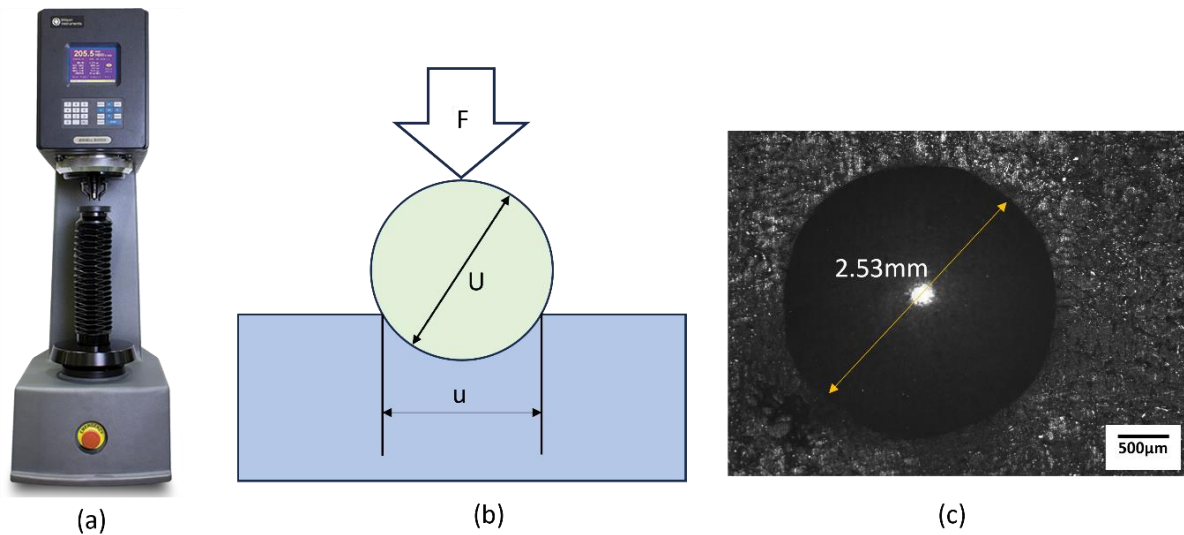


Figure 3.21 Brinell hardness tests used in the this study (a) Wilson BH3000 (Buehler, UK) Brinell hardness tester (b) illustration of Brinell hardness test (c) an example of indentation with measured diameter of impression, in Al-8Si alloy solidified at 0.34°C/s

3.6.3 Tensile testing

Tensile experiments were conducted both at room temperature and elevated temperatures on ASTM B557 standard round mechanical test bars with a gauge diameter of ϕ 6.35mm and a gauge length of 50mm. A universal material testing machine (Instron ® 5560) (Figure 3.22) equipped with Bluehill software was utilized for assessing yield strength, tensile strength, and Young's modulus. Testing procedures adhered to ASTM E8/E8M and ASTM E21 standards for room and elevated temperatures of 150°C, 250°C, and 300°C, respectively. The ramp rate for room temperature tests was set at 1mm/min, while the straining rate for high-temperature tests was maintained at 0.0002/s. During experimentation, an external extensometer with a gauge length of 50 mm was manually affixed to each specimen to ensure precise strain measurement at room temperature. Yield strength was determined as the 0.2% yield strength exhibited on the stress-strain curve. For high-temperature evaluations, specimens were enclosed within a chamber featuring a heating coil, with temperature monitoring facilitated by

a K type thermocouple. Each specimen was held for a duration of 5 hours, and three samples were tested at each temperature, with the average value being reported.



Figure 3.22 Picture of Instron 5500 universal electromechanical tester with ambient and high temperature tensile testing set up.

3.7 Statistical analysis

To evaluate the significance of the improvement in the R^2 values, obtained by fitting a Hall-Petch type relationship between yield strength and new perimeter based parameter (p') when compared to conventional Hall-Petch relationship between yield strength and λ_2 , a paired t-test was conducted. The paired t-test is a statistical method used to compare the means of two related groups. It is typically used when there are two measurements on the same subjects. In present case, the BHN values of Al-Si alloys were measured with respect to corresponding p' and λ_2 , therefore paired t-test is chosen. For a set of paired data points (X_i, Y_i) where $i = 1, 2, \dots, n$, the paired t-test involves the following steps [135,136]:

- Calculate the difference (d_i) for each data point : $d_i = X_i - Y_i$
- Calculate the mean of the differences (\bar{d}) : $\bar{d} = \frac{1}{n} \sum_{i=1}^n d_i$
- Calculate the standard deviation of the differences (s_d) : $s_d = \sqrt{\frac{1}{n-1} \sum_{i=1}^n (d_i - \bar{d})^2}$
- Calculate the t-statistic t_s : $t_s = \frac{\bar{d}}{s_d/\sqrt{n}}$
- Determine the degrees of freedom df : $df = n - 1$

The t-statistic is then compared against the critical value from the t-distribution with $n-1$ degrees of freedom to determine the significance of the result.

4 Influence of grain morphology on the strengthening behaviour of Al-Si alloys

4.1 Introduction

As discussed in introduction chapter, the dendrites exhibit intricate morphologies and consideration of grain morphology on the prediction of strengthening behaviour of a material remains a less explored topic. To address this gap, this chapter aims to study the correlation between the strength and perimeter-based parameter (p') associated with the dendritic complexity. In order to study this, we have (i) systematically controlled the solidification rate to affect λ_2 and p' for a given alloy composition, (ii) controlled morphology of the grain via solute (Si, Ce) content at wide range of cooling rates and (iii) used image processing software to measure p' and other microstructural features. To quantify the mechanical properties, Brinell hardness is used as a strength indicator, since strength and hardness are known to follow a linear relationship in Al alloys. To minimize the solid solution and avoid precipitation strengthening contribution, the low solubility element such as Si (maximum solubility 1.65wt.%) is used to control the morphology. To assess the potential change in the preferential growth direction of the α -Al, which in turn affects the HP constant, we have devised the directional solidification for Al-Si alloys with various Si solute content and have characterized

the orientation dendrites using EBSD mapping and have reported the misorientation of directionally grown dendrites with $\langle 100 \rangle$ direction.

4.2 Theoretical aspect - Correlation between dendrite perimeter and λ_2

To utilise the interfacial area associated parameter into HP relation, visualization of 3-D structure is required via sophisticated *in situ* measurements [137–140] such as micro CT, high energy X-ray synchrotron facilities etc. It has been confirmed that the interfacial area concentration (ratio of dendrite surface area and its volume) has a similar behaviour with interfacial length concentration (ratio of dendrite perimeter and projected area) [34,35]. Therefore, as a practically viable route, to capture the change in interfacial area induced by the change in morphology of a grain, a two-dimensional inspection can be adopted by measuring the perimeter of dendrite in a unit area of the micrograph which are shown to be equivalent parameters [34]. Recent developments in image processing software [128] provides the flexibility and accuracy in making quantitative measurements to capture change in perimeter associated with the morphological changes of a grain.

The 2-D shape of primary and secondary arm tips in a dendrite is conventionally considered as parabolic [141]. Figure. 4.1 shows a typical dendrite, which can be divided into two parts i.e. primary and secondary arm, for geometrical calculations. Mathematical equations for the arc length of a parabola are used to formulate the perimeter of a dendrite [142]. The perimeter of the dendrite, p_{total} is formulated in Eqs. (4.1) to (4.6) with a and b denoting the primary arm length and width, and c and e denoting the secondary arm length and width, respectively.

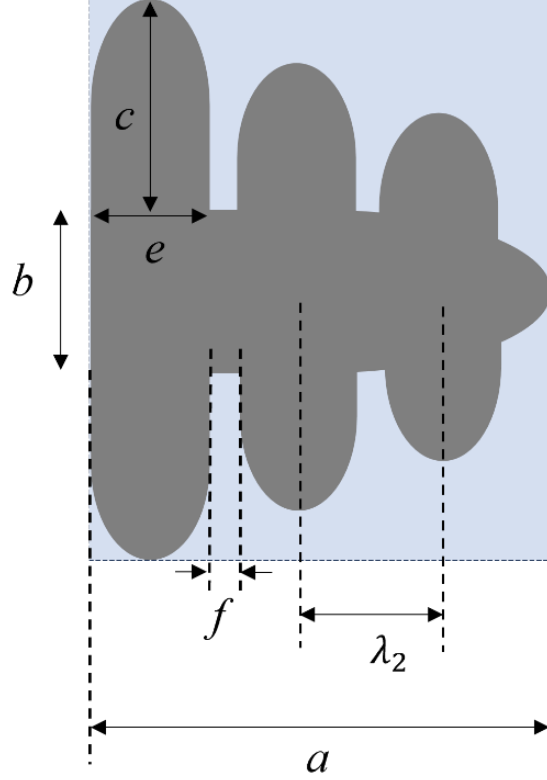


Figure 4.1 Illustration of a dendrite.

$$p_{\text{primary arm}} = \frac{1}{2} \sqrt{b^2 + 16a^2} + \frac{b^2}{8a} \ln \left(\frac{4a + \sqrt{b^2 + 16a^2}}{b} \right) - \frac{5e}{4} \quad (4.1) \quad [142]$$

$$p_{\text{secondary arm}} = \sum_{i=1}^z \sqrt{e^2 + 16c_i^2} + \sum_{i=1}^z \frac{e^2}{4c_i} \ln \left(\frac{4c_i + \sqrt{e^2 + 16c_i^2}}{e} \right) \quad (4.2) \quad [142]$$

$$c_i = c - \left(\frac{c}{z} \right) (i - 1) \quad (4.3)$$

$$p_{\text{total}} = p_{\text{primary arm}} + p_{\text{secondary arms}} \quad (4.4)$$

$$A = a(2c + b) \quad (4.5)$$

$$p' = \frac{A}{p_{\text{total}}} \quad (4.6)$$

Eq. (4.3) accounts for varied length scale of secondary arms where z is the number of secondary arms in the dendrite. To generate a theoretical data set, a dendrite with a length of 5000 μm , width of 100 μm and the longest secondary arm length of 400 μm is considered. The guideline for selecting these parameters are based on practically observed values for dendrites solidified in gravity die casting solidification condition. The gap between the two consecutive secondary arms is assumed to be 1/4 of the width of an arm i.e. $f = e/4$ which leads to $\lambda_2 = 5e/4$. Figure 4.2 shows the relationship between the calculated p' and λ_2 for the set of dendrites with increasing number of secondary arms from 20 to 300. In this calculation, the length of the primary dendrite a (5000 μm) and the maximum height of secondary arm, $2c+b$ (900 μm) are always kept constant. The ratio between area of the envelope enclosing the dendrite i.e. $A = a(2c+b)$ and p_{total} is the new parameter (p') and its variation with λ_2 is shown in Figure 4.2.

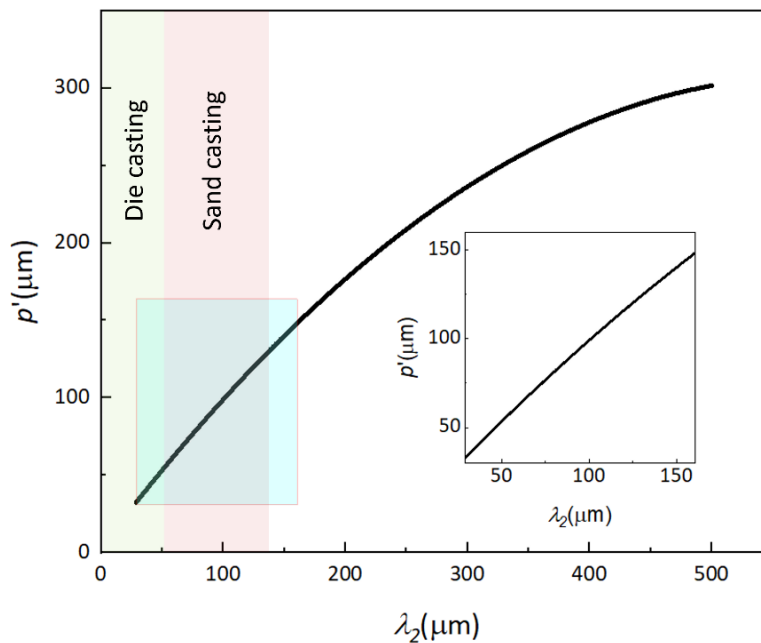


Figure 4.2 The relationship between calculated p' using Eq. 4.6 and λ_2 , showing non-linearity in wide range of cooling conditions. Inset shows the consistency of non-linearity in the practical casting conditions. Shaded regions show the range of λ_2 in Al alloys cast through die casting and sand casting conditions[143–147]

The change in λ_2 represents the change in solidification rate and as can be seen in Figure 4.2, there exist non-linear relationship between λ_2 and p' in entire range of solidification conditions. The inset shows relationship under practical processing solidification conditions with a consistent non-linearity. Although at first instance in practical solidification conditions, the non-linearity is not significant, however in a wide range of cooling rates, this non linearity is evident. This non-linear relationship demands to replace d or λ_2 in HP relation to p' because the dislocation pile-up takes place at the grain boundary and interfacial area occupied by the grain boundary is highly dependent on the morphology of the dendrite structure. In 2-D, this feature can be captured by measuring the p' via measuring the perimeter of a grain from a microstructure using well established image processing tools. The inverse of p' reflects the degree of complexity of dendritic morphology in a unit area.

4.3 Microstructure observation

Figure 4.3 shows the macroetched microstructures of Al, solidified at different cooling rates. The influence of cooling rate on the grain size is clear as average grain diameter decreases from $\sim 18000 \mu\text{m}$ at $0.000167 \text{ }^\circ\text{C/s}$ to $\sim 2200 \mu\text{m}$ at $0.34 \text{ }^\circ\text{C/s}$. Similarly, the Effect of Si on grain size is also significant and is shown in Figure 4.4. The average grain size measured for Al-8Si at $0.000167 \text{ }^\circ\text{C/s}$ was $\sim 8750 \mu\text{m}$ (Figure 4.4(d)). For complete eutectic composition, the microstructure shows the diminished dendritic structure and with primary Si rods nucleating from the crucible walls (Figure 4.4(e)).

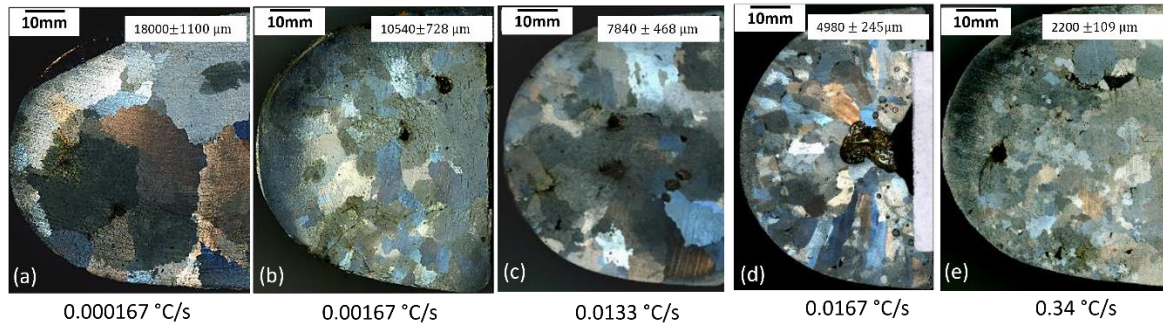


Figure 4.3 Macroetched microstructures of Al solidified at (a) 0.000167 °C/s (b) 0.00167 °C/s (c) 0.0133 °C/s (d) 0.0167 °C/s (e) 0.34 °C/s. Grain size decreases significantly varying from several mm to μm from lowest to highest cooling rate. Average grain size is shown in the respective microstructures.

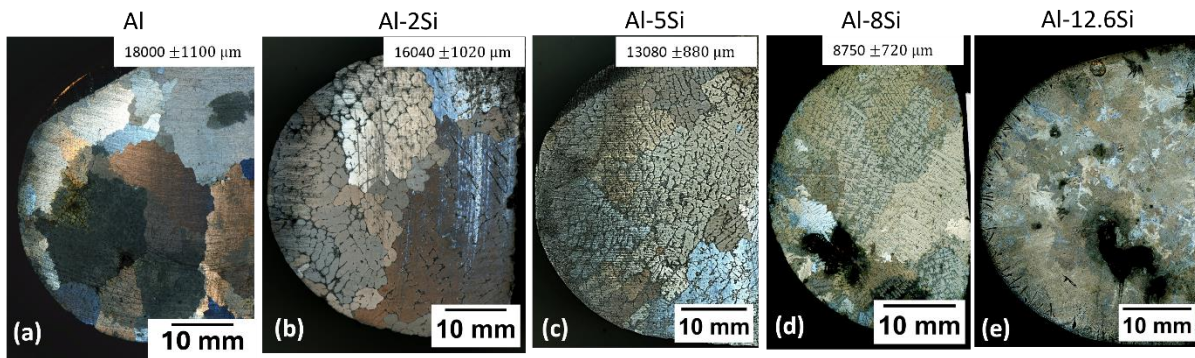


Figure 4.4 Macroetched microstructures of (a) Al (b) Al-2Si (c) Al-5Si (d) Al-8Si (e) Al-12.6Si cooled at 0.000167 °C/s, highlighting the influence of Si content on the grain size. Grain size decreases significantly with increasing Si content. Average grain size is shown in the respective microstructures.

To highlight the wide range of grain size and morphology of dendrites, macroetched microstructure of Al-2Si alloy solidified at various cooling rates is presented in Figure 4.5

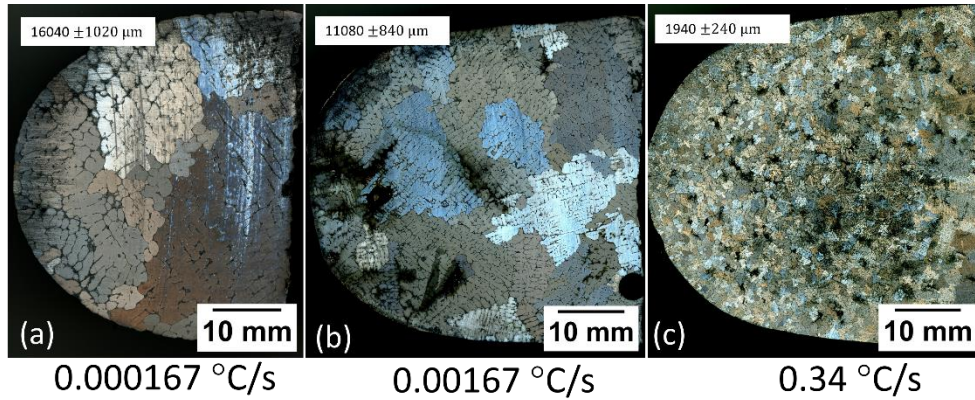


Figure 4.5 Microstructures of Al-2Si solidified at (a) 0.000167 °C/s (b) 0.00167 °C/s (c) 0.34 °C/s. For a constant Si concentration, grain structure gets finer as the cooling rate increases. Average grain size is shown in the respective microstructures.

Figure 4.6 shows the microstructures of all alloys solidified at several cooling rates. The morphology of α -Al dendrites (Figure 4.6) is strongly observed to be dependent on the cooling rate and Si content. For a constant cooling rate of 0.000167°C/s, the value of λ_2 decreases from 1100 μm to 509 μm when Si content increased from 2 to 8 wt.%. This trend was prevalent at other cooling rates as well. The refinement of λ_2 of dendrites with increasing solute content by the virtue of retarded growth velocity due to reduced constitutional undercooling [148,149] is a well discussed phenomenon and is clear in the microstructures.

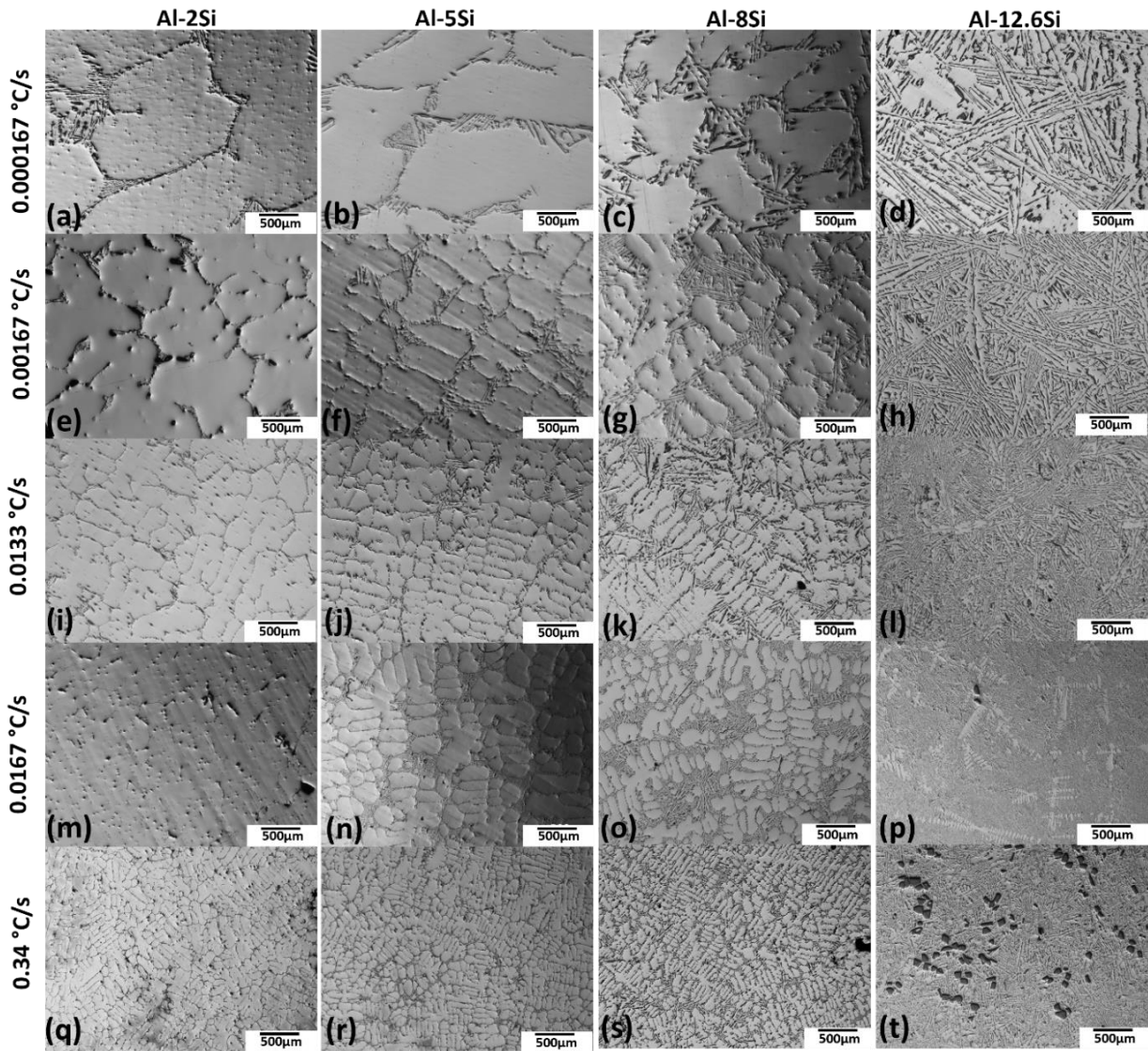


Figure 4.6 As cast microstructures of Al-Si binary alloys at several cooling conditions and compositions.

The effect of cooling rate is also evident on the change in morphology of eutectic Si. In general, eutectic Si morphology is changing from coarse rod to fine needles with increasing cooling rate and as the Si content increases the size increases (Figure 4.7). A shift in the eutectic point as evidenced by the presence of primary Si at higher cooling rate [150] can be seen in Al-12.6Si alloy with eutectic composition (Figure 4.7d).

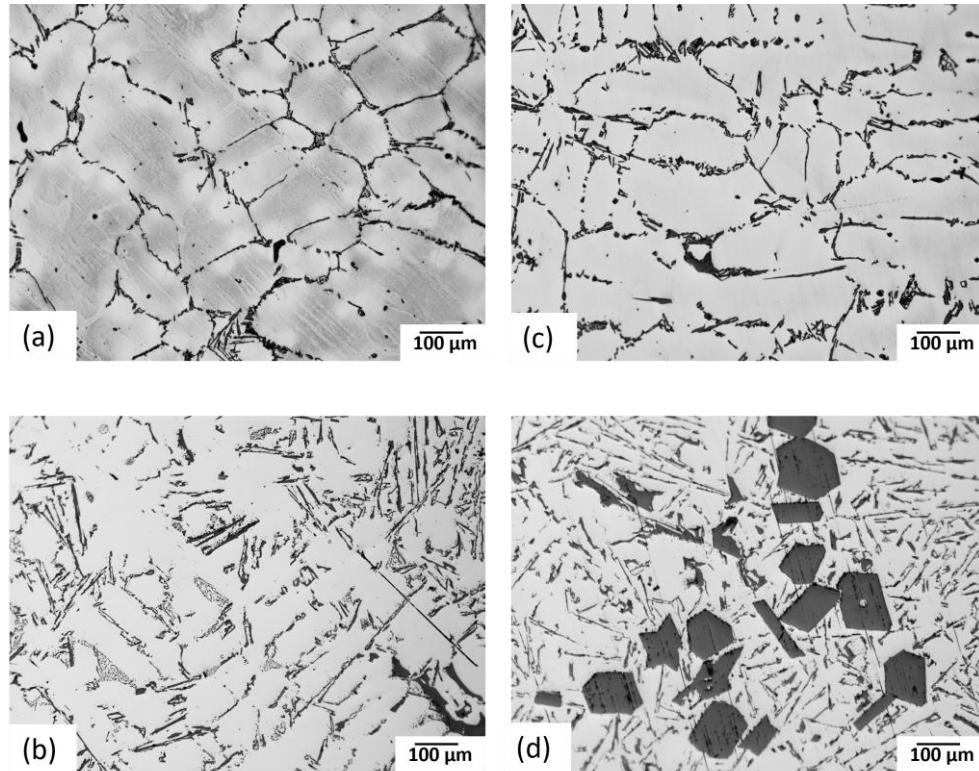


Figure 4.7 As polished microstructures of (a) Al-2Si (b) Al-5Si (c) Al-8Si and (d) Al-12.6 Si solidified at 0.34 °C/s. Si morphology changes with the increasing Si content as eutectic Si becomes coarser. Change in eutectic point can be inferred in fast cooled Al-12.6 alloy with formation of primary Si.

The measured λ_2 as a function of cooling rate, \dot{T} , is shown in Figure 4. 8 (a) and is well described by $\lambda_2 \propto \dot{T}^{-n}$ relationship with $n = 1/3$. The theoretical approach for the prediction of λ_2 as a function of solute composition and cooling rate was proposed by Kattamis and Fleming [151] . In this model, similar to Oswald ripening, the coarsening of bigger dendritic arm occurs at the expense of thinner secondary dendritic arms. The model posits that the coarsening process is primarily driven by diffusion, as solute atoms migrate from smaller to larger dendritic arms, remelting the thinner dendritic arm and thickening the thicker arm in the process. According to this model, λ_2 is given as

$$\lambda_2 = 5.5(Mt_f)^n \quad (4.7)$$

where

$$M = \frac{-\Gamma D \ln \left[\frac{C_b}{C_o} \right]}{l(1 - k^*)(C_b - C_o)} \quad (4.8)$$

where Γ is the Gibbs–Thomson coefficient, D is diffusion coefficient in liquid, l is the slope of liquidus, k^* is partitioning coefficient, C_o is the solute composition and C_b is the composition of the liquid at the base of dendrite which is reached at the solidification time t_f . In a eutectic solidification process, C_b is equal to the eutectic composition and n is the coarsening exponent, which is reported to be 1/3 [152].

By substituting $t_f = \Delta T / \dot{T}$ in Eq.(4.7), where ΔT is the freezing range of the alloys, the Eq. (4.7) can be written as

$$\lambda_2 = M' \dot{T}^{-n} \quad (4.9)$$

where

$$M' = 5.5 \left(\frac{-\Gamma D \ln \left[\frac{C_b}{C_o} \right]}{l(1 - k^*)(C_b - C_o)} \Delta T \right)^n \quad (4.10)$$

The fit parameter M' as a function of Si content is shown as inset to Figure 4.8(a) and agrees with the calculated values for various Al-Si alloys from Kattamis and Fleming model. As shown in Figure 4.8(b), similar to the relationship between λ_2 and \dot{T} , the relationship between p' and \dot{T} is observed to follow $p' \propto \dot{T}^{-m}$.

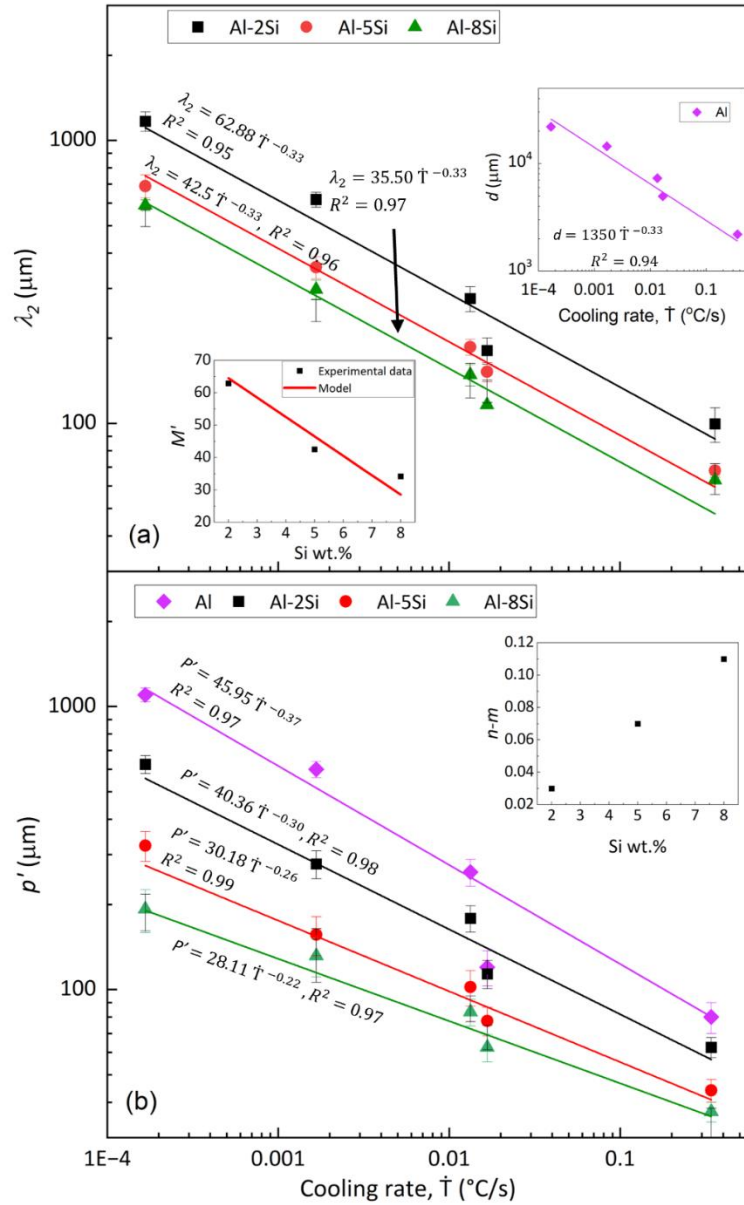


Figure 4.8 Variation of (a) λ_2 as a function of cooling rate and (b) p' as a function of cooling rate. Solid lines are the best-fit to $\lambda_2 \propto \dot{T}^{-n}$ and $p' \propto \dot{T}^{-m}$ with the inset of relation between $n-m$ and Si content

The best fit parameters are shown in the Figure 4.8(b) and it is observed that the difference between n and m increases with increasing Si content (Inset to Figure 4.8(b)) due to change in morphology from highly dendritic structure at higher solute content to more faceted like structure at lower solute content. At low solute content the value of m approaches the value of

n due to near faceted type grains. However, at higher solute content, n and m values deviate noticeably suggesting the importance of considering p' in HP relation rather than d or λ_2 . Conversely, when the experimental data is fitted to the curve with $m = 1/3$, the fit resulted in low regression coefficient (R^2) values for Al-Si alloys, shown in Figure 4.9(a).

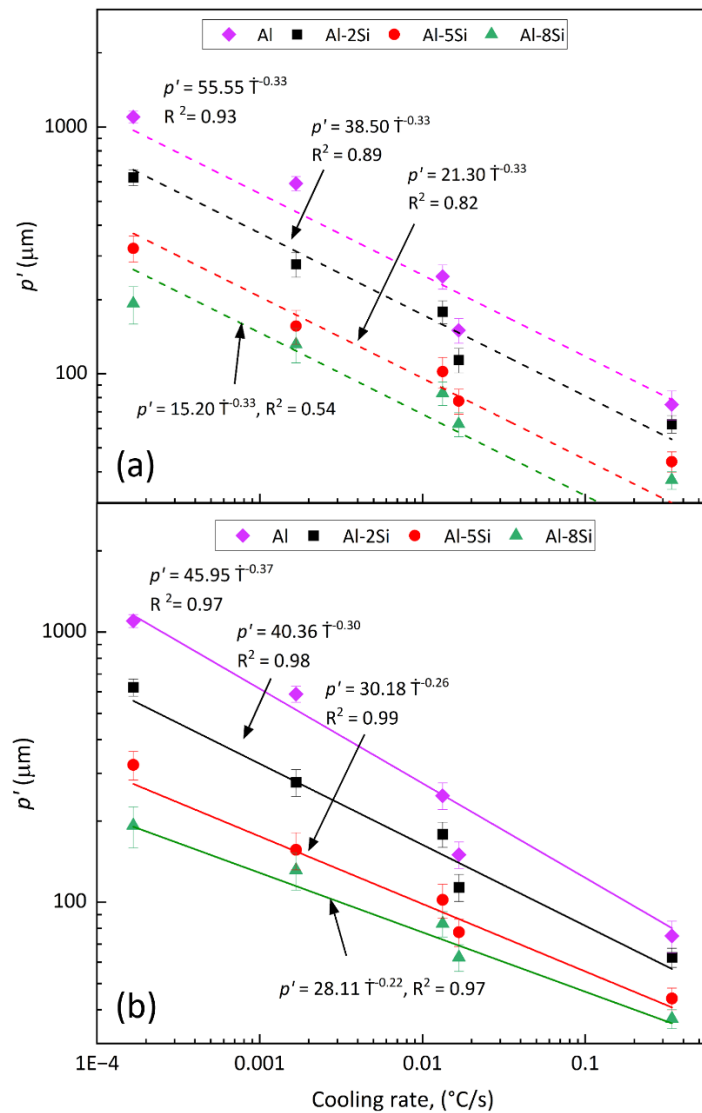


Figure 4.9 Plot showing the poor value of coefficient of regression when (a) $p' \propto \dot{T}^{-m}$ (dashed line) is fitted in the experimentally measured data with a value of m taken $1/3$ (b) $p' \propto \dot{T}^{-m}$ (solid line) type relationship is fitted in experimental data with best fitted values of m .

4.4 Dendrite perimeter

Figure 4.10 shows experimentally measured λ_2 and p' for Al-8Si alloy solidified under wide range of cooling rates. The data for high cooling rates, in shaded region, were obtained by analysing the cross sections of samples obtained from Cu based wedge mould cast samples. Rapid change in $1/p'$ vs λ_2 at higher cooling rate (i.e. lower λ_2) indicates that degree of grain complexity changes significantly with small change in λ_2 . As demonstrated in Figure 4.2, the non-linearity between the λ_2 and p' persists in the experimental data (Figure 4.10) as well and it is the key to relate the strength of a material to the perimeter of the dendrites, which accounts for changes in morphology, rather than λ_2 .

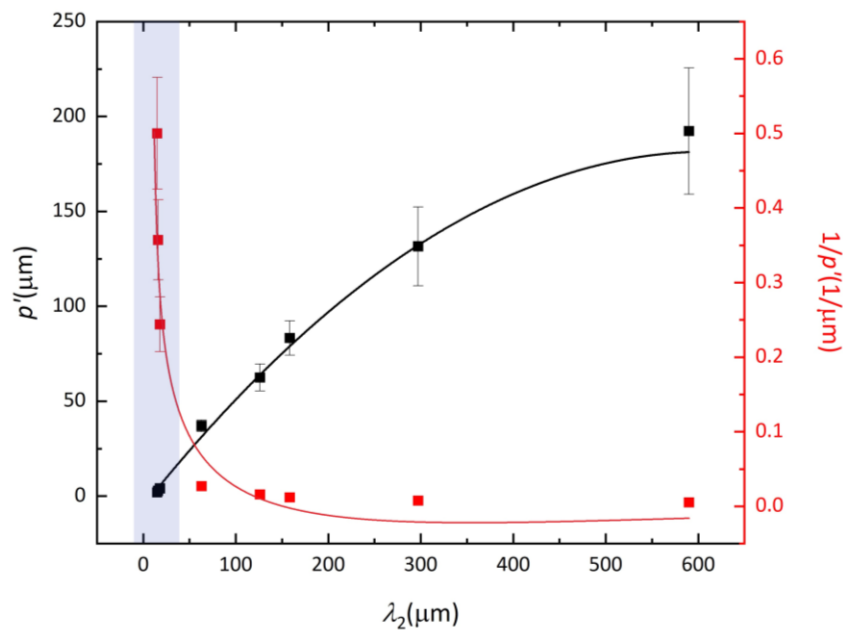


Figure 4.10 Relation between experimental p' and λ_2 showing the nonlinearity in Al-8 wt.% Si alloy. For comparison purpose, $1/p'$ vs λ_2 is also plotted. Solid lines are guide to the eye. Shaded region is the data obtained from analysing wedge mould casting.

4.5 Correlation between hardness and p'

Figure 4.11 shows the Brinell hardness of all the studied alloys. As expected, the hardness increases with the increase eutectic Si content and with increasing cooling rate. The load bearing effect of eutectic Si increases with the increase in volume fraction of Si and with increasing cooling rate, the refinement of grains contributes to the increase in hardness.

In the Al-12.6Si alloy, the microstructure is entirely eutectic. As the cooling rate increases, the morphology of the silicon phase transitions from a lathe-like structure to a fine lamellar configuration. This transformation is associated with an enhancement in hardness, which correlates with the increasing cooling rate.

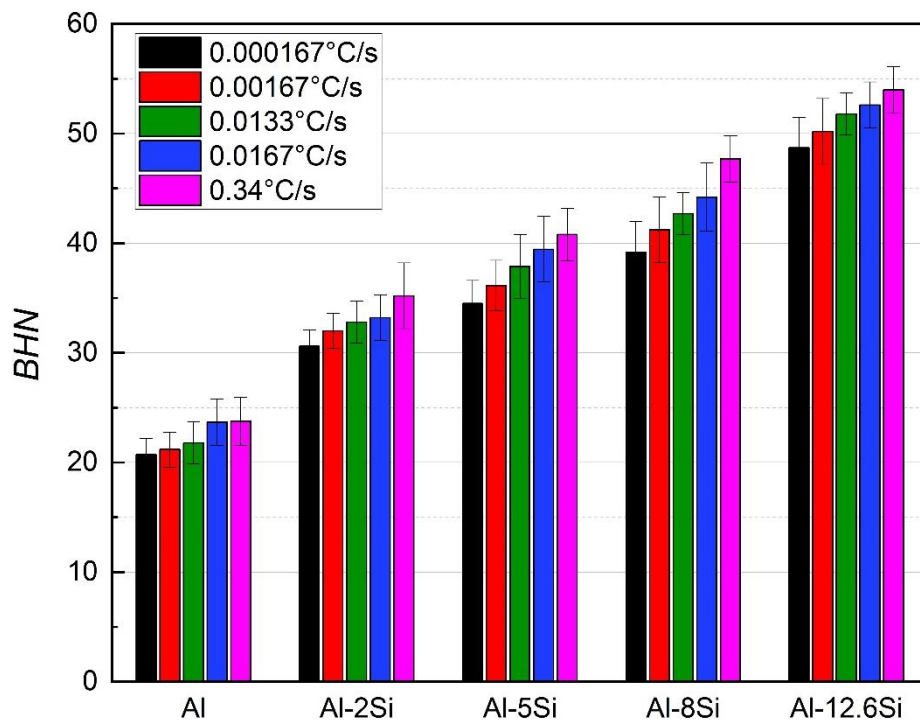


Figure 4.11 Brinell hardness of all alloys at several cooling rates.

In Al-Si alloys, as the hardness is known to linearly related with YS [153–155], here we have measured BHN for all alloys to study the effect of primary Al grain morphological change on the strengthening of alloy and plotted (Figure 4.12) as a function of d , λ_2 and p' for all studied

alloys. The data is fitted to HP type relations ($BHN = BHN_{o,d} + k/\sqrt{d}$, $BHN = BHN_{o,\lambda_2} + k'/\sqrt{\lambda_2}$, and $BHN = BHN_{o,p'} + k''/\sqrt{p'}$). Although at first glance the graphs look similar, the regression coefficients show a better value when p' is considered compared to that of d and λ_2 for all alloys. This demonstrates the importance of considering p' for accounting the changes in strengthening of a material associated with the change in morphology of primary Al grain from spherical to highly dendritic structure. As the grain boundaries pin the dislocations, the higher the grain perimeter per unit area, the higher the accumulation of dislocations.

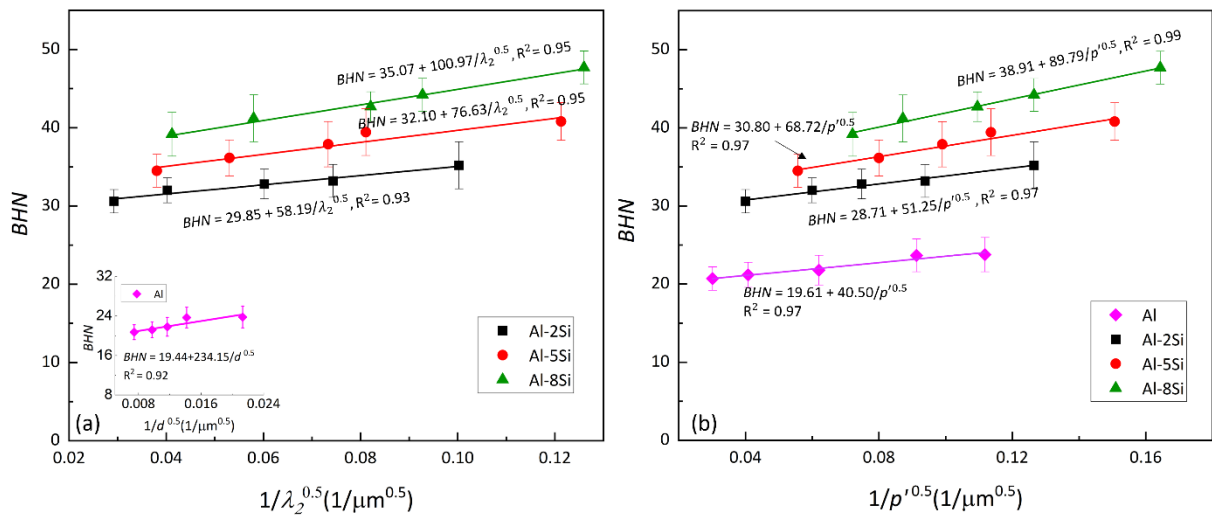


Figure 4.12 Relationship between (a) BHN and λ_2 and (b) BHN and p' . Solid lines are linear fit to the HP type relationships.

4.6 Strength contribution from α -Al dendrites

The HP constants, denoted as k' and k'' , exhibit an upward trend as the Si content increases. This phenomenon is likely attributed to variations in the eutectic Si content. The strengthening effect emanating from eutectic colonies is intricately linked to the interlamellar spacing within the eutectic structure. Empirical evidence substantiates that the strength contribution adheres to a HP type relationship [156–159], providing experimental validation for this correlation. The hardness of a eutectic system is given by

$$BHN_e = BHN_{o,e} + k_e f_e \lambda_e^{-0.5} \quad (4.11)$$

where λ_e is the interlamellar spacing, k_e is the slope of HP type relation with λ , $BHN_{o,e}$ is the intercept and BHN_e is the hardness of the alloy with eutectic composition (Al-12.6 wt.% Si), f_e is 1 (the volume fraction of eutectic). λ_e for Al-12.6 wt.% Si alloys solidified under various cooling rates is measured from microstructures using the method reported in ref [160]. To obtain k_e , the BHN data shown in Figure 4.11 for Al-12.6wt.% Si alloy, has been fitted to Eq. (4.11). To extract the hardness contribution associated with the changes in morphology of Al grains, the contribution from eutectic fraction must be subtracted from the overall response of alloy. The hardness response from α -Al matrix is given by

$$BHN_m = BHN - k_e f_e \lambda_j^{-0.5} \quad (4.12)$$

where, BHN_m is the true contribution in hardness from α -Al dendrites and BHN is the hardness of alloy. λ_j is the interlamellar spacing of eutectic structure of a hypoeutectic alloy. Experimentally the average interlamellar spacing λ_j is observed to be dependent on the composition and is measured for Al-2Si, Al-5Si and Al-8Si. It is to be noted that the second term ($k_e f_e \lambda_j^{-0.5}$) in Eq. (4.12) represents the hardness contribution from the eutectic fraction in hypoeutectic Al-Si alloys. The true contribution from α -Al to the measured hardness as a function of λ_2 and p' is shown in Figure 4.13 and their HP type relationships are given by

$$BHN_m = BHN'_{o,\lambda_2} + k'_m \lambda_2^{-0.5} \quad (4.13)$$

$$BHN_m = BHN'_{o,p'} + k''_m p'^{-0.5} \quad (4.14)$$

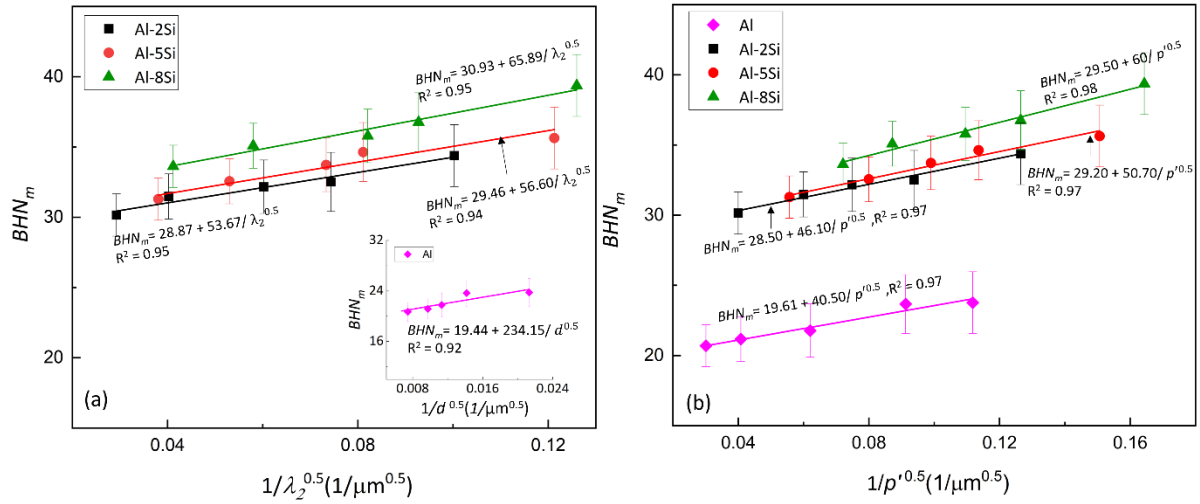


Figure 4.13 Relationship between (a) BHN_m and λ_2 and (b) BHN_m and p' . The solid line is a fit to the HP relationship

The R^2 values (given in Figure 4.13) shows better value when p' is considered in HP relation when compared to that of d or λ_2 for all alloys. This again demonstrates that it is important to consider p' for accounting the changes in strengthening of a material associated with the change in morphology of primary Al grain from spherical to highly dendritic structure. To reiterate the importance of considering perimeter for practical commercial Al-Si alloy, data for Al-8Si (a typical practical cast alloy) is shown in Figure 4.14, where R^2 is observed to improve from 0.93 to 0.98 which is very significant change from practical application view point.

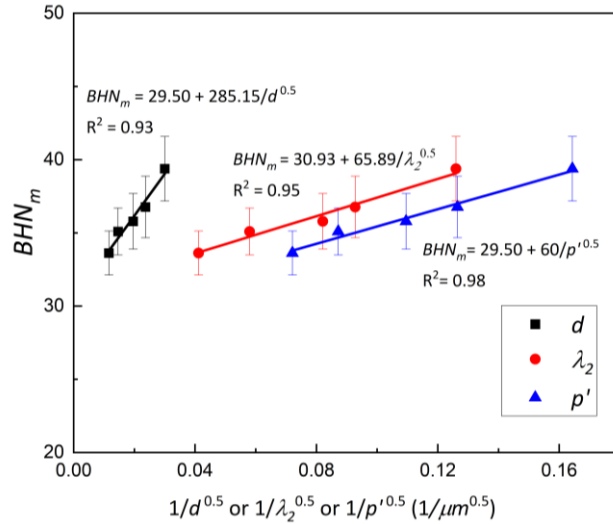


Figure 4.14 HP type relationship between (a) BHN_m and p' , (b) BHN_m and λ_2 and (c) BHN_m and d for Al-8Si alloy solidified at various cooling rates. The legends are experimental data and the solid lines are linear fit.

To illustrate changes in hardness associated with friction stress of a matrix, both BHN and BHN_m data has been plotted in Figure 4.15. Two distinct observations can be made from this graph, firstly the effect of Si on the intercept i.e. $BHN'_{o,p'}$ is higher than the pure Al even after the removing the hardness contribution from the eutectic fraction and secondly the slope, i.e. k''_m increases with the Si content.

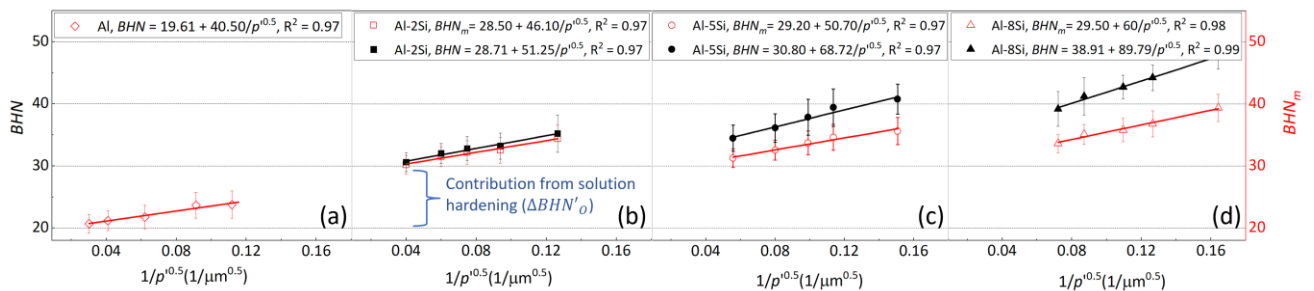


Figure 4.15 HP type relationship between BHN_m and p' for all Al-Si alloy systems highlighting the contribution of solution strengthening on the hardness and effect of Si content on the k''_m value.

The friction stress σ_0 in Eq. (4.15), represented by the intercept on y -axis of HP relationship plot, has several components [161]

$$\sigma_0 = \sigma_{CRSS} + \sigma_p + \Delta\sigma_{SS} \quad (4.15)$$

where, σ_{CRSS} is the critical resolved shear stress, $\Delta\sigma_{SS}$ is the improvement due to solid solution and σ_p is the residual stress due to the dislocations associated with thermomechanical processing.

The first component of friction stress, i.e. σ_{CRSS} is known to depend on the slip system activated during deformation. The number of active slip systems during mechanical test is dependent on the grain orientation and loading direction. Generally, slip systems with higher Schmid factor requires small applied stress to initiate slip. Compression [162], tensile [163,164] tests on Al single crystal showed higher YS for crystals with [111] orientation than that of [100] and [110] orientations. In as cast polycrystalline material, the grains are randomly oriented with respect to applied load and therefore the σ_{CRSS} contribution remains unaffected for all studied alloys. Although thermomechanical process can have a profound effect on the σ_0 in Al alloys [165], as the current study is limited to casting process, σ_p can be neglected in these as cast materials.

The third component $\Delta\sigma_{SS}$ in Eq.(4.15), can be predicted by Fleischer model [166]

$$\Delta\sigma_{SS} = LGb\varepsilon_{SS}^{\frac{3}{2}}\sqrt{c_s} \quad (4.16)$$

where, L is orientation factor which is 3.06 for FCC material , G is shear modulus (25GPa) , b is burgers vector (0.28nm), c_s is the atomic solute concentration and ε_{SS} is the lattice strain, which can be given by

$$\varepsilon_{SS} = |\varepsilon'_G - \beta\varepsilon_b| \quad (4.17)$$

where ε'_G is the modulus mismatch parameter and is given by

$$\varepsilon'_G = 1/1 + 0.5\varepsilon_G \quad (4.18)$$

And ε_G is the modulus mismatch and ε_b is the strain mismatch due to difference in atomic radii of solute and matrix atoms.

Eq. (4.16) leads to a value of $\Delta\sigma_{ss} = 2.5\text{MPa}$ which equates to Vickers hardness number (HVN) of 8 based on the relationship between HVN and σ for Al-Si binary alloy [167]. The enhanced BHN'_o ($\Delta BHN'_o$ shown in Figure 4.17(b)), when 2% Si is added to Al, is originated from solid solution formation, which has been reported elsewhere [168,169].

By introducing 2 wt.% Si in Al, in addition to increase in BHN'_o , the HP constant (k''_m) value is observed to increase, which can also be attributed to the Si solute in Al matrix as the experimental conditions are far from the equilibrium solidification conditions. For multicomponent alloys, Toda-Caraballo et al. [161] have proposed a general expression for HP constant as a function of solute content and it is given by

$$k = k_{Al} + \sum X_i \Delta k \quad (4.19)$$

where, k_{Al} is the HP constant for Al matrix and X_i is the solute content and $\Delta k = (\vartheta\Delta G + \gamma\Delta\mathbf{b})$, where ϑ and γ are constants dependent on the magnitude of burger vector \mathbf{b} and shear modulus G [161]. From Eq. 22 it is clear that k is strongly dependent on the solute content, ΔG and $\Delta\mathbf{b}$. The change in HP constant as function of solute content has been observed [22,170] in Mg-Zn system and Toda-Caraballo et al. [161] have successfully fitted the experimental data with Eq. (4.19). Since, the solubility of Si in Al is ≤ 1.65 wt.%, based on Eq. (4.19), k''_m should not increase beyond 1.65 wt.% of Si addition. However, as shown in Figure 16 (c) and (d), increase in k''_m is still noticeable in alloys with 5wt.% and 8wt.% Si.

4.7 Influence of dendrite growth direction on Hall-Petch constant

Several studies [91,92] have attributed the change in HP constant, on the active deformation modes which are dependent on the grain orientation and loading direction. In HCP materials, thermomechanical processing is observed to alter the crystallographic texture [171] which affects the k value [83,84,94] significantly. For instance, k value measured under tension for friction stir processed AZ31 alloy was $160 \text{ MPa } \mu\text{m}^{1/2}$, whereas, for its hot extruded counterparts, k value was $303 \text{ MPa } \mu\text{m}^{1/2}$ [80]. In another study, the variation of k value from 228 to 158 and $411 \text{ MPa } \mu\text{m}^{1/2}$ was observed, when the tension direction varies from 0° to 45° and 90° away from the normal direction of a hot-rolled AZ31 plate [83], respectively. In FCC materials, although relatively lesser studies are available, this effect was reported in electrodeposited Ni with different grain orientations [172]. In the current study, no specific effort was made to alter orientation of grains and the grains are expected to be randomly oriented. The only variable in present study is the solute content, and solute induced dendrite orientation transition (DOT) is known to occur in Al and Mg alloys due to the weak anisotropy of solid-liquid interfacial energy [16,31,99,173]. Gonzales et al. [99] have observed change in the growth morphology of Al from $\langle 100 \rangle$ to $\langle 110 \rangle$ growth directions as Zn content was increased from 25 wt.% to 60 wt.%. Similar observations were made in Al-Ge systems, where primary dendrite arms were found to be growing in $\langle 100 \rangle$ direction in Al-20 wt.% Ge alloys, $\langle 110 \rangle$ direction in Al-46 wt.% Ge, and both $\langle 100 \rangle$ and $\langle 110 \rangle$ directions growing simultaneously at an intermediate composition of Al-29 wt.% Ge [174].

To explore the potential influence of Si content on the preferred growth direction of Al dendrites in Al-Si alloys, directional solidification experiments were conducted and EBSD mapping was employed to assess the grain orientation as a function of Si content. Figure 4.16 shows the polarized micrographs of directionally solidified Al, Al-5Si and Al-8Si. It is clear

that the growth of grain in Al and dendrites in Al-5 and 8Si alloys is directional throughout the sample. While the morphology of grains appears finer at the bottom of the samples, the growth of primary trunks is nearly parallel at the top. Secondary arms were observed to be protruding from the primary trunks at $\sim 45^\circ$ (Figure 4.17), whereas in Al samples the grains were columnar without any lateral growth. The effect of Si on the dendrite morphology is evident as dendrites in Al-8Si specimen is finer than Al-2Si counterparts.

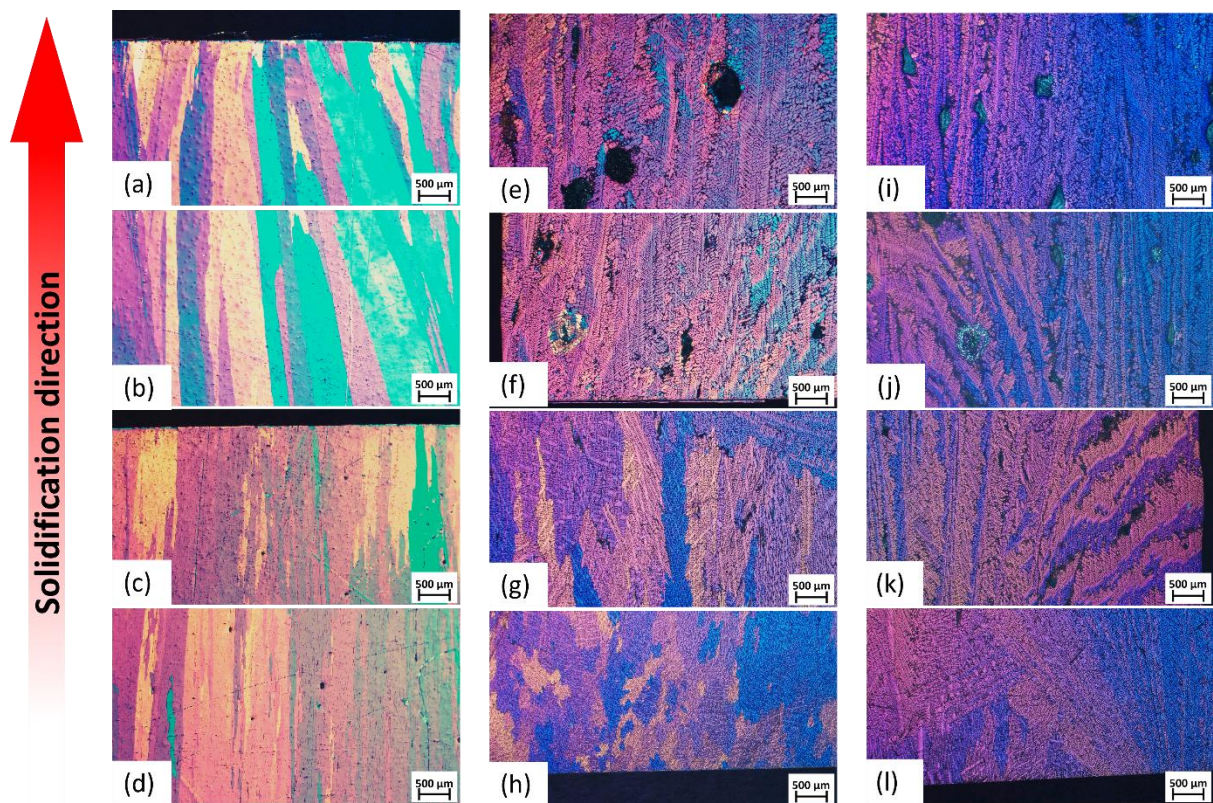


Figure 4.16 polarised micrographs of directionally solidified (a-d) Al, (e-h) Al-5Si, (i-l) Al-8Si

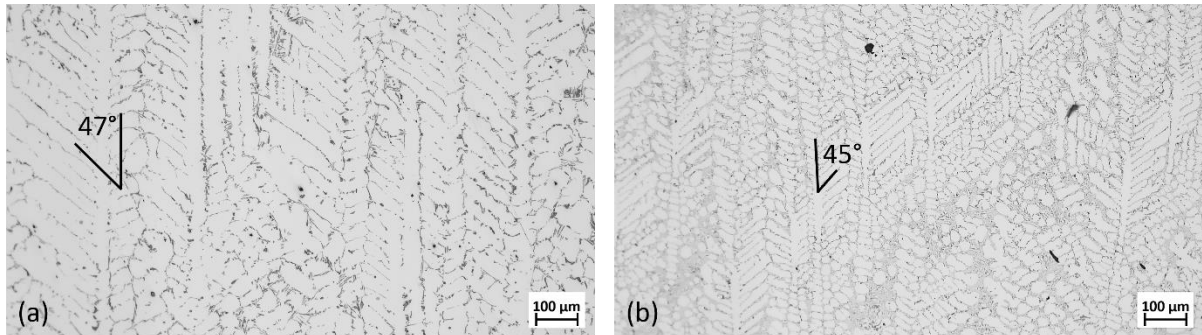


Figure 4.17 Optical micrographs of DS Al-2Si and Al-8Si alloys, showing the angle between the primary and secondary arms

Figure 4.18 shows the EBSD mapping of directionally solidified Al and Al-8Si alloy with inverse pole figures with varying colour indicating different crystallographic orientations of α -Al dendrites. It is clear that the deviation of growth direction of primary trunk and secondary arms from the natural tendency of Al dendrites to grow in $\langle 100 \rangle$ is influenced by the Si concentration. As can be seen in Figure 4.19, for pure Al sample, the measured growth direction is consistent with reported $\langle 100 \rangle$ [173], whereas with increasing Si content, the preferred growth orientation has deviated progressively from $\langle 100 \rangle$ to close to $\langle 110 \rangle$ in Al-8Si alloy.

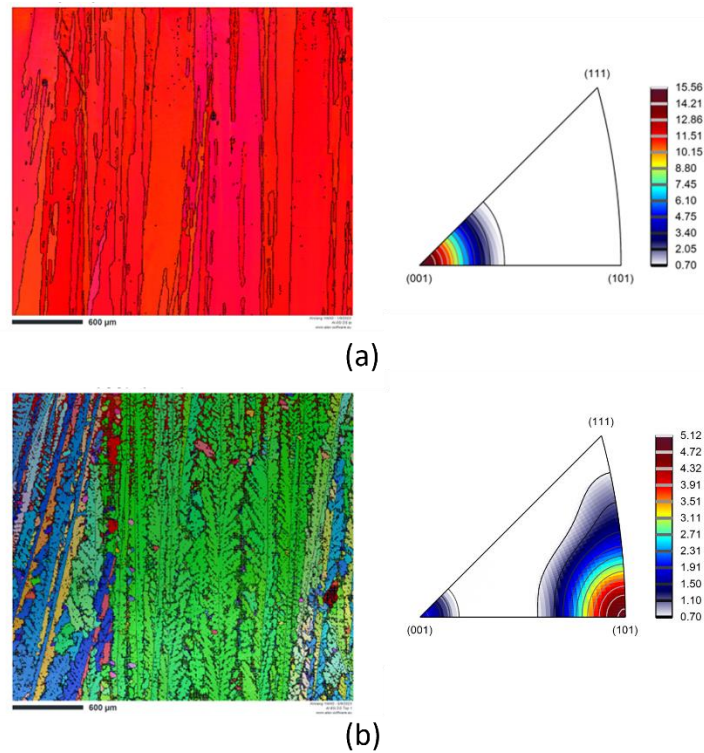


Figure 4.18 EBSD mapping of (a) Al and (b) Al-8Si, indicating the transformation of preferred growth direction of dendrites in DS samples

Though the permanent mould casting employed here to investigate HP-type relation leads to randomly oriented grains, however, the preferential growth of individual dendrite will follow the tendency presented in Figure 4.19 in which the Si content has strong influence on preferential growth direction.

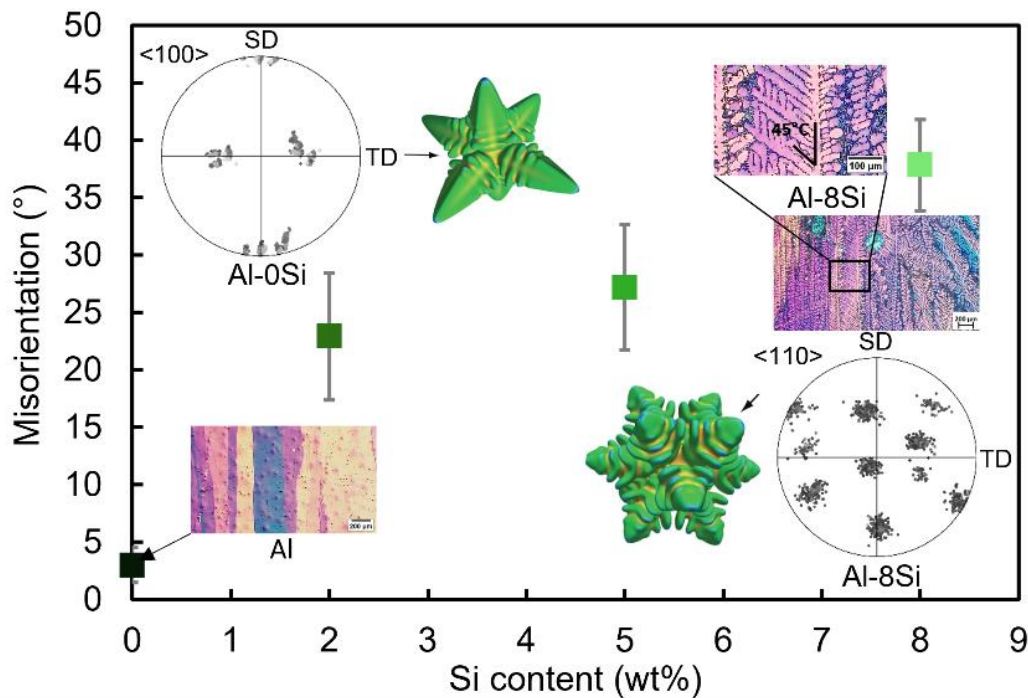


Figure 4.19 Plot showing the variation of angle between the α -Al growth direction and the principal crystal axis as a function of Si content. The optical micrographs showing columnar grain morphology as a consequence of directional solidification. Pole figures of columnar grains, shown as inset, showing the dendrite orientation transition from $\langle 100 \rangle$ for Al and to $\langle 110 \rangle$ for Al-8Si alloys. For Al-8Si alloy, 45° side branching within the columnar dendrite can be observed in the microstructure. Examples of equiaxed grains with $\langle 100 \rangle$ and $\langle 110 \rangle$ growth orientations generated from phase field is reprinted from Ref. [175].

Dislocation dynamics simulation on the textured FCC grains [6] with different morphologies has been confirmed to affect the HP constant strongly. On the other hand, the reported HP-type relation in this study is analysed based on randomly oriented bulk material. Although to our best knowledge the effect of change in dendritic growth direction on the HP constant in such situation is not reported in literature, based on the theoretical study from Jiang et al.[6], it is likely to affect k values.

4.8 Statistical significance of p'

In the previous sections, it has been discussed that the new novel perimeter based parameter is convenient to measure for a variety of microstructures and considering p' in a HP type relationship shows an improvement in the R^2 values of experimental data. However, this improvement seems to be marginal. To evaluate the significance of these improvements, statistical analysis is performed. Since the R^2 values are measured for each alloy in two different conditions i.e. when λ_2 is considered and when p' is considered, a paired 2 tailed t-test is conducted on the R^2 values of fitted HP type relationship in experimental data between BHN_m vs λ_2 and p' .

A t-test is a statistical method used to determine whether there is a significant difference between the means of two groups. It is particularly useful when dealing with small sample sizes and unknown population variances. In present data, t- test on R^2 values of the all studied alloys and Al has been carried out to calculate p_t value and to evaluate significant difference in the quality of fit of new generic HP relationship and conventional HP relationship. A p_t value less than 0.05 indicates a significant difference, whereas a p_t value equal to or greater than 0.05 indicates no significant difference[135,176]. Table 4.1 presents the R^2 values of the generic HP relationship and conventional HP relationship fitted to the experimental data.

Table 4-1: R^2 values of generic HP relationship and conventional HP relationship

Material	R^2	
	$BHN_m = BHN'_{o,\lambda_2} + k'_m \lambda_2^{-0.5}$	$BHN_m = BHN'_{o,p'} + k''_m p'^{-0.5}$
Al	0.92	0.97
Al-2Si	0.95	0.97
Al-5Si	0.94	0.97
Al-8Si	0.95	0.98

The formulation used for the calculation of p_t value is presented in experimental chapter.

In present study, the analysis was conducted on the statistical analysis module in Origin software and the value was determined to be 0.0140 which indicates a significant improvement of R^2 when new generic HP relationship is considered.

4.9 Conclusion

A new perimeter based parameter, p' has been introduced to account for the grain complexity and a new HP relationship has been proposed. We mathematically demonstrated the nonlinear variation of p' with λ_2 , showing the importance of considering perimeter of a grain to predict the YS. The conclusions of this chapter are the following:

- p' holds a nonlinear relationship with λ_2 over a wide range of cooling rates both mathematically and experimentally. This non-linearity becomes more dominant with the increasing Si content.
- The relationship between the hardness contribution of α -Al , BHN_m , and p' can be expressed in a HP type relationship. This modified HP type relationship shows a better value of coefficient of regression (> 0.96) for all the alloys than the conventional HP type relationship. This improvement is significant which is confirmed by t-test.
- The HP slope increases with the increasing Si content, which is attributed to the preferential growth direction of α -Al dendrites. The dendrites were found to grow in $\langle 001 \rangle$ direction, which changed to $\langle 101 \rangle$ direction when Si concentration increased to 8 wt.%.

5 Effect of dendritic morphology on the strength of Al-Ce alloys

5.1 Introduction

In previous chapter, the relation between the new perimeter based parameter, namely p' and strength of Al-Si binary alloys was proposed. To explore further in this direction, a series of Al-Ce binary alloys were studied in present chapter to expand the applicability of $BHN_m = BHN'_{o,p'} + k''_m p'^{-0.5}$ relationship.

Due to negligible solubility of Ce in Al (0.001at.%), Al-Ce binary alloys solidifies in dendritic structure of Al grains surrounded by $Al_{11}Ce_3$ intermetallic solidified by eutectic reaction. Although $Al_{11}Ce_3$ is high in hardness, the overall strength of Al-Ce alloys do not show much improvement. This implies that the major source of strengthening in Al-Ce binary alloys is grain boundary strengthening. To further the study of effect of grain morphology on the strength of metallic materials and to verify the accuracy of the new proposed generic HP relationship in other Al alloy system, the effect of grain morphology on the hardness behaviour of Al-Ce binary alloys were studied.

5.2 Microstructural observations

Figure 5.1 shows the microstructure of all the Al-Ce binary alloys at several cooling rates. The microstructures of Al-Ce alloys consist of an aluminium matrix and secondary intermetallic phases. The hypoeutectic compositions in Al-Ce alloys system are known to solidify by

dendritic growth of proeutectic Al phase followed by the eutectic solidification of $\text{Al}_{11}\text{Ce}_3$ phase. The microstructure of alloys with hypoeutectic compositions constitutes of α -Al dendrites and $\text{Al}_{11}\text{Ce}_3$ intermetallic in the inter-dendritic regions. Similar to Al-Si alloys, SDAS of α -Al dendrites and morphology of $\text{Al}_{11}\text{Ce}_3$ intermetallic shows dependence on the cooling rate and Ce content. SDAS was found to decrease with the increasing Ce concentration and cooling rate. For a given composition, the morphology of $\text{Al}_{11}\text{Ce}_3$ phase shows periodically arranged lamellae at all cooling rates. However, the interlamellar spacing increases with the increasing Ce content at a constant cooling rate. Similar observations were reported by Czerwinski et al. in Al-5, 10, 11, 12 and 20 wt.% Ce alloys. As indicated by Czerwinski and AmirKhiz [18], the microstructure of Al-Ce shows significant changes based on the cerium (Ce) content. For a fully eutectic composition of Al-14Ce, although the predominant area was covered by the lamellar $\text{Al}_{11}\text{Ce}_3$, as seen in the bottom right corner of Figure 5.1. For higher cooling rates, there is also a morphology where the $\text{Al}_{11}\text{Ce}_3$ phase is blocky with larger interlamellar distances. In hypereutectic alloy composition, the primary $\text{Al}_{11}\text{Ce}_3$ were in rod like structure at slower cooling rate and blocky in higher cooling rates. These morphologies of primary $\text{Al}_{11}\text{Ce}_3$ phase are reported in literature. Nevertheless, similar to Al-Si binary alloys, the effect of cooling rate is clear in affecting the SDAS of the α -Al dendrites.

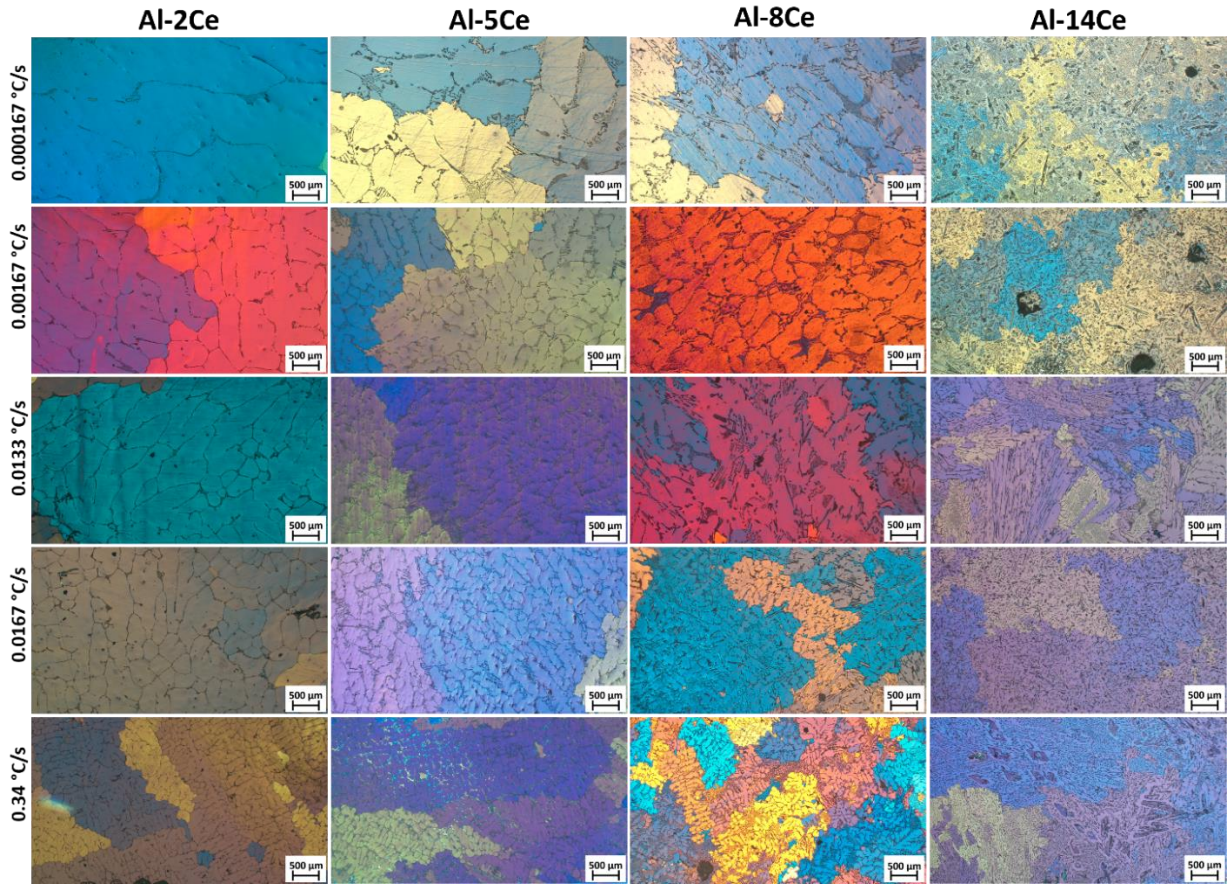


Figure 5.1 As cast microstructures of Al-Ce binary alloys at several cooling conditions and compositions.

The conventional mathematical model predicting the SDAS at a given cooling rates was given by Kattamis, following the $\lambda_2 \propto \dot{T}^{-n}$ relation, where $n = 1/3$. This model was applied to predict the SDAS of Al-Ce alloys at hypoeutectic compositions. Experimental results with fitted model for all as cast alloys is shown in Figure 5.2. The fitted model in the experimental dataset demonstrates high coefficients of regression values ($R^2 > 0.95$), indicating a strong agreement between the model and the experimental data.

Similar to the relationship between λ_2 and \dot{T} , the relationship between p' and \dot{T} is observed to follow $p' \propto \dot{T}^{-m}$. The best fit parameters in this relationship is shown in Figure 5.3. But the value of m decreases with the increasing Ce content, indicating the influence of solute content

on the dendritic complexity in terms of interfacial area. The value of m approaches $1/3$ as the Ce content decreases, as the grain morphology in low solute alloys is near faceted which is similar to the grains in pure Al. When the data is fitted with the same equation but with $m=1/3$, the curve results in low values of coefficient of regression, shown in Figure 5.4. Although the R^2 values of Al-8Ce shows a satisfactory fit to the data as the difference between n and m is lowest in all the alloys. The difference between m and n values is shown in the inset of Figure 5.3. This observation reiterates the importance of considering p' in HP relationship to accommodate the morphological effect of grains on the YS.

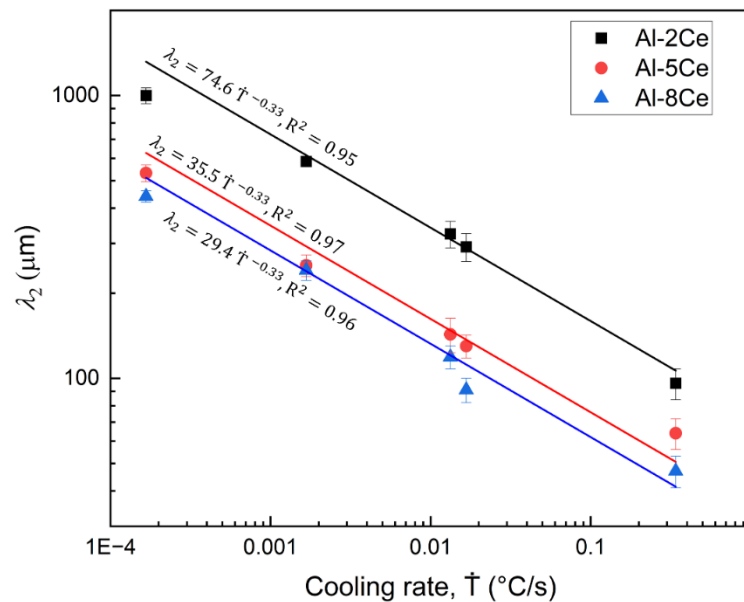


Figure 5.2 . Variation of λ_2 as a function of cooling rate with solid lines being the Kattamis and Flemming coarsening model.

As shown in the previous chapter, the relationship between λ_2 and p' follows a nonlinear relationship theoretically which was further demonstrated to be consistent with the experimental data of Al-8Si alloy. This non-linear relationship persists in Al-8Ce alloy as well. Figure 5.5 shows the experimentally measured SDAS and p' for Al-8Ce alloy solidified over a wide range of cooling rates. The non-linear relationship between λ_2 and p' is observed to be

persistent in Al alloys with increasing Si and Ce content. This demonstrates the importance of p' in capturing the variation of grain morphology in Al alloys.

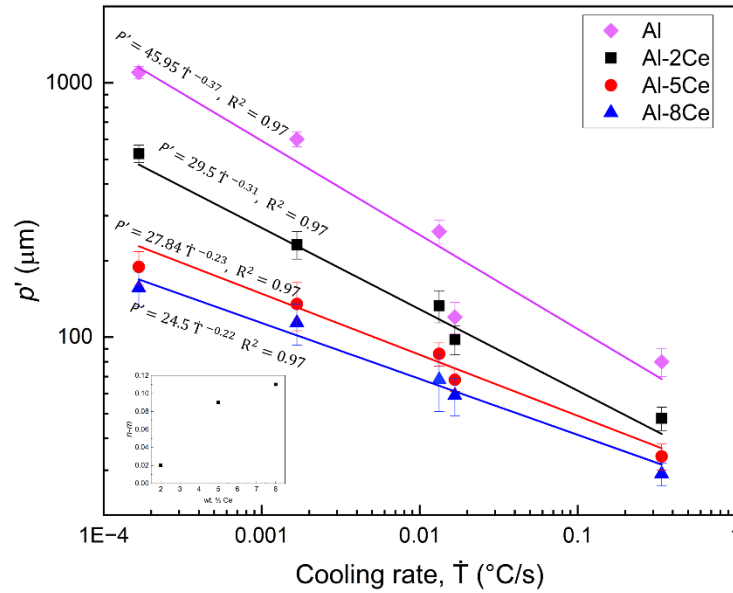


Figure 5.3 Variation of p' as a function of cooling rate. Solid lines are the best-fit

$p' \propto \dot{T}^{-m}$ with the inset of relation between $n-m$ and Ce content.

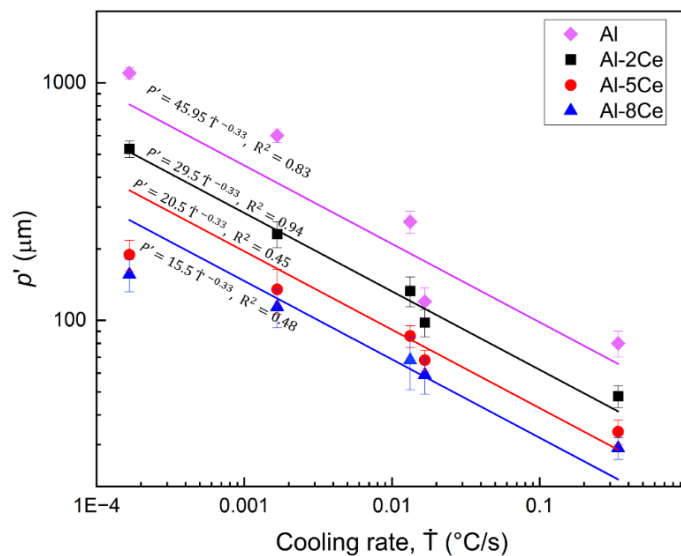


Figure 5.4 Relationship between p' and cooling rate when data is fitted with $p' \propto \dot{T}^{-m}$

type of equation with $m = 0.33$.

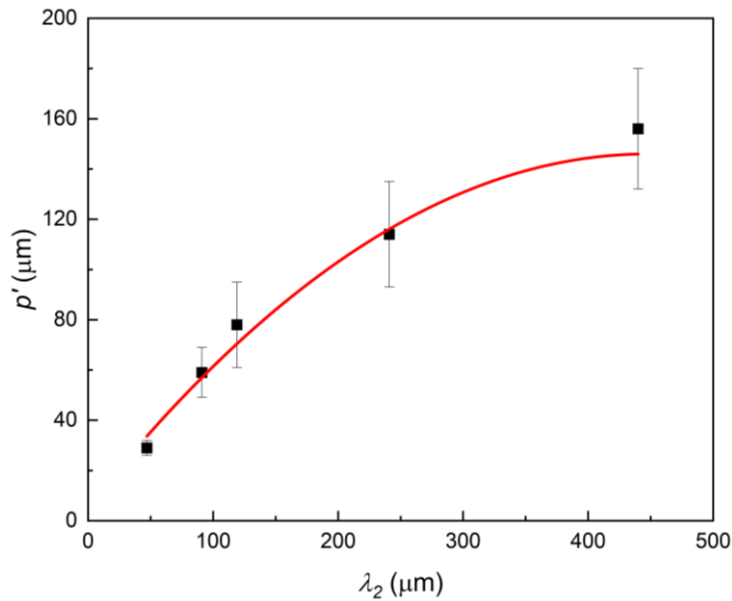


Figure 5.5 Relation between experimental p' and λ_2 showing the nonlinearity in Al-8Ce alloy. Solid line is guide to the eye.

5.3 Hardness of Al-Ce alloys at various cooling rates

Figure 5.6 shows the hardness of all studied alloy systems, solidified at several cooling rates. The hardness trend of Al-Ce system shows the same trend as the Al-Si system, with increasing hardness as the cooling rate and Ce content increases. The morphology of $\text{Al}_{11}\text{Ce}_3$ phase is reported to change into fine lamellar as the cooling rate increases [177], which increases the load bearing capacity of the eutectic structure resulting in higher hardness of alloys solidified at higher cooling rates. As compared to Al-Si alloys, the increment in hardness in Al-Ce is less. In study by Czerwinski and Babak[178] the hardness of the as-cast Al-5Ce alloy, measuring 35 HV, slightly surpassed the typical range of 20–25 HV for commercial aluminium. Elimination of proeutectic Al occurred when the Ce content was raised to 10 weight percent, resulting in an alloy hardness of 46 HV. Subsequent increases in Ce content to 15 wt.% and 20 wt.% led to hardness values of 50 HV and 59 HV, respectively. The reason for this low contribution in hardness from the eutectic has been previously reported to be due to

incoherency of $Al_{11}Ce_3$ phase with Al matrix. The hardness of $Al_{11}Ce_3$ phase has been reported to be 350HV whereas the hardness of Al matrix is 35HV, still the hardness of $Al_{11}Ce_3$ phase doesn't translates into the overall hardness of the eutectic alloy. The reported crystallographic orientation relationships imply the presence of partial coherency during the nucleation and initial stages of eutectic growth and solidification in the lamellar Al/ $Al_{11}Ce_3$ eutectic. However, as the eutectic phase ($Al_{11}Ce_3$) progressed, its coherence with aluminium (Al) is lost. The diminished coherency is anticipated to adversely affect the strengthening properties of the $Al_{11}Ce_3$ eutectic phase. The orientation relationships between $Al_{11}Ce_3$ and Al in the eutectic structure, leading to partial coherency, were determined as $[0\ 0\ 1]_{Al} \parallel [\bar{1}\ 1\ 1]_{Al_{11}Ce_3}$ with $(0\ 4\ \bar{4})_{Al} \parallel (\bar{2}\ 0\ 0)_{Al_{11}Ce_3}$ and $[0\ 1\ 1]_{Al} \parallel [\bar{3}\ 0\ 1]_{Al_{11}Ce_3}$ with $(\bar{2}\ 0\ 0)_{Al} \parallel (0\ 6\ 0)_{Al_{11}Ce_3}$. The lack of strengthening by $Al_{11}Ce_3$ phase is also reflected in YS behaviour of Al-Ce alloys. Weiss et al. [179] have reported the room temperature tensile strength of Al-6, 12, 16 Ce binary alloys. The yield strength of as cast samples was measured to be 30, 58 and 68 MPa respectively, which is significantly lower than the conventional Al-Si alloys. Although the increase in hardness with increasing Ce content is not significant, the increase in hardness of a given composition with increasing cooling rate is still noticeable. Since the contribution to hardness from $Al_{11}Ce_3$ phase is negligible, it can be expected that the major contribution in hardness is from the α - Al grains.

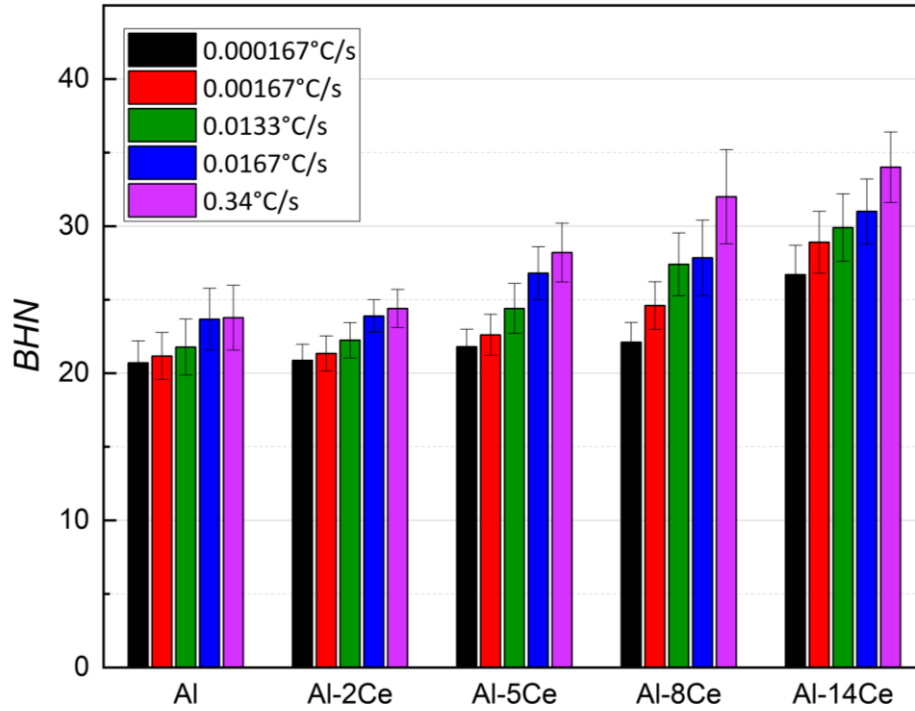


Figure 5.6. Brinell hardness of all alloys at several cooling rates.

Due to a linear relationship between the hardness and YS in Al alloys, in present study, Brinell hardness is used to indicate the strength of alloys. The data is fitted to conventional HP type relation between the measured BHN and λ_2 ($BHN = BHN_{o,\lambda_2} + k'/\sqrt{\lambda_2}$, where BHN_{o,λ_2} , is the intercept and k' is the HP constants) is shown in Figure 5.7. The conventional HP type relationship fits well in the measured data with satisfactory coefficients of regression values ($92 \leq R^2 \leq 95$).

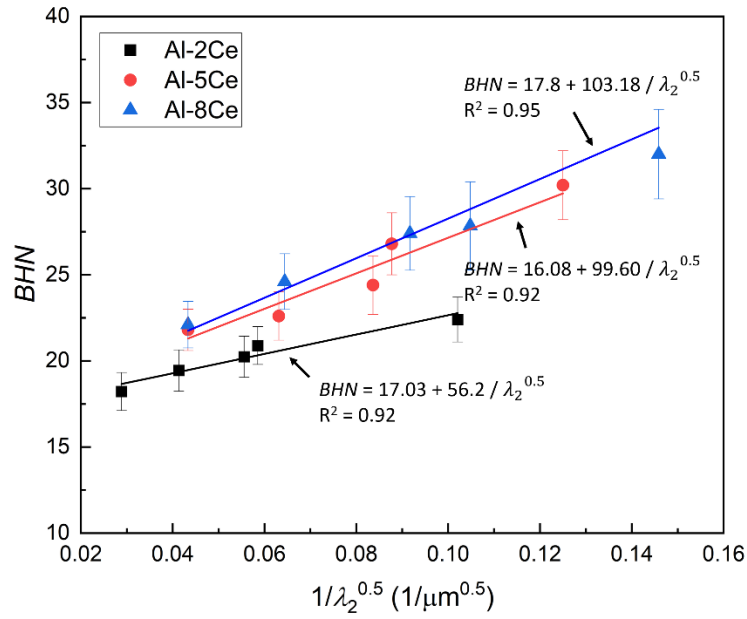


Figure 5.7. HP type relationship between BHN and λ_2 for all the Al-Ce binary alloys

The HP type relationship between the p' and BHN is shown in Figure 5.8. The data is fitted in equation $BHN = BHN_{o,p'} + k''/\sqrt{p'}$, where $BHN_{o,p'}$ is the intercepts and k'' is the HP constant. The measured data fits well into the new HP type relationship and moreover the improvement in coefficients of regression is still noticeable in all the alloys with R^2 values ranging from 0.97 to 0.99 showing an excellent fitting of the hardness data with p' . Although the BHN in both the equations presented in Figure 5.6 and 5.7 is the hardness of the bulk of material which includes the combined hardness of Al matrix and the eutectic fraction, considering p' rather than λ_2 affects the coefficients of regression significantly.

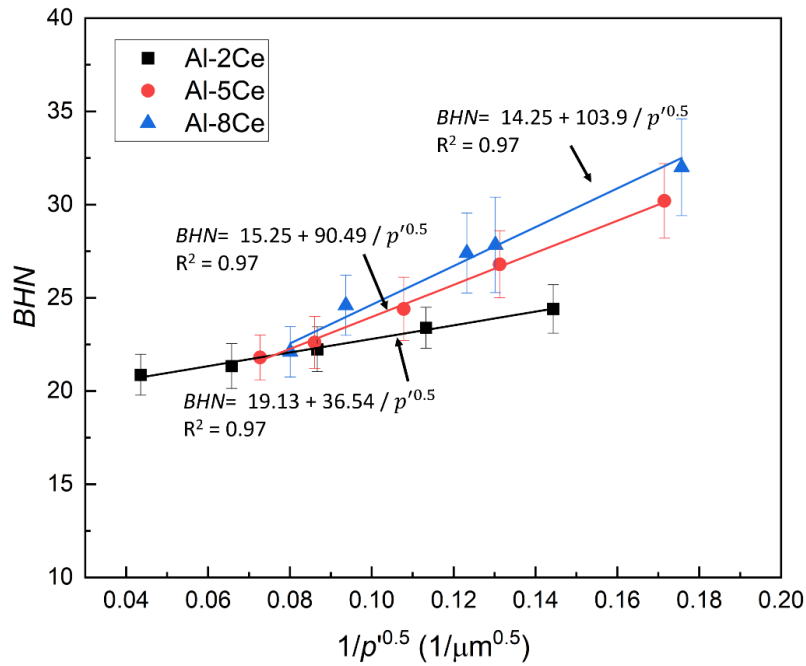


Figure 5.8 Relationship between BHN and p' . Solid lines are fit to the experimental data with the new HP relationship.

5.4 Hardness contribution from eutectic fraction

To accurately measure the hardness contribution from the morphological change of Al dendrites, the contribution from the eutectic colonies should be deduced from the bulk hardness of alloys. In chapter 4, the approach used was based on the reduction of hardness in conjunction to relationship of hardness and interlamellar spacing correlation in purely eutectic alloys. This approach was practically feasible for Al-Si alloys as the interlamellar spacing between eutectic Si particles in eutectic pool is consistent and easy to measure. In the case of Al-Ce alloys, the pure eutectic alloy composition (Al-14Ce) possesses a nonuniform distribution of eutectic and primary $\text{Al}_{11}\text{Ce}_3$ phase.

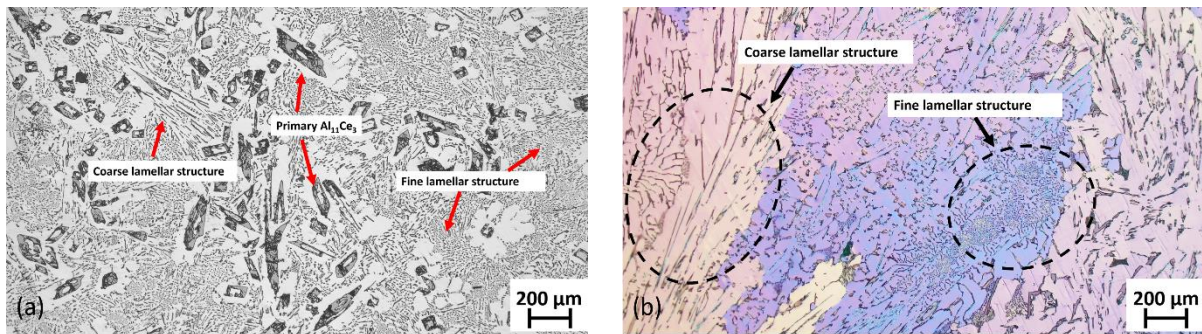


Figure 5.9. Optical microstructures of Al-14Ce alloys solidified at (a) 0.000167 °C/s (b) 0.0133 °C/s

Figure 5.9, highlights the regions with nonuniform eutectic structures. Figure 5.9(a) shows three morphologies within the eutectic region. Firstly, the blocky primary $\text{Al}_{11}\text{Ce}_3$ phase are present in matrix, secondly, the coarse $\text{Al}_{11}\text{Ce}_3$ with high interlamellar spacing and third is the fine $\text{Al}_{11}\text{Ce}_3$ with small interlamellar spacing. In Al-14Ce alloy solidified at 0.0133 °C/s, the interlamellar spacing was measured to be as low as 8 μm and as high as 90 μm (shown in dotted circles in Figure 5.9(b)).

Same feature was noticed at hypoeutectic compositions, one example is illustrated in Figure 5.10. Al-2Ce alloy solidified at 0.000167 °C/s shown in Figure 5.10(a) shows the fine lamellar structure at the interdendritic regions and some traces of coarser lamellar $\text{Al}_{11}\text{Ce}_3$ phase. Whereas, in samples solidified at 0.34 °C/s, the morphology of eutectic $\text{Al}_{11}\text{Ce}_3$ phase is unrecognizable as the phases are very fine making it harder to apply HP type relationship between hardness and interlamellar spacing.

Due to such discrepancies, the approach adapted in Al-Si will not be accurate in Al-Ce alloys. Therefore, a rule of mixture approach has been adopted to deduct the hardness contribution from eutectic fraction.

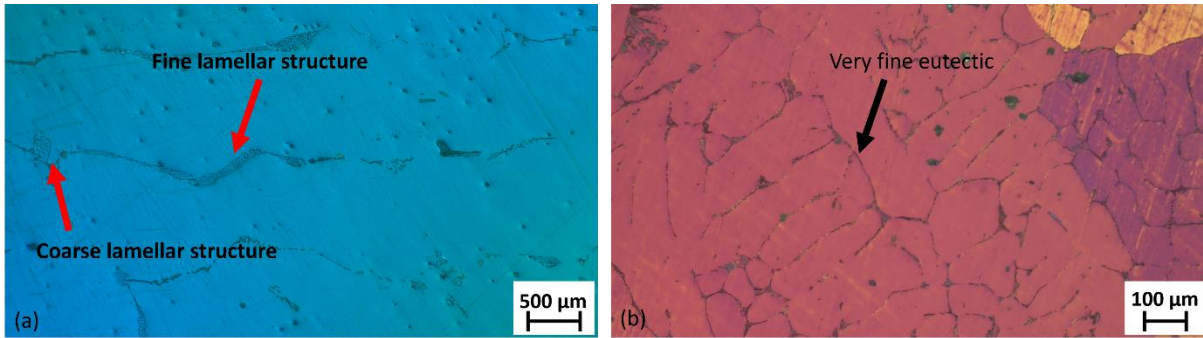


Figure 5.10 Microstructures of Al-2Ce solidified at(a) 0.000167° C and (b) 0.034° C, showing the very fine and coarse morphology of $Al_{11}Ce_3$ phase.

$$BHN = V_m BHN_m + V_e BHN_e \quad (5.1)$$

where BHN_m and BHN_e are the hardness of matrix and hardness of an alloy with complete eutectic composition, and V_m, V_e are the volume fractions of the matrix and eutectic phase.

The eqn. (5.1) can be rewritten as

$$BHN_m = \frac{BHN - V_e BHN_e}{V_m} \quad (5.2)$$

$$\text{And } V_e + V_m = 1$$

Since, the solubility of Ce in Al is negligible, no Ce is expected to be present in the Al matrix. Since Ce is only in the eutectic phase, the volume fraction of $Al_{11}Ce_3$ in Al-2Ce, Al-5Ce and Al-8Ce alloys at room temperature was found to be 0.022, 0.057 and 0.093 by using the thermocalc.

Figure 5.11 shows the relation between the actual hardness contribution i.e. BHN_m from the Al dendrites and the SDAS of hypoeutectic Al-Ce alloys. The data has been fitted with HP type relationship, given by

$$BHN_m = BHN'_{o,\lambda_2} + k'_m \lambda_2^{-0.5} \quad (5.3)$$

where BHN'_{o,λ_2} is the intercepts and k'_m is the HP constant. The fitting of equations shows a satisfactory regression values i.e. 0.92, 0.92 and 0.93 for Al-2Ce, Al-5Ce and Al-8Ce alloys respectively. Two observations can be made in this graph, firstly the change in slope and secondly the consistent value of BHN'_{o,λ_2} . In Al-Si binary alloys there was a consistent change noticed in the BHN'_{o,λ_2} value. Since the intercept on y-axis in HP type relationship represents the friction stress of the material, no change in the intercept indicates constant friction stress irrespective of the change in Ce concentration. However, the slope shows an increase with increasing Ce content. As discussed in chapter 4, such change in slope is often associated with the active deformation mode present in the material which is decided by the texture and loading direction. Since no process was done to affect the texture of the alloys, this change in slope is suspected to be associated with the change in growth orientation of the Al dendrites.

Figure 5.12 shows the relationship between the BHN_m and p' in Al-2Ce, Al-5Ce and Al-8Ce alloys. The experimental data has been fitted with the new HP relationship given by

$$BHN_m = BHN'_{o,p'} + k''_m p'^{-0.5} \quad (5.4)$$

$BHN'_{o,p'}$ is the intercept and k''_m is the HP constant. Similar to Figure 4.17, the change in the slope with the increasing Ce content is evident, with k''_m changing from 35 to 101 for Al-2Ce alloy to Al-8Ce alloy. The importance of considering the p' in accounting for the morphology of a dendrite is reiterated with the improvement of the R^2 values when the perimeter associated parameter is considered for predicting the hardness of Al-Ce alloys. The R^2 values (given in Figure 5.12) are higher when p' is considered in HP relation when compared to that of λ_2 for all alloys. This observation is consistent in all the cases and all the alloy systems with $R^2 \geq$

0.97, which indicated an excellent fit of the new HP type relationship into the experimental data of hypoeutectic Al-Ce alloys.

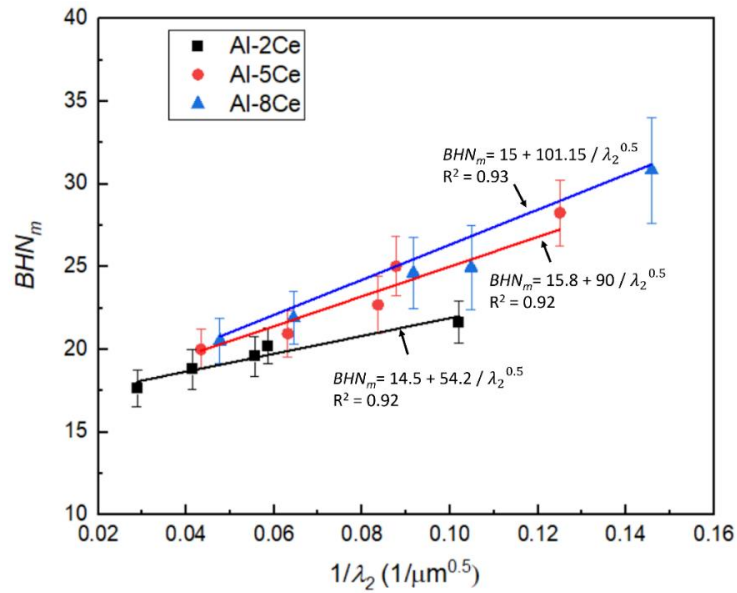


Figure 5.11 Relationship between (a) BHN_m and λ_2 , the solid lines are fits to the HP relationships given in Eqs. (5.3)

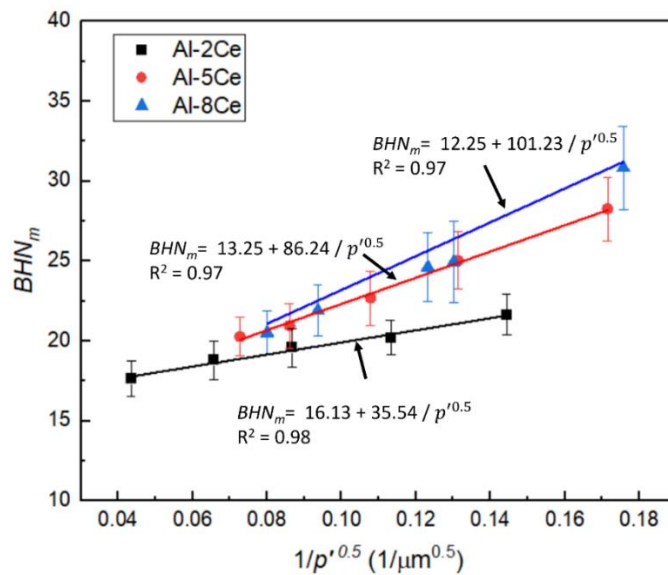


Figure 5.12 Relationship between (a) BHN_m and p' The solid lines are fits to the new HP relationships given in Eqs. (5.4)

Although the fits show excellent R^2 values, unlike prior cases, wherein the change in the intercepts on the y axis showed very less change, in Figure 5.12, when p' is considered, the intercept shows a decrease in value with increasing Ce concentration. This observation shows an opposite trend in the change in values of $BHN'_{o,p'}$ in case of Al-Si binary alloys where, the $BHN'_{o,p'}$ showed an increasing trend with increasing Si content.

To highlight the importance of considering p' to account for the change in dendritic morphology induced by changing the solute concentration and cooling in HP type model to predict the hardness/ strength of an alloy, the measure data with new and conventional HP relationship has been presented in Figure 5.13.

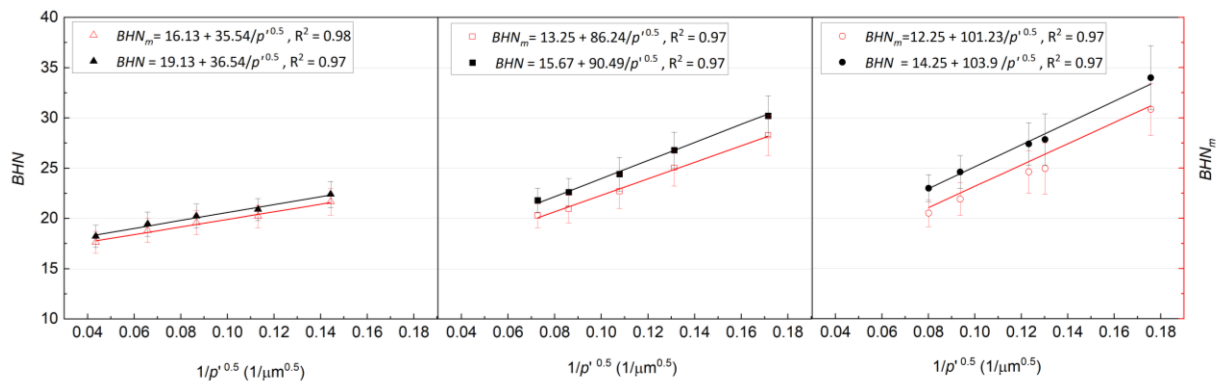


Figure 5.13 HP type relationships [BHN_m vs p' and BHN vs p'] for all Al-Ce alloy systems.

A significant increase in intercept due to solid solution strengthening contribution to the hardness can be clearly seen. Increase in k''_m value with the increased Ce content can also be seen.

Two distinctions can be made from Figure 5.13, firstly, the change in HP slope, i.e. k''_m values increasing with the increasing Ce even after the reduction of hardness contribution from eutectic fraction and secondly, the change in intercept in y-axis, i.e. $BHN'_{o,p'}$ decreasing with increasing Ce content. $BHN'_{o,p'}$ which represents the friction stress in HP relationship has three constituents, which are

$$\sigma_o = \sigma_{CRSS} + \sigma_p + \Delta\sigma_{SS} \quad (5.5)$$

where, σ_{CRSS} is the critical resolved shear stress, $\Delta\sigma_{SS}$ is the improvement in strength due to solid solution and σ_p is the residual stress due to the dislocations associated with thermomechanical processing.

Since the solubility of Ce in Al is negligible, the contribution from solution strengthening is negligible. σ_p in present study is also negligible as no thermomechanical processing has been applied to studied alloys. The third component, σ_{CRSS} is known to depend on the active slip system in the material. It is clear that σ_{CRSS} component decreases with the increasing Ce content and it can be speculated that increase in Ce content, the slip activity changes subjected to texture evolution.

5.5 Conclusion

The applicability of new novel perimeter-based parameter p' has been explored in Al-2Ce, Al-5Ce and Al-8Ce binary alloys. The nonlinear relationship between p' and λ_2 is persistent in Al-8Ce alloy which reinforces the need of considering p' in relating the strength of an alloy with the morphology of grains. The new HP relationship shows a satisfactory fit with the experimentally measured hardness with corresponding p' . The average coefficient of regression values show improvement when p' ($R^2 \geq 0.97$) is considered instead of λ_2 ($R^2 \geq 0.92$). The change in HP constant (k''_m) with increasing Ce is consistent with the observation made in Al-Si alloys in previous chapter, indicating towards the texture evolution of α -Al grains with increasing Ce content.

6 Influence of grain morphology on the strength of Mg alloys

6.1 Introduction

In previous chapters, the effect of grain morphology on the hardness behaviour of Al-Si and Al-Ce binary alloys using HP model has been explored and a new novel perimeter based parameter has been proposed to capture the change in the morphology of grains. However, the effect of change in grain size on the degree of strengthening of Al alloys remains limited due to a low HP constant. To explore the applicability of considering the p' to account for the complexity of grains in a wide range of metals that exhibit complex grain morphologies, Mg alloys were also studied.

Mg alloys often exhibits a wide range of HP constant due to their limited slip systems. As discussed in chapter 2, the variation in k values has been linked with active slip system during deformation. The k value of AZ91 alloy in particular has been reported to vary from 244 MPa $\mu\text{m}^{1/2}$ in extruded samples to 138 MPa $\mu\text{m}^{1/2}$ in samples processed by equal channel angular extrusion process. These values are considerably higher than the HP values of Al alloys, indicating a high sensitivity of YS to d and λ_2 . To exploit the higher HP constant of Mg alloys in new HP relationship, three Mg alloys were studied in this chapter. Commercial AZ91D alloy along with Mg-5Al and Mg-9Al binary alloys were studied and comparison between conventional and new HP relationship are presented.

6.2 Microstructure analysis of Mg alloys

First model alloy chosen was a commercial AZ91D alloy with nominal composition of Mg–9.08Al–0.62Zn–0.26Mn. Due to a high concentration of solute as compared to other AZ series alloys, AZ91D alloy exhibits a dendritic morphology of grains which is beneficial to study the variation of p' with the SDAS at different cooling rates. To investigate the effect of dendritic morphology on the strengthening behaviour of AZ91D alloy, specimens with varied grain morphologies were produced by solidifying molten AZ91D alloy inside a Cu based wedge mould. The geometry of wedge mould casting provides different cooling rates at different locations which results in the varied grain size and morphology of AZ91D alloy across the length. The melt was prepared in an electrical resistance furnaces fitted with steel liners. To prevent the potential fire hazard due to the high oxidation tendency of Mg alloy melt, protective N_2+SF_6 gas coverage was provided in the furnace. Following melting, the melt was poured at a temperature of 680°C into a wedge mould, which was preheated at 200°C to eliminate any moisture.

To evaluate the effect of variable cooling rate induced by the wedge-shaped geometry, microstructural analysis was conducted on the sections at different locations along the straight line. Figure 6.1 shows the polarised microstructure of samples extracted from the cross section of AZ91D alloy produced by wedge mould casting. The tip of casting cools with the highest cooling rate whereas the cooling rate at the bottom of the casting is the lowest. To produce a large array of grain morphologies by the virtue of varying cooling rates, two more solidification experiments were conducted by solidifying AZ91D inside a steel crucible at ambient temperature and inside a switch off furnace with protective N_2+SF_6 gas. Figure 6.2 shows the microstructures of samples solidified in ambient temperature and inside a switched off furnace.

The specimen exhibits dendritic microstructures with equiaxed grains of solid solution of aluminium in magnesium, α -Mg (hexagonal close packed structure) and eutectic β -Mg₁₇Al₁₂ phase. Figure 6.3 shows the SEM micrograph of AZ91D alloy highlighting the eutectic β -Mg₁₇Al₁₂ phase's uniform distribution in the interdendritic region throughout the specimen.

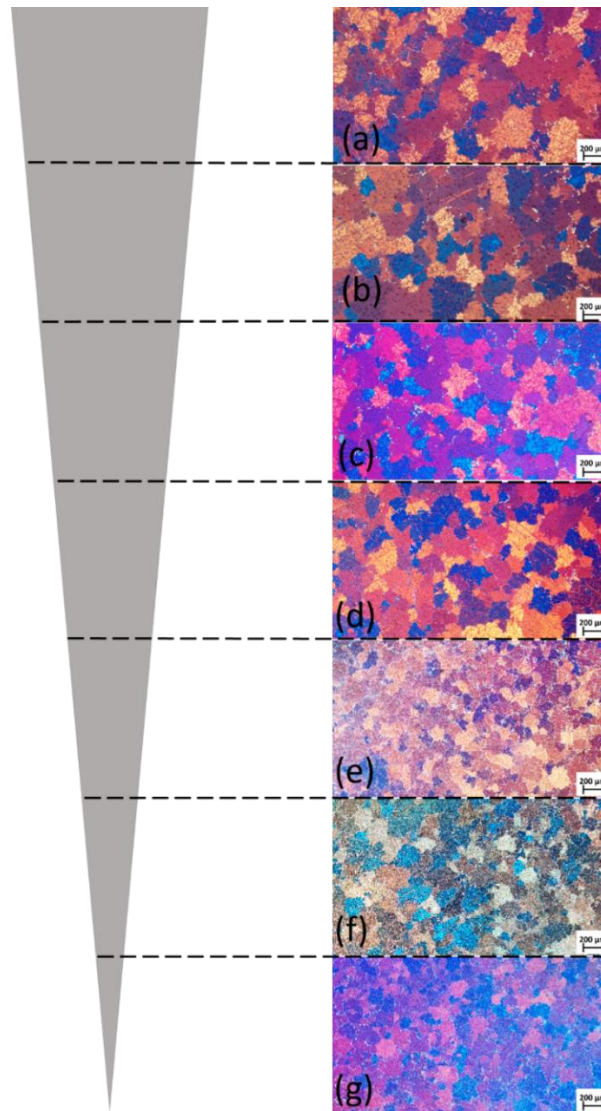


Figure 6.1. Microstructural variations across the cross-section of AZ91 alloy cast in a wedge mould casting, highlighting the change in grain size with changing cooling rates.

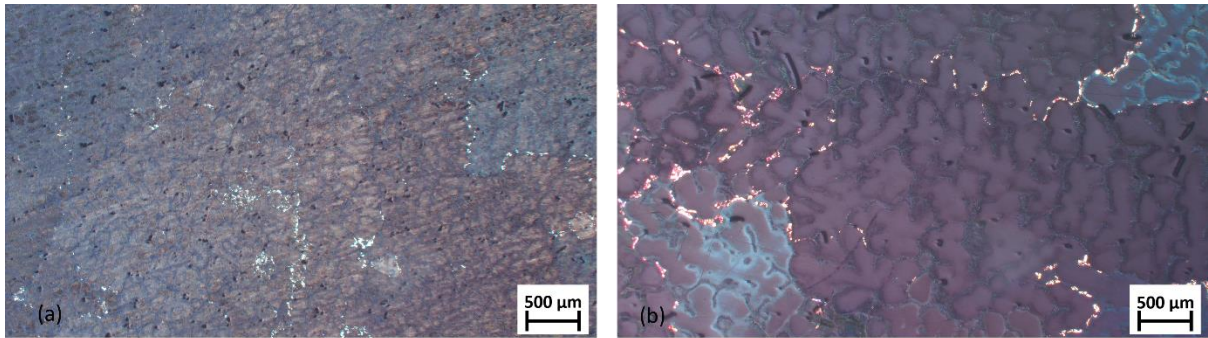


Figure 6.2 Microstructures of as cast AZ91D alloy, solidified at (a) 0.11°C/s (b) 0.011°C/s

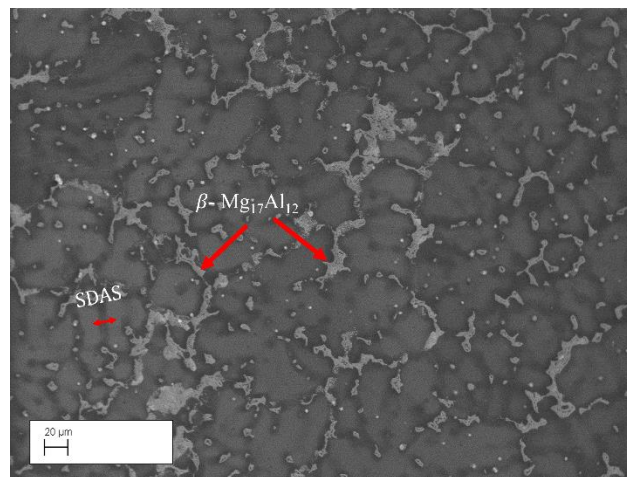


Figure 6.3 SEM microstructure of as cast AZ91 D alloy highlighting the β - $Mg_{17}Al_{12}$ phase and illustrating the SDAS measurement.

Generally, β - $Mg_{17}Al_{12}$ phase can be characterized into two categories, i.e. (1) continuous precipitation and (2) discontinuous precipitation. Continuous precipitates mainly produce asymmetrical plate shaped phases, with a BCC structure. Whereas, discontinuous phases form lamellar structure of α -Mg and β - $Mg_{17}Al_{12}$. These morphologies are associated with their nucleation and growth conditions. Generally, during non-equilibrium solidification of the as-cast AZ91D alloy, due to relatively a higher cooling rate, Al is not homogenous in melt. After the primary solidification of α -Mg matrix. The resulting melt, which is rich in Al undergoes eutectic solidification into the divorced eutectic ($\alpha+\beta$). In a study by Wu et al.[180], A numerical model utilizing the cellular automaton (CA) method was developed to simulate the microstructure evolution of magnesium alloy during the cold-chamber high-pressure die

casting (HPDC) process. It was observed that the nucleation of eutectic α -Mg initiates in proximity to the primary α -Mg and subsequently grows during the solidification stage. Concurrently, the eutectic β -Mg₁₇Al₁₂ nucleates and grows independently during the early phase of eutectic solidification. As the solidification progresses, the two eutectic phases impinge on each other, leading to a cooperative and competitive growth mode. In further cooling process, β -Mg₁₇Al₁₂ precipitates into α -Mg matrix, especially in the divorced eutectic α -Mg matrix for its high Al content [181,182]. The phase formation process in AZ91D alloy can be given as:

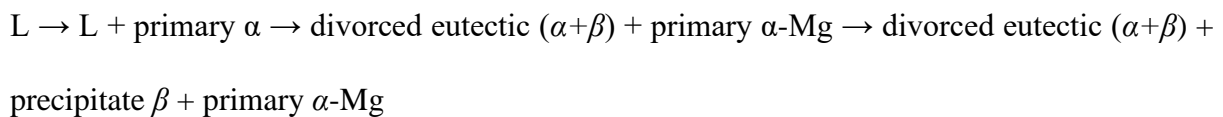


Figure 6.4 shows the SEM micrograph and EDS spectrum of as-cast AZ91 Mg alloy. As can be seen in the microstructure, the as-cast microstructure consists of α -Mg matrix and a large volume fraction of β -Mg₁₇Al₁₂ intermetallic compound which can be characterised as lathe like morphology in the interdendritic pool. Lamellar structure of discontinuous divorced eutectic ($\alpha+\beta$) can also be noticed surrounding the continuous β -Mg₁₇Al₁₂ particles.

Apart from eutectic compounds, fine and spherical Al-Mn particles are also observed inside the α -Mg grains. The formation of AlMn particles has been reported to be at a higher temperature, prior to the nucleation of α -Mg grains and have equiaxed polygonal morphology [183,184].

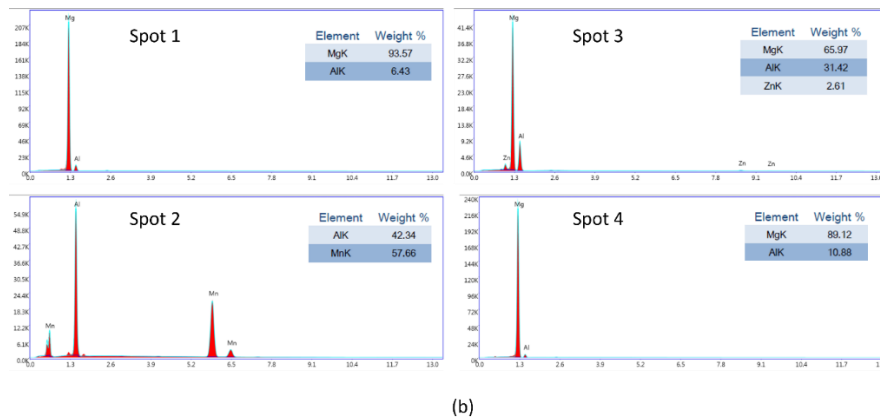
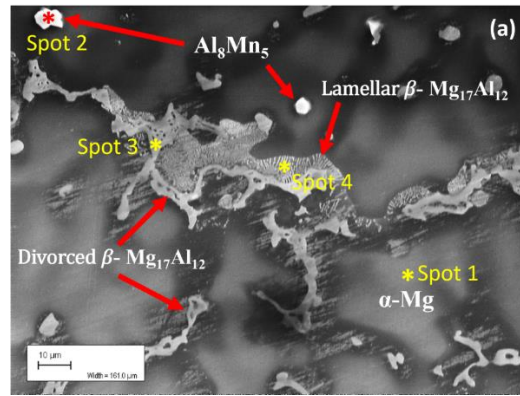


Figure 6.4 (a) SEM micrograph of as cast AZ91D alloy highlighting the continuous and discontinuous precipitates pointed by red arrows (b) EDX peaks for major secondary phases in the matrix. Spot 1: Matrix, spot 2: Al-Mn based secondary particle, spot 3: divorced β -Mg₁₇Al₁₂ phase, spot 4: lamellar β -Mg₁₇Al₁₂ phase.

Similar variation of the grain structure was observed in Mg-5 and 9 wt.% Al binary alloys. Figure 6.5 shows the as cast microstructures of Mg-5 and 9 wt.% Al alloys solidified using wedge mould casting. The influence of cooling rate and solute content is evident on the grain size and morphology of grains. The grain size decreases with the increase in Al content and towards the tip of the wedge. Figure 6.5(b) illustrates the grain size variation as the function of distance from the wedge tip showing the decrease in the average grain diameter with increasing cooling rate, moving down the wedge mould.

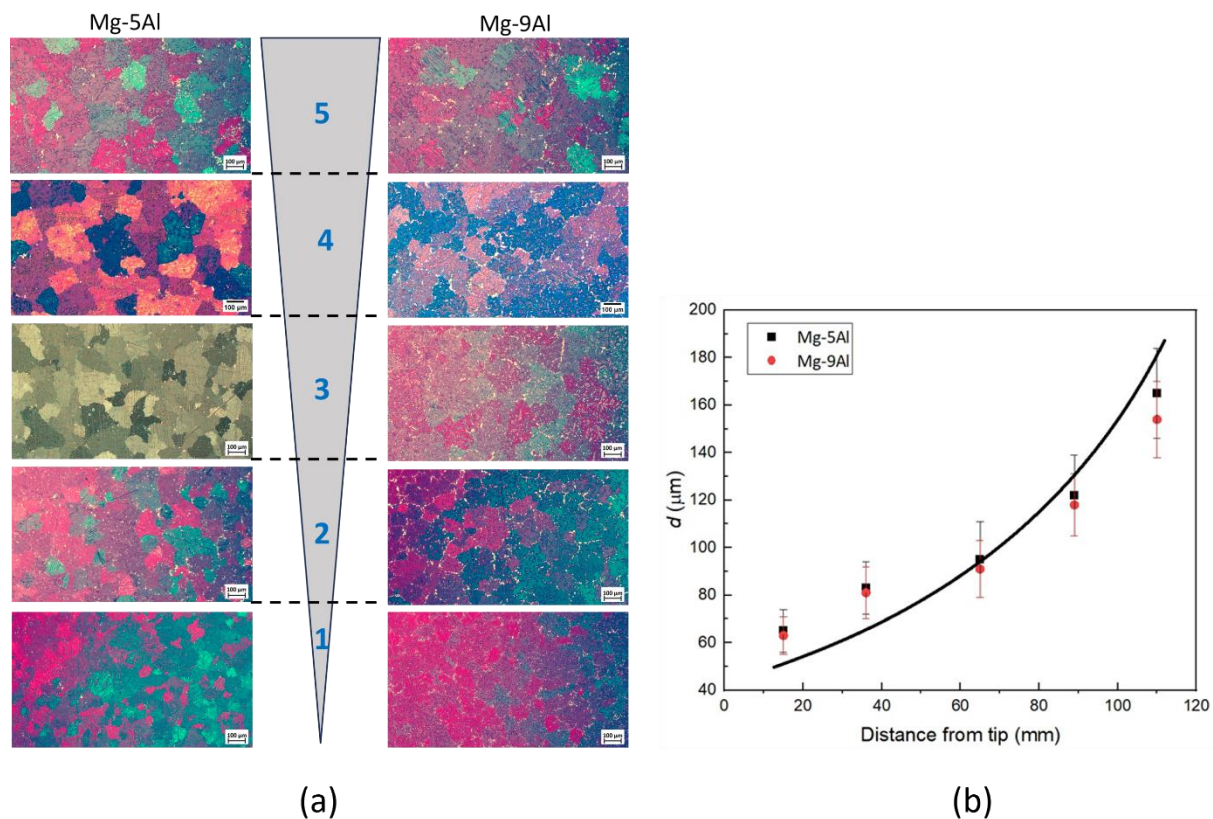


Figure 6.5 Optical micrographs of as cast (a) Mg-5Al and Mg-9Al binary alloys cast in wedge mould. The morphology of grains has been altered by varying the solute concentration and the grain size variation has been induced by variable cooling rates along the length of wedge mould casting (b) grain size as a function of distance from the tip of the wedge mould casting, solid line is the guide to eye.

6.2.1 Effect of cooling rate on the grain size in AZ91D alloy

As can be seen from Figure 6.1, higher cooling rate condition results in a finer morphology of α -Mg dendrites and lower cooling rates results in coarser dendrites. To quantitatively compare the effect of cooling rate on the grain diameter, the SDA and p' of as cast material, measurements were made at the locations in the wedge. The variation of SDAS, d and p' measured at different locations in the wedge are shown in Figure 6.6(a)-(c). It is clear that the

grain size (d), dendritic arm spacing (SDAS) and p' shows similar trend and decreases with the increasing cooling rates.

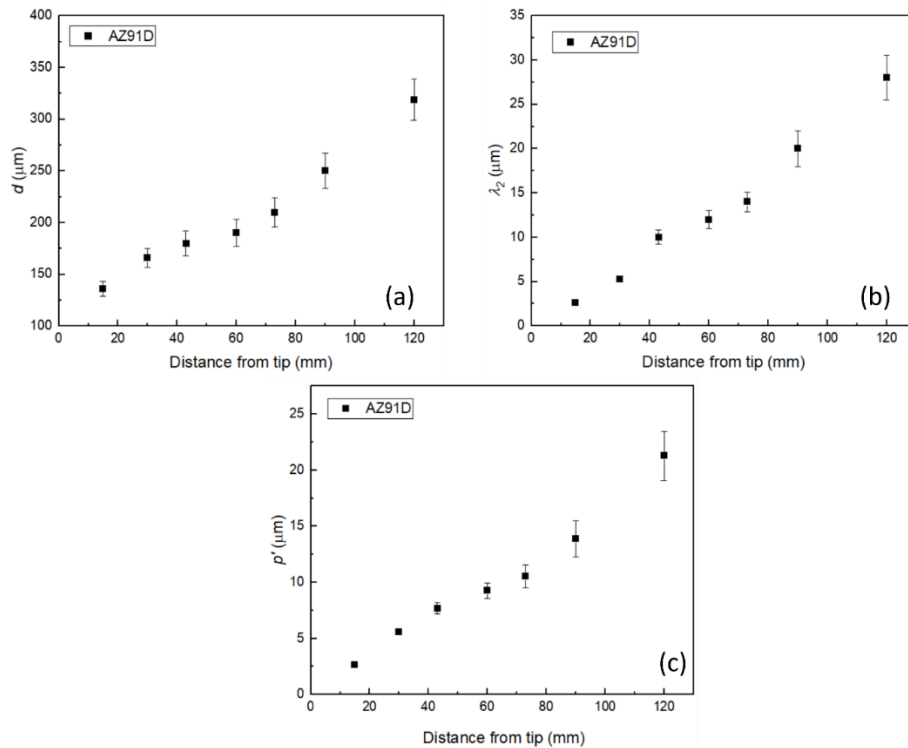


Figure 6.6 Effect of variable cooling rates on the microstructural features of AZ91D alloy was evaluated by measuring grain size, SDAS and p' at different distance from the tip of wedge. (a) Variation of measured average grain diameter (d) at different locations in wedge (b) λ_2 of dendrites and (c) p' measured at different distances from the tip of wedge.

The effect of changing cooling rate on the grain size, across the length of wedge is clear from Figure 6.6. A significant reduction in the grain size from 319 μm at 120 mm from the tip of the wedge to 136 μm at 12mm from the tip of the wedge is noticeable. Similarly, the dendritic arm spacing and p' shows the same trend and decreases towards the tip of wedge samples. The SDAS of dendrite at 120 mm from the tip was measured to be 28 μm , which reduces to 2.5 μm for the finest dendrite at 12 mm from the tip, showing a significant refining of dendritic

structure with increasing cooling rate. The relationship between the cooling rate and SDAS can be given by a fitting a relationship of the form

$$\lambda_2 = Y\dot{T}^{-n} \quad (6.1)$$

where Y is the proportionality constant. The value of Y and n was calculated by replotting the data present in ref [185–187], shown in Figure 6.7. Since in present study, the values of SDAS are within the range of measured SDAS values presented in ref [185–187], Eq. (6.1) is applicable in present experimental data. The value of Y and n were used to calculate the cooling rate of specimen solidified at room temperature and inside a switched off furnace (Figure 6.2)

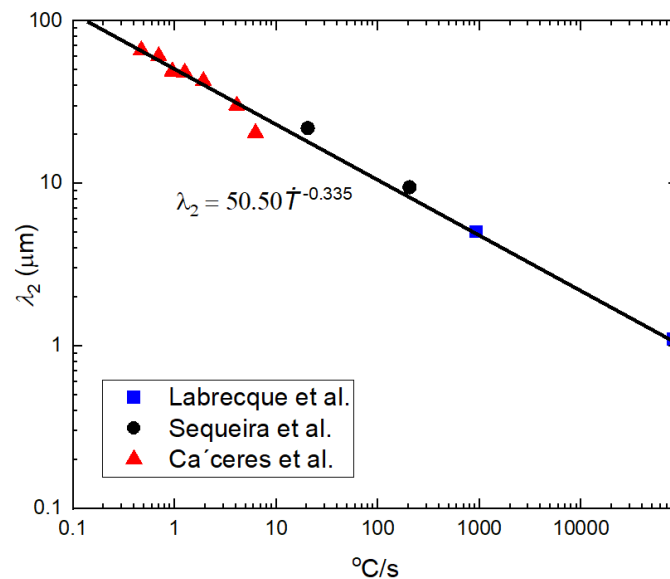


Figure 6.7 λ_2 as a function of the cooling rate for alloy AZ91D from data present in the literature [185–187]. Solid line is the fitted equation (6.1)

The cooling rate also affects the morphology of β - $Mg_{17}Al$ phase. Figure 6.8 shows the SEM micrographs of samples extracted from the top and bottom of wedge mould casting, indicating the effect of variation of cooling rate in wedge mould on the refinement of β - $Mg_{17}Al$ phase.

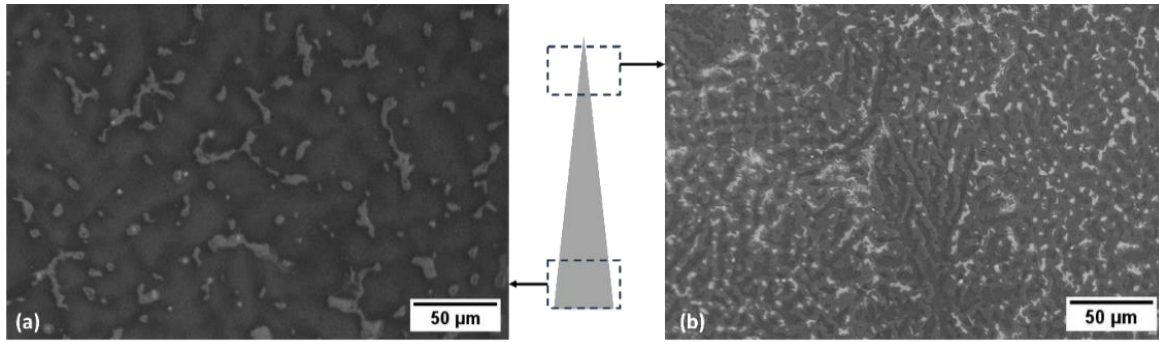


Figure 6.8. SEM micrographs of as cast AZ91D wedge mould casting at top and bottom ends

The size of the secondary phase particles increases significantly from top to bottom. As the dendrites become finer, the interdendritic region becomes smaller and β -Mg₁₇Al phase in the eutectic pool becomes smaller. Although the size of the particles are much smaller at the tip, their number is much greater in comparison to the bottom. The spacing between eutectic β -Mg₁₇Al₁₂ phase particles also increases with the decrease of cooling rate, which indicates the coarsening of secondary dendrite arm spacing. These observations are in agreement with observations made by Khan et al.[188] and Azqadan et al.[189], wherein AZ91D alloys were solidified in a Cu based V shapes wedge mould for variable cooling rates resulting in refined dendrites and decrease in the size of eutectic β -Mg₁₇Al₁₂ phase particles.

6.2.2 SDAS and p' correlation in AZ91D alloy

As discussed in chapter 4 and 5, the correlation between p' and λ_2 in Al alloys hold a nonlinear relationship over a wide range of cooling rates and highlights the need for considering the novel perimeter associated parameter which captures the change in dendritic morphology with changing solute content and cooling rates. To obtain the relationship between p' and λ_2 in Mg alloys, λ_2 was measured at 6 different locations to obtain an average value at a given position in wedge mould casting. In AZ91D alloy, the nonlinearity between p' and λ_2 persists over a

wide range of cooling rates. Figure 6.9 shows the experimentally measured data from wedge mould casting and samples solidified at ambient temperature and inside a switch off furnace. The nonlinear variation of p' with changing SDAS emphasizes the importance of considering the morphology of a grain to predict the strength of an alloy.

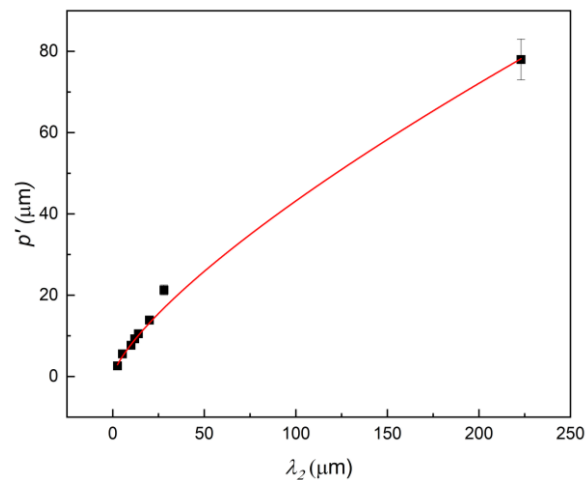


Figure 6.9. Relation between experimental p' and λ_2 showing the nonlinearity in AZ91D alloy. Solid line is guide to the eye.

6.3 Mechanical properties evaluation

Due to relatively smaller average grain diameter of grains in samples solidified in wedge mould casting as compared to Al-Si and Al-Ce binary alloys studied in previous chapters, Vickers hardness tests was chosen instead of Brinell hardness tests, as a strength indicator. To quantify the effect of grain size and dendritic morphology, Vickers hardness tests were conducted at different locations on the wedge mould casting. Figure 6.10 shows the location and corresponding values of hardness measurements taken on the cross section of wedge mould casting. 7 indents were taken in each location and average value is reported. The effect of change in grain size due to the variation of cooling rates is evident in the microstructures presented in Figure 6.10 which is reflected in the hardness response of the material, as the

minimum hardness value of 66 *HVN* was measured in the top most section with average grain size of 319 μm , which increases significantly to 80 *HVN* as the grain size decreases to 136 μm in the lowermost section of the wedge. This effect can be largely attributed to the combined effect of grain boundary strengthening and load bearing effect by second phase particles. As discussed earlier, the tendency of grain boundaries to act as an obstacle to dislocation motion results in the enhanced strength and coarsening of grains reduces the grain boundary density resulting in reduced hardness.

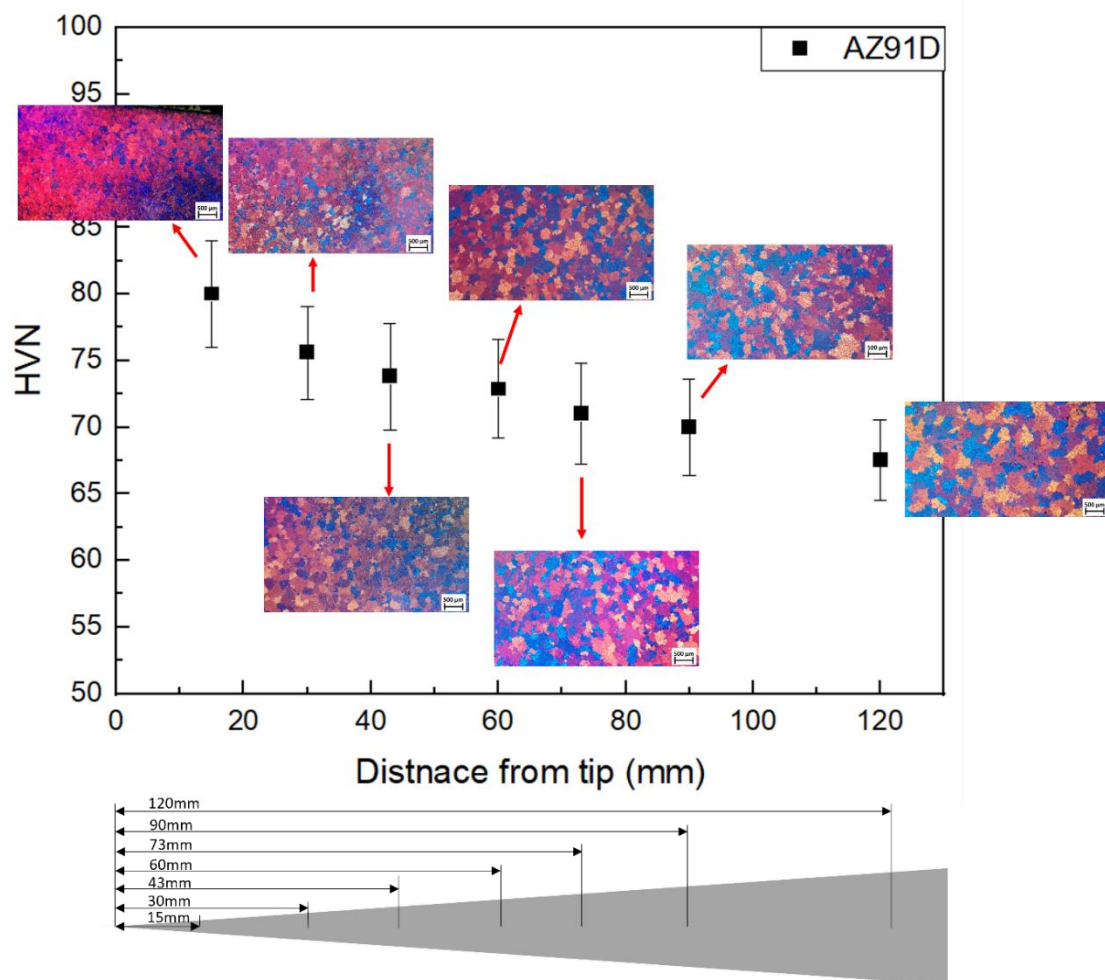


Figure 6.10 Graph showing the variation of hardness at different locations represented by the distance from the tip of the wedge mould casting and corresponding microstructures of the cross section at which the hardness measurements were taken

Figure 6.11 shows the relationship between the measured HVN and average grain diameter of grains in the shown microstructures in Figure 6.10. The HP type relationship between HVN and d can be represented as

$$HVN = HVN_{o,d} + k_d/\sqrt{d} \quad (6.2)$$

where, $HVN_{o,d}$ is intercept and k_d is the slope of HP type relationship. The Eq. (6.2) shows a satisfactory fit to the measured data with coefficient of regression value of 0.95. Noticeably, the slope of equation, i.e. k_d shows a considerably higher ($283 \text{ MPa}\mu\text{m}^{1/2}$) value than Al alloys, signifying a higher rate of hardening when compared with Al alloys. These observations are in agreement with previously reported values.

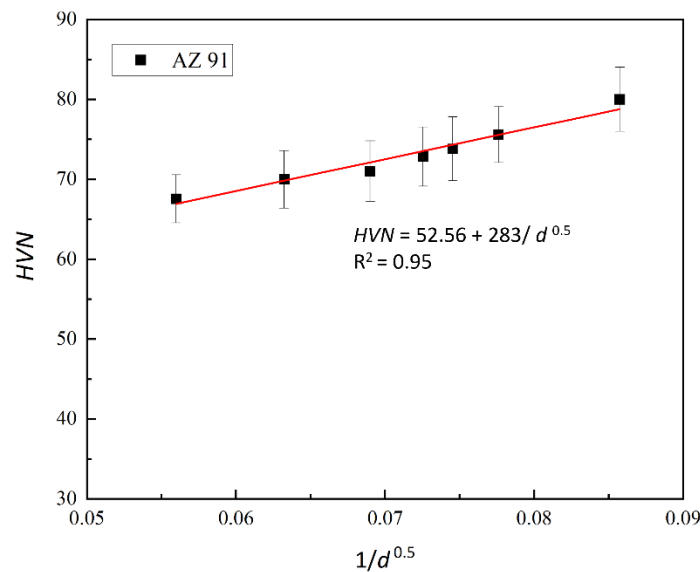


Figure 6.11 Relationship between the HVN and average grain diameter (d). The solid line is the fit to HP type relationship. The hardness values were measured at different locations in the wedge mould casting and corresponding grain size at the same location was measured.

Figure 6.12 shows the variation of *HVN* with changing SDAS and p' . The experimental data has been fitted with HP type relationships that can be given by

$$HVN = HVN_{o,\lambda_2} + k' / \sqrt{\lambda_2} \quad (6.3)$$

$$HVN = HVN_{o,p'} + k'' / \sqrt{p'} \quad (6.4)$$

where, HVN_{o,λ_2} and $HVN_{o,p'}$ are the intercepts on the y axis and k' and k'' are the HP constants.

Two distinct observations can be made by these graphs. Firstly, the change in HP constant when SDAS and p' are considered in HP type relationship is considerable. When a HP type equation (given in Eqn. 6.2) is fitted between the experimentally measured hardness and average grain diameter (d), the k_d value was $283 \text{ MPa}\mu\text{m}^{1/2}$, however in Eqn. (6.3) and (6.4), the k' and k'' values are much lower, i.e. $34.2 \text{ MPa}\mu\text{m}^{1/2}$ and $31.5 \text{ MPa}\mu\text{m}^{1/2}$ respectively.

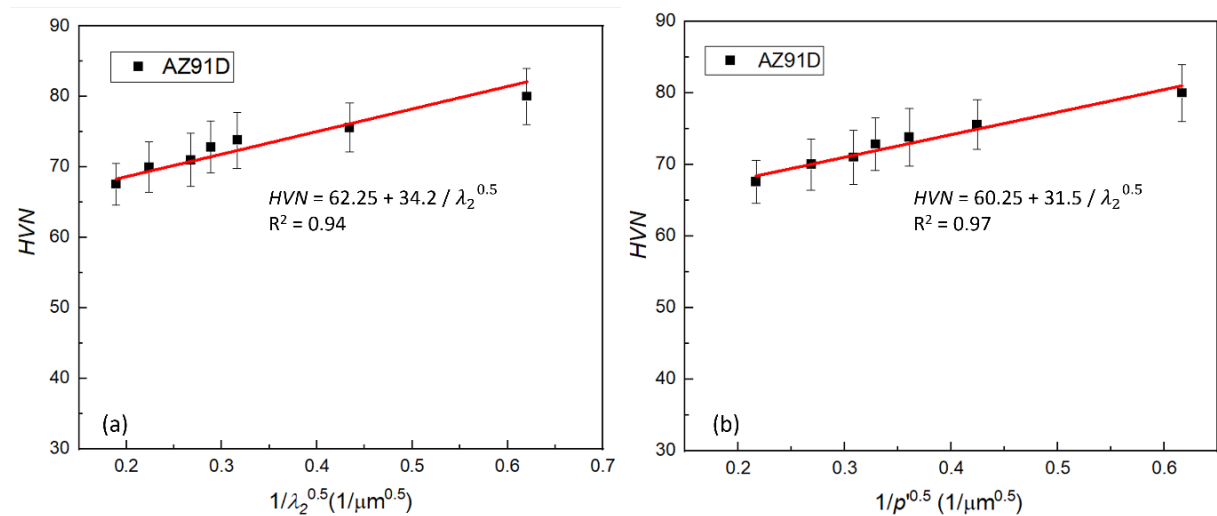


Figure 6.12 Relationship between the *HVN* and (a) λ_2 (b) p' . The solid lines are the fit to HP type relationship, given by $HVN = HVN_{o,\lambda_2} + k' / \lambda_2^{0.5}$, and $HVN = HVN_{o,p'} + k'' / p'^{0.5}$

Secondly, the improvement in coefficient of regression value when p' is considered can be observed in Figure 6.12(b), showing the importance of considering p' as an effective parameter to demonstrate the dendritic complexity in Mg alloys. Similar observations can be made in Mg-

Al binary alloy, where generic HP relationship shows a better fitting to the experimental data with a coefficient of regression value of 0.98. From Figure 6.13, it can be observed that increasing Al content in Mg influences the HP constant, as HP constant increases from 304 to 478 MPa $\mu\text{m}^{1/2}$ in conventional HP relationship and from 131.56 to 185.75 MPa $\mu\text{m}^{1/2}$ in the case of generic HP relationship when Al concentration changes from 5 to 9 wt.%.

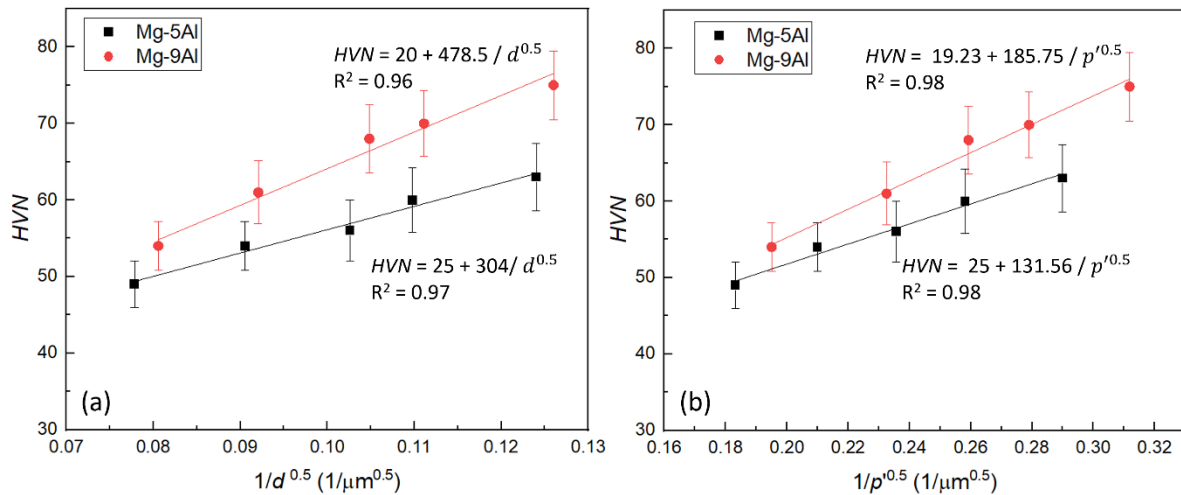


Figure 6.13 Relationship between the HVN and (a) d (b) p' . The solid lines are the fit to HP type relationship, given by $HVN = HVN_{o,d} + k' / \lambda_2^{0.5}$, and $HVN = HVN_{o,p'} + k'' / p'^{0.5}$

6.3.1 Microstructural features and yield strength correlation

To further demonstrate the applicability of p' in relating YS and dendritic complexity by HP model, tensile tests were conducted on the specimens extracted from the wedge mould casting. The tensile tests on extracted specimens were conducted in two conditions. First set of tensile experiment was conducted on as cast specimen and second set of experiment was conducted on solution treated specimen.

In as cast eutectic alloy, the major sources of strengthening are (a) grain boundary strengthening (b) solution strengthening and (c) precipitate strengthening. In Mg-Al alloys, the strength contributors are α Mg dendrites, β - $\text{Mg}_{17}\text{Al}_{12}$ and AlMn particles. The strength

contribution from α Mg is solely dependent on the solute concentration and grain boundary structure. Whereas, the strength contribution from secondary particles is dependent on the volume fraction and morphology of the particles. Although the distribution of β -Mg₁₇Al₁₂ is uniform throughout the specimen, the brittle nature of this phase has been reported to be detrimental for the mechanical properties for AZ series alloys. In a study by Sarvesh et al. [190], the individual mechanical properties of β -Mg₁₇Al₁₂ and Al₈Mn₅ particles were assessed using nanoindentation test technique. X-ray microtomography was used to characterize the 3D structure of these particles. The elastic modulus of Mg₁₇Al₁₂, Al₈Mn₅, and the matrix were determined to be 67.5 ± 6.8 , 146.8 ± 8.2 , and 46.1 ± 3.6 GPa, respectively. Similarly, the hardness values for Mg₁₇Al₁₂, Al₈Mn₅, and the matrix were measured at 3.8 ± 0.6 , 9.4 ± 0.4 , and 1.2 ± 0.2 GPa, respectively. The 3D characterization of each phase, combined with fractography analysis, indicated that the alloy damage initiates with plastic deformation in the matrix, particularly near the β -Mg₁₇Al₁₂ particles and at locations of stress concentration. This is subsequently followed by the fracture of these particles, confirming the brittle property of β -Mg₁₇Al₁₂ phase. Brittle behaviour of β -Mg₁₇Al₁₂ has also been proven theoretically by Wang et al. [191] using density functional theory (DFT) calculations. G/K ratio also known as Pugh's ratio where G is shear modulus and K is the bulk modulus of a material is generally used to measure the nature of a materials failure, a high value indicates a brittle failure and a lower value implies ductile failure[192]. Pugh's ratio of β -Mg₁₇Al₁₂ was theoretically calculated to be 0.52, indicating a brittle behaviour of β -Mg₁₇Al₁₂ phase. α -Mg grains in alloys in as cast condition are observed to be surrounded by coarse β -Mg₁₇Al₁₂ phase leading to the limited ductility during deformation. Whereas, a structure of fine, homogenous lamellar α Mg + β -Mg₁₇Al₁₂ distributing in α -Mg matrix improves the formability of magnesium alloys significantly. To eliminate the effect morphology of Mg₁₇Al₁₂ phase, from the overall

strengthening of the alloy and to make the matrix homogenous, the tensile specimen was solution treated at 420°C for 12 hours.

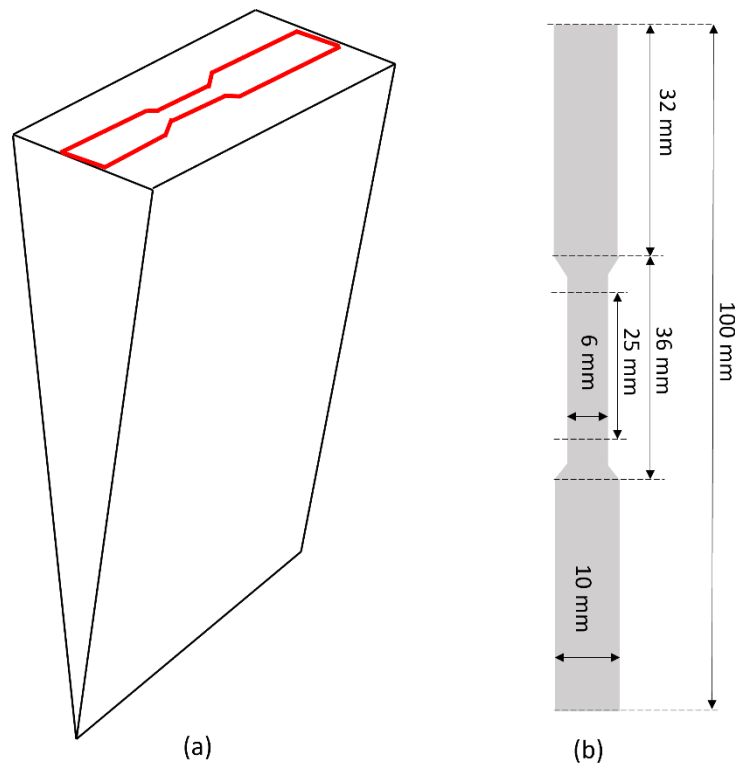


Figure 6.14 Illustration of wedge mould casting, showing (a) the area of extraction of tensile specimen (b) dimensions of the ASTM E8 subsized samples.

The wedge mould was divided into 8 sections, equidistant from the tip of wedge, and tensile samples were extracted along the length of wedge. Figure 6.14 shows the illustration of the region of specimen extraction from wedge mould casting and dimensions of ASTM E8 subsized samples tested in this study. Figure 6.15 shows the sections chosen for tensile bars extraction and corresponding polarised microstructures of the tensile bars in as cast and solution treated conditions.

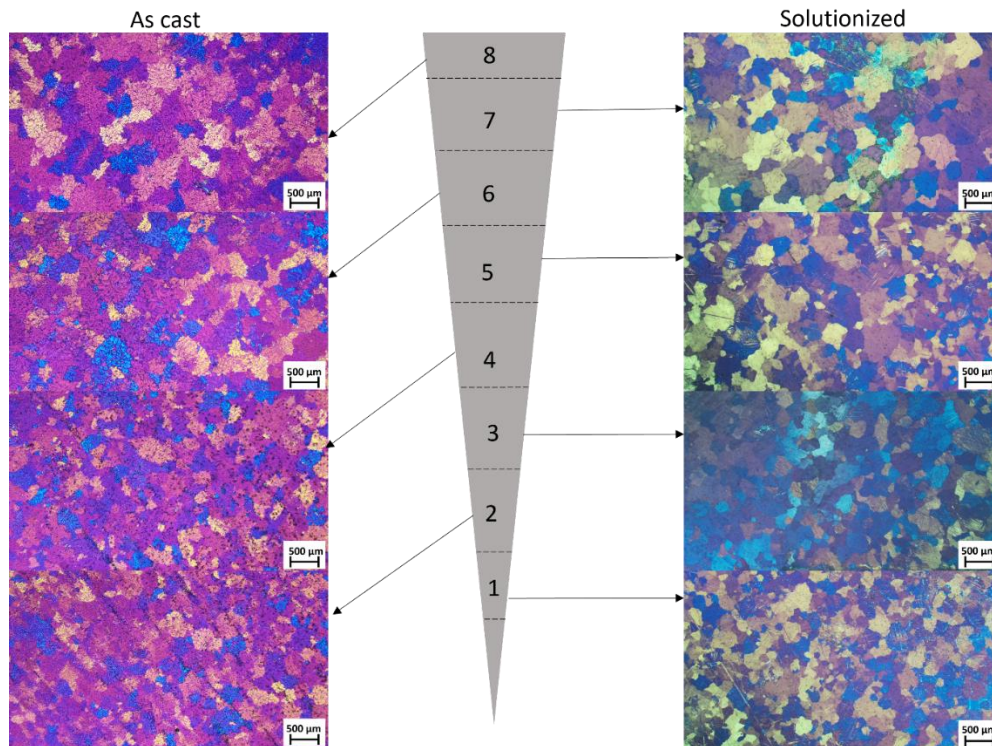


Figure 6.15 Illustration of the wedge mould casting showing the sections of tensile bar extraction. The polarised micrographs shows the corresponding microstructures of the tensile specimen in as cast and solution treated conditions.

Figure 6.15 shows the variation of grain size as a function of position on the wedge. The variation of grain size in Figure 6.15 is consistent with micrographs presented in Figure 6.1. The effect of changing cooling rate on the grain size is clear from the graph as grain size decreases as the cooling rate decreases at different positions in the wedge. The effect of solution heat treatment on β -Mg₁₇Al₁₂ phase resulted in dissolution of these precipitates into the matrix as these phases are known to be unstable at high temperatures[181,193,194].

Figure 6.16 shows the SEM micrographs of solution treated specimen. It is clear that the solution treatment at 420° C for 12 h resulted in almost complete dissolution of β -Mg₁₇Al₁₂ phase. Similar results were reported at different temperatures ranging from 380 -410°C in complete elimination of β -Mg₁₇Al₁₂ particles [194,195]. The solution treatment also removed

the dendritic microstructure, resulting in equiaxed globular grains with Zn and Al in solid solution which is confirmed by the EDS point mapping. However, the AlMn particles are still noticeable in the matrix. The melting point of these particles is reported to be 1048°C making them immune to solution treatment[196,197].

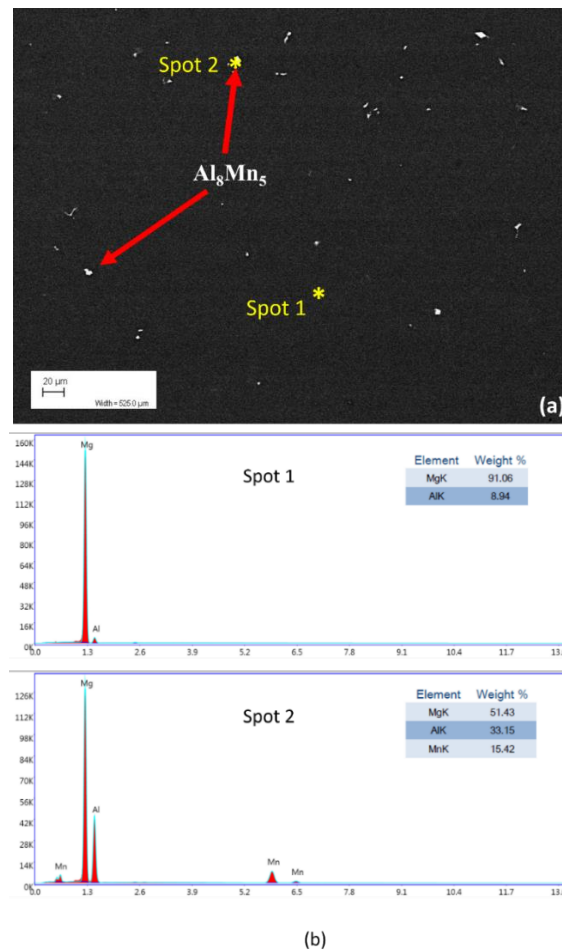


Figure 6.16 SEM microstructure of AZ91D alloy in (a) solution treated condition (b) EDS peaks and corresponding elemental point analysis of undissolved secondary phase and matrix, highlighted by red arrows.

No change in the average grain diameter of the grains after solution treatment was noticed which can be seen in Figure 6.17.

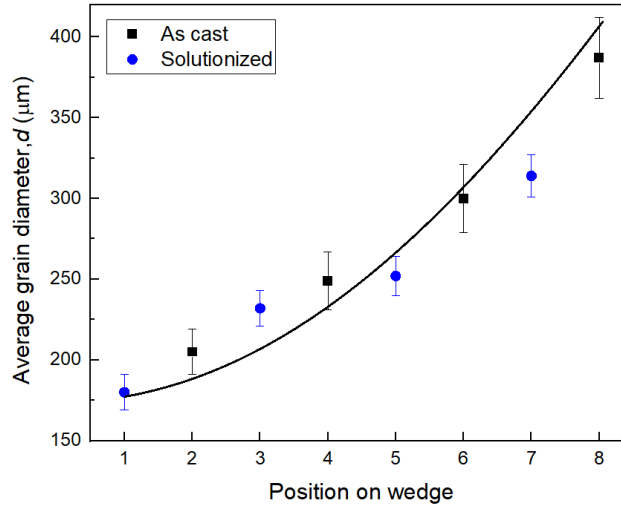


Figure 6.17 The grain sizes as a function of the position in the wedge cast sample of AZ91D alloy in as cast and solution treated conditions. The solid line is guide to eye.

Figure 6.18 shows the hardness variation of as cast and solution treated specimen as a function of position in the wedge. A decrease in the hardness noticed when the specimen were solution treated, with highest *HVN* for solution treated samples being 76 and lowest being 62. Whereas, in as cast specimen, the highest measured hardness value was 80 and lowest being 66. This decrease in hardness in AZ alloys after solution treatment is reported in several studies [196–198]. The hardness of a material is dependent on several factors, namely the strength of second phases, volume fraction of second phases, grain boundary structure etc. In cast alloys in present study, a certain casting stress due to solidification process is expected to be present, which would have been released during the heating process, resulting in reduced hardness. Simultaneously, at certain temperature, the eutectic structure in alloy would decompose and the solute atoms would migrate to the matrix resulting in supersaturated Mg grains, causing lattice distortion and improving the hindrance to dislocation movement resulting in solid solution strengthening of alloy and increasing the hardness. The third factor contributing to the hardness response of an alloy is the characteristics of second phases. In Mg-Al-Zn alloys, the

volume fraction and morphology of $Mg_{17}Al_{12}$ phase dictates the overall hardening behaviour of alloy, as hardness of $Mg_{17}Al_{12}$ phase is reported to be higher [195] than the matrix and dissolution of $Mg_{17}Al_{12}$ has a detrimental effect on the hardness of alloy and solution treatment do not result in increased hardness. Overall, in present study, the reduction in hardness can be attributed to the dissolution of hard $Mg_{17}Al_{12}$ phase.

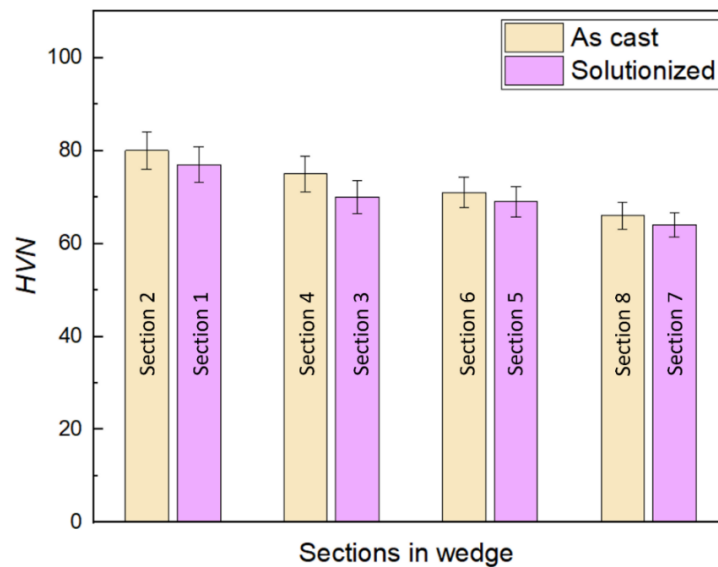


Figure 6.18 Measured hardness values of tensile specimen in as cast and solution treated conditions.

6.3.2 Yield strength- grain size and morphology correlation in as cast condition

The yield strength obtained from tensile tests are plotted with average grain diameter in as cast condition in Figure 6.19. The experimental data has been fitted with the HP relationship $\sigma = \sigma_0 + k d^{-0.5}$, where, σ is the measured yield strength of the alloy, σ_0 is the friction stress required to start a dislocation, d is the average grain diameter and k is the intercept on y axis also known as HP constant.

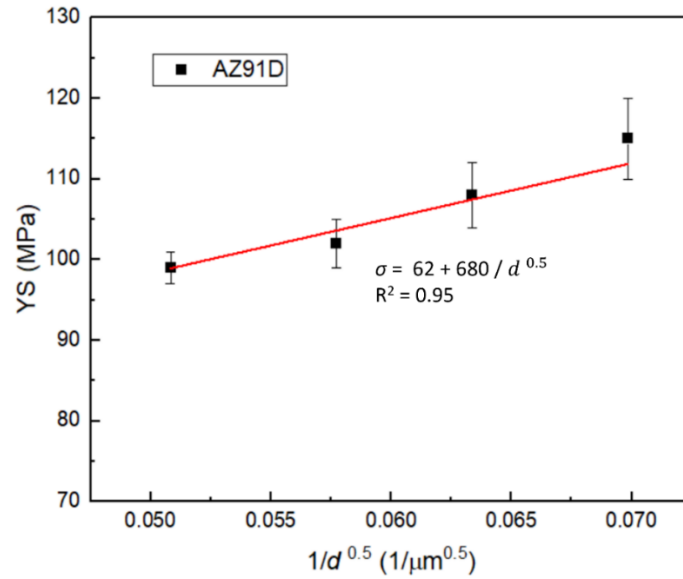


Figure 6.19 Relation between YS and average grain diameter of AZ91D alloy in as cast condition. The experimental data has been fitted with the conventional HP relation of the form $\sigma = \sigma_0 + k d^{-0.5}$.

The measured value of HP slope in Figure 6.19 is $680\text{MPa}\mu\text{m}^{1/2}$ and friction stress was measured to be 62MPa. The measured value of coefficient of regression is 0.95, showing a satisfactory fit of experimental data in the conventional HP relationship. Similarly, the variation of YS as a function of SDAS has been plotted in Figure 6.20. The data has been fitted with the HP type relationship of form

$$\sigma = \sigma_{0,\lambda} + k^* \lambda_2^{-0.5} \quad (6.5)$$

where λ_2 is the corresponding SDAS of the dendrites and k^* is the HP constant. The value of friction stress shows a similar value of 67MPa. The HP constant decreases to $206.35\text{MPa}\mu\text{m}^{1/2}$ and coefficient of regression value is measured to be 0.95 showing a satisfactory fit of data in HP relationship.

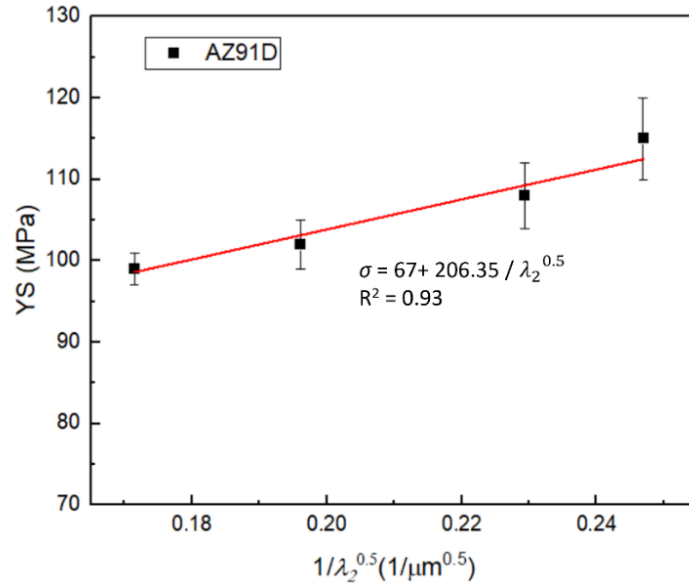


Figure 6.20 Relationship between YS and SDAS in AZ91D alloy in as cast condition. Solid line the HP relationship fitted to the experimental data.

Figure 6.21 shows the relationship between YS and p' . The experimental data has been fitted to the equation

$$\sigma = \sigma_{o,p} + k_p p'^{-0.5} \quad (6.6)$$

where $\sigma_{o,p}$ is the intercept on the y axis and k is the slope. No significant change in the value of intercept is noticed, however the value of slope has been observed to reduce significantly from $680 \text{ MPa}\mu\text{m}^{1/2}$ in Eqn.(6.5) to $178 \text{ MPa}\mu\text{m}^{1/2}$ in Eqn.(6.6). This change in slope (k value) when p' is considered in HP relationship, was observed in Al-Si alloys as well. Since Mg alloys exhibits a higher value HP constant than Al alloys, this change is considerable in AZ91 alloy [199]. However, an improvement in the coefficient of regression value is noticeable, highlighting the importance of considering p' to capture the grain morphology to predict the YS of a material.

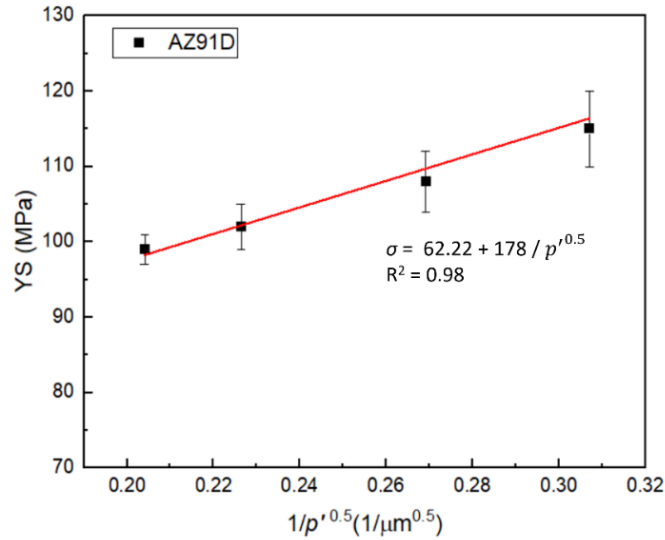


Figure 6.21 Relationship between YS and p' in AZ91D alloy in as cast condition. Solid line the HP relationship fitted to the experimental data.

6.3.3 Yield strength- grain size and morphology correlation in as solution treated material

The relationship between YS and average grain diameter (d) and p' of solution treated AZ91D samples is shown in Figure 6.22. The experimental data has been fitted with HP relationships $\sigma = \sigma_0 + k d^{-0.5}$ and $\sigma = \sigma_0 + k_p p'^{-0.5}$ where k and k_p are the HP constants. Two distinct features are noticeable in these graphs, firstly the decrease in slope in second scenario when p' is considered is significant and aligns with the observations made in as cast Al-Si and AZ91D alloys. Secondly, the improvement in the coefficient of regression values from 0.94 to 0.99 shows an excellent fit of experimental data when p' is considered in HP type relationship is consistent with previous observations in as cast Al-Si and Al-Ce alloys.

While the grain morphology in solution-treated samples may not be as intricate as that observed in high-solute-content Al-Si, Al-Ce, and as-cast AZ91D alloys, the application of the generic HP-type relation to experimental data, covering a spectrum of grain morphologies from faceted

to highly dendritic structures, demonstrates the versatility of this equation in accurately depicting the influence of grain morphology on the yield strength (YS) of a material.

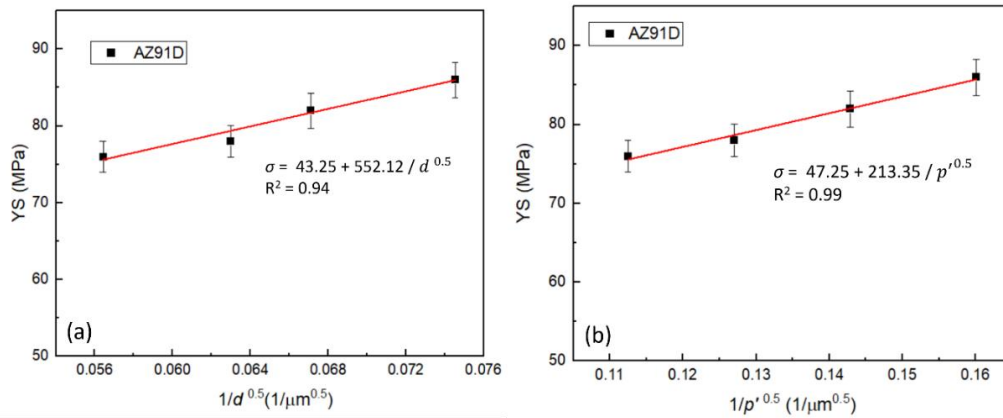


Figure 6.22 Relationship between the YS and (a) d (b) p' . The solid lines are the fit to HP type relationship, given by $\sigma = \sigma_0 + k d^{-0.5}$, and $\sigma = \sigma_0 + k_p p'^{-0.5}$.

6.4 Conclusion

Expanding the application of generic HP relationship, Mg alloys are studied in this chapter. Several morphologies of commercial AZ91 and Mg-Al binary alloys were produced by solidifying alloys at variable cooling rates and controlling the solute content and subsequently tensile and hardness tests were conducted. Following conclusions can be made

- Nonlinear relationship between p' and SDAS persists in AZ91D alloy for samples solidified at various cooling rates.
- Generic HP relationship fits well in the experimentally measured data and considering p' in HP relationship yields better R^2 values for a wide range of grain morphologies.
- The value of HP constant changes drastically from $680\text{MPa}\mu\text{m}^{1/2}$ in conventional HP relationship ($\sigma = \sigma_0 + k d^{-0.5}$) to $178\text{MPa}\mu\text{m}^{1/2}$ ($\sigma = \sigma_0 + k_p p'^{-0.5}$) in generic HP relationship for AZ91 alloy in as cast condition. Similarly, in solution treated condition, HP constant was noticed to change from $552\text{MPa}\mu\text{m}^{1/2}$ to $213\text{MPa}\mu\text{m}^{1/2}$.

7 Development of high thermally stable Al-Ce alloys

7.1 Introduction

As discussed in chapter 2, low solubility of Ce in Al results in dendritic structure of grains and formation of $\text{Al}_{11}\text{Ce}_3$ intermetallic. The morphology of $\text{Al}_{11}\text{Ce}_3$ phase constitutes of fine lamellae in hypoeutectic composition and a combination of lamellar eutectic and plate like primary intermetallic in hypereutectic compositions, shown in Figure 7.1. $\text{Al}_{11}\text{Ce}_3$ has been proven to have a minimal contribution in the strength of Al-Ce based alloys. However, $\text{Al}_{11}\text{Ce}_3$ is known to show a high thermal stability, due to low diffusion of Ce in Al ($\sim 5 \times 10^{-19} \text{ m}^2/\text{s}$ at 400°C) [200]. The lamellar structure of $\text{Al}_{11}\text{Ce}_3$ has been reported to show excellent coarsening resistance at high temperatures, which results in negligible degradation of mechanical properties of Al-Ce alloys at high temperatures [201]. For instance, no change in the Vickers microhardness and microstructure was observed in Al-12.5Ce alloy after isothermal aging at 322 and 400°C for 8 and 12 weeks respectively. However, due to lack of coherency between the Al matrix and $\text{Al}_{11}\text{Ce}_3$ particles, the strength of these alloys is often less than the other commercial Al alloys. The exceptional thermal stability of $\text{Al}_{11}\text{Ce}_3$ phase still remains the centre of interest for designing alloys with superior thermal stability. To elevate the properties of Al alloys, Sc and Zr offers a good potential to improve thermal stability and mechanical properties. For instance, Kipling[202] demonstrated that Al-0.06Sc achieved a microhardness of 429MPa after isochronal aging at 325°C for 3h, whereas, addition of 0.06Zr resulted in a peak hardness of 295MPa after aging at 500°C . This improvement was attributed

to the formation of nanoscale Al_3Zr and Al_3Sc precipitates, which strengthen the matrix. Similarly, Pan et al.[203]reported the effect of Sc and Zr addition on the mechanical properties of as-cast Al-Mg alloys. The tensile strength, yield strength and elongation of 315.6 MPa, 170.1 MPa and 21.1%, respectively were reported in Al-5Mg-0.2Sc-0.1Zr. Addition of Sc and Zr in Al-Ce binary alloys has also been reported to improve the strength. Wang et al. [121] reported the YS of Al-5Ce-0.2Sc-0.2Zr to be 156MPa after isothermal aging at 320°C for 2h.

In the course of investigating the grain morphology and strength correlation in Al-Ce binary alloys, the exceptional thermal stability of these alloys was observed. This discovery prompted further exploration of the Al-Ce binary system, particularly focusing on the $\text{Al}_{11}\text{Ce}_3$ intermetallic phase. Consequently, a series of Al-Ce based alloys were developed and studied with the goal of creating high-strength materials that retain their mechanical properties at both room and elevated temperatures. This approach broadens the scope of this thesis by examining an alloy system that holds potential for industrial applications, while also exploring the fundamental aspects of grain structures.

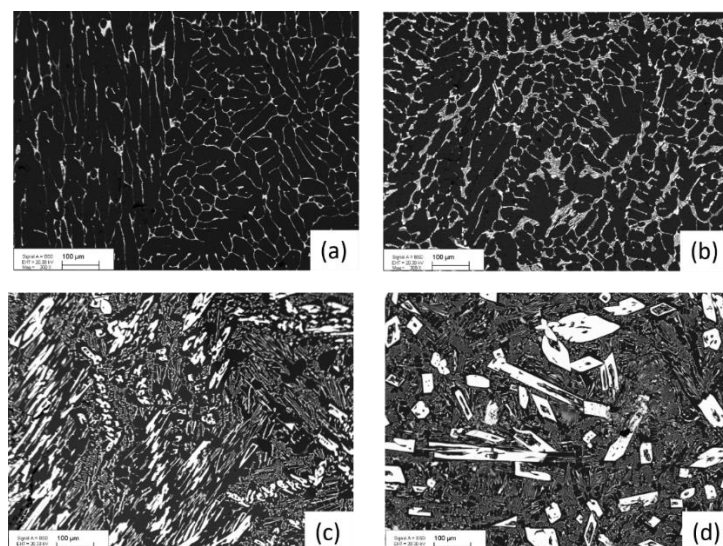


Figure 7.1 SEM micrographs of Al-Ce binary alloys (a) Al-2Ce (b) Al-5Ce (c) Al-20Ce (d) Al-30Ce.

7.2 Spheroidization of eutectic Si

The structural properties of Al-Si alloys is dictated by distribution and morphology of Si particles which act as strong second phase in Al matrix. However, the needle like morphology of eutectic Si can have detrimental effects on the alloy's ductility and toughness[204–206]. In as cast Al-Si alloy, altering the morphology of Si particles, also known as modification or spheroidization of eutectic Si from needle to ellipsoid-shaped particles has been reported to enhance the mechanical and conductive properties of material. Spheroidization involves refining the Si particles within the alloy, transforming them from a needle like lamellar morphology into a more spherical shape. By promoting the formation of rounded silicon particles, spheroidization minimizes stress concentrations and improves the distribution of Si in the matrix, resulting in improved mechanical properties such as increased ductility and fatigue resistance. The evolution of Si due to heat treatment has been reported to follow three steps[206–208]

- (a) Disintegration
- (b) Spheroidization
- (c) Growth of Si in matrix

The initial stages of disintegration and fragmentation occurs primarily at the junctions of the branches or the necks of Si particles. Subsequently, spheroidization takes place in the fragmented portions, leading to the creation of spherical particles [209,210]. Furthermore, growth of fragmented Si particles occur through mechanism analogous to Oswald ripening wherein, dissolution of small crystals and redeposition into the surface of larger particles occur, as large particles are energetically favoured. Modification of eutectic Si can be categorised in two categories (a) process based (b) composition based. Spheroidization of Si by either modifying the melts or heat treating the cast alloys has been a viable means of modifying

eutectic Si. Refinement of Si can be achieved by processes like semi solid processing, ultrasonic melt treatment, magnetic stirring of the melt etc[211–213]. For instance, Hernández et al. [211] reported the refinement of Si in Al-15.6Si alloy after applying electromagnetic stirring and vibration to the melt. Second common process to spheroidize the Si particles is by conducting heat treatment of the alloy. Since, the spheroidization is linked with the diffusivity of Si in Al, the temperature and time of heat treatment greatly affect the morphology of Si. For example, Wang et al.[205] reported the spheroidization of Al-12Si alloy at eutectic temperature for three hours. A shape factor was used to quantify the change in morphology of Si, which was measured to be 0.8 out of a maximum value of 1, indicating a high degree of spheroidization. Similarly, Li et al.[213] reported the spheroidization of Si after isothermal heat treatment of Al-7Si alloy at 520°C, over a range of duration from 30 min to 48 h. The change in morphology was quantified by a shape factor, which changed from ~ 0.67 in as cast condition to ~ 0.75 after heat treatment for 24h. In case of Al-Ce alloys, coarsening of $Al_{11}Ce_3$ is also reported by several researchers [214,215]. Zachary et al. [215] heat treated Al-12Ce, Al-12Ce-0.4Mg, and Al-12Ce-4Si-0.4Mg to standard T6 treatment at 537°C for 8h. Coarsening of eutectic $Al_{11}Ce_3$ was observed in all alloys. In a similar study by Czerwinski [214], Al-5, 10, 15 and 20 wt.% Ce alloys were heat treated at 500°C for 168h and mechanical properties were measured. Due to such long exposure at high temperatures, coarsening of $Al_{11}Ce_3$ was observed, which was reflected in reduced microhardness and compression strength of these alloys.

However, in the present study, relatively lower temperature range for heat treatment has been employed to make a direct comparison of coarsening of eutectic Si in Al-Si and $Al_{11}Ce_3$ in Al-Ce alloy respectively.

7.3 Thermal stability of eutectic Si and Al₁₁Ce₃ phases

Although spheroidization can have some positive effects on the mechanical properties of Al-Si alloys, the degree of coarsening of Si particles can also quantify the thermal stability of this phase. To make a comparison between the thermal stability of Al-Si and Al-Ce binary alloys, coarsening of Si in Al-5Si alloy and Al₁₁Ce₃ phase in Al-5Ce alloy has been studied by implementing isothermal and isochronal ageing experiments. For isothermal ageing experiments, alloys were heat treated at 400°C for 0.5, 1, 2, 6, 10, 24 and 72h and morphology of eutectic structures was assessed using image processing software. For isochronal ageing experiments, A-5Si alloy was heat treated for 1h at 380, 430, 480, 530 and 580°C, whereas, Al-5Ce alloy was heat treated for 370, 420, 470, 520, 570 and 640°C. To quantify the change in morphology of eutectic particles, a shape factor also known as circularity has been used. The circularity of a particle indicates the closeness of a shape to a perfect circle and is given by [216]

$$Circularity = \frac{1}{\eta} \sum \frac{P_{eu}^2}{4\pi A_{eu}} \quad (7.1)$$

where, η is the number of particles analysed, P_{eu} and A_{eu} are perimeter and area of a particle. The value of circularity will yield unity for a perfect circle and for shapes deviating from a circle, $Circularity < 1$.

Figure 7.2 shows the optical microstructures of Al-5Si and Al-5Ce alloys after isothermal aging at 400°C. The change in morphology of eutectic Si is evident after 72h of aging. It can be noticed that the spheroidization was initiated after 6h of aging (Figure 7.2(j)) and reached a maximum after 72h. This is also reflected in the circularity values. In as cast samples the value of circularity of needle shaped Si particles was measured to be 0.55, which increases to 0.8 when alloy was annealed for 10h indicating that the particles have spheroidized. On the other

hand, Al-5Ce showed minimal change in the morphology of $\text{Al}_{11}\text{Ce}_3$ as circularity changes from 0.65 in case of as cast sample to 0.66 when annealed for 24h. This lack of coarsening of $\text{Al}_{11}\text{Ce}_3$ indicates the superior thermal stability of Al-Ce alloys.

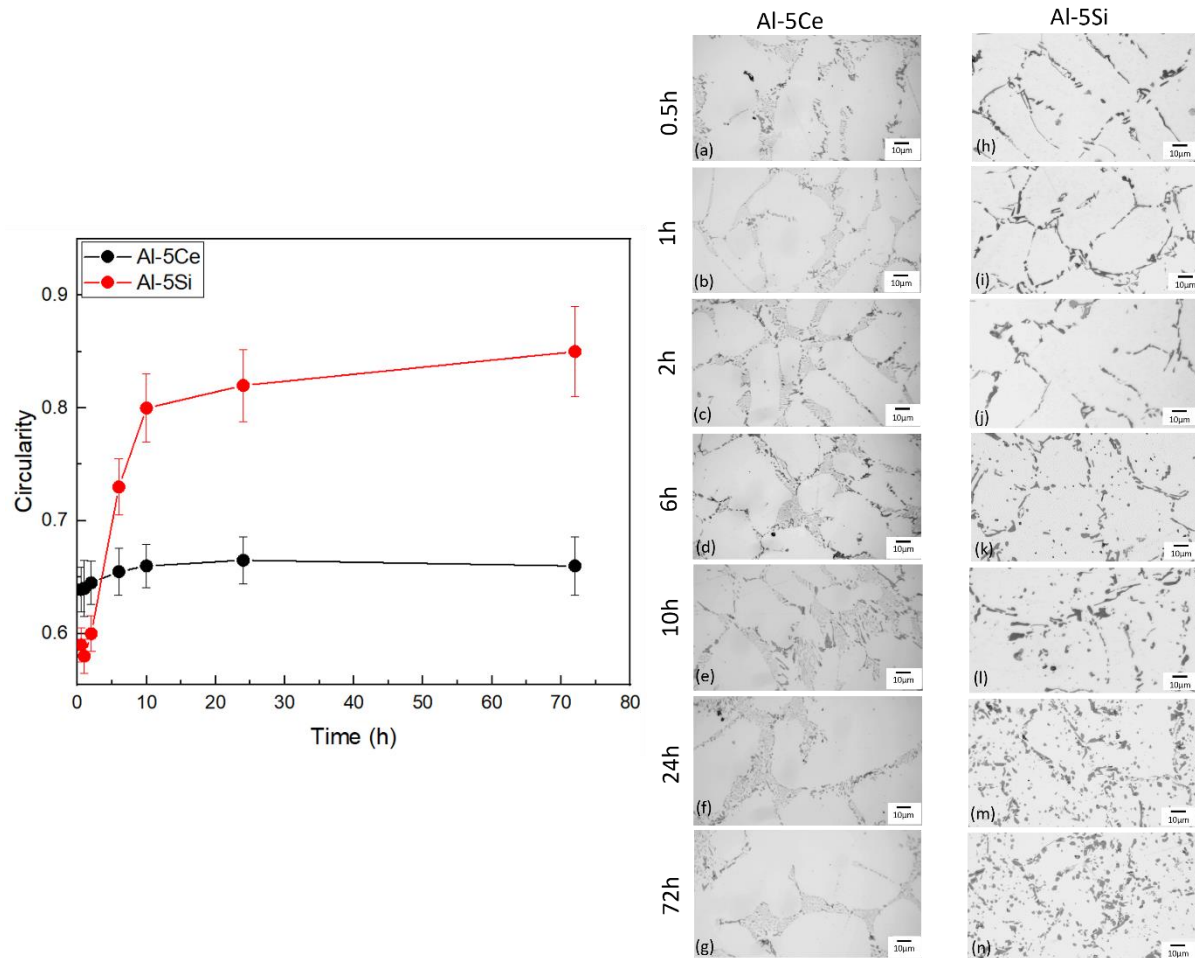


Figure 7.2 Plot showing the change in morphology of eutectic Si and $\text{Al}_{11}\text{Ce}_3$ particles during isothermal ageing experiments conducted at 400°C , aiming to initiate the spheroidization of eutectic particles over varying time durations. The circularity shape descriptor is employed to quantify the morphology of these particles, which indicates how close a shape is to a perfect circle.

As previously mentioned, the extent of spheroidization is directly correlated with the diffusion of silicon Si atoms within the Al matrix. Analysis of microstructures presented in Figures 7.2 suggests that the diffusion of Si atoms in the Al matrix intensifies at elevated annealing

temperatures. It can be inferred that as the annealing temperature rises, the optimal time required for spheroidization to initiate decreases.

Microtomography analysis of Al-Si alloys reveals that eutectic silicon in Al-Si alloys forms an interconnected network [209,210] often considered corals. Under high temperatures, these corals undergo disintegration, resulting in the formation of spherical particles. To calculate the disintegration time of Si particles, Ogris et al. [208] introduced a model for Al-Si binary alloys, following a model previously developed Stüwe and Kolednik [217]. In their study, Stüwe and Kolednik studied the disintegration of potassium-filled cylinders within tungsten, and calculated the disintegration time for the formation of spherical structures. Subsequently, this model was effectively applied to determine the spheroidization time of cementite plates within pearlite iron by Werner [218], giving

$$t_{max} = \frac{32\pi^2}{9} \times \frac{KT}{D_s \gamma} \times \left(\frac{\rho}{\varphi}\right)^4 \times \ln\left(\frac{\rho}{\varphi}\right) \quad (7.2)$$

where K is Boltzmann constant, φ is the covalent atomic diameter of Si atom, ρ is the Si particle radius and D_s is the diffusion coefficient given by,

The diffusion coefficient of Si atoms in Al matrix can be determined by Fick's first law

$$D_s = D_o \times \exp\left(-\frac{E_{A,inter} - E_{A,v}}{R_g T}\right) \quad (7.3)$$

where, $E_{A,inter}$ signifies the activation energy for interdiffusion of Si in Al, $E_{A,v}$ is the activation energy for vacancy formation, R_g is the gas constant and T is the temperature and D_o is a frequency factor. It can be seen that the increase in temperature will increase the diffusion process.

The values used for the calculation of disintegration time is taken from the literature and is given in table 7.1[207,219]

Table 7-1 numeral values used for the calculation of disintegration time of Si particles

$E_{A,inter}$	148.6 kJ mol ⁻¹
$E_{A,v}$	74.3 kJ mol ⁻¹
R	8.314 Jmol ⁻¹ K ⁻¹
γ	1Jm ⁻²
K	1.38×10^{-23} JK ⁻¹
φ	2.22×10^{-10} m
D_o	2.29×10^{-4} m ² s ⁻¹

Figure 7.3 shows the relationship between the experimentally measured radius of Si corals and disintegration time at 400°C. The solid line is the fitted model given in equations 7.1 and 7.2. The model fits well with the experimental data. It is clear from the graph that the disintegration of eutectic silicon particles at 400°C predominates during the initial hours of heat treatment, up to approximately 10 hours. Subsequently, the spheroidization of silicon coral branches becomes evident in Figure 7.1(m) and (n). Whereas Al-5Ce alloy shows little to no change in the morphology which is reflected in a circularity value.

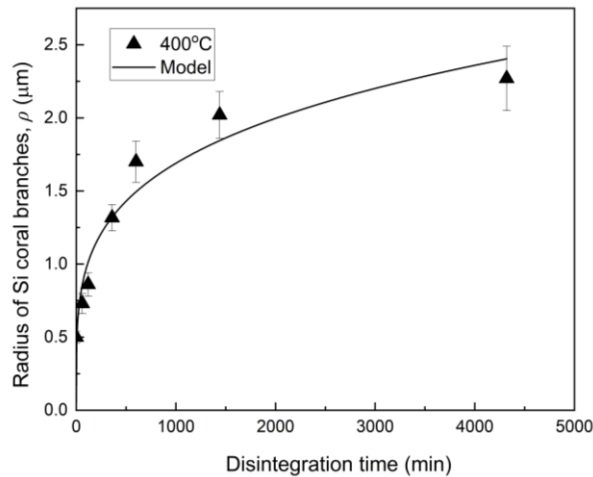


Figure 7.3 Relationship between experimentally measured radius of Si coral branches (ρ) and disintegration time at 400°C. Solid line is the fitted model given in Equations 8.1 and 8.2.

To evaluate the spheroidization behaviour of Si and $\text{Al}_{11}\text{Ce}_3$ particles with changing temperature, isochronal annealing experiments were conducted at temperatures ranging from 380 to 580°C for 1h in case of Al-5Si alloy. Whereas for Al-5Ce alloy, temperature range selected was from 370 to 640°C. Figure 7.4 shows the microstructures of Al-Si alloy heat treated at different temperatures for 1h. Similar to isothermal heat treatment, spheroidization of Si particles is observed in Al-5Si alloy with increasing temperature. The initiation of spheroidization can be seen when temperature was 430°C (Figure 7.4(b)). Furthermore, sample heated at 580°C shows completely spheroidized eutectic Si particles.

Figure 7.5 shows the SEM micrographs of Al-5Ce alloy subjected to heat treatment. It can be observed that the effect of heat on the morphology of $\text{Al}_{11}\text{Ce}_3$ was minimal. This observation is quantified by the circularity values of Si and $\text{Al}_{11}\text{Ce}_3$ particles, shown in Figure 7.6.

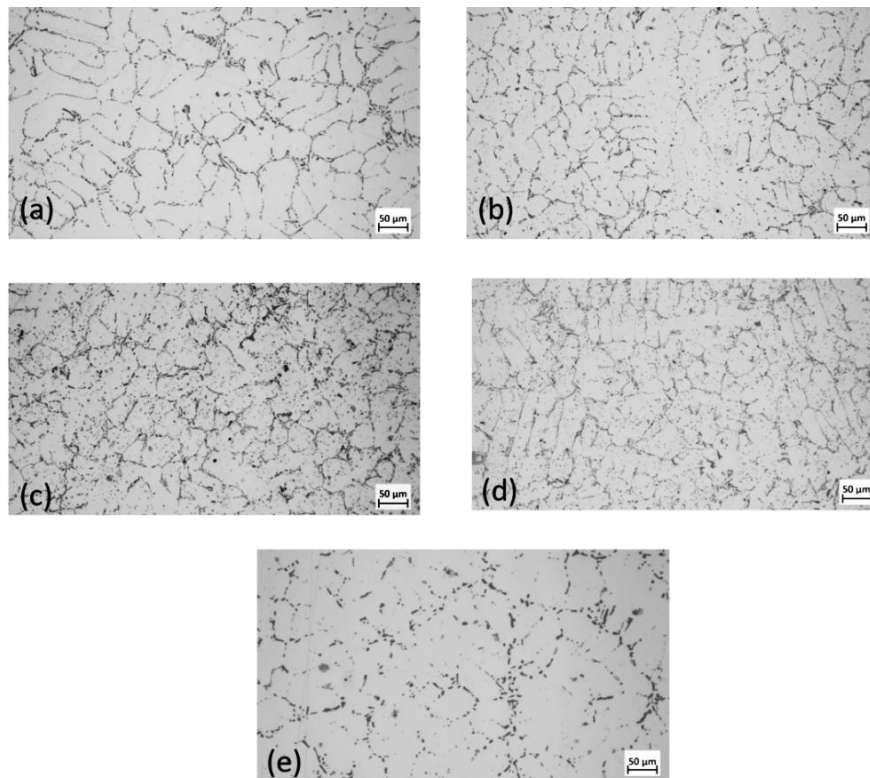


Figure 7.4 Optical micrographs of Al-5Si alloy after 1h heat treatment at (a) 380°C (b) 430°C (c) 480°C (d) 530°C (e) 580°C.

Figure 7.6 shows the circularity of eutectic particles as a function of annealing temperature. Circularity of Si particles increased significantly with the increasing annealing time. Circularity changed from 0.56 in samples heat treated at 380°C to 0.76 in samples heat treated at 420°C pointing out a significant change in the morphology of Si particles with changing annealing temperature. This observation aligns with the measurements made by Ibrahim et al. [204]. However, in Al-5Ce, circularity shows a minute change, from 0.62 to 0.66 with increasing annealing temperature.

It is clear from the spheroidization experiments that the thermal stability of $Al_{11}Ce_3$ particles is superior to eutectic Si particles and it is also reflected in the hardness of heat treated of Al-10Ce alloy (Figure 7.7).

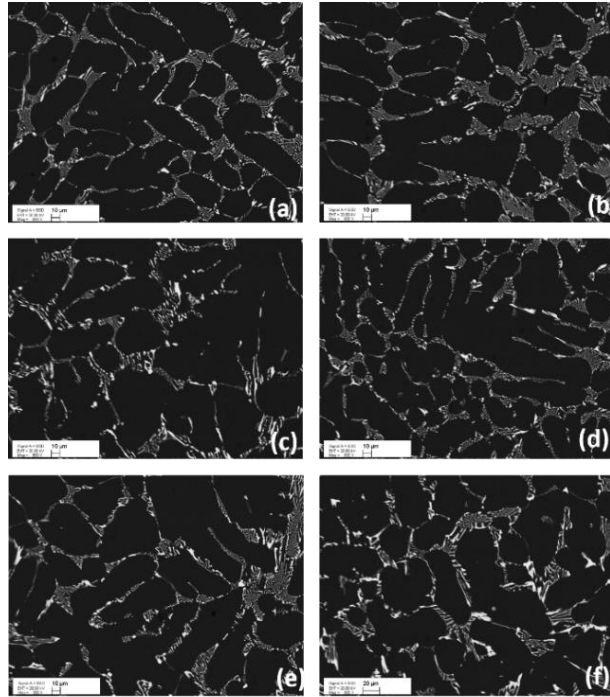


Figure 7.5 SEM micrographs of Al-5Ce alloy heat treated for 1h at (a) 370°C (b) 420 °C (c) 470°C (d) 520°C (e) 570°C (f) 640°C.

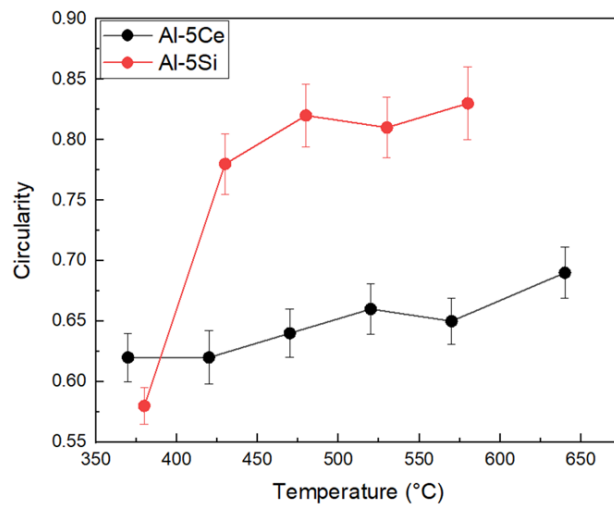


Figure 7.6 Plot showing the change in morphology, quantified by circularity of eutectic Si and Al₁₁Ce₃ particles during spheroidization experiments conducted at different temperatures with 1h holding time.

Owing to the coarsening resistance of $Al_{11}Ce_3$ phase in the Al-10Ce alloy, Al-10Ce binary alloy was chosen for the evaluation of hardness after heat treatment because Al-10Ce. Figure 7.7 shows the hardness of Al-10Ce binary alloy heat treated at $400^\circ C$ for up to 100h. To quantify the coarsening resistance of $Al_{11}Ce_3$ phase, aspect ratio (AR) of $Al_{11}Ce_3$ phase were measured by fitting equivalent ellipses, and is also presented. It is clear that superior thermal stability of $Al_{11}Ce_3$ phase results in minimal change in the hardness of the alloy and AR of eutectic phase.

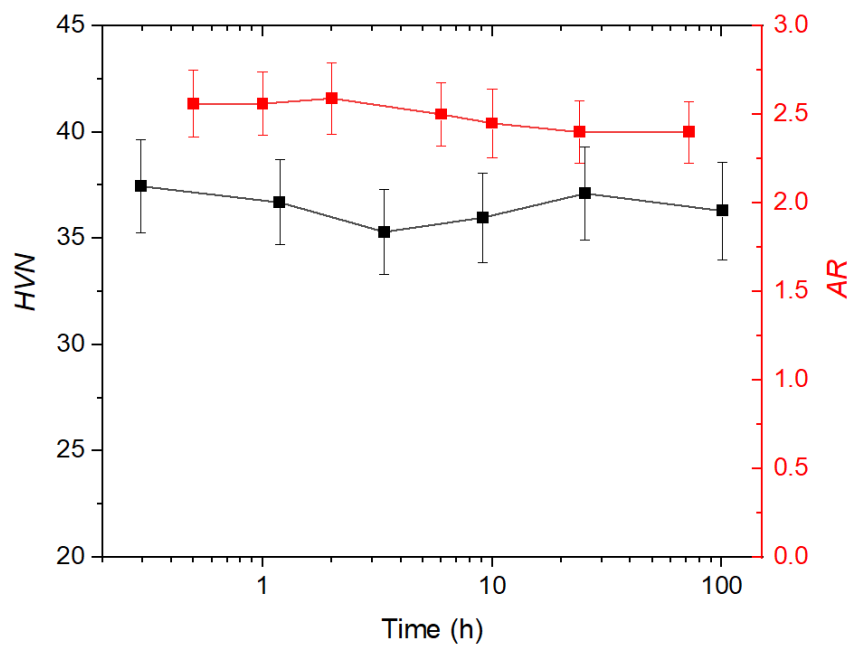


Figure 7.7 plot illustrates the hardness variation of an Al-10Ce alloy subjected to heat treatment for different durations at $400^\circ C$, showcasing minimal property degradation of Al-Ce alloys at elevated temperatures.

7.4 Thermal stability of Al-Ce binary alloys

To explore the high thermal stability of Al-Ce alloys, new alloys were produced and tested at room and elevated temperatures. Alloying elements like Sc, Zr, Si and Mg were used for alloying and die casting methods were used to fabricate the alloys. In total 6 alloys were fabricated with compositions given in table 7.2

Table 7-2 Nomenclature and composition of alloys

Nomenclature	Composition
Alloy 1	Al-10Ce
Alloy 2	Al-10Ce-0.2Zr
Alloy 3	Al-10Ce-0.2Zr-0.2Sc
Alloy 4	Al-10Ce-0.2Zr-0.4Sc
Alloy 5	Al-10Ce-0.6Si-1.2Mg
Alloy 6	Al-10Ce-0.6Si-1.2Mg-0.2Zr-0.2Sc

7.5 As cast microstructure of die cast alloys

Figure 7.8 shows the optical micrographs of all alloy compositions in as cast condition produced through gravity die casting method using a book mould to solidify the melt. Figure 7.8(a) shows the typical near eutectic microstructure of Al-Ce binary alloy with $Al_{11}Ce_3$ colonies. More than half of the area in microstructure had $Al_{11}Ce_3$ with a few dendrites of αAl . Similar microstructure can be seen in Al-10Ce-0.2Zr with dense $Al_{11}Ce_3$ pools and several αAl dendrites. The most recognizable feature in this sample is the morphology of dendrites which is refined and equiaxed in nature. Figure 7.8(c) shows the combined effect of 0.2Zr-0.2Sc, on the morphology of dendritic structure which is coarser as compared with other samples. For higher Sc addition, a much finer microstructure can be seen in Figure 7.8(d). The eutectic shows very fine morphology along with the fine αAl region. The refinement of αAl dendrites and $Al_{11}Ce_3$ lamellar due to Sc/Zr addition is widely reported in literature [220–223]. Figure 7.9 shows the back scattered electron (BSE) image of Alloy 2,3 and 4 highlighting the lamellar refinement of $Al_{11}Ce_3$ pools. Formation of $Al_3(Sc/Zr)$ particles is also observed in Alloy 4 (Figure 7.9(c)). $Al_3(Sc, Zr)$ particles serves as potent heterogenous nucleation sites for αAl grains, owing to the similar crystal structure of Al, resulting in refinement of αAl grains[224,225]. The presence of $Al_3(Sc, Zr)$ particles in the centre of αAl grains shown in Figure 7.9 (c) confirms the nucleation of grains on $Al_3(Sc, Zr)$ particles, ultimately refining the

grain structure. With the addition of Mg and Si, the morphology of eutectic changes (Figure 7.10(a)) and becomes coarser than rest of the samples. Two types of morphologies of the eutectic are observed in sample 5 and 6. First is the fine $\text{Al}_{11}\text{Ce}_3$ phase and second is the rod like eutectics protruding from the $\text{Al}_{11}\text{Ce}_3$ colonies, which were revealed by the Al_2CeSi_2 phase through EDS analysis, shown in Figure 7.10 (a). In Alloy 6, similar morphology of Al_2CeSi_2 phase was identified and with addition of Sc (0.2 wt.%) and Zr (0.2wt.%), a reduction in the grain size was also observed with average grain diameter of $\sim 25\mu\text{m}$. Although $\text{Al}_3\text{Sc,Zr}$ particles were not observed within the microstructure, few particles were identified within the eutectic (Figure 7.10(c)(f) and (g)), indicating the formation of few $\text{Al}_3\text{Sc,Zr}$ particles due to local segregation leading to the observed grain refinement. Similar observations were reported in a study by Mohammed et al.[226].

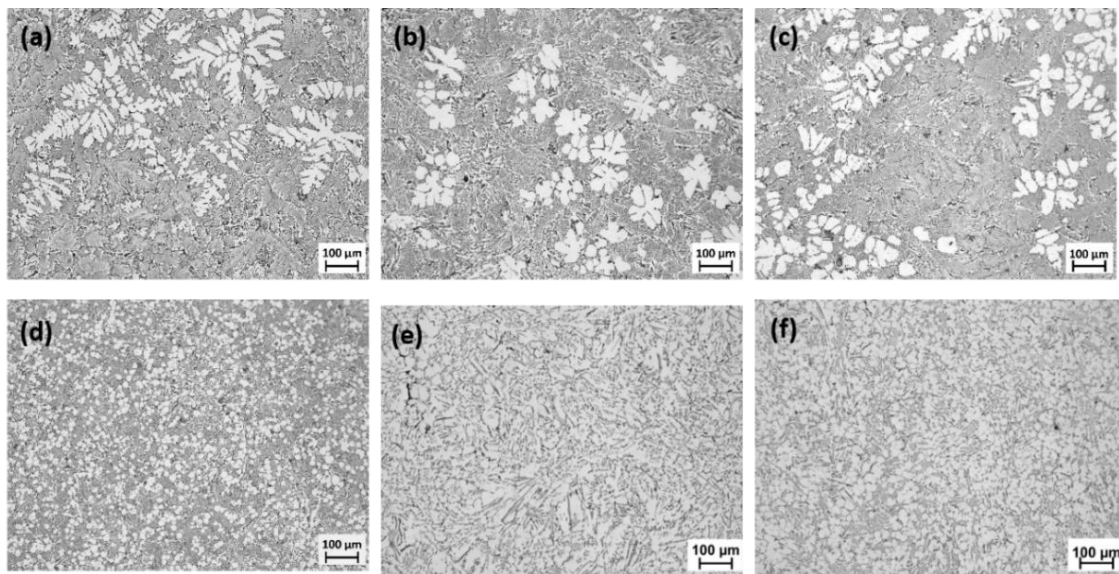


Figure 7.8 Microstructures of alloys in as cast condition (a) alloy 1 (b) alloy 2 (c) alloy 3 (d) alloy 4 (e) alloy 5 (f) alloy 6.

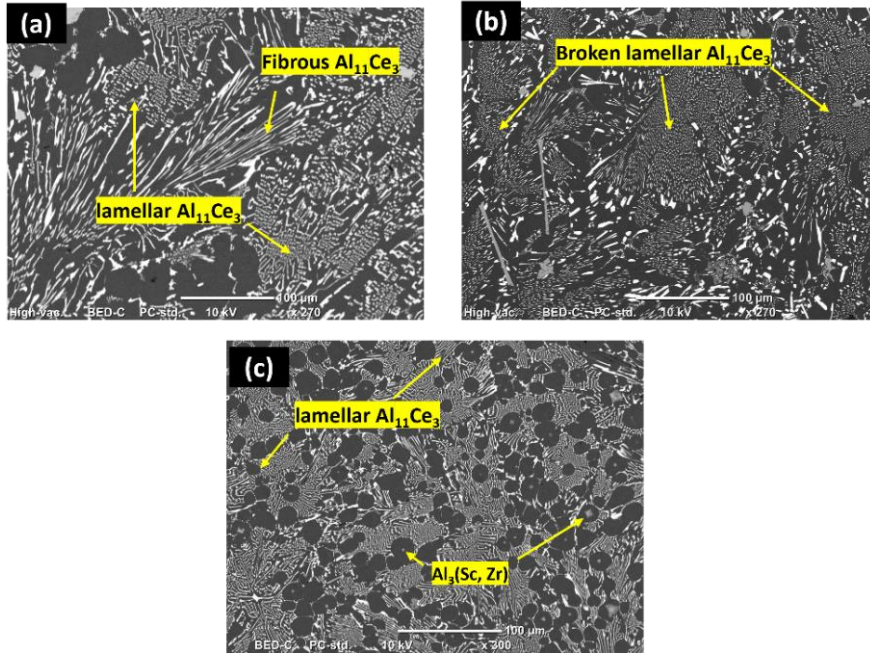


Figure 7.9 Structure of Al₁₁Ce₃ shown in SEM images of (a) Alloy 2 (b) Alloy 3; Al₃(Sc, Zr) precipitates in (c) Alloy 4.

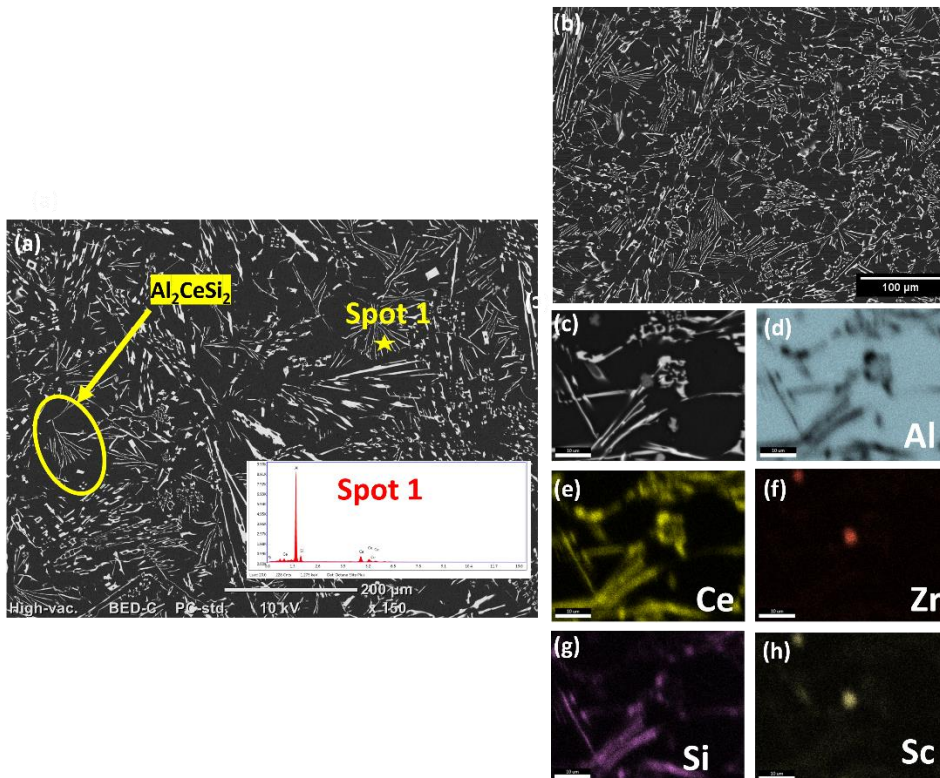


Figure 7.10 SEM micrograph of as cast (a) Alloy 5 with EDS point analysis of Al₂CeSi₂ phase; (b) BSE image of Alloy 6, (c) high magnification BSE image of Alloy 6; EDS element maps of (d) Al, (e) Ce, (f) Zr, (g) Si and (h) Sc.

7.6 Thermal stability of developed alloys

Hardness of as cast Alloys 1,2,3,4,5 and 6 is presented in Figure 7.11 and ageing response of Alloys 1,2,3 and 4 is shown in Figure 7.12. For Alloys 5 and 6, the heat treatment procedure was done on as cast and solution treated samples and is presented in Figure 7.13 and 7.14.

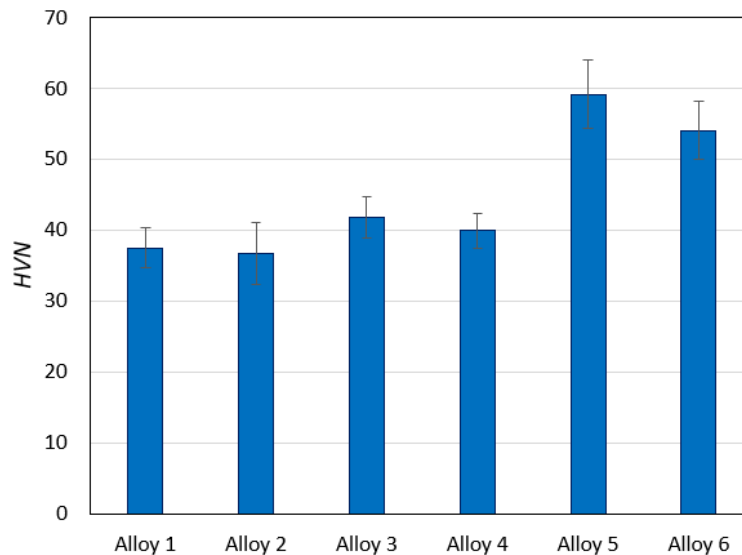


Figure 7.11 Hardness of alloys in as cast condition.

The hardness of alloys 1,2,3 and 4 do not show much effect of alloying elements in as cast condition. The hardness shows a little increment from 37 to ~ 40 with the addition of Sc but no change was observed by Zr addition.

After ageing, hardness of alloys 1,2,3 and 4 remains unchanged at lower temperature of 250°C after 1 and 3 hours of heat treatment, but at 350°C and 400°C, alloy 3 and 4 shows a sudden jump after 1 hour. After 1 hour of heat treatment at 300°C, the hardness of alloy 4 reaches 70HV and rises up to 90HV after 25 hours and shows very less decline even after 100 hours.

Whereas at 250°C, rise in hardness was gradual and the peak hardness of 97HV was recorded after 25 hours of heat treatment. Same trend was observed at 350°C as well where, alloy 3 and 4 reached their peak hardness after 25 hours and showed a very slow decline after 100 hours.

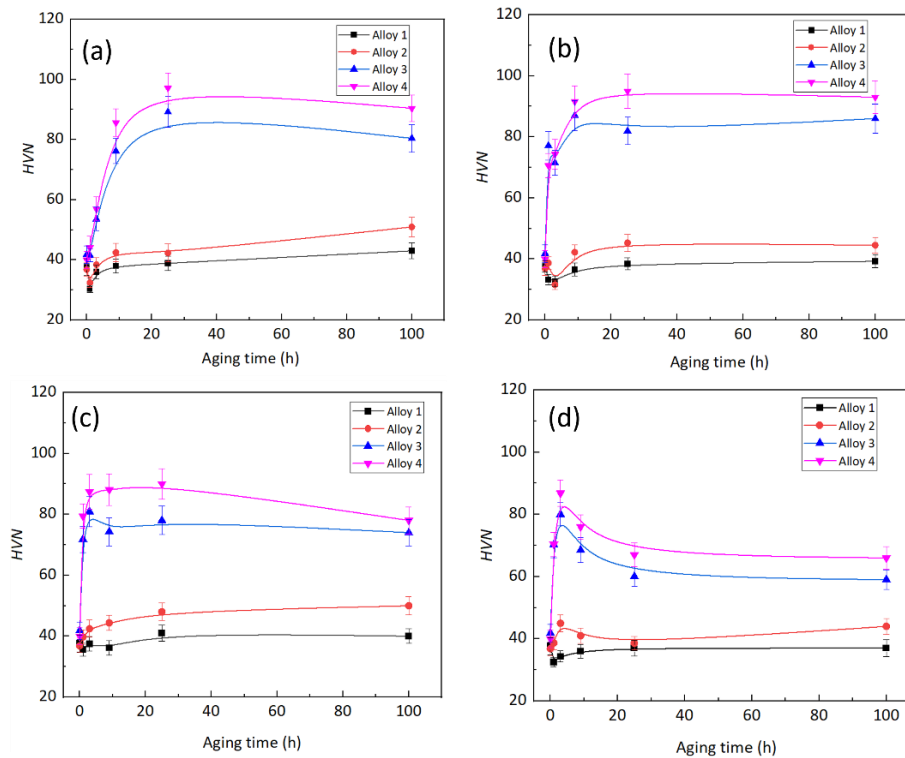


Figure 7.12 Ageing response of Alloy 1,2,3 and 4 at (a) 250°C (b) 300°C (c) 350°C (d) 400°C.

At 400°C, the observed peak (86HV) was at 3 hours followed by a gradual decline after 25 hours. The change in hardness after ageing is only recorded in alloys containing Sc. For alloy1, there was negligible change in hardness throughout. Alloy 2 also showed a minute change in hardness after 25 hours at 300°C and 350°C but no substantial effect of adding Zr was observed, supposedly due to low Zr content. Whereas, in alloy 3 and 4, where the combined effect of Zr and Sc is clearly visible due to the formation of nano scaled $Al_3(Sc, Zr)$ at higher temperatures. But these precipitates tend to coarsen and lose their effectiveness after long exposure to high temperature. Nonetheless, a higher degree of thermal stability at 300°C is evident after long hours of exposure in Sc and Zr containing alloys.

For alloy 5 and 6, a different scheme of heat treatment was chosen, due to the higher solubility of Mg in Al [227]. Alloy 5 and 6 were first solution treated at 540°C for 5 hours followed by

water quenching and subsequent ageing at 250°C. Figure 7.13 shows the hardness values of as cast and solution treated alloy 5 and 6.

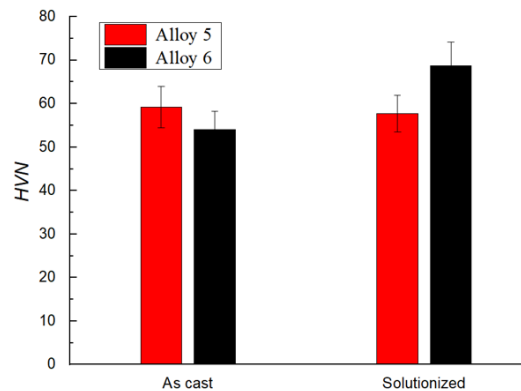


Figure 7.13 Hardness of alloy 5 and 6 in as cast and solution treated condition.

Both alloys show better hardness than alloys 1,2,3 and 4 in as cast condition. Where alloy 1-4 showed a similar hardness value of ~38HV, alloy 5 in as cast showed a value of 59HV. After solution treatment, no recognizable change in hardness was observed in alloy 5. This rise is prominently due to the presence of Mg and Si in aluminium matrix providing effective solution strengthening. Whereas in alloy 6, the hardness rises after the heat treatment, from 54 to 68. This could be the combined effect of dissolved Mg and formation of precipitates. Figure 7.13 shows the ageing response of solution treated alloy 5 and 6 at 250°C. Alloy 6 with 0.2wt.% Sc showed a little response to the temperature and showed better hardness from alloy 5 but the overall response of both the alloys was not similar to alloy1-4. Although both the alloys retained their hardness even after long exposure of temperature, no elevation in hardness was recorded at any point. This negligible response to ageing can be attributed to the ripening of $Al_3(Sc, Zr)$ precipitates. During the solution treatment at 540°C, the $Al_3(Sc, Zr)$ precipitates lost their potency to strengthen the alloy. Nonetheless, in as cast condition, Mg and Si addition is proven to improve the strength at room temperature.

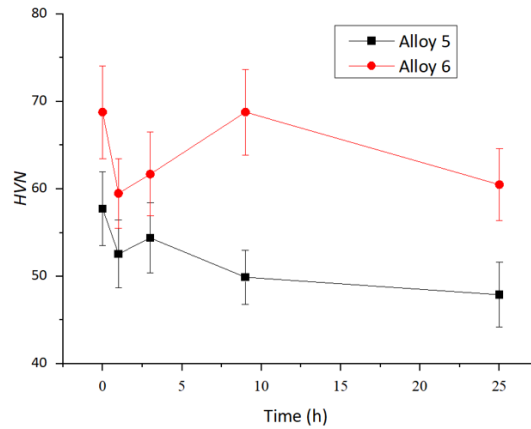


Figure 7.14 Ageing response of alloys 5 and 6 after solution treatment.

7.7 Microstructure after heat treatment

Figure 7.15 shows the microstructure of Al-10Ce base alloy after different heat treatments. No noticeable difference in the microstructure is visible even after longer ageing time at high temperature. The eutectic remains finer and unresponsive to the ageing temperature. This observation aligns with hardness behaviour of the alloy as well, as no change in the hardness is noticed after ageing. The eutectic phase of $Al_{11}Ce_3$ remains stable and retains the strength after ageing without any visible change in morphology.

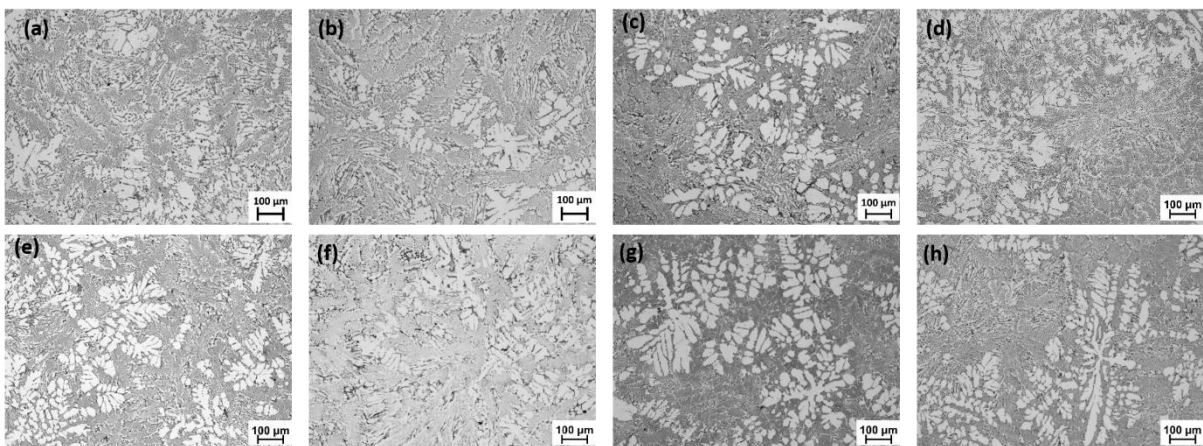


Figure 7.15 Microstructures of alloy 1 (Al-10Ce) after 1 and 25 hours of ageing at 250°C, 300°C, 350°C and 400°C; (a) 250°C for 1 h (b) 300°C for 1 (c) 350°C for 1 h (d) 400°C for 1 h (e) 250°C for 25 h (f) 300°C for 25 h (g) 350°C for 25 h (h) 400°C for 25 h.

Figure 7.16 shows the microstructure of alloy 2 after ageing at different temperatures. A little modification in the morphology of the eutectic is visible after ageing at 400°C for longer duration of time.

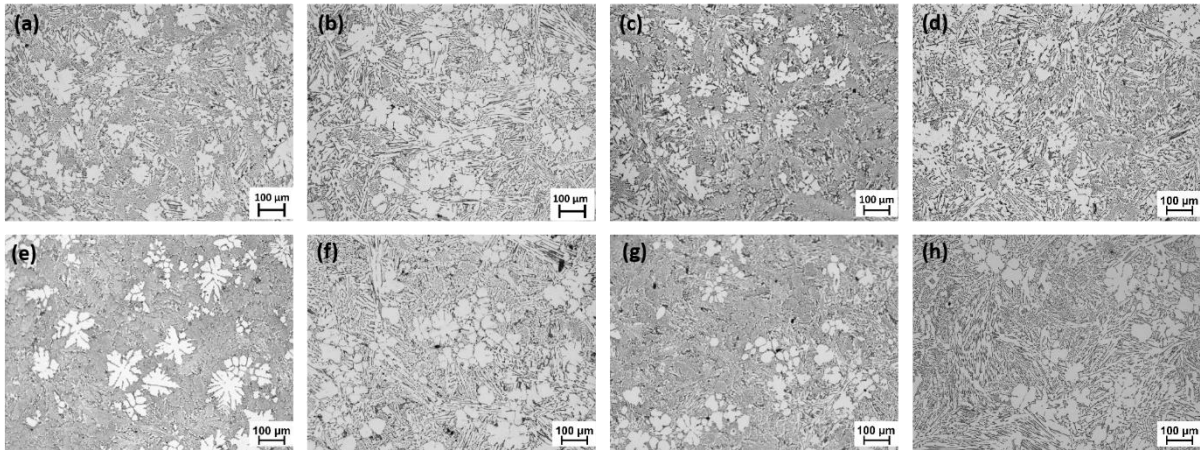


Figure 7.16 Microstructures of alloy 2 after 1 and 25 hours of ageing at 250°C, 300°C, 350°C and 400°C; (a) 250°C for 1 (b) 300°C for 1 h (c) 350°C for 1 h (d) 400°C for 1 h (e) 250°C for 25 h (f) 300°C for 25 h (g) 350°C for 25 h (h) 400°C for 25 h.

Coarsening of eutectic to a small extent can be noticed in Figure 7.16 (d) and (h). The morphology of eutectic which showed no response to the temperature in binary alloy, tend to coarsen in alloy 2 at high temperature.

Figure 7.17 shows the HRTEM image of Alloy 2 peak aged at 300°C. The formation of Al_3Zr particles is clear from Figure 7.17(b). The enhancement in hardness can be attributed to the hindrance of dislocation movement facilitated by the pinning effect of Al_3Zr particles, thereby leading to Orowan hardening.

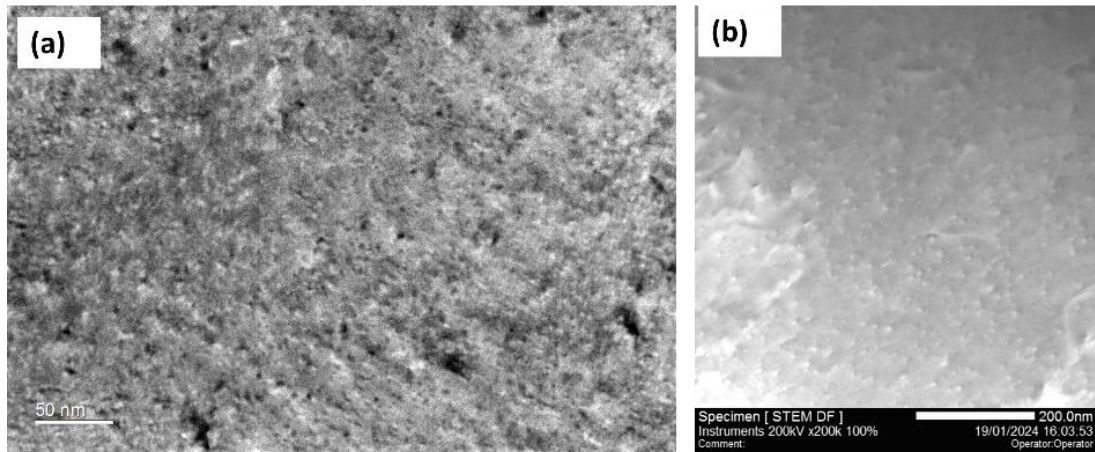


Figure 7.17 STEM images of Alloy 2 peak aged at 300°C.

Although no drastic change in the hardness was recorded at any ageing condition, the alloy tends to retain its strength at higher temperature due to thermally stable $Al_{11}Ce_3$ phase and low wt.% of Zr provided strengthening by grain refinement [119].

Figure 7.18 shows the microstructure of alloy 3 after ageing. Similar to alloy 2, a small amount of modification is visible in alloy 3 at high temperature. A small change in the morphology of eutectic phase is recognizable in Figure 7.18 (d). Coarsening of eutectics is observed when the alloy was exposed to high temperature for a long duration of time.

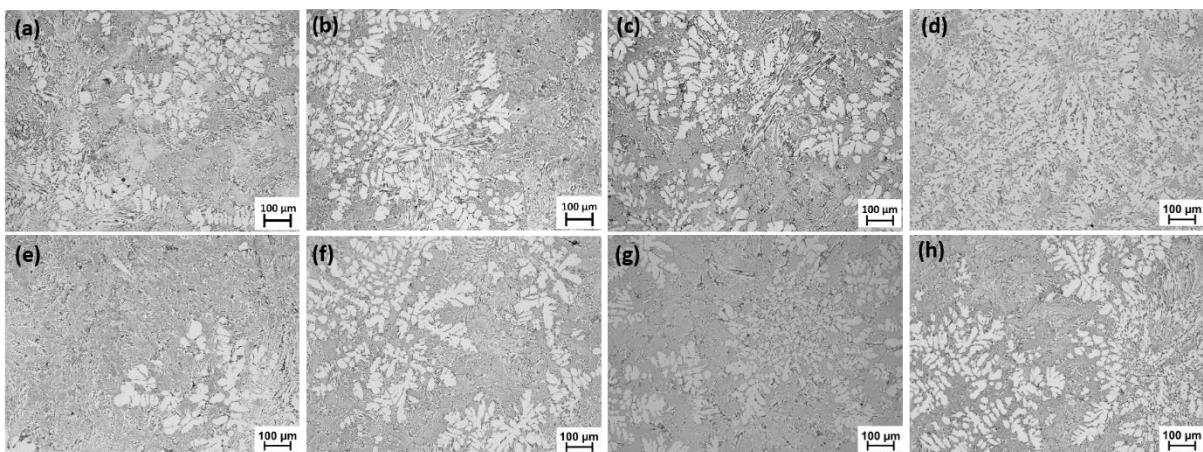


Figure 7.18 Microstructures of alloy 3 after 1 and 25 hours of ageing at 250°C, 300°C, 350°C and 400°C; (a) 250°C at 1 h (b) 300°C at 1 h (c) 350°C at 1 h (d) 400°C at 1 h (e) 250°C at 25 h (f) 300°C at 25 h (g) 350°C at 25 h (h) 400°C at 25 h.

The hardness response of the material shows the effect of Sc addition on the mechanical behaviour. The sharp elevation of hardness with Sc addition indicates the formation of $\text{Al}_3\text{Sc,Zr}$ precipitates which are not visible under optical microscope. Figure 7.19 shows the bright field and HRTEM images of Alloy 3 peak aged at 300°C showing a high number density particles in Al matrix which were identified as nanoscale $\text{Al}_3\text{Sc,Zr}$ precipitates. After 100 hours of ageing, there's a gradual decline in the hardness of Alloy 3. This observation is evident at 400°C and is the clear indication of coarsening of $\text{Al}_3\text{Sc,Zr}$ precipitates.

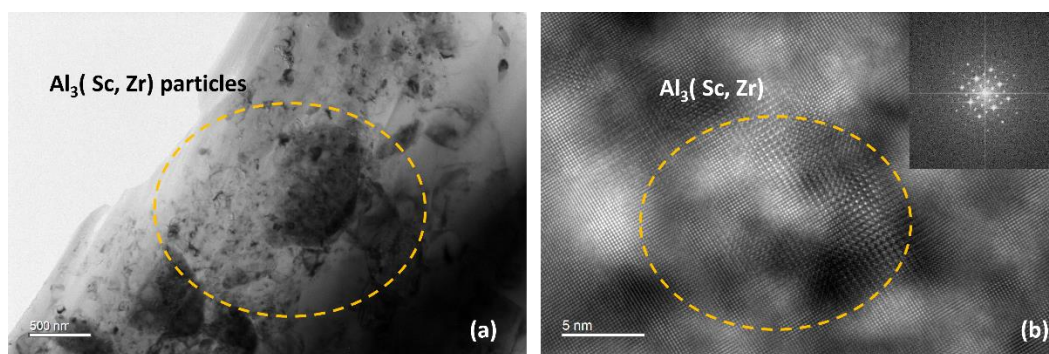


Figure 7.19 (a) TEM bright field image of Alloy 3 peak aged at 300°C (b) HRTEM of Alloy 3 peak aged at 300°C .

Figure 7.20 shows the microstructure of alloy 4 after ageing. Alloy 4 shows a distinct microstructure even in as cast condition. Very fine dendritic structure of αAl can be seen with fine eutectic colonies spread uniformly within the sample. Coarsening of eutectic was also visible at high temperature (Figure 7.20(h)). Similar to Alloy 3, Alloy 4 showed the influence of Sc addition to a greater extent and sharp change in hardness was recorded after ageing indicating the formation of $\text{Al}_3(\text{Sc,Zr})$ precipitates, which is confirmed by HRTEM and brightfield image of Alloy 4 peak aged at 300°C (Figure 7.21). Uniformly distributed nanoscale $\text{Al}_3(\text{Sc,Zr})$ precipitates were observed in Al matrix. The interface of these particles was found to be in coherence with the matrix, resulting in effective strengthening of Alloy 4.

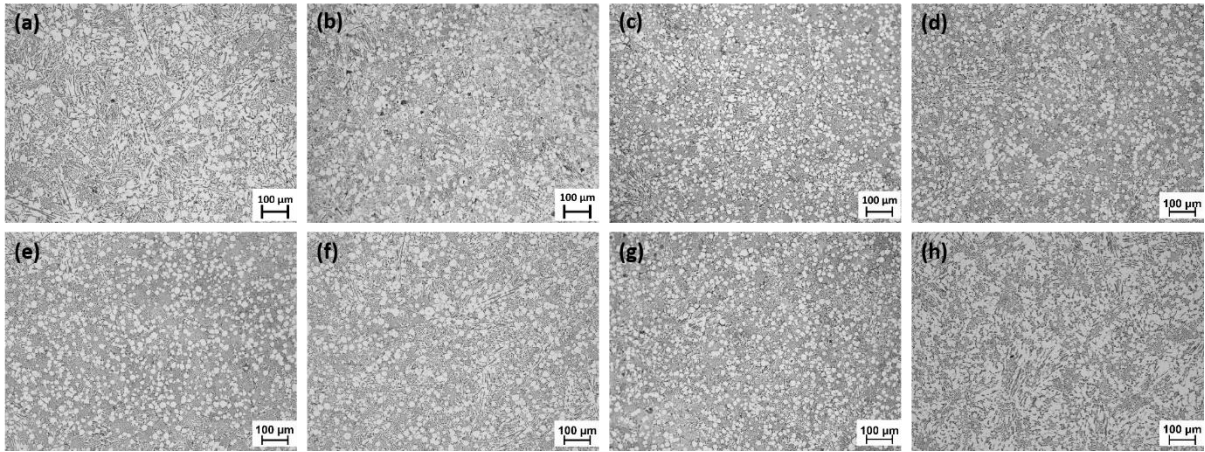


Figure 7.20 Microstructures of alloy 4 after 1 and 25 hours of ageing at 250°C, 300°C, 350°C and 400°C; (a) 250°C for 1 h (b) 300°C for 1 h (c) 350°C for 1 h (d) 400°C for 1 h (e) 250°C for 25 h (f) 300°C for 25 h (g) 350°C for 25 h (h) 400°C for 25 h.

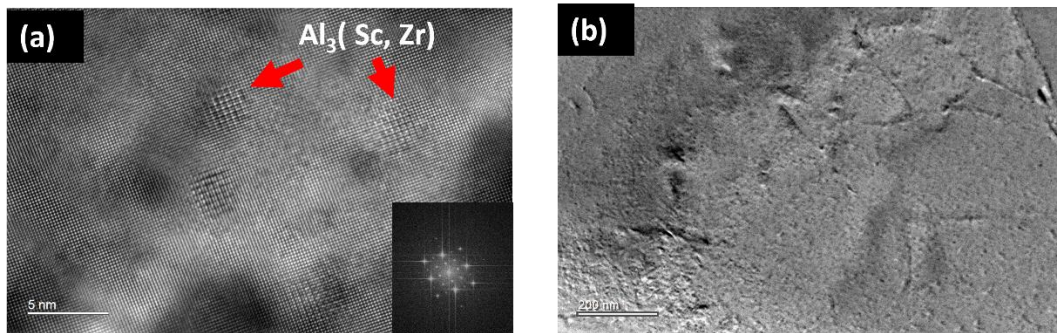


Figure 7.21 (a) HRTEM of Alloy 4 peak aged at 300°C with corresponding FFT pattern (b) Bright field image of peak aged Alloy 4.

As cast and solution treated microstructure of alloy 5 and 6 are presented in Figure 7.22. A more uniform distribution of eutectic colonies is recognizable in both the alloys. The eutectic colonies show a more refined structure when solution treated at 540°C for one hour. Alloy 6 shows a microstructure similar to alloy 4 with very fine α Al dendrites. After solution treatment, the eutectic in alloy 6 tend to coarsen. Within the eutectic colonies, some needle shaped precipitates are also visible in solution treated samples. These eutectics could be the Si rich phase but a thorough study of chemical composition of precipitates is needed.

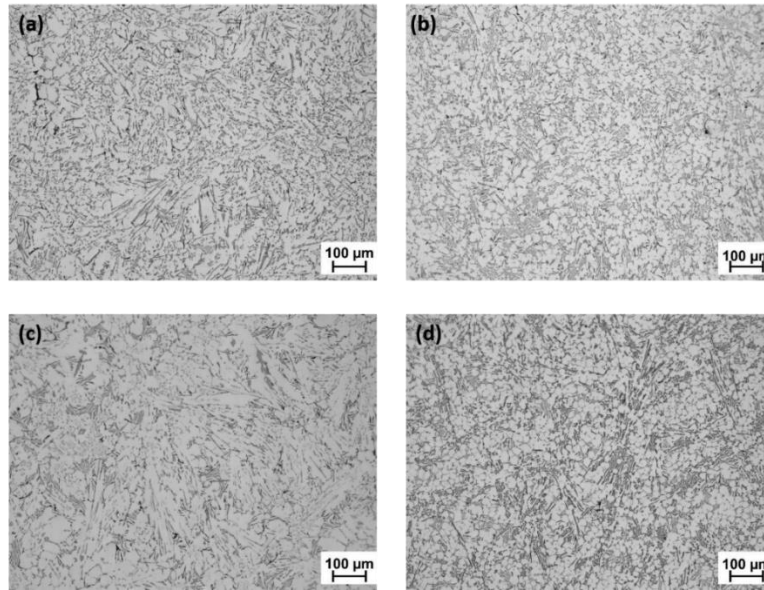


Figure 7.22 Microstructures of (a) as cast alloy 5 (b) as cast alloy 6 (c) solution treated alloy 5 (d) solution treated alloy 6.

Evolution of microstructure of alloy 5 and 6 in solution treated conditions with ageing at 250°C is shown in Figure 7.23. Coarsening of the α Al region is visible in both the ageing conditions. After ageing for 25 hours, eutectic tends to get finer. It can be noted from fig 7.23(b), that $Al_{11}Ce_3$ phase which is unresponsive to the temperature has shown change in the morphology and has become fine rod-shaped eutectic. Similar observations can be made in alloy 6, the $Al_{11}Ce_3$ has become finer and the rod-shaped Si rich phase are now more uniformly distributed in the matrix however, no considerable impact on the hardness was observed, as the hardness remains constant during the ageing. Nonetheless, these observations can help in understanding the impact of Si on the precipitation of Ce.

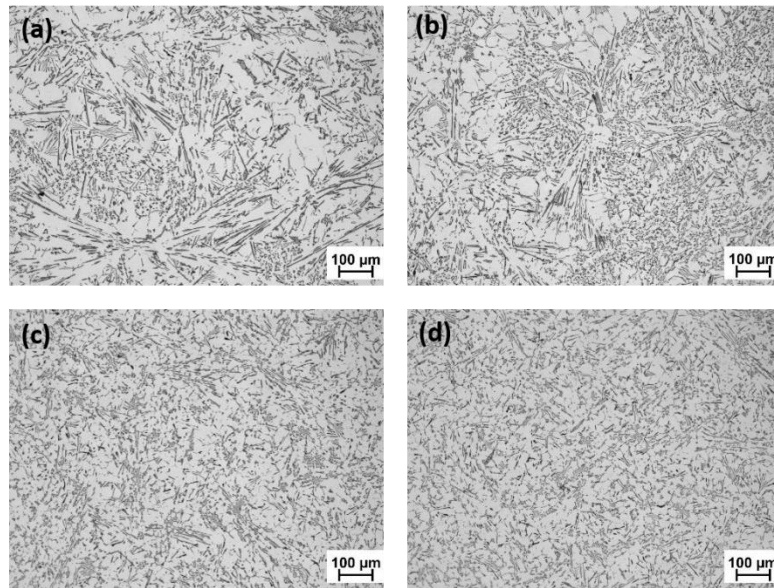


Figure 7.23 Microstructures of solution treated alloy 5 and 6 after ageing at 250°C; (a) alloy 5 aged for 1 h (b) alloy 5 aged for 25 h (c) alloy 6 aged for 1 h (d) alloy 6 aged for 25 h.

7.8 Fabrication through HPDC route

After studying the ageing behaviour, high pressure die casting trials were done on all alloys. The aim of casting the alloys under high pressure was to incorporate high cooling rate to increase the solid solubility of alloying elements in aluminium matrix. In alloy 5 and 6, this effect was expected to yield a higher hardness by the solid solution strengthening from dissolved Mg along with precipitation of Sc and Zr. Initial trials were done on all alloys using tensile bar dies due to potential sticking of the dies. During the first few trial runs, problem of sticking of cast on dies was encountered. To eliminate this problem, 0.25wt.% Mn and 0.75wt.% Fe was added to the alloys. Mn and Fe are known to reduce soldering and sticking of the cast on the dies.

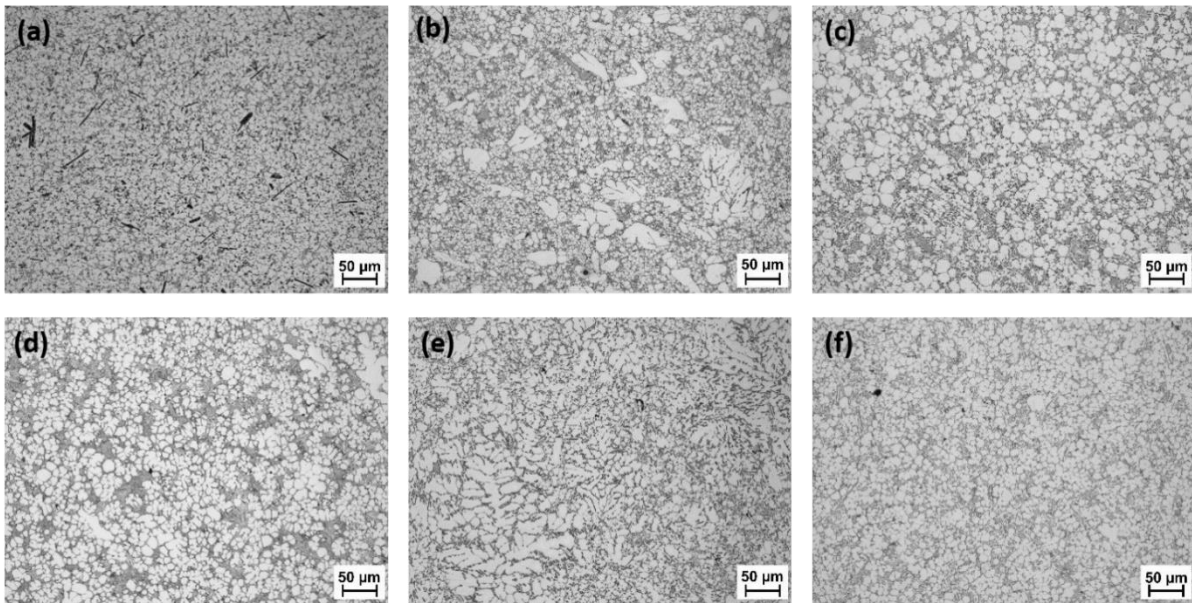


Figure 7.24 Microstructures of alloys cast by HPDC (a) alloy 1 (b) alloy 2 (c) alloy 3 (d) alloy 4 (e) alloy 5 and (f) alloy 6.

After several trials, sticking of dies was minimised. The microstructures of alloys in as cast condition are shown in Figure 7.24. The effect of high cooling rate is evident in the microstructure as a very fine dendritic structure can be seen in all alloys. For Al-10Ce binary alloy, the microstructure comprised of fine α Al dendrites with eutectic pools in the interdendritic regions. Whereas, for other alloys, a relatively coarser microstructure is observed. In alloy 2, the eutectic colonies are uniformly distributed within the microstructure with comparatively coarser dendrites. Alloy 3, 4 and 6 showed same level of refinement of α Al dendrites and interconnected $Al_{11}Ce_3$ phase, whereas alloy 5 showed a coarsening in eutectic. The hardness behaviour again shows a higher dependence on Sc content. All alloys showed a better hardness than the samples cast by permanent mould casting with alloy 6 showing the highest hardness value in as cast condition. The hardness values of these alloys are given in Figure 7.25.

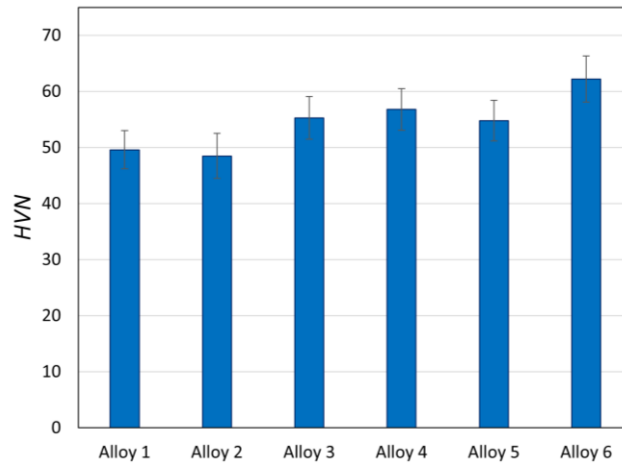


Figure 7.25 Hardness of alloy 1, 2,3,4, 5 and 6 cast by HPDC in as cast condition.

Although this elevation in hardness can be attributed to the finer grain structure, the solubility of Mg and Si in aluminium matrix is the highest contributor of strength. Owing to high cooling rate in HPDC, the supersaturated solid solution of α Al with Mg is easier to achieve. HPDC proves to elevate the as cast strength of material than sample cast from conventional casting route. Overall, the combined effect of high cooling rate in terms of solid solution strengthening and precipitation of $Al_3(Sc, Zr)$ phase at high temperature has been proven to be effective in strengthening the alloy at room and elevated temperatures.

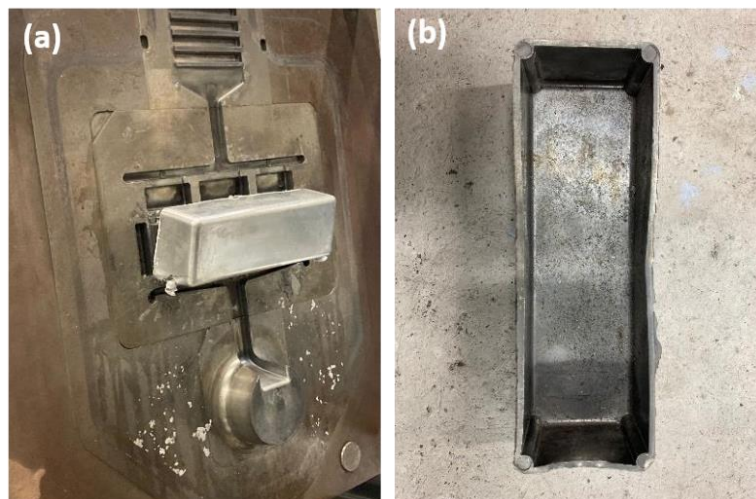


Figure 7.26 Fabrication of box component using industrial casting route.

Owing to the superior strength of alloy 6 as compared to other alloys, fabrication of an industrial component was done. Figure 7.26 shows an industrial component fabricated from the HPDC route. No problem of sticking or soldering was encountered and it can be concluded that the composition of alloy 6 can be suitable candidate for industrial casting process.

7.9 Mechanical behaviour at room and elevated temperature

Tensile tests on ASTM B557 standard round mechanical test bars with a gauge diameter of ϕ 6.35mm and a gauge length of 50mm were conducted at room and elevated temperatures of 150, 250 and 300°C. ASTM E8/E8M and ASTM E21 standards were followed for ambient tensile tests and high temperature tensile tests, respectively. The ramp rate for ambient tensile tests was controlled at 1mm/min, and the straining rate for high temperature tensile tests was maintained at 0.0002/s.

Figure 7.27 shows the tensile behaviour of alloy 1, 3,5 and 6 at all temperatures. To evaluate the improvement of high temperature mechanical strength of these alloys, a comparison has been made with high temperature mechanical properties of Mg-Re alloy presented in a study by Lingyun et al. [228]. To achieve a nominal strengthening of alloys through precipitation strengthening, Alloys were heat treated at corresponding testing temperatures for 4 hours and were held at same temperature during the tensile tests for 2 hours. At room temperature, alloy 6 shows the best yield and UT strength of 145 and 250 MPa and the least YS and UTS was shown by alloy 5 with ~115 and ~205 MPa. Alloy 3 shows a nominal YS and UTS of ~125 and ~225 MPa respectively. As the test temperature increases, the properties also degrades. The YS and UTS of Alloy 6 at 300°C was measured to be ~90 and ~110 MPa showing the lowest retention as compared to Alloy 3 and 5. Amongst all alloys, alloy 3 shows a very minute deviation in the YS even at 300°C. The YS and UTS of Alloy 3 at 300°C was ~110 and ~120 MPa respectively, showing the highest retention of strength amongst all alloys. As discussed

earlier, high temperature exposure can promote the formation of Al_3Sc , Zr precipitates which was shown in previous sections, can effectively enhance the mechanical properties of alloys at high temperatures.

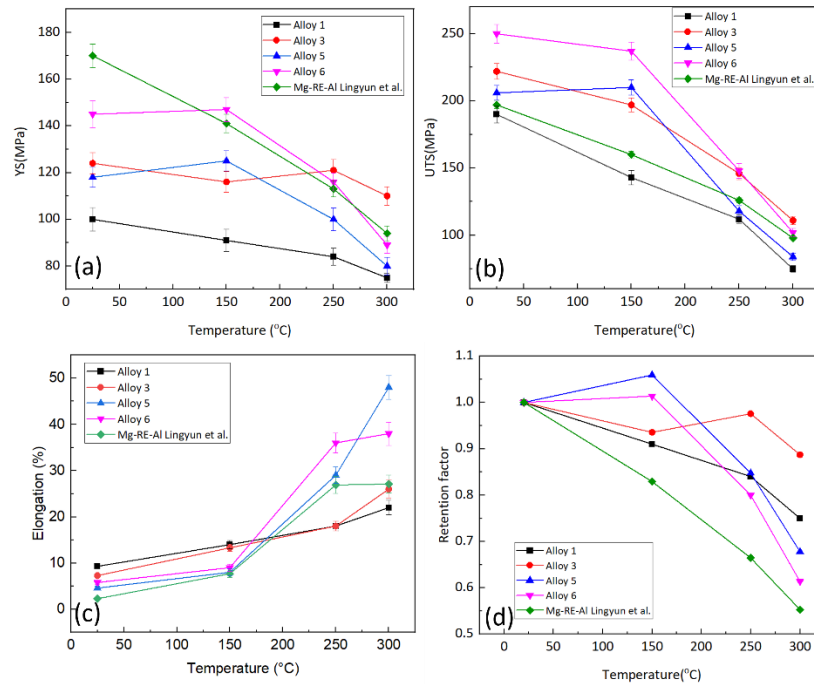


Figure 7.27 Tensile behaviour of newly developed alloys at ambient and elevated temperatures (a) yield strength (b) UTS (c) elongation (d) retention factor.

6.7 Conclusions

1. A series of Al-Ce alloys with various composition of Mg, Si, Zr and Sc were cast using permanent mould casting and high pressure die casting methods. Ageing behaviour of all alloys was studied and addition of Sc and Zr was found to be the major contributor in strength in the form of $\text{Al}_3(\text{Sc}, \text{Zr})$ nanoprecipitates at high temperature. At room temperature, solid solution strengthening from Mg contributed in the strengthening of as cast material.

2. $\text{Al}_{11}\text{Ce}_3$ particles show resistance to coarsening during spheroidization experiments. The circularity of $\text{Al}_{11}\text{Ce}_3$ changed from 0.64 to 0.66, while the circularity of eutectic Si changed from 0.55 to 0.8 during isothermal annealing at 400°C .
3. The eutectic morphology of alloys containing Zr and Sc shows a fine lamellar structure which changes its morphology to thin rods after ageing. For Mg and Si containing alloys (5 and 6) only rod-shaped eutectics were noticed in the interdimeric regions with some degree of coarsening after overageing.
4. Solution treatment of alloy 5 and 6 is detrimental for the high temperature stability. At 540°C , ripening of the precipitates results in the lost strength of the alloys.
5. In as cast condition, alloys cast in HPDC shows higher strength due to fine grain size and interconnect network of eutectic. Alloy 3 exhibits high mechanical strength at elevated temperatures. Alloy 6 shows the highest YS of 147 MPa at room temperature which declines to 89 MPa at 300°C . Alloy 3 shows the highest YS of 110 MPa at 300°C and 124 MPa at room temperature, with an average retention factor of 0.94.

8 Conclusion

Hall and Petch observed that the difference between the flow stress of a polycrystal and that of a single crystal is directly proportional to the inverse of the square root of the average grain diameter. Over the last six decades, this relationship has undergone extensive discussion across a spectrum of metallic materials and has found application in computational alloy design approaches. The distance between the dislocation source and the grain boundary is deemed to be half the diameter of the average grain size. Given that non-equiaxed grain morphologies, ranging from rosette to dendritic, are prevalent in materials where the distance between the dislocation source and the grain boundary radially varies, this thesis underscores the significance of introducing a perimeter-associated parameter to accommodate changes in grain morphology. A generic Hall-Petch relation $\sigma = \sigma_0 + k_m''/\sqrt{p'}$ has been proposed, wherein p' represents the area per unit perimeter, a parameter that can be accurately measured experimentally using digital image processing tools.

A series of Al-Si and Al-Ce binary alloys and AZ91D alloy with a range of dendritic morphologies were synthesized by controlling solute content and cooling rates. The key conclusions are as follows:

- For dendritic grain morphology, p' exhibits a nonlinear relationship with λ_2 over a broad range of cooling rates, substantiated both mathematically and experimentally. This non-linearity becomes more pronounced with the increasing complexity of dendritic structures, underscoring the importance of considering grain perimeter in predicting YS.

- The generic Hall-Petch type relationship yields a superior coefficient of regression (> 0.97) for alloys with diverse grain morphologies compared to the conventional Hall-Petch relationship, which relies on either d or λ_2 .
- The Hall-Petch constant is observed to increase with rising Si content, attributed to the shift in the preferential growth direction of α -Al dendrites from $\langle 001 \rangle$ to $\langle 110 \rangle$ when Si concentration increases to 8 wt.%.
- The new Hall-Petch relationship shows a diverse application in range of alloys including Mg alloys. The coefficient of regression shows a high value when p' is considered to capture the morphology of as cast dendritic grains and solution treated faceted grains.
- This enhanced generic Hall-Petch relation offers a more accurate and comprehensive description of the intricate interplay between grain morphology complexity and material strength. As modern image processing tools can precisely measure grain perimeters, incorporating this generic relation into computational alloy design approaches holds promise for enhancing accuracy.
- $\text{Al}_{11}\text{Ce}_3$ particles show higher resistance to coarsening than eutectic Si particles during isothermal and isochronal annealing experiments.
- Al-Ce shows higher thermal stability than the cast Al-Si alloys. Addition of Sc and Zr to Al-Ce results in high YS at high temperature due to formation of nanoscale $\text{Al}_3\text{Sc/Zr}$ precipitates. The retention factor for Al-10Ce-0.2Sc-0.2Sc was measured to be 0.9 at 300°C whereas for other alloys, retention factor ranged from 0.58 to 0.68.

9 Suggestions for future work

This thesis presents a new generic HP relationship which relies on the morphological changes of grain structure. In present study, the dendritic morphology was varied by controlling the solute and cooling rate and a generic HP relationship is proposed. However to elucidate the fundamentals of grain boundary structure and strength correlation and to further the applicability of new HP relationship, following experiments are suggested

- A change in the HP constant was noticed in Al-Ce binary alloys with increasing Ce content. To characterize the effect of Ce on the texture evolution of dendrites, a systematic EBSD analysis on the directionally solidified Al-Ce alloys with varying Ce content is needed.
- Present study presents the mechanical property analysis of AZ91D alloy over a small range of cooling rate when compared with the analysis presented for Al alloys. Expanding the range of cooling rates is needed to characterize the variation of HP constant in Mg alloys.
- As discussed in literature review chapter, HP relationship has been explained by several models with pile up model being the most widely accepted. To understand the grain boundary structure and YS correlation, development of theoretical model to formulate the new HP relationship is required.
- Since, new HP relationship relies on the interaction of dislocations and grain boundaries. To characterize the dislocations accumulation at the grain boundaries, TEM analysis of deformed grains with known orientation and varying morphology is recommended.

9.1 Effect of particles on the modification of dendritic morphology

Morphology of grains are reported to be modified by the addition of particles. Several studies have shown the influence of particles on the change in morphology of dendritic structures in Al and Mg alloys. Modification of morphology such as multiple splitting, branching and curving mechanisms of the dendrite arms are observed. When these particles become incorporated into the dendritic structure, they can influence the growth kinetics and crystallographic orientations of the dendrites, leading to alterations in their morphology. For example, in Al dendrites, the presence of particles can disrupt the regular growth pattern, resulting in the formation of branched or irregular dendritic shapes. Similarly, in Mg dendrites, the interaction between foreign particles and the dendritic growth front can lead to the formation of secondary arms or the suppression of dendritic growth in certain directions, ultimately affecting the overall morphology of the dendrites. As mentioned in literature review chapter, particles acts as nucleating sites, initiating heterogeneous nucleation of grains and influencing the grain structure. To move in this direction, attempts were made to incorporate ceramic particles in Al alloys. Due to low wettability of ceramics in liquid Al, producing composite structures with homogenous distribution of particles is a big challenge. However, in situ formation of particles by addition of grain refiners grants the flexibility to produce composite structures. Preliminary attempts were made to produce in situ composites with varying TiB_2 particle concentration incorporated by Al_3TiB grain refiner. Figure 9.1 shows the optical and SEM micrographs of as solidified Al_3TiB grain refiner.

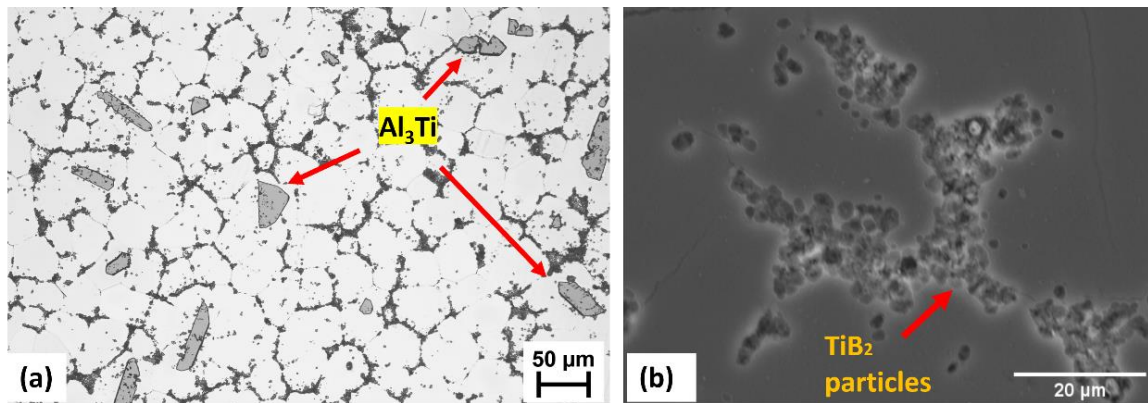


Figure 9.1 Microstructure of 3TiB grain refiner showing (a) formation of particles and Al₃Ti phase (b) SEM micrograph showing TiB₂ clusters at the grain boundary.

Figure 9.2 shows the microstructures of Al-2Si alloy, refined by in situ TiB₂ particles. Microstructures of references containing free Ti corresponding to the composite counterparts are also presented. It is clear that particles acts as nucleating sites and results in the refinement of Al dendrites. It can be noticed that increasing the particle content eliminates the dendritic growth of grains and results in formation of globular grains. To systematically evaluate the influence of particles on the strengthening of an alloy, solidification experiments with varying concentrations of particles and there influence on the mechanical strength is needed.

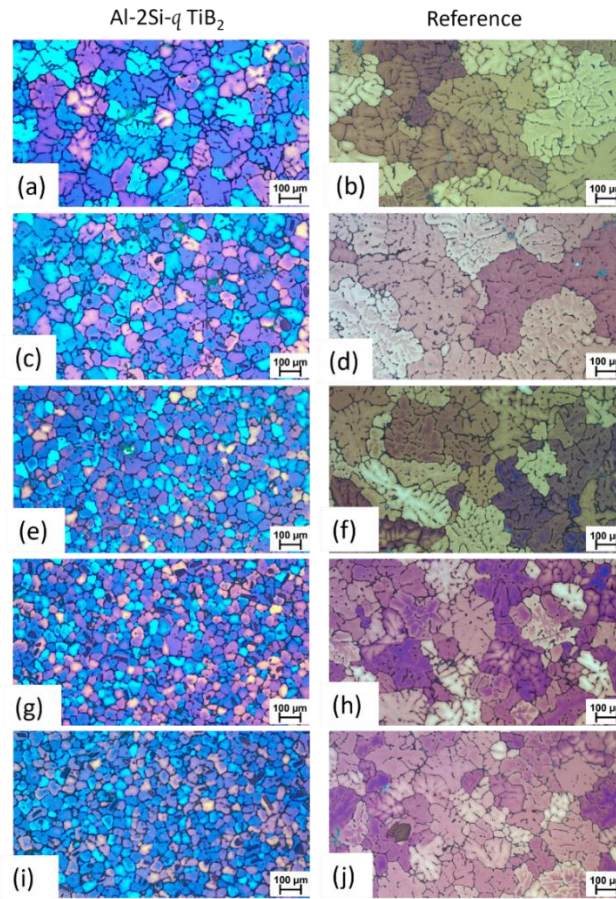


Figure 9.2 Optical micrographs of Al-2Si alloy with q wt.% TiB_2 grain refiner ,where $q =$ (a) 0.25 (c) 0.5 (e) 1 (g) 2 (i) 2.5 and their reference counterparts.

References

- [1] E.O.Hall, The Deformation and Ageing of Mild Steel: III Discussion of Results, *Proc. Phys. Soc. B* 64 (1951) 747–753. <https://doi.org/10.1088/0370-1301/64/9/303>.
- [2] N.J. Petch, The Cleavage Strength of Polycrystals, *Journal of the Iron and Steel Institute* 174 (1953) 25–28.
- [3] Z.C. Cordero, B.E. Knight, C.A. Schuh, Six decades of the Hall–Petch effect – a survey of grain-size strengthening studies on pure metals, *International Materials Reviews* 61 (2016) 495–512. <https://doi.org/10.1080/09506608.2016.1191808>.
- [4] P. Van Houtte, On the Equivalence of the Relaxed Taylor Theory and the Bishop-Hill Theory for Partially Constrained Plastic Deformation of Crystals, *Materials Science and Engineering* 55 (1982) 69–77. [https://doi.org/10.1016/0025-5416\(82\)90085-4](https://doi.org/10.1016/0025-5416(82)90085-4).
- [5] L. Delannay, M.R. Barnett, Modelling the combined effect of grain size and grain shape on plastic anisotropy of metals, *Int J Plast* 32–33 (2012) 70–84. <https://doi.org/10.1016/j.ijplas.2011.12.002>.
- [6] M. Jiang, B. Devincere, G. Monnet, Effects of the grain size and shape on the flow stress: a dislocation dynamics study, *International Journal of Plasticity* 113 (2019) 111–124. <https://doi.org/10.1016/j.ijplas.2018.09.008>.
- [7] G. Wang, M.S. Dargusch, M. Qian, D.G. Eskin, D.H. StJohn, The role of ultrasonic treatment in refining the as-cast grain structure during the solidification of an Al-2Cu alloy, *J Cryst Growth* 408 (2014) 119–124. <https://doi.org/10.1016/j.jcrysgro.2014.09.018>.
- [8] M. Easton, C. Davidson, D. St. John, Grain morphology of as-cast wrought aluminium alloys, in: *Mater Trans*, 2011: pp. 842–847. <https://doi.org/10.2320/matertrans.L-MZ201118>.
- [9] H.T. Li, M. Xia, P. Jarry, G.M. Scamans, Z. Fan, Grain refinement in a AlZnMgCuTi alloy by intensive melt shearing: A multi-step nucleation mechanism, *J Cryst Growth* 314 (2011) 285–292. <https://doi.org/10.1016/j.jcrysgro.2010.10.168>.
- [10] M. Qian, A. Ramirez, An approach to assessing ultrasonic attenuation in molten magnesium alloys, *J Appl Phys* 105 (2009). <https://doi.org/10.1063/1.3054374>.
- [11] R. Daudin, S. Terzi, P. Lhuissier, J. Tamayo, M. Scheel, N. Hari Babu, D.G. Eskin, L. Salvo, Particle-induced morphological modification of Al alloy

- equiaxed dendrites revealed by sub-second in situ microtomography, *Acta Mater* 125 (2017) 303–310. <https://doi.org/10.1016/j.actamat.2016.12.005>.
- [12] Enyu Guo, Sansan Shuai, Daniil Kazantsev, Shyamprasad Karagadde, A.B. Phillion, Tao Jing, Wenzhen Li, Peter D. Lee, The influence of nanoparticles on dendritic grain growth in Mg alloys, *Acta Mater* 152 (2018) 127–137. <https://doi.org/10.1016/j.actamat.2018.04.023>.
- [13] H.T. Li, M. Xia, P. Jarry, G.M. Scamans, Z. Fan, Grain refinement in a AlZnMgCuTi alloy by intensive melt shearing: A multi-step nucleation mechanism, *J Cryst Growth* 314 (2011) 285–292. <https://doi.org/10.1016/j.jcrysgro.2010.10.168>.
- [14] M.A. Easton, H. Kaufmann, W. Fragner, The effect of chemical grain refinement and low superheat pouring on the structure of NRC castings of aluminium alloy Al-7Si-0.4Mg, *Materials Science and Engineering A* 420 (2006) 135–143. <https://doi.org/10.1016/j.msea.2006.01.078>.
- [15] D.H. StJohn, M.A. Easton, M. Qian, Controlling the semisolid grain size during solidification, in: *Solid State Phenomena*, Trans Tech Publications Ltd, 2008: pp. 355–360. <https://doi.org/10.4028/www.scientific.net/ssp.141-143.355>.
- [16] M. Yang, S.M. Xiong, Z. Guo, Effect of different solute additions on dendrite morphology and orientation selection in cast binary magnesium alloys, *Acta Mater* 112 (2016) 261–272. <https://doi.org/10.1016/j.actamat.2016.04.014>.
- [17] M. Furukawa, Z. Horita, M. Nemoto, R.Z. Valiev, T.G. Langdon, Microhardness measurements and the Hall-Petch relationship in an Al Mg alloy with submicrometer grain size, *Acta Mater* 44 (1996) 4619–4629. [https://doi.org/10.1016/1359-6454\(96\)00105-X](https://doi.org/10.1016/1359-6454(96)00105-X).
- [18] S. Yoshida, T. Ikeuchi, T. Bhattacharjee, Y. Bai, A. Shibata, N. Tsuji, Effect of elemental combination on friction stress and Hall-Petch relationship in face-centered cubic high / medium entropy alloys, *Acta Mater* 171 (2019) 201–215. <https://doi.org/10.1016/j.actamat.2019.04.017>.
- [19] T. Huang, L. Shuai, A. Wakeel, G. Wu, N. Hansen, X. Huang, Strengthening mechanisms and Hall-Petch stress of ultrafine grained Al-0.3%Cu, *Acta Mater* 156 (2018) 369–378. <https://doi.org/10.1016/j.actamat.2018.07.006>.
- [20] S. Nagarjuna, M. Srinivas, K.K. Sharma, The grain size dependence of flow stress in a Cu-26Ni-17Zn alloy, *Acta Mater* 48 (2000) 1807–1813. [https://doi.org/https://doi.org/10.1016/S1359-6454\(99\)00464-4](https://doi.org/https://doi.org/10.1016/S1359-6454(99)00464-4).
- [21] J.P. Weiler, J.T. Wood, R.J. Klassen, R. Berkmortel, G. Wang, The effect of grain size on the flow stress determined from spherical microindentation of die-cast

- magnesium AM60B alloy, in: *J Mater Sci*, 2005: pp. 5999–6005. <https://doi.org/10.1007/s10853-005-1295-2>.
- [22] C.H. Caceres, G.E. Mann, J.R. Griffiths, Grain size hardening in Mg and Mg-Zn solid solutions, *Metall Mater Trans A Phys Metall Mater Sci* 42 (2011) 1950–1959. <https://doi.org/10.1007/s11661-010-0599-2>.
- [23] M.A. Herbert, C. Sarkar, R. Mitra, M. Chakraborty, Microstructural evolution, hardness, and alligating in the Mushy state rolled cast Al-4.5Cu alloy and In-situ Al4.5Cu-5TiB2 composite, *Metall Mater Trans A Phys Metall Mater Sci* 38 A (2007) 2110–2126. <https://doi.org/10.1007/s11661-007-9264-9>.
- [24] M. Maleki, F. Jamei, M. Emamy, H. Mirzadeh, Microstructure and mechanical properties of as-cast and wrought Mg–Ni in-situ formed alloys, *Materials Science and Technology* (2022). <https://doi.org/10.1080/02670836.2022.2154934>.
- [25] Z. hua Hu, X. Peng, G. hua Wu, D. qiang Cheng, W. cai Liu, L. Zhang, W. jiang Ding, Microstructure evolution and mechanical properties of rheo-processed ADC12 alloy, *Transactions of Nonferrous Metals Society of China (English Edition)* 26 (2016) 3070–3080. [https://doi.org/10.1016/S1003-6326\(16\)64439-4](https://doi.org/10.1016/S1003-6326(16)64439-4).
- [26] H.M. Guo, A. sheng Zhang, B. Hu, Y. Ding, X.B. Liu, Refining microstructure of AZ91 magnesium alloy by introducing limited angular oscillation during initial stage of solidification, *Materials Science and Engineering A* 532 (2012) 221–229. <https://doi.org/10.1016/j.msea.2011.10.083>.
- [27] J. Wang, Y. Liu, J. Zhu, Y. Liu, X. Su, Effect of Complex Modification on Microstructure and Mechanical Properties of Hypoeutectic Al–Si, *Metallography, Microstructure, and Analysis* 8 (2019) 833–839. <https://doi.org/10.1007/s13632-019-00584-7>.
- [28] Hengcheng Liao Yu, SunGuoxiong Sun, Correlation between mechanical properties and amount of dendritic α -Al phase in as-cast near-eutectic Al–11.6% Si alloys modified with strontium, *Materials Science and Engineering A* 335 (2002) 62–66. [https://doi.org/10.1016/S0921-5093\(01\)01949-9](https://doi.org/10.1016/S0921-5093(01)01949-9).
- [29] B.P. Reis, M.M. Lopes, A. Garcia, C.A. dos Santos, The correlation of microstructure features, dry sliding wear behavior, hardness and tensile properties of Al-2wt%Mg-Zn alloys, *J Alloys Compd* 764 (2018) 267–278. <https://doi.org/10.1016/j.jallcom.2018.06.075>.
- [30] L. Bolzoni, M. Nowak, N. Hari Babu, Grain refinement of Al-Si alloys by Nb-B inoculation. Part II: Application to commercial alloys, *Mater Des* 66 (2015) 376–383. <https://doi.org/10.1016/j.matdes.2014.08.067>.

- [31] T. Haxhimali, A. Karma, F. Gonzales, M. Rappaz, Orientation selection in dendritic evolution, *Nat Mater* 5 (2006) 660–664. <https://doi.org/10.1038/nmat1693>.
- [32] L. Gránásy, T. Pusztai, T. Börzsönyi, J.A. Warren, J.F. Douglas, A general mechanism of polycrystalline growth, *Nat Mater* 3 (2004) 645–650. <https://doi.org/10.1038/nmat1190>.
- [33] L. Gránásy, T. Pusztai, J.A. Warren, J.F. Douglas, T. Börzsönyi, V. Ferreiro, Growth of “dizzy dendrites” in a random field of foreign particles, *Nat Mater* 2 (2003) 92–96. <https://doi.org/10.1038/nmat815>.
- [34] Q. Li, C. Beckermann, Scaling behavior of three-dimensional dendrites, *Phys Rev E* 57 (1998) 3176–3188. <https://doi.org/https://doi.org/10.1103/PhysRevE.57.3176>.
- [35] E. Hurlimann, R. Trittibach, U. Bisang, J.H. Bilgram, Integral parameters of xenon dendrites, *Phys Rev A (Coll Park)* 46 (1992) 6579–6595. <https://doi.org/https://doi.org/10.1103/PhysRevA.46.6579>.
- [36] D. M. Stefanescu, R. Ruxanda, *Fundamentals of solidification*, Mater. Park. OH ASM Int, Cham, 2004. <https://doi.org/10.1007/978-3-319-48117-3>.
- [37] J.W. Gibbs, On the Equilibrium of Heterogeneous Substances, *Trans. Conn. Acad. Arts Sci.* (1876) 108–248.
- [38] M. Volmer, A. Weber, Germ-formation in oversaturated figures, *Zeitschrift Für Physikalische Chemie-Stoichiometrie Und Verwandtschaftslehre* (1926) 277–301.
- [39] M. Nowak, *Development of Niobium-Boron grain refiner for Al-Si alloys*, Brunel University, 2011.
- [40] M. Remzi Abul, *Microstructural Development and Mechanical Properties of Drop Tube Atomized Binary Al-Fe and Ternary Al-Fe-Si Alloys*, 2022.
- [41] D. Turnbull, Kinetics of Heterogeneous Nucleation, *J. Chem. Phys.* 18 (1950) 198–203.
- [42] David A. Porter, Kenneth E. Easterling, Mohamed Y. Sherif, *Phase Transformations in Metals and Alloys*, 4th ed., CRC Press, 2021. <https://doi.org/https://doi.org/10.1201/9781003011804>.
- [43] Christian J.W., *The Theory of Transformations in Metals and Alloys*, Pergamon, 1965.

- [44] W.W. Mullins, R.F. Sekerka, Stability of a planar interface during solidification of a dilute binary alloy, *J Appl Phys* 35 (1964) 444–451. <https://doi.org/10.1063/1.1713333>.
- [45] J.A. Warren, J.S. Langer, Prediction of dendritic spacings in a directional-solidification experiment, *Phys Rev E* 47 (1993) 2702–2712. <https://doi.org/10.1103/PhysRevE.47.2702>.
- [46] A. Papapetrou, Untersuchungen über dendritisches Wachstum von Kristallen, *Für Krist.-Cryst. Mater.* 92 (1935) 89–130.
- [47] G. Ivantsov, Temperature field around a spherical, cylindrical, and needle-shaped crystal, growing in a pre-cooled melt, *Dokl. Akad. Nauk SSSR* 58 (1947) 567–569.
- [48] G. Horvay, J.W. Cahn, Dendritic and spheroidal growth, *Acta Metallurgica* 9 (1961) 695–705. [https://doi.org/10.1016/0001-6160\(61\)90008-6](https://doi.org/10.1016/0001-6160(61)90008-6).
- [49] B. Nenchev, Modelling and Analysis of Solidification Shrinkage and Defect Prediction in Metals, University of Leicester, 2020. <https://doi.org/https://doi.org/10.25392/leicester.data.21959885.v1>.
- [50] M.A. Chopra, M.E. Glicksman, N.B. Singh, Dendritic solidification in binary alloys, *Metallurgical Transactions A* 19 (1988) 3087–3096. <https://doi.org/https://doi.org/10.1007/BF02647736>.
- [51] E. Acer, E. Çadrlı, H. Erol, H. Kaya, M. Gündüz, Effects of Growth Rates and Compositions on Dendrite Arm Spacings in Directionally Solidified Al-Zn Alloys, *Metall Mater Trans A Phys Metall Mater Sci* 48 (2017) 5911–5923. <https://doi.org/10.1007/s11661-017-4337-x>.
- [52] M.A. Tschopp, J.D. Miller, A.L. Oppedal, K.N. Solanki, Characterizing the local primary dendrite arm spacing in directionally solidified dendritic microstructures, *Metall Mater Trans A Phys Metall Mater Sci* 45 (2014) 426–437. <https://doi.org/10.1007/s11661-013-1985-3>.
- [53] J. Hunt, Solidification and casting of metals, The Metal Society, London, 1979.
- [54] W. Kurz, D.J. Fisher, Dendrite growth at the limit of stability: tip radius and spacing, *Acta Metallurgica* 29 (1981) 11–20.
- [55] R. Trivedi, Theory of dendritic growth during the directional solidification of binary alloys, *J Cryst Growth* 49 (1980) 219–232. [https://doi.org/https://doi.org/10.1016/0022-0248\(80\)90157-8](https://doi.org/https://doi.org/10.1016/0022-0248(80)90157-8).
- [56] K. Somboonsuk, J.T. Mason, R. Trivedi, Interdendritic Spacing: Part I. Experimental Studies, *Metall Trans A* 15 (1984) 967–975.

- [57] S.-C. Huang, M.E. Glicksman, Overview 12: Fundamentals of dendritic solidification—I. Steady-state tip growth, *Acta Metallurgica* 29 (1981) 701–715.
- [58] R. Trivedi, Interdendritic Spacing: Part II, *Metall Trans A* 15 (1984) 977–982.
- [59] F.Z. Kattamis, Dendritic coarsening during solidification, *J Cryst Growth* 15 (1972) 20–24. [https://doi.org/https://doi.org/10.1016/0022-0248\(72\)90315-6](https://doi.org/https://doi.org/10.1016/0022-0248(72)90315-6).
- [60] M. Paliwal, I.H. Jung, The evolution of the growth morphology in Mg-Al alloys depending on the cooling rate during solidification, *Acta Mater* 61 (2013) 4848–4860. <https://doi.org/10.1016/j.actamat.2013.04.063>.
- [61] T. Okamoto, K. Kishitake, Dendritic structure in unidirectionally solidified aluminium, tin, and zinc base binary alloys, *J Cryst Growth* 29 (1975) 137–146.
- [62] J.D. Eshelby, F.C. Frank, F.R.N. Nabarro, XLI. The equilibrium of linear arrays of dislocations., *The London, Edinburgh, and Dublin Philosophical Magazine and Journal of Science* 42 (1951) 351–364. <https://doi.org/10.1080/14786445108561060>.
- [63] J.D. Eshelby, F.C. Frank, F.R.N. Nabarro, XLI. The equilibrium of linear arrays of dislocations., *The London, Edinburgh, and Dublin Philosophical Magazine and Journal of Science* 42 (1951) 351–364. <https://doi.org/10.1080/14786445108561060>.
- [64] J. C. M. Li, Petch Relation and Grain Boundary Sources, *Transactions of the Metallurgical Society of AIME* 227 (1963) 239–247.
- [65] L.E. Murr, Some Observations of Grain Boundary Ledges and Ledges as Dislocation Sources in Metals and Alloys, *Metall Trans A* 6 (1975). <https://doi.org/https://doi.org/10.1007/BF02658408>.
- [66] Y. Li, A.J. Bushby, D.J. Dunstan, The Hall-Petch effect as a manifestation of the general size effect, *Proceedings of the Royal Society A: Mathematical, Physical and Engineering Sciences* 472 (2016). <https://doi.org/10.1098/rspa.2015.0890>.
- [67] Bernstein I.M., Rath B.B., The Relation Between Grain-Boundary Orientation and Intergranular Cracking, *Surf Sci* 31 (1972) 101.
- [68] Conrad H, Feuerstein S, Rice L., Effects of grain size on the dislocation density and flow stress of niobium, *Materials Science and Engineering* 2 (1967) 157–168.
- [69] Conrad H., Effect of Grain Size on the Lower Yield and Flow Stress of Iron and Steel, *Acta Metallurgica* 11 (1963) 75–77.
- [70] Cottrell. A., *Dislocation and plastic flow in crystals.*, Oxford Univ. Press McGraw-Hill (1953) 223.

- [71] M. Kato, Hall-petch relationship and dislocation model for deformation of ultrafine-grained and nanocrystalline metals, *Mater Trans* 55 (2014) 19–24. <https://doi.org/10.2320/matertrans.MA201310>.
- [72] M.A. Meyers, E. Ashworth, A model for the effect of grain size on the yield stress of metals, *Philosophical Magazine A* 46 (1982) 737–759. <https://doi.org/10.1080/01418618208236928>.
- [73] Baldwin WM, Yield strength of metals as a function of grain size, *Acta Metallurgica* 6 (1958) 139–141. [https://doi.org/10.1016/0001-6160\(58\)90136-6](https://doi.org/10.1016/0001-6160(58)90136-6).
- [74] M. Aghaie-Khafri, F. Honarvar, S. Zanganeh, Characterization of grain size and yield strength in AISI 301 stainless steel using ultrasonic attenuation measurements, *J Nondestr Eval* 31 (2012) 191–196. <https://doi.org/10.1007/s10921-012-0134-z>.
- [75] J.C.M. Li, Y.T. Chou, The Role of Dislocations in the Flow Stress Grain Size Relationships, *Metall Trans* 1 (1970) 1145–1159. <https://doi.org/https://doi.org/10.1007/BF02900225>.
- [76] R. Zhou, A. Roy, V. V. Silberschmidt, A crystal-plasticity model of extruded AM30 magnesium alloy, *Comput Mater Sci* 170 (2019) 109140. <https://doi.org/10.1016/J.COMMATSCI.2019.109140>.
- [77] L. Tian, L. Wang, H. Wu, H. Wang, L. Zheng, K.S. Shin, Recent research advances in Mg single crystal based on the crystal orientations : A review, *Journal of Materials Research and Technology* 27 (2023) 5572–5593. <https://doi.org/10.1016/j.jmrt.2023.10.273>.
- [78] A. Akhtar, E. Teghtsoonian, Solid solution strengthening of magnesium single crystals—ii the effect of solute on the ease of prismatic slip, *Acta Metallurgica* 17 (1969) 1351–1356. [https://doi.org/10.1016/0001-6160\(69\)90152-7](https://doi.org/10.1016/0001-6160(69)90152-7).
- [79] X. Liu, W.A. Curtin, Mechanism of thermally-activated prismatic slip in Mg, *Acta Mater* 262 (2024). <https://doi.org/10.1016/j.actamat.2023.119402>.
- [80] Y.N. Wang, C.I. Chang, C.J. Lee, H.K. Lin, J.C. Huang, Texture and weak grain size dependence in friction stir processed Mg-Al-Zn alloy, *Scr Mater* 55 (2006) 637–640. <https://doi.org/10.1016/j.scriptamat.2006.06.005>.
- [81] Y. Chino, M. Mabuchi, R. Kishihara, H. Hosokawa, Y. Yamada, K. Shimojima, H. Iwasaki, Mechanical Properties and Press Formability at Room Temperature of AZ31 Mg Alloy Processed by Single Roller Drive Rolling, 2002.
- [82] H. Yu, Y. Xin, M. Wang, Q. Liu, Hall-Petch relationship in Mg alloys: A review, *J Mater Sci Technol* 34 (2018) 248–256. <https://doi.org/10.1016/j.jmst.2017.07.022>.

- [83] Y. Wang, H. Choo, Influence of texture on Hall-Petch relationships in an Mg alloy, *Acta Mater* 81 (2014) 83–97. <https://doi.org/10.1016/j.actamat.2014.08.023>.
- [84] W. Yuan, S.K. Panigrahi, J. Su, R.S. Mishra, Influence of grain size and texture on Hall – Petch relationship for a magnesium alloy, *Scr Mater* 65 (2011) 994–997. <https://doi.org/10.1016/j.scriptamat.2011.08.028>.
- [85] A. Jain, O. Duygulu, D.W. Brown, C.N. Tomé, S.R. Agnew, Grain size effects on the tensile properties and deformation mechanisms of a magnesium alloy, AZ31B, sheet, *Materials Science and Engineering: A* 486 (2008) 545–555. <https://doi.org/10.1016/j.msea.2007.09.069>.
- [86] D. Kim, J.H. Kim, M.G. Lee, Y.S. Lee, S.H. Kang, J.H. Kim, M.G. Lee, Y.S. Lee, S.H.K. Experimental, D. Kim, J.H. Kim, M. Lee, Y.S. Lee, S. Kang, Experimental investigation into effect of annealing treatment on springback of magnesium alloy sheets Experimental investigation into effect of annealing treatment on springback of magnesium alloy sheets, 8917 (2013). <https://doi.org/10.1179/143307511X12858956848191>.
- [87] R. Armstrong, I. Codd, R.M. Douthwaite, N.J. Petch, The plastic deformation of polycrystalline aggregates, *Philosophical Magazine* 7 (1962) 45–58. <https://doi.org/10.1080/14786436208201857>.
- [88] D. V. Wilson, J.A. Chapman, Effects of preferred orientation on the grain size dependence of yield strength in metals, *Philosophical Magazine* 8 (1963) 1543–1551. <https://doi.org/10.1080/14786436308207317>.
- [89] D. Wu, J. Zhang, J.C. Huang, H. Bei, T.G. Nieh, Grain-boundary strengthening in nanocrystalline chromium and the Hall-Petch coefficient of body-centered cubic metals, *Scr Mater* 68 (2013) 118–121. <https://doi.org/10.1016/j.scriptamat.2012.09.025>.
- [90] R.W. Armstrong, Theory of the tensile ductile-brittle behavior of poly-crystalline h.c.p. materials, with application to beryllium, *Acta Metallurgica* 16 (1968) 347–355. [https://doi.org/10.1016/0001-6160\(68\)90021-7](https://doi.org/10.1016/0001-6160(68)90021-7).
- [91] H. Yu, Y. Xin, M. Wang, Q. Liu, Hall-Petch relationship in Mg alloys: A review, *J Mater Sci Technol* 34 (2018) 248–256. <https://doi.org/10.1016/j.jmst.2017.07.022>.
- [92] H. Yu, C. Li, Y. Xin, A. Chapuis, X. Huang, Q. Liu, The mechanism for the high dependence of the Hall-Petch slope for twinning/slip on texture in Mg alloys, *Acta Mater* 128 (2017) 313–326. <https://doi.org/10.1016/j.actamat.2017.02.044>.

- [93] F. Guo, H. Yu, C. Wu, Y. Xin, C. He, Q. Liu, The mechanism for the different effects of texture on yield strength and hardness of Mg alloys, *Sci Rep* 7 (2017). <https://doi.org/10.1038/s41598-017-08966-z>.
- [94] B. Guan, Y. Xin, X. Huang, P. Wu, Q. Liu, Quantitative prediction of texture effect on Hall–Petch slope for magnesium alloys, *Acta Mater* 173 (2019) 142–152. <https://doi.org/10.1016/j.actamat.2019.05.016>.
- [95] J.J. Hoyt, M. Asta, A. Karma, Atomistic and continuum modeling of dendritic solidification, *Materials Science and Engineering R: Reports* 41 (2003) 121–163. [https://doi.org/10.1016/S0927-796X\(03\)00036-6](https://doi.org/10.1016/S0927-796X(03)00036-6).
- [96] S. Henry, P. Jarry, P.-H. Jouneau, M. Rappaz, Electron Backscattered Diffraction Investigation of the Texture of Feathery Crystals in Aluminum Alloys, *Metall Mater Trans A* 28 (1997) 207–213. <https://doi.org/https://doi.org/10.1007/s11661-997-0097-3>.
- [97] S. Henry, T. Minghetti, M. Rappaz, Dendrite growth morphologies in Aluminium alloys, *Acta Mater* 46 (1998) 6431–6443. [https://doi.org/https://doi.org/10.1016/S1359-6454\(98\)00308-5](https://doi.org/https://doi.org/10.1016/S1359-6454(98)00308-5).
- [98] A.S. Moroz, Y. Durandet, M. Rappaz, EBSD characterization of dendrite growth directions, texture and misorientations in hot-dipped Al–Zn–Si coatings, *Acta Mater* 49 (2001) 529–541. [https://doi.org/https://doi.org/10.1016/S1359-6454\(00\)00322-0](https://doi.org/https://doi.org/10.1016/S1359-6454(00)00322-0).
- [99] F. Gonzales, M. Rappaz, Dendrite Growth Directions in Aluminum-Zinc Alloys, *Metall Mater Trans A* 37 (2006) 2797–2806. <https://doi.org/https://doi.org/10.1007/BF02586112>.
- [100] J. Friedli, J.L. Fife, P. Di Napoli, M. Rappaz, X-ray tomographic microscopy analysis of the dendrite orientation transition in Al-Zn, in: *IOP Conf Ser Mater Sci Eng*, 2012. <https://doi.org/10.1088/1757-899X/33/1/012034>.
- [101] J.Y. Wang, N. Li, R. Alizadeh, M.A. Monclús, Y.W. Cui, J.M. Molina-Aldareguía, J. LLorca, Effect of solute content and temperature on the deformation mechanisms and critical resolved shear stress in Mg-Al and Mg-Zn alloys, *Acta Mater* 170 (2019) 155–165. <https://doi.org/10.1016/j.actamat.2019.03.027>.
- [102] J. Du, A. Zhang, Z. Guo, M. Yang, M. Li, F. Liu, S. Xiong, Effect of additional solute elements (X= Al, Ca, Y, Ba, Sn, Gd and Zn) on crystallographic anisotropy during the dendritic growth of magnesium alloys, *J Alloys Compd* 775 (2019) 322–329. <https://doi.org/10.1016/j.jallcom.2018.10.145>.
- [103] J.D. Roehling, D.R. Coughlin, J.W. Gibbs, J.K. Baldwin, J.C.E. Mertens, G.H. Campbell, A.J. Clarke, J.T. McKeown, Rapid solidification growth mode

transitions in Al-Si alloys by dynamic transmission electron microscopy, *Acta Mater* 131 (2017) 22–30. <https://doi.org/10.1016/j.actamat.2017.03.061>.

- [104] O. Uzun, T. Karaaslan, M. Gogebakan, M. Keskin, Hardness and microstructural characteristics of rapidly solidified Al-8-16 wt.%Si alloys, *J Alloys Compd* 376 (2004) 149–157. <https://doi.org/10.1016/j.jallcom.2004.01.017>.
- [105] L.L. Ge, R.P. Liu, G. Li, M.Z. Ma, W.K. Wang, Solidification of Al-50 at.%Si alloy in a drop tube, *Materials Science and Engineering: A* 385 (2004) 128–132. <https://doi.org/10.1016/j.msea.2004.06.037>.
- [106] B.J.E. Dorn, Some fundamental experiments on high temperature creep, *J Mech Phys Solids* 8 (1954) 85–116. [https://doi.org/https://doi.org/10.1016/0022-5096\(55\)90054-5](https://doi.org/https://doi.org/10.1016/0022-5096(55)90054-5).
- [107] R.L. Carlson, Investigation of compressive-creep properties of Aluminium columns at elevated temperatures, Battelle Memorial Institute (1952). <https://doi.org/https://apps.dtic.mil/sti/tr/pdf/ADA076046.pdf>.
- [108] D. Weiss, Improved High-Temperature Aluminum Alloys Containing Cerium, *J Mater Eng Perform* 28 (2019) 1903–1908. <https://doi.org/10.1007/s11665-019-3884-2>.
- [109] L. Wang, R. Qi, B. Ye, Communication Improved Tensile Strength of Al-5Ce Alloy by Permanent Magnet Stirring, *Metallurgical and Materials Transactions A* 51 (2020) 1972–1977. <https://doi.org/10.1007/s11661-020-05723-2>.
- [110] K.A. Gschneidner, M.E. Verkade, Selected cerium phase diagrams, 1974.
- [111] M.C. Gao, N. Ünlü, G.J. Shiflet, M. Mihalkovic, M. Widom, Reassessment of Al-Ce and Al-Nd binary systems supported by critical experiments and first-principles energy calculations, *Metall Mater Trans A Phys Metall Mater Sci* 36 (2005) 3269–3279. <https://doi.org/10.1007/s11661-005-0001-y>.
- [112] F. Czerwinski, F. Czerwinski, Critical Assessment 36 : Assessing differences between the use of cerium and scandium in aluminium alloying scandium in aluminium alloying, 0836 (2020). <https://doi.org/10.1080/02670836.2019.1702775>.
- [113] F. Czerwinski, On the Al–Al₁₁Ce₃ Eutectic Transformation in Aluminum–Cerium Binary Alloys, *Materials* 13 (2020). <https://doi.org/https://doi.org/10.3390/ma13204549>.
- [114] F. Czerwinski, Cerium in aluminum alloys, *J Mater Sci* 55 (2020) 24–72. <https://doi.org/10.1007/s10853-019-03892-z>.

- [115] Aoke Jiang, Solidification Behaviors of Proeutectic Al₃Sc and Al- Al₃Sc Eutectic in Hypereutectic Al-Sc Undercooled, Purdue University , 2021.
- [116] A.B. Shubin, K.Y. Shunyaev, T. V Kulikova, Problem of the Thermodynamic Properties of Liquid Aluminum Alloys with Scandium, 2008 (2008) 364–369. <https://doi.org/10.1134/S0036029508050029>.
- [117] D.N. Seidman, E.A. Marquis, D.C. Dunand, Precipitation strengthening at ambient and elevated temperatures of heat-treatable Al (Sc) alloys, 50 (2002) 4021–4035. [https://doi.org/https://doi.org/10.1016/S1359-6454\(02\)00201-X](https://doi.org/https://doi.org/10.1016/S1359-6454(02)00201-X).
- [118] N.Q. Vo, D.C. Dunand, D.N. Seidman, Improving aging and creep resistance in a dilute Al-Sc alloy by microalloying with Si, Zr and Er, Acta Mater 63 (2014) 73–85. <https://doi.org/10.1016/j.actamat.2013.10.008>.
- [119] K.E. Knipling, D.C. Dunand, D.N. Seidman, Nucleation and Precipitation Strengthening in Dilute Al-Ti and Al-Zr Alloys, 38 (2007). <https://doi.org/10.1007/s11661-007-9283-6>.
- [120] A. Deschamps, L. Lae, P. Guyot, In situ small-angle scattering study of the precipitation kinetics in an Al – Zr – Sc alloy, 55 (2007) 2775–2783. <https://doi.org/10.1016/j.actamat.2006.12.015>.
- [121] L. Wang, B. Ye, Y. Bai, B. Zhao, W. Ding, Materials Science & Engineering A Effect of Zr and Sc micro-additions on the microstructure and mechanical properties of as-cast Al-5Ce alloy, Materials Science & Engineering A 822 (2021) 141654. <https://doi.org/10.1016/j.msea.2021.141654>.
- [122] H.A. Hanna, F. Shehata, Friction and wear of Al-Si alloys, Lubrication Engineering 49 (1993) 473–476. <https://doi.org/10.1361/asmhba00>.
- [123] H.R. Ammar, M. Baig, A.H. Seikh, J.A. Mohhamed, Effect of alloying elements on thermal stability of nanocrystalline Al alloys, Transactions of Nonferrous Metals Society of China (English Edition) 31 (2021) 11–23. [https://doi.org/10.1016/S1003-6326\(20\)65475-9](https://doi.org/10.1016/S1003-6326(20)65475-9).
- [124] A.S. Anasyida, A.R. Daud, M.J. Ghazali, Dry sliding wear behaviour of Al-12Si-4Mg alloy with cerium addition, Mater Des 31 (2010) 365–374. <https://doi.org/10.1016/j.matdes.2009.06.007>.
- [125] Z. Lu, X. Li, L. Zhang, Thermodynamic Description of Al-Si-Mg-Ce Quaternary System in Al-Rich Corner and Its Experimental Validation, J Phase Equilibria Diffus 39 (2018) 57–67. <https://doi.org/10.1007/s11669-017-0607-y>.
- [126] O. Adole, Influence of Al-Nb-B grain refiner addition on the microstructure of aluminium alloys, Brunel University , 2022.

- [127] X. Dong, H. Yang, X. Zhu, S. Ji, High strength and ductility aluminium alloy processed by high pressure die casting, *J Alloys Compd* 773 (2019) 86–96. <https://doi.org/10.1016/j.jallcom.2018.09.260>.
- [128] C.A. Schneider, W.S. Rasband, K.W. Eliceiri, NIH Image to ImageJ: 25 years of image analysis, *Nat Methods* 9 (2012) 671–675. <https://doi.org/10.1038/nmeth.2089>.
- [129] R.K. Biswas, F. Bin Ahmed, M.E. Haque, A.A. Provasha, Z. Hasan, F. Hayat, D. Sen, Effects of Steel Fiber Percentage and Aspect Ratios on Fresh and Harden Properties of Ultra-High Performance Fiber Reinforced Concrete, *Applied Mechanics* 2 (2021) 501–515. <https://doi.org/10.3390/applmech2030028>.
- [130] C. Igathinathane, L.O. Pordesimo, E.P. Columbus, W.D. Batchelor, S.R. Methuku, Shape identification and particles size distribution from basic shape parameters using ImageJ, *Comput Electron Agric* 63 (2008) 168–182. <https://doi.org/10.1016/j.compag.2008.02.007>.
- [131] Z. Gácsi, The application of digital image processing to materials science, in: *Materials Science Forum*, Trans Tech Publications Ltd, 2003: pp. 213–220. <https://doi.org/10.4028/www.scientific.net/msf.414-415.213>.
- [132] B. Beausir, J.J. Fundenberger, Analysis Tools for Electron and X-Ray Diffraction, ATEX - Software. Universite de Lorraine-Metz.www.atex-software.eu, Analysis Tools for Electron and X-Ray Diffraction, ATEX - Software (2017).
- [133] M., Humbert, F., Wagner, H., Moustahfid, C. Esling, Determination of the Orientation of a Parent [beta] Grain from the Orientations of the Inherited [alpha] Plates in the Phase Transformation from Body-Centred Cubic to Hexagonal Close Packed, *J Appl Crystallogr* 28 (1995) 571–576.
- [134] X. Yang, Particle Dispersion in Aluminium and Magnesium Alloys, 2016.
- [135] M. Xu, D. Fralick, J.Z. Zheng, B. Wang, X.M. Tu, C. Feng, The differences and similarities between two-sample t-test and paired t-test, *Shanghai Arch Psychiatry* 29 (2017) 184–188. <https://doi.org/10.11919/j.issn.1002-0829.217070>.
- [136] N.C. Matthew King, C. Ponay, D. Keen Domingo, N. Matthew King, J. Lorenzo Lopez, A. Mondares, FilCon: Filipino Sentiment Lexicon Generation Using Word Level-Annotated Dictionary-Based and Corpus-Based Cross Lingual Approach, 2015. <https://www.researchgate.net/publication/279947154>.
- [137] N. Limodin, L. Salvo, E. Boller, M. Suéry, M. Felberbaum, S. Gailliègue, K. Madi, In situ and real-time 3-D microtomography investigation of dendritic solidification in an Al-10 wt.% Cu alloy, *Acta Mater* 57 (2009) 2300–2310. <https://doi.org/10.1016/j.actamat.2009.01.035>.

- [138] O. Ludwig, M. Dimichiel, L. Salvo, M. Suéry, P. Falus, In-situ Three-Dimensional Microstructural Investigation of Solidification of an Al-Cu Alloy by Ultrafast X-Ray Microtomography, *Metall Mater Trans A* 36 (2005) 1515–1523. <https://doi.org/10.1007/s11661-005-0243-8>.
- [139] L. Sturz, A. Theofilatos, Two-dimensional multi-scale dendrite needle network modeling and x-ray radiography of equiaxed alloy solidification in grain-refined Al-3.5 wt-%Ni, *Acta Mater* 117 (2016) 356–370. <https://doi.org/10.1016/j.actamat.2016.06.005>.
- [140] A. Bogno, H. Nguyen-Thi, G. Reinhart, B. Billia, J. Baruchel, Growth and interaction of dendritic equiaxed grains: In situ characterization by synchrotron X-ray radiography, *Acta Mater* 61 (2013) 1303–1315. <https://doi.org/10.1016/j.actamat.2012.11.008>.
- [141] D. V. Alexandrov, P.K. Galenko, The shape of dendritic tips, *Philosophical Transactions of the Royal Society A: Mathematical, Physical and Engineering Sciences* 378 (2020). <https://doi.org/10.1098/rsta.2019.0243>.
- [142] Engineering fundamentals, Parabola - arc length, (n.d.). <https://www.efunda.com/math/areas/IndexArea.cfm> (accessed August 1, 2024).
- [143] Y. Li, J. Liu, W. Huang, S. Zhang, Microstructure related analysis of tensile and fatigue properties for sand casting aluminum alloy cylinder head, *Eng Fail Anal* 136 (2022). <https://doi.org/10.1016/j.engfailanal.2022.106210>.
- [144] K. Ishfaq, M.A. Ali, N. Ahmad, S. Zahoor, A.M. Al-Ahmari, F. Hafeez, Modelling the mechanical attributes (roughness, strength, and hardness) of Al-alloy A356 during sand casting, *Materials* 13 (2020). <https://doi.org/10.3390/ma13030598>.
- [145] M. Okayasu, S. Takeuchi, M. Yamamoto, H. Ohfuji, T. Ochi, Precise Analysis of Microstructural Effects on Mechanical Properties of Cast ADC12 Aluminum Alloy, *Metall Mater Trans A Phys Metall Mater Sci* 46 (2015) 1597–1609. <https://doi.org/10.1007/s11661-015-2747-1>.
- [146] F. Nikolić, I. Štajduhar, M. Čanadija, Casting microstructure inspection using computer vision: Dendrite spacing in aluminum alloys, *Metals (Basel)* 11 (2021). <https://doi.org/10.3390/met11050756>.
- [147] E. Hajjari, M. Divandari, An investigation on the microstructure and tensile properties of direct squeeze cast and gravity die cast 2024 wrought Al alloy, *Mater Des* 29 (2008) 1685–1689. <https://doi.org/10.1016/j.matdes.2008.04.012>.
- [148] R.C. Sales, P.F. Junior, K.G. Paradela, W.J.L. Garção, A.F. Ferreira, Effect of solidification processing parameters and silicon content on the dendritic spacing

- and hardness in hypoeutectic Al-Si alloys, *Materials Research* 21 (2018).
<https://doi.org/10.1590/1980-5373-MR-2018-0333>.
- [149] C.D. Ridgeway, C. Gu, A.A. Luo, Predicting primary dendrite arm spacing in Al–Si–Mg alloys: effect of Mg alloying, *J Mater Sci* (2019).
<https://doi.org/10.1007/s10853-019-03558-w>.
- [150] Q.C. Jiang, C.L. Xu, H.Y. Wang, J.G. Wang, Y.F. Yang, Estimation of the shifting distance of the eutectic point in hypereutectic Al-Si alloys by the lever rule, *Scr Mater* 56 (2007) 329–332.
<https://doi.org/10.1016/j.scriptamat.2006.11.023>.
- [151] D.D. Reeves, T.Z. Kattamis, A model for isothermal coarsening, *Scripta Metallurgica* 5 (1971) 223–230. [https://doi.org/https://doi.org/10.1016/0036-9748\(71\)90013-5](https://doi.org/https://doi.org/10.1016/0036-9748(71)90013-5).
- [152] T. Okamoto, K. Kishitake, Dendritic structure in unidirectionally solidified aluminium, tin, and zinc base binary alloys, *J Cryst Growth* 29 (1975).
[https://doi.org/https://doi.org/10.1016/0022-0248\(75\)90217-1](https://doi.org/https://doi.org/10.1016/0022-0248(75)90217-1).
- [153] F. Vnuk, M. Sahoo, R. Van De Merwe, R.W. Smith, The hardness of Al-Si eutectic alloys, *Journal of Material Science* 14 (1979) 975–982.
<https://doi.org/10.1007/BF00550730>.
- [154] S. Khan, A. Ourdjini, Q.S. Hamed, M.A.A. Najafabadi, R. Elliott, Hardness and mechanical property relationships in directionally solidified aluminium-silicon eutectic alloys with different silicon morphologies, *J Mater Sci* 28 (1993) 5957–5962. <https://doi.org/10.1007/BF00365208>.
- [155] P. Zhang, S.X. Li, Z.F. Zhang, General relationship between strength and hardness, *Materials Science and Engineering A* 529 (2011) 62–73.
<https://doi.org/10.1016/j.msea.2011.08.061>.
- [156] R. Kakitani, R. V. Reyes, A. Garcia, J.E. Spinelli, N. Cheung, Relationship between spacing of eutectic colonies and tensile properties of transient directionally solidified Al-Ni eutectic alloy, *J Alloys Compd* 733 (2018) 59–68.
<https://doi.org/10.1016/j.jallcom.2017.10.288>.
- [157] P. Pandey, S.K. Makineni, B. Gault, K. Chattopadhyay, On the origin of a remarkable increase in the strength and stability of an Al rich Al-Ni eutectic alloy by Zr addition, *Acta Mater* 170 (2019) 205–217.
<https://doi.org/10.1016/j.actamat.2019.03.025>.
- [158] I. Baker, F. Meng, Lamellar coarsening in Fe₂₈Ni₁₈Mn₃₃Al₂₁ and its influence on room temperature tensile behavior, *Acta Mater* 95 (2015) 124–131.
<https://doi.org/10.1016/j.actamat.2015.05.006>.

- [159] L. Wang, B. Ye, W. Huang, W. Ding, Theoretical model of yield strength for eutectic colony microstructure materials, *Scr Mater* 231 (2023). <https://doi.org/10.1016/j.scriptamat.2023.115443>.
- [160] M. Gündüz, H. Kaya, E. Çadirli, A. Özmen, Interflake spacings and undercoolings in Al-Si irregular eutectic alloy, *Materials Science and Engineering: A* 369 (2004) 215–229. <https://doi.org/10.1016/j.msea.2003.11.020>.
- [161] I. Toda-Caraballo, E.I. Galindo-Nava, P.E.J. Rivera-Díaz-Del-Castillo, Understanding the factors influencing yield strength on Mg alloys, *Acta Mater* 75 (2014) 287–296. <https://doi.org/10.1016/j.actamat.2014.04.064>.
- [162] J.C.F. Millett, S.J. Fensin, G.D. Owen, B.P. Eftink, C. Lear, G. Whiteman, G.T. Gray, The mechanical and microstructural response of single crystal aluminium to one dimensional shock loading: The effects of orientation, *Acta Mater* 246 (2023). <https://doi.org/10.1016/j.actamat.2023.118727>.
- [163] W.F. Hosford, R.L. Fleischer, W.A. Backofen, Tensile deformation of aluminum single crystals at low temperatures, *Acta Metallurgica* 8 (1960) 187–199. [https://doi.org/https://doi.org/10.1016/0001-6160\(60\)90127-9](https://doi.org/https://doi.org/10.1016/0001-6160(60)90127-9).
- [164] J.H. Wu, W.Y. Tsai, J.C. Huang, C.H. Hsieh, G.R. Huang, Sample size and orientation effects of single crystal aluminum, *Materials Science and Engineering: A* 662 (2016) 296–302. <https://doi.org/10.1016/j.msea.2016.03.076>.
- [165] D. Zhou, H. Wang, D.W. Saxey, O. Muránsky, H. Geng, W.D.A. Rickard, Z. Quadir, C. Yang, S.M. Reddy, D. Zhang, Hall–Petch Slope in Ultrafine Grained Al-Mg Alloys, *Metall Mater Trans A Phys Metall Mater Sci* 50 (2019) 4047–4057. <https://doi.org/10.1007/s11661-019-05329-3>.
- [166] R.L. Fleischer, Substitutional solution hardening, *Acta Metallurgica* 11 (1963) 203–208. [https://doi.org/https://doi.org/10.1016/0001-6160\(63\)90213-X](https://doi.org/https://doi.org/10.1016/0001-6160(63)90213-X).
- [167] D. Tabor, The hardness of solids, *Review of Physics in Technology* 1 (1970) 145–179. <https://doi.org/10.1088/0034-6683/1/3/I01>.
- [168] M. Liu, H. Fu, C. Xu, W. Xiao, Q. Peng, H. Yamagata, C. Ma, Precipitation kinetics and hardening mechanism in Al-Si solid solutions processed by high pressure solution treatment, *Materials Science and Engineering: A* 712 (2018) 757–764. <https://doi.org/10.1016/j.msea.2017.12.033>.
- [169] Hisao Mii, Senoo Masafumi, Fujishiro Ikulya, Solid solubility of Si in Al under high pressure, *Jpn J Appl Phys* 15 (1975) 777–783. <https://doi.org/10.1143/JJAP.15.777>.

- [170] G. Mann, J.R. Griffiths, C.H. Cáceres, Hall-Petch parameters in tension and compression in cast Mg-2Zn alloys, in: *J Alloys Compd*, 2004: pp. 188–191. <https://doi.org/10.1016/j.jallcom.2003.12.052>.
- [171] Y.N. Wang, J.C. Huang, Texture analysis in hexagonal materials, *Mater Chem Phys* 81 (2003) 11–26. [https://doi.org/10.1016/S0254-0584\(03\)00168-8](https://doi.org/10.1016/S0254-0584(03)00168-8).
- [172] A. Godon, J. Creus, S. Cohendoz, E. Conforto, X. Feaugas, P. Girault, C. Savall, Effects of grain orientation on the Hall-Petch relationship in electrodeposited nickel with nanocrystalline grains, *Scr Mater* 62 (2010) 403–406. <https://doi.org/10.1016/j.scriptamat.2009.11.038>.
- [173] J. Friedli, J.L. Fife, P. Di Napoli, M. Rappaz, Dendritic growth morphologies in Al-Zn alloys - Part I: X-ray tomographic microscopy, in: *Metall Mater Trans A Phys Metall Mater Sci*, 2013: pp. 5522–5531. <https://doi.org/10.1007/s11661-013-1912-7>.
- [174] M. Becker, J.A. Dantzig, M. Kolbe, S.T. Wiese, F. Kargl, Dendrite orientation transition in Al-Ge alloys, *Acta Mater* 165 (2019) 666–677. <https://doi.org/10.1016/j.actamat.2018.12.001>.
- [175] J. Friedli, P. Di Napoli, M. Rappaz, J.A. Dantzig, Phase-field modeling of the dendrite orientation transition in Al-Zn alloys, in: *IOP Conf Ser Mater Sci Eng*, 2012. <https://doi.org/10.1088/1757-899X/33/1/012111>.
- [176] S. Wilkerson, S.D. Wilkerson, *Application of the Paired t-test*, 2008.
- [177] Z.C. Sims, O.R. Rios, D. Weiss, P.E.A. Turchi, A. Perron, J.R.I. Lee, T. Tian, J.A. Hammons, M. Bagge-hansen, T.M. Willey, K. An, Y. Chen, A.H. King, S.K. McCall, High Performance Aluminum-Cerium Alloys for High- Temperature Applications, *JOM* 68 (2016) 1940–1947. <https://doi.org/https://doi.org/10.1007/s11837-016-1943-9>.
- [178] F. Czerwinski, B.S. Amirkhiz, On the Al-Al₁₁Ce₃ eutectic transformation in aluminum-cerium binary alloys, *Materials* 13 (2020) 1–27. <https://doi.org/10.3390/ma13204549>.
- [179] D. Weiss, O.R. Rios, Z.C. Sims, S.K. McCall, R.T. Ott, Casting Characteristics of High Cerium Content Aluminum Alloys, *Light Metals 2017. The Minerals, Metals & Materials Series*. Springer, Cham. (2017). https://doi.org/https://doi.org/10.1007/978-3-319-51541-0_28.
- [180] M. Wu, S. Xiong, Modeling of microstructure evolution of magnesium alloy during the high pressure die casting process, in: *IOP Conf Ser Mater Sci Eng*, 2012. <https://doi.org/10.1088/1757-899X/33/1/012078>.

- [181] P. Prakash, D. Toscano, S.K. Shaha, M.A. Wells, H. Jahed, B.W. Williams, Effect of temperature on the hot deformation behavior of AZ80 magnesium alloy, *Materials Science and Engineering: A* 794 (2020). <https://doi.org/10.1016/j.msea.2020.139923>.
- [182] R. Shi, Nonisothermal dissolution kinetics on Mg₁₇Al₁₂ intermetallic in Mg-Al alloys, *Journal of Magnesium and Alloys* 10 (2022) 2421–2432. <https://doi.org/10.1016/j.jma.2021.02.007>.
- [183] Y. Tamura, Y. Kida, H. Tamehiro, N. Kono, H. Soda, A. McLean, The effect of manganese on the precipitation of Mg₁₇Al₁₂ phase in magnesium alloy AZ 91, *J Mater Sci* 43 (2008) 1249–1258. <https://doi.org/10.1007/s10853-007-2276-4>.
- [184] G. Zeng, J.W. Xian, C.M. Gourlay, Nucleation and growth crystallography of Al₈Mn₅ on B₂-Al(Mn,Fe) in AZ91 magnesium alloys, *Acta Mater* 153 (2018) 364–376. <https://doi.org/10.1016/j.actamat.2018.04.032>.
- [185] C.H. Cáceres, A. Blake, The strength of concentrated Mg-Zn solid solutions, *Physica Status Solidi A Appl Res* 194 (2002) 147–158. [https://doi.org/10.1002/1521-396X\(200211\)194:1<147::AID-PSSA147>3.0.CO;2-L](https://doi.org/10.1002/1521-396X(200211)194:1<147::AID-PSSA147>3.0.CO;2-L).
- [186] C. Labrecque, R. Angers, R. Tremblay, D. Dublin, Inverted disk centrifugal atomization of AZ91 magnesium alloy, *Canadian Metallurgical Quarterly* 36 (1997) 169–175. [https://doi.org/https://doi.org/10.1016/S0008-4433\(97\)00007-4](https://doi.org/https://doi.org/10.1016/S0008-4433(97)00007-4).
- [187] Sequeira .W.P., Murray M.T., Dunlop G.L., StJohn. D.H., Proc. TMS Symposium on automotive alloys, Proc. TMS Symposium on Automotive Alloys (February 9–13, Orlando, FA.), The Minerals Metals and Materials Society (TMS), Warrendale, PA (1997) 169–183.
- [188] Md.I. Khan, A.O. Mostafa, M. Aljarrah, E. Essadiqi, M. Medraj, Influence of Cooling Rate on Microsegregation Behavior of Magnesium Alloys, *J Mater* 2014 (2014) 1–18. <https://doi.org/10.1155/2014/657647>.
- [189] E. Azqadan, J. Uramowski, A.A. Roostaei, S.B. Behraves, A. Javaid, B.W. Williams, M.A. Wells, H. Jahed, The effect of cooling rate and degassing on microstructure and mechanical properties of cast AZ80 magnesium alloy, *Materials Science and Engineering: A* 844 (2022). <https://doi.org/10.1016/j.msea.2022.143176>.
- [190] R. Sarvesha, W. Alam, A. Gokhale, T.S. Guruprasad, S. Bhagavath, S. Karagadde, J. Jain, S.S. Singh, Quantitative assessment of second phase particles characteristics and its role on the deformation response of a Mg-8Al-0.5Zn alloy, *Materials Science and Engineering: A* 759 (2019) 368–379. <https://doi.org/10.1016/j.msea.2019.05.052>.

- [191] J. Wang, L. Niu, Y. Zhang, J. Chen, J. Jiang, D. Song, B. Li, G. Ying, J. Cheng, A. Ma, Is Mg₁₇Al₁₂ ductile or brittle? A theoretical insight, *Journal of Magnesium and Alloys* 11 (2023) 936–944. <https://doi.org/10.1016/j.jma.2021.06.006>.
- [192] R.P. Thompson, W.J. Clegg, Predicting whether a material is ductile or brittle, *Curr Opin Solid State Mater Sci* 22 (2018) 100–108. <https://doi.org/10.1016/j.cossms.2018.04.001>.
- [193] Z. Xu, L. Huang, M. Li, Z. Zhu, C. Liu, Influences of Mg₁₇Al₁₂ Phase Morphology on the Mechanical Properties of AZ80 Magnesium Alloy Subjected to Aging, *Metals (Basel)* 12 (2022). <https://doi.org/10.3390/met12060928>.
- [194] J.Y. Li, J.X. Xie, J.B. Jin, Z.X. Wang, Microstructural evolution of AZ91 magnesium alloy during extrusion and heat treatment, *Transactions of Nonferrous Metals Society of China (English Edition)* 22 (2012) 1028–1034. [https://doi.org/10.1016/S1003-6326\(11\)61279-X](https://doi.org/10.1016/S1003-6326(11)61279-X).
- [195] S. Kumar, D. Kumar, J. Jain, J.K. Hirwani, Influence of load, sliding speed, and microstructure on wear response of AZ91 Mg alloy, *Proceedings of the Institution of Mechanical Engineers, Part J: Journal of Engineering Tribology* 230 (2016) 1462–1469. <https://doi.org/10.1177/1350650116638601>.
- [196] Z. wei Wang, H. Yan, W. xian Huang, Effect of solution treatment on microstructure and hardness of rheo-forming AZ91-Y alloy, *China Foundry* 13 (2016) 383–388. <https://doi.org/10.1007/s41230-016-6053-3>.
- [197] J.H. Jun, Effect of solution treatment on mechanical properties of cast AZ91-(Ca) alloys, *Archives of Metallurgy and Materials* 64 (2019) 265–269. <https://doi.org/10.24425/amm.2019.126247>.
- [198] W. Zhou, A. Aprilia, C.K. Mark, Mechanisms of cracking in laser welding of magnesium alloy AZ91D, *Metals (Basel)* 11 (2021). <https://doi.org/10.3390/met11071127>.
- [199] C. Do Lee, Effect of grain size on the tensile properties of magnesium alloy, *Materials Science and Engineering: A* 459 (2007) 355–360. <https://doi.org/10.1016/j.msea.2007.01.008>.
- [200] C. Weiping, Diffusion of cerium in the aluminium lattice, *Journal of Material Science Letters* 16 (1997) 1824–1826. <https://doi.org/https://link.springer.com/content/pdf/10.1023/A:1018572803223.pdf>.
- [201] Y. Liu, R.A. Michi, D.C. Dunand, Cast near-eutectic Al-12.5 wt.% Ce alloy with high coarsening and creep resistance, *Materials Science and Engineering: A* 767 (2019). <https://doi.org/10.1016/j.msea.2019.138440>.

- [202] K.E. Knipling, D.N. Seidman, D.C. Dunand, Ambient- and high-temperature mechanical properties of isochronally aged Al-0.06Sc, Al-0.06Zr and Al-0.06Sc-0.06Zr (at.%) alloys, *Acta Mater* 59 (2011) 943–954. <https://doi.org/10.1016/j.actamat.2010.10.017>.
- [203] D. Pan, S. Zhou, Z. Zhang, M. Li, Y. Wu, D. Pan, S. Zhou, Z. Zhang, M. Li, Y. Wu, Effects of Sc (Zr) on the microstructure and mechanical properties of as-cast Al – Mg alloys Effects of Sc (Zr) on the microstructure and mechanical properties of as-cast Al – Mg alloys, 0836 (2017). <https://doi.org/10.1080/02670836.2016.1270573>.
- [204] M. Ibrahim, M. Abdelaziz, A. Samuel, H. Doty, F. Samuel, Spheroidization and Coarsening of Eutectic Si Particles in Al-Si-Based Alloys, *Advances in Materials Science and Engineering 2021* (2021). <https://doi.org/10.1155/2021/6678280>.
- [205] J. Wang, J. Zhu, Y. Liu, H. Peng, X. Su, Effect of spheroidization of eutectic Si on mechanical properties of eutectic Al-Si alloys, *J Mater Res* 33 (2018) 1773–1781. <https://doi.org/10.1557/jmr.2018.144>.
- [206] V. Páramo, R. Colás, E. Velasco, S. Valtierra, Spheroidization of the Al-Si Eutectic in a Cast Aluminum Alloy, *J. of Materi Eng and Performance* 9 (2000) 616–622. <https://doi.org/https://doi.org/10.1361/105994900770345467>.
- [207] E. Ogris Dipl, Development of Al-Si-Mg Alloys for Semi-Solid Processing and Silicon Spheroidization Treatment (SST) for Al-Si Cast Alloys, 2002. <https://doi.org/https://www.research-collection.ethz.ch/bitstream/handle/20.500.11850/147109/eth-26100-01.pdf>.
- [208] E. Ogris, H. Lüchinger, P.J. Uggowitzer, Silicon spheroidization treatment of thixoformed Al-Si-Mg alloys, *Materials Science Forum* 396–402 (2002) 149–154. <https://doi.org/10.4028/www.scientific.net/msf.396-402.149>.
- [209] G. Requena, G. Garcés, M. Rodríguez, T. Pirling, P. Cloetens, 3D architecture and load partition in eutectic Al-Si alloys, *Adv Eng Mater* 11 (2009) 1007–1014. <https://doi.org/10.1002/adem.200900218>.
- [210] F. Lasagni, A. Lasagni, E. Marks, C. Holzapfel, F. Mücklich, H.P. Degischer, Three-dimensional characterization of “as-cast” and solution-treated AlSi12(Sr) alloys by high-resolution FIB tomography, *Acta Mater* 55 (2007) 3875–3882. <https://doi.org/10.1016/j.actamat.2007.03.004>.
- [211] F.C. Robles Hernández, J.H. Sokolowski, Comparison among chemical and electromagnetic stirring and vibration melt treatments for Al-Si hypereutectic alloys, *J Alloys Compd* 426 (2006) 205–212. <https://doi.org/10.1016/j.jallcom.2006.09.039>.

- [212] S. Nafisi, R. Ghomashchi, Grain refining of conventional and semi-solid A356 Al-Si alloy, *J Mater Process Technol* 174 (2006) 371–383. <https://doi.org/10.1016/j.jmatprotec.2006.02.012>.
- [213] K. Li, J. Zhang, X. Chen, Y. Yin, Y. He, Z. Zhou, R. Guan, Microstructure evolution of eutectic Si in Al-7Si binary alloy by heat treatment and its effect on enhancing thermal conductivity, *Journal of Materials Research and Technology* 9 (2020) 8780–8786. <https://doi.org/10.1016/j.jmrt.2020.06.021>.
- [214] F. Czerwinski, Thermal stability of aluminum–cerium binary alloys containing the Al–Al₁₁Ce₃ eutectic, *Materials Science and Engineering: A* 809 (2021). <https://doi.org/10.1016/j.msea.2021.140973>.
- [215] Z.C. Sims, D. Weiss, S.K. Mccall, M.A. Mcguire, R.T. Ott, T.O.M. Geer, O. Rios, P.A.E. Turchi, Cerium-Based , Intermetallic-Strengthened Aluminum Casting Alloy : High-Volume Co-product Development, *JOM* 68 (2016) 1940–1947. <https://doi.org/10.1007/s11837-016-1943-9>.
- [216] J.R. Grace, A. Ebneyamini, Connecting particle sphericity and circularity, *Particuology* 54 (2021) 1–4. <https://doi.org/10.1016/j.partic.2020.09.006>.
- [217] H.P. Stüwe, O. Kolednik, Shape instability of thin cylinders, *Acta Metallurgica* 36 (1988) 1705–1708.
- [218] E. Werner, The spheroidization of thin plates, *Acta Metallurgica* 37 (1989) 2047–2053. [https://doi.org/10.1016/0001-6160\(89\)90090-4](https://doi.org/10.1016/0001-6160(89)90090-4).
- [219] H. Demirtaş, E. Karakulak, N.H. Babu, Heat Treatment Conditions for High-Performance High-Pressure Die-Cast Al–Si–Cu–Mg Alloy, *Adv Eng Mater* (2023). <https://doi.org/10.1002/adem.202301196>.
- [220] W. Wang, Q. Pan, F. Jiang, Y. Yu, G. Lin, X. Wang, J. Ye, D. Pan, Z. Huang, S. Xiang, J. Li, B. Liu, Microstructure evolution and performances of Al-0.7Mg-0.6Si-0.2Ce-X (X[dbnd]Sc, Y and Zr) alloys with high strength and high electrical conductivity, *J Alloys Compd* 895 (2022). <https://doi.org/10.1016/j.jallcom.2021.162654>.
- [221] J. Xiao, Z. Zhang, J. Ye, Z. Wang, K. Dai, J. Li, R. Guan, Microstructure and property optimization of Al–8Ce alloys: Electromagnetic stirring and Sc–Zr microalloying, *Journal of Materials Research and Technology* 28 (2024) 3133–3143. <https://doi.org/10.1016/j.jmrt.2023.12.253>.
- [222] J. Ye, K. Dai, Z. Wang, J. Chen, M. Gao, R. Guan, Beneficial effects of Sc/Zr addition on hypereutectic Al–Ce alloys: Modification of primary phases and precipitation hardening, *Materials Science and Engineering: A* 835 (2022). <https://doi.org/10.1016/j.msea.2022.142611>.

- [223] S. Zhou, Z. Zhang, M. Li, D. Pan, H. Su, X. Du, P. Li, Y. Wu, Effect of Sc on microstructure and mechanical properties of as-cast Al-Mg alloys, *Mater Des* 90 (2016) 1077–1084. <https://doi.org/10.1016/j.matdes.2015.10.132>.
- [224] M. Yi, P. Zhang, C. Yang, P. Cheng, S. Guo, G. Liu, J. Sun, Improving creep resistance of Al-12 wt.% Ce alloy by microalloying with Sc, *Scr Mater* 198 (2021). <https://doi.org/10.1016/j.scriptamat.2021.113838>.
- [225] J.U. Rakhmonov, D. Weiss, D.C. Dunand, Comparing evolution of precipitates and strength upon aging of cast and laser-remelted Al–8Ce–0.2Sc–0.1Zr (wt.%), *Materials Science and Engineering: A* 840 (2022). <https://doi.org/10.1016/j.msea.2022.142990>.
- [226] A.A. Mohammed, S. Chankitmongkol, S. Wang, D.G. Eskin, U. Patakham, C. Limmaneevichitr, P. Pandee, Enhancing ambient and elevated temperature performance of hypoeutectic Al–Ce cast alloys by Al₃(Sc,Zr) precipitate, *Journal of Materials Research and Technology* 28 (2024) 1188–1197. <https://doi.org/10.1016/j.jmrt.2023.12.021>.
- [227] V. Raghavan, Al-Ce-Mg (Aluminum-Cerium-Magnesium), *J Phase Equilibria Diffus* 28 (2007) 453–455. <https://doi.org/10.1007/s11669-007-9136-4>.
- [228] X. Dong, L. Feng, S. Wang, E.A. Nyberg, S. Ji, A new die-cast magnesium alloy for applications at higher elevated temperatures of 200–300 °C, *Journal of Magnesium and Alloys* 9 (2021) 90–101. <https://doi.org/10.1016/j.jma.2020.09.012>.